General Disclaimer

One or more of the Following Statements may affect this Document

- This document has been reproduced from the best copy furnished by the organizational source. It is being released in the interest of making available as much information as possible.

- This document may contain data, which exceeds the sheet parameters. It was furnished in this condition by the organizational source and is the best copy available.

- This document may contain tone-on-tone or color graphs, charts and/or pictures, which have been reproduced in black and white.

- This document is paginated as submitted by the original source.

- Portions of this document are not fully legible due to the historical nature of some of the material. However, it is the best reproduction available from the original submission.

Produced by the NASA Center for Aerospace Information (CASI)

NATIONAL AERONAUTICS AND SPACE ADMINISTRATION

The Deep Space Network
Progress Report 42-36

September and October 1976

(NASA-CR-149275) THE DEEP SPACE NETWORK Progress Report, Sep. - Oct. 1976 (Jet Propulsion Lab.) 163 p HC A08/MF A01 CSCL 22B G3/12

N77-14044 THRU N77-14064 Unclas 58296

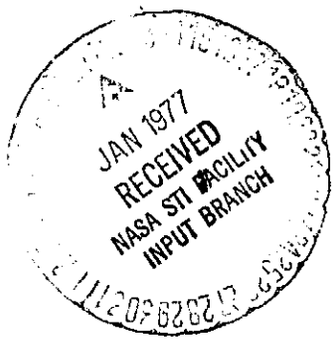

JET PROPULSION LABORATORY
CALIFORNIA INSTITUTE OF TECHNOLOGY
PASADENA, CALIFORNIA

December 15, 1976

NATIONAL AERONAUTICS AND SPACE ADMINISTRATION

The Deep Space Network
Progress Report 42-36

September and October 1976

JET PROPULSION LABORATORY
CALIFORNIA INSTITUTE OF TECHNOLOGY
PASADENA, CALIFORNIA

December 15, 1976

Preface

Beginning with Volume XX, the Deep Space Network Progress Report changed from the Technical Report 32- series to the Progress Report 42- series. The volume number continues the sequence of the preceding issues. Thus, Progress Report 42-20 is the twentieth volume of the Deep Space Network series, and is an uninterrupted follow-on to Technical Report 32-1526, Volume XIX.

This report presents DSN progress in flight project support, tracking and data acquisition (TDA) research and technology, network engineering, hardware and software implementation, and operations. Each issue presents material in some, but not all, of the following categories in the order indicated.

Description of the DSN

Mission Support
- Ongoing Planetary/Interplanetary Flight Projects
- Advanced Flight Projects

Radio Science

Special Projects

Supporting Research and Technology
- Tracking and Ground-Based Navigation
- Communications—Spacecraft/Ground
- Station Control and Operations Technology
- Network Control and Data Processing

Network and Facility Engineering and Implementation
- Network
- Network Operations Control Center
- Ground Communications
- Deep Space Stations

Operations
- Network Operations
- Network Operations Control Center
- Ground Communications
- Deep Space Stations

Program Planning
- TDA Planning
- Quality Assurance

In each issue, the part entitled "Description of the DSN" describes the functions and facilities of the DSN and may report the current configuration of one of the five DSN systems (Tracking, Telemetry, Command, Monitor & Control, and Test & Training).

The work described in this report series is either performed or managed by the Tracking and Data Acquisition organization of JPL for NASA.

Contents

PRECEDING PAGE BLANK NOT FILMED

Station Control and Operations Technology

Network Control and Data Processing

NETWORK AND FACILITY ENGINEERING AND IMPLEMENTATION

Network

Quality Assurance

OPERATIONS

Network Operations

Deep Space Stations

N77-14045

Network Functions and Facilities

N. A. Renzetti
Office of Tracking and Data Acquisition

The objectives, functions, and organization of the Deep Space Network are summarized; deep space station, ground communication, and network operations control capabilities are described.

The Deep Space Network (DSN), established by the National Aeronautics and Space Administration (NASA) Office of Tracking and Data Acquisition under the system management and technical direction of the Jet Propulsion Laboratory (JPL), is designed for two-way communications with unmanned spacecraft traveling approximately 16,000 km (10,000 miles) from Earth to the farthest planets of our solar system. It has provided tracking and data acquisition support for the following NASA deep space exploration projects: Ranger, Surveyor, Mariner Venus 1962, Mariner Mars 1964, Mariner Venus 1967, Mariner Mars 1969, Mariner Mars 1971, and Mariner Venus Mercury 1973, for which JPL has been responsible for the project management, the development of the spacecraft, and the conduct of mission operations; Lunar Orbiter, for which the Langley Research Center carried out the project management, spacecraft development, and conduct of mission operations; Pioneer, for which Ames Research Center carried out the project management, spacecraft development, and conduct of mission operations; and Apollo, for which the Lyndon B. Johnson Space Center was the project center and the Deep Space Network supplemented the Manned Space Flight Network (MSFN), which was managed by the Goddard Space Flight Center (GSFC). It is providing tracking and data acquisition support for Helios, a joint U.S./West German project; and Viking, for which Langley Research Center provides the project management, the Lander spacecraft, and conducts mission operations, and for which JPL also provides the Orbiter spacecraft.

The Deep Space Network is one of two NASA networks. The other, the Spaceflight Tracking and Data Network, is under the system management and technical direction of the Goddard Space Flight Center. Its function is to support manned and unmanned Earth-orbiting satellites. The Deep Space Network supports lunar, planetary, and interplanetary flight projects.

From its inception, NASA has had the objective of conducting scientific investigations throughout the solar system. It was recognized that in order to meet this objective, significant supporting research and advanced technology development must be conducted in order to

provide deep space telecommunications for science data return in a cost effective manner. Therefore, the Network is continually evolved to keep pace with the state of the art of telecommunications and data handling. It was also recognized early that close coordination would be needed between the requirements of the flight projects for data return and the capabilities needed in the Network. This close collaboration was effected by the appointment of a Tracking and Data Systems Manager as part of the flight project team from the initiation of the project to the end of the mission. By this process, requirements were identified early enough to provide funding and implementation in time for use by the flight project in its flight phase.

As of July 1972, NASA undertook a change in the interface between the Network and the flight projects. Prior to that time, since 1 January 1964, in addition to consisting of the Deep Space Stations and the Ground Communications Facility, the Network had also included the mission control and computing facilities and provided the equipment in the mission support areas for the conduct of mission operations. The latter facilities were housed in a building at JPL known as the Space Flight Operations Facility (SFOF). The interface change was to accommodate a hardware interface between the support of the network operations control functions and those of the mission control and computing functions. This resulted in the flight projects assuming the cognizance of the large general-purpose digital computers which were used for both network processing and mission data processing. They also assumed cognizance of all of the equipment in the flight operations facility for display and communications necessary for the conduct of mission operations. The Network then undertook the development of hardware and computer software necessary to do its network operations control and monitor functions in separate computers. This activity has been known as the Network Control System Implementation Project. A characteristic of the new interface is that the Network provides direct data flow to and from the stations; namely, metric data, science and engineering telemetry, and such network monitor data as are useful to the flight project. This is done via appropriate ground communication equipment to mission operations centers, wherever they may be.

The principal deliverables to the users of the Network are carried out by data system configurations as follows:

- The DSN Tracking System generates radio metric data; i.e., angles, one- and two-way doppler and range, and transmits raw data to Mission Control.
- The DSN Telemetry System receives, decodes, records, and retransmits engineering and scientific data generated in the spacecraft to Mission Control.
- The DSN Command System accepts coded signals from Mission Control via the Ground Communications Facility and transmits them to the spacecraft in order to initiate spacecraft functions in flight.

The data system configurations supporting testing, training, and network operations control functions are as follows:

- The DSN Monitor and Control System instruments, transmits, records, and displays those parameters of the DSN necessary to verify configuration and validate the Network. It provides operational direction and configuration control of the Network, and provides primary interface with flight project Mission Control personnel.
- The DSN Test and Training System generates and controls simulated data to support development, test, training and fault isolation within the DSN. It participates in mission simulation with flight projects.

The capabilities needed to carry out the above functions have evolved in three technical areas:

(1) The Deep Space Stations, which are distributed around Earth and which, prior to 1964, formed part of the Deep Space Instrumentation Facility. The technology involved in equipping these stations is strongly related to the state of the art of telecommunications and flight–ground design considerations, and is almost completely multimission in character.

(2) The Ground Communications Facility provides the capability required for the transmission, reception, and monitoring of Earth-based, point-to-point communications between the stations and the Network Operations Control Center at JPL, Pasadena, and to the mission operations centers, wherever they may be. Four communications disciplines are provided: teletype, voice, high-speed, and wideband. The Ground Communications Facility uses the capabilities provided by common carriers throughout the world, engineered into an integrated system by Goddard Space Flight Center, and controlled from the communications Center located in the Space Flight Operations Facility (Building 230) at JPL.

(3) The Network Operations Control Center is the functional entity for centralized operational control of the Network and interfaces with the users. It has two separable functional elements; namely, Network Operations Control and Network Data Processing. The functions of the Network Operations Control are:

- Control and coordination of Network support to meet commitments to Network users.
- Utilization of the Network data processing computing capability to generate all standards and limits required for Network operations.
- Utilization of Network data processing computing capability to analyze and validate the performance of all Network systems.

The personnel who carry out the above functions are located in the Space Flight Operations Facility, where mission operations functions are carried out by certain flight projects. Network personnel are directed by an Operations Control Chief.

The functions of the Network Data Processing are:

- Processing of data used by Network Operations Control for control and analysis of the Network.
- Display in the Network Operations Control Area of data processed in the Network Data Processing Area.
- Interface with communications circuits for input to and output from the Network Data Processing Area.
- Data logging and production of the intermediate data records.

The personnel who carry out these functions are located approximately 200 meters from the Space Flight Operations Facility. The equipment consists of minicomputers for real-time data system monitoring, two XDS Sigma 5s, display, magnetic tape recorders, and appropriate interface equipment with the ground data communications.

N77-14046

DSN Ground Communications Facility

M. S. Glenn
TDA Engineering

The Ground Communications Facility has been designed to provide reliable Earth-based, point-to-point voice and data communications as part of the DSN Tracking and Data Acquisition System.

I. Introduction

The Ground Communications Facility (GCF) is one of the three functional elements of the Deep Space Network and provides the capability required for the transmission, reception, and monitoring of voice and data communications between the various locations of the DSN. The GCF uses common carrier circuits engineered by the NASA Communications (NASCOM) Division of the Goddard Space Flight Center, interconnected to specialized switching, terminal, and monitor equipment, integrated into a world-wide system, and operated in support of space flight missions. The GCF is composed of five subsystems: Teletype, Voice, High-Speed, Wideband, and Monitor. The Office of Tracking and Data Acquisition of the Jet Propulsion Laboratory provides the technical direction and systems management of the GCF and acts as the representative of NASCOM for communications switching functions on the west coast.

II. GCF–NASCOM Interrelationships

The interrelationships at the programmatic level between the Jet Propulsion Laboratory-developed Ground Communications Facility and the Goddard Space Flight Center NASCOM are characterized as follows:

(1) NASCOM

(a) Provides ground communications of all operational data for all NASA missions, including those supported by the DSN.

(b) Accepts and supports communications requirements established by the DSN.

(c) Establishes basic characteristics of NASA operational ground communications subsystems, such as teletype line rate, high-speed block size, and wideband circuit capability.

(2) GCF

(a) Provides ground communications for all DSN missions using the services of NASCOM.

(b) Establishes additional characteristics of all GCF subsystems, such as block multiplexing and error correction.

III. Objectives and Goals

The GCF design is based on standardized communication techniques to provide more efficient transmission of user data and simple user and NASCOM interfaces. These objectives are met by:

(1) Providing message switching and routing.

(2) Transmitting data which are essentially transparent, i.e., user data are accepted and delivered in estab' shed formats and without additional errors.

(3) Minimizing project-dependent equipment within the GCF.

(4) Providing centralized data records.

The continuing goals of the GCF are to provide highly reliable and cost-effective data transmission while maintaining a capability balance between the DSN and users, and include:

(1) Equipment and routing redundancy to minimize single-point-of-failure impact.

(2) Error performance which does not degrade data beyond RF-link error performance.

(3) Design coordinated with NASCOM Development Program.

IV. Configuration and Functional Subsystems

The current GCF configuration, including the related NASCOM functions, is shown in Fig. 1. This configuration is functionally organized into High-Speed Data, Wideband Data, Voice, Teletype, and Monitor Subsystems.

A. High-Speed Data Subsystem

The High-Speed Data (HSD) Subsystem consists of assemblies that switch, transmit, receive, record, process, distribute, test, and monitor digital data and is used for the transmission of:

(1) All digital data of the DSN command, tracking, and monitor and control systems.

(2) All low- or medium-rate data of the DSN telemetry system and the DSN test and training system.

(3) All GCF monitor and control data.

The High-Speed Data Subsystem provides a capability for transmitting and receiving serial bit stream formatted data over four-wire circuits having a 3.0-kHz bandwidth. This serial bit stream is impressed on communication circuits at a continuous line bit rate divided into message segments referred to as high-speed blocks. The two key characteristics are:

(1) Data blocks containing user data bits to be transmitted.

(2) Filler blocks containing filler bits provided by GCF equipment when the user data bit rate is insufficient to maintain the fixed line bit rate required by design specifications.

Each block is divided into three parts, header, text, and ending. Formats for the data blocks and filler blocks are illustrated in Tables 1 and 2.

The current plans are to provide the functional capabilities illustrated in Fig. 2 and to standardize at a 1200-bit message segment and a line bit rate of 7200 b/s. Other planned changes include conversion from a 33-bit to a 22-bit error polynomial and increasing the number of bits reserved in the data block ending from 36 to 40 bits to provide error correction, by re-transmission, for short outages or errors in GCF data transmission. The purpose of these changes is to significantly reduce the error for nonreal-time replay of data. Figure 3 illustrates HSD Subsystem configuration which is planned for the CY 1977 and CY 1978 time period. The two configurations are required to provide continuous project support during the period of conversion from the existing Ground Data System to the new one for support of the Mariner Jupiter–Saturn and Pioneer Venus Projects.

B. Wideband Data Subsystem

The Wideband Data Subsystem consists of assemblies that switch, transmit, receive, process, distribute, test, and monitor data requiring the use of bandwidths greater than those provided by standard high-speed channels. The Wideband Data Subsystem illustrated in Fig. 4 includes standard wideband circuits as well as intersite-microwave capabilities. The Wideband Subsystem is used for:

(1) Telemetry data.

(2) Simulation data.

(3) Test and training data.

(4) Data interchange within the DSN including operational control.

(5) Intrasite communications and timing signals.

The wideband data circuits to the deep space stations contain serial bit streams impressed on communication circuits at a continuous line bit rate typically 27.6, 28.5, 50, 168, or 230.4 kilobits per second divided into 2400- or 4800-bit message segments. Similar to the high-speed data,

the message segments or data blocks contain user bits to be transmitted and filler bits provided by the GCF equipment when the user data bit rate is insufficient to maintain the fixed line bit rate required by design specifications. The data blocks are also divided into three parts: head, text, and ending, as illustrated in Tables 3 and 4.

C. Voice Subsystem

The Voice Subsystem consists of assemblies that switch, transmit, receive, distribute, test, and monitor transmissions originally generated in vocal form and includes capabilities between the facilities of the Deep Space Network and to the Mission Control Centers. The functional capabilities and key characteristics include:

(1) Standard voice-data grade circuits for all traffic.

(2) Conferencing capability on one intercontinental circuit during noncritical periods for all deep space stations supporting a single project; individual circuits for each DSS during critical periods, resources permitting.

(3) User-controlled intercom switching.

(4) Circuits used for high-speed data transmission (backup) if required.

(5) Voice traffic recording in the central communications terminal upon request.

D. Teletype Subsystem

This subsystem consists of assemblies that switch, transmit, receive, distribute, test, and monitor digital signals originally generated in Baudot format at a teletype (TTY) rate of 100 words per minute. The operational use of teletype continues to be de-emphasized and is used primarily for emergency, backup operational transmissions and administrative communications. Services and key characteristics include:

(1) Handling Air Force Eastern Test Range (AFETR)-generated predicts for DSN initial acquisiton.

(2) Transmitting non-operational messages between the JPL Message Center and other locations.

(3) Use of standard NASCOM format and the NASCOM communications processor for message switching.

E. Monitor and Control Subsystem

The Monitor and Control Subsystem consists of assemblies that gather, calculate, record, display, and report the operational configurations, status, and performance of the GCF subsystems. A central monitor processor has been designed to receive inputs from other GCF subsystems as necessary to permit internal assessment of performance, problem detection, isolation, and correction.

V. Typical Configuration

The Viking Project represented one of the most extensive users of the GCF because of the two orbiting and two lander spacecraft and extended critical phases of the mission. The project requirements were largely met with standard GCF circuit configuration as was the intended goal. Illustrated in Fig. 5 is the GCF configuration used during the primary mission phase following touchdown.

Acknowledgments

I am indebted to J. P. McClure, R. H. Evans, F. E. Bond, J. W. Capps, and J. Santana for comments and material used in this article.

Table 1. High-speed data block composition

Subdivision	22-bit Error polynomial		33-bit Error polynomial	
	Word	Bits	Word	Bits
Header	1 thru 7 (16 bits each)	112	1 thru 7 (16 bits each)	112
	8	8	8	8
Text	8 (Bit 9) thru 73 (Bit 8)	1040	8 (Bit 9) thru 73 (Bit 12)	1044
Ending	73 (Bit 9) thru 75 (Bit 16)	40	73 (Bit 13) thru 75 (Bit 16)	36
Totals	75	1200	75	1200

Table 2. High-speed filler block composition

Subdivision	22-bit Error polynomial		33-bit Error polynomial	
	Word	Bits	Word	Bits
Header	1 thru 3 (16 bits each)	48	1 thru 3 (16 bits each)	48
Text	4 (Bit 1) thru 73 (Bit 8)	1112	4 (Bit 1) thru 73 (Bit 12)	1116
Ending	73 (Bit 9) thru 75 (Bit 16)	40	73 (Bit 13) thru 75 (Bit 16)	36
Totals	75	1200	75	1200

Table 3. Wideband data block composition

Subdivision	Word	Bits
Header	1 thru 7 (16 bits each)	112
	8	8
Text	8 (Bit 9) thru 298 (Bit 12)	4644
Ending	298 (Bit 13) thru 300 (Bit 16)	36
Totals	300	4800

Table 4. Wideband filler block composition

Subdivision	Word	Bits
Header	1 thru 3 (16 bits each)	48
Text	4 (Bit 1) thru 298 (Bit 13)	4716
Ending	298 (Bit 13) thru 300 (Bit 16)	36
Totals	300	4800

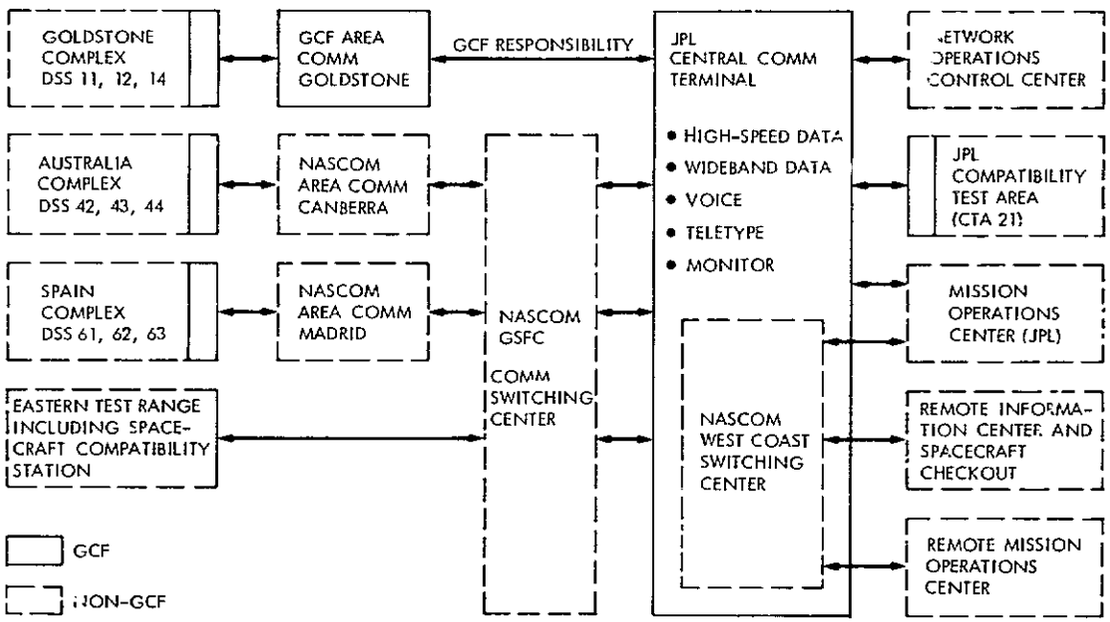

Fig. 1. GCF configuration

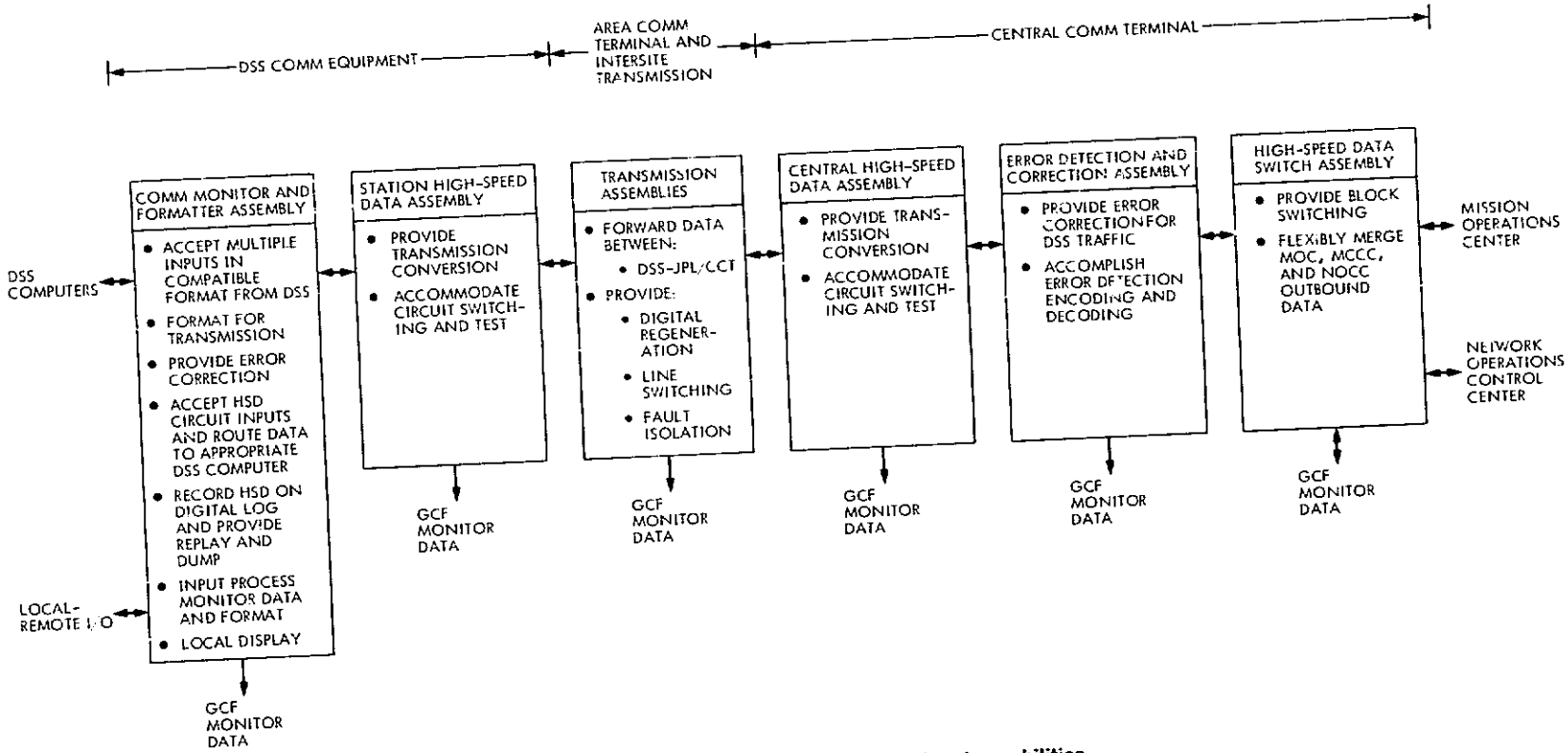

Fig. 2. GCF High-Speed Data Subsystem functional capabilities

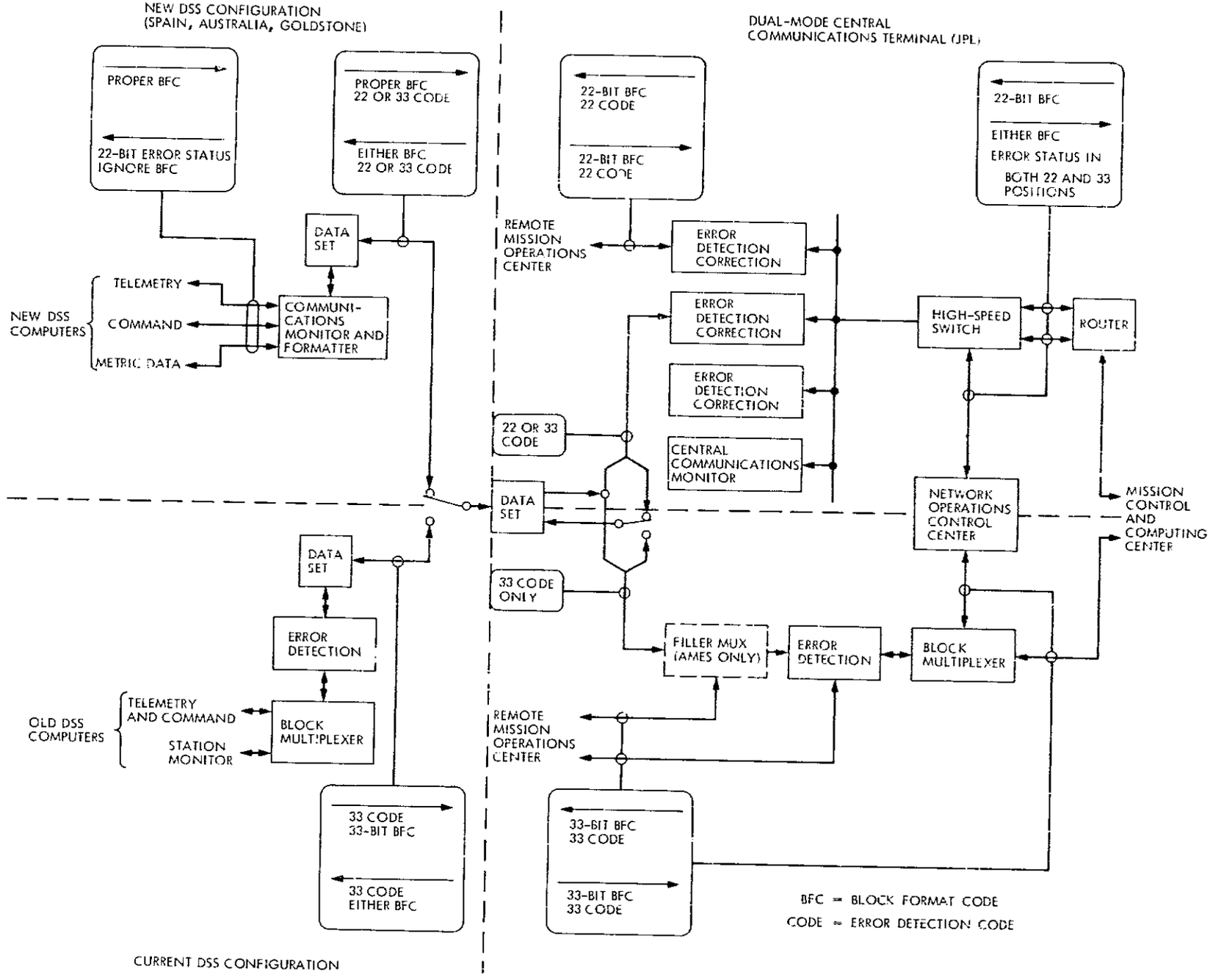

Fig. 3. GCF High-Speed Data Subsystem configuration and interfaces (CY 1977 and 1978)

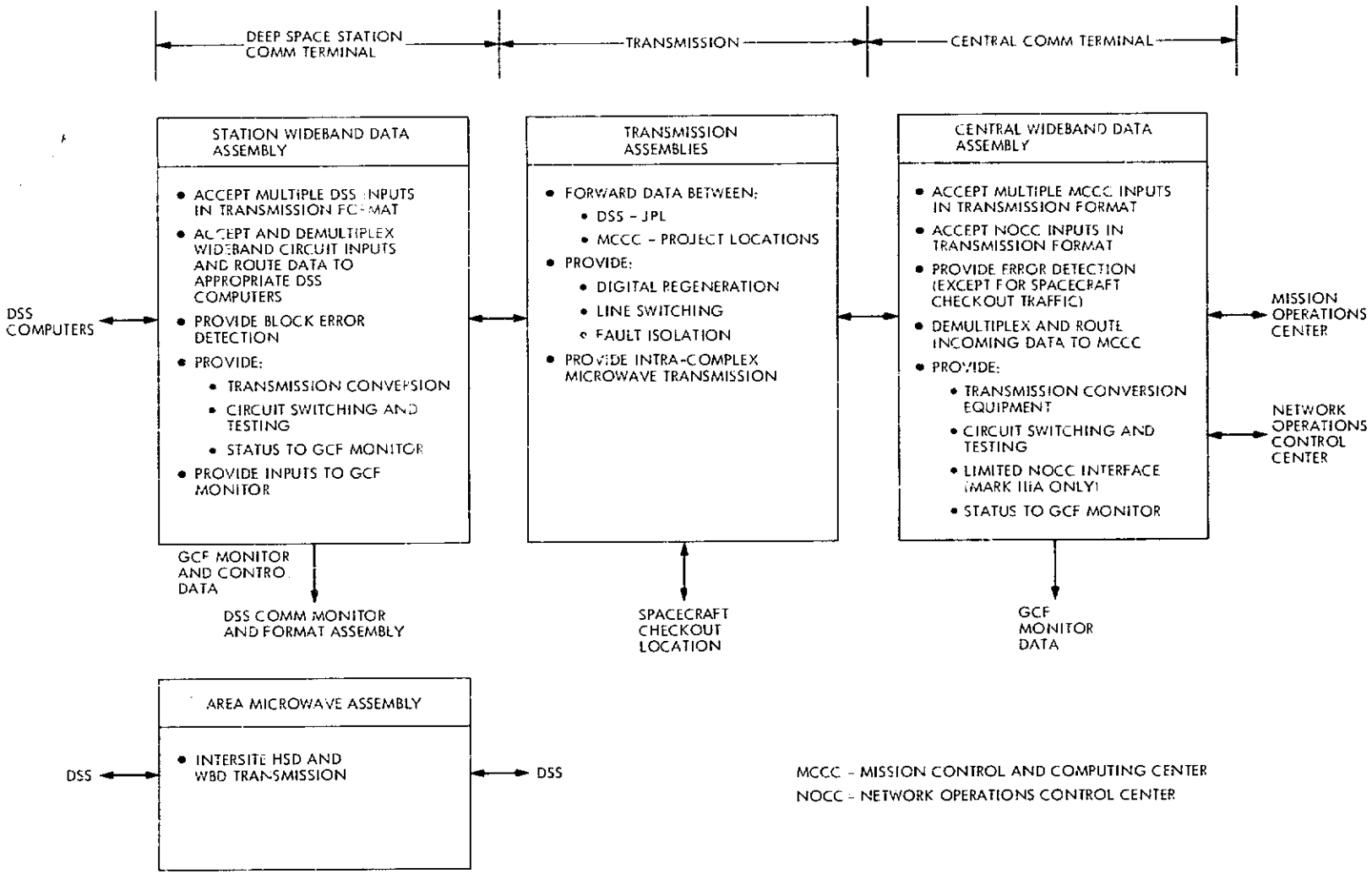

Fig. 4. GCF Wideband Subsystem

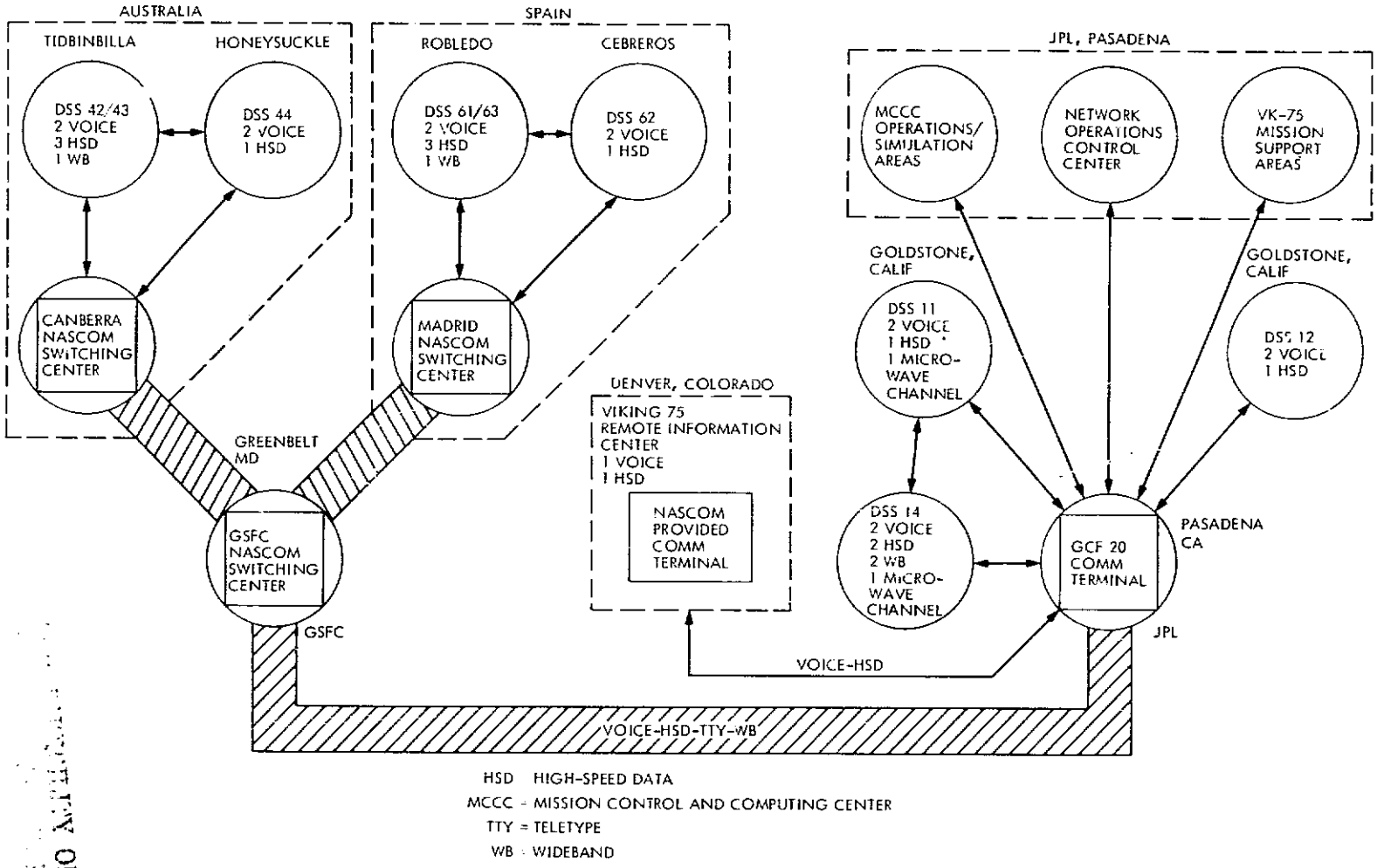

Fig. 5. DSN support locations and GCF–NASCOM circuit requirements for Viking 1975

ORIGINAL PAGE IS OF POOR QUALITY

N77-14047

Viking Mission Support

D. W. Johnston and T. Howe
DSN Network Operations Section

This report covers the most significant Viking Mission events supported by the DSN during August and September 1976. Intermediate Data production and DSS support are also summarized for this period. Viking DSN Discrepancy Report activity for the period January 1975 through September 1976 is also included.

I. Introduction

The previous report in this series described the final preparation and testing prior to the Mars orbit insertion of Viking 1, the Mars orbit insertion, separation and landing of Viking Lander 1 (VL-1), and concluded with the Viking 2 approach maneuver on 27 July 1976. This report continues from that point and describes the sequence of events pertaining to the insertion through landing of Viking 2.

II. DSN Mission Operations Activities

A. Viking Operations Activities

Table 1 lists the significant Viking 1 and Viking 2 activities supported by the DSN during this reporting period.

The DSN supported a total of 18 significant events during this two-month period. On August 1, Viking Orbiter 1 (VO-1) was already in orbit, with Viking Lander 1 on the surface of Mars sending data daily via direct and relay links. Viking 2 was approaching Mars, 7 days away from Mars orbit insertion (MOI).

B. DSS Support

Table 2 lists the tracking hours, per station, of the Viking spacecraft and the number of commands transmitted from each station during this reporting period.

C. Intermediate Data Record Status

During this reporting period the DSN data record capability provided the Viking Project Data Support Group with 394 original telemetry Intermediate Data Records (IDR), of which 378 IDRs were delivered within the 24-hour after-loss-of-signal requirement. The average data throughput for this reporting period was 99.99 percent of the available data.

Table 3 is a breakdown of IDR production per DSS.

D. Viking Discrepancy Reports

A summary of Viking Discrepancy Reports (DR) covering the period from 1 January 1975 to 26 September 1976 is shown in Table 4.

III. DSN Special Activity Support

A. Dual Orbiter Tracking

The tracking of both Viking Orbiters by a single 64-m DSS began on August 6. Both Orbiters had been within the beamwidth of 64-m antennas for the three days prior to Mars orbit insertion of Orbiter 2, however the Viking Project chose the option of pointing the antenna at a single spacecraft in order to maximize data return. DSN predicts had shown that on August 3, a signal loss of 24 dB would result on one spacecraft while the antenna was pointed directly at the other. This loss would be reduced to just 4 dB for both spacecraft by midpoint tracking. True midpoint tracking was accomplished by using the (right ascension/declination) planetary mode of antenna drive in which hour angle (HA) and declination (dec) position coordinates are computed by inputting HA and dec for the three days beginning with the day of track. Offsets were then used to obtain midpoint tracking.

B. Viking 2 Mars Orbit Insertion

The Viking 2 MOI was successfully supported on August 7 by Madrid DSS 63 with DSS 62 as backup. The same series of events associated with MOI of Viking 1 were repeated for Viking 2. The spacecraft science subcarrier was turned off, then the spacecraft was rolled, the low-gain antenna selected, the spacecraft yawed, and then rolled again so that the high-gain antenna pointed at Earth. The high-gain antenna was then selected and the high-rate subcarrier turned on and modulated by 2 kb/s data. A loss of uplink and downlink lock occurred during the yaw turn.

A DSS exciter ramp was started a one-way light time prior to the predicted uplink loss of lock. A short insurance sweep was then executed to agree with the time at which the spacecraft was commanded back to the high-gain antenna. This tuning assured a two-way lock for MOI burn.

The MOI burn lasted approximately 39 minutes, 35 seconds, and resulted in an orbit of 27.4 hours, just 0.2 hour greater than the desired orbit. The periapsis altitude of 1519 kilometers was achieved and exceeded the desired altitude by only 19 kilometers.

Following the motor burn, the reverse order of roll, low-gain antenna, yaw, roll, and high-gain antenna took place, and an exciter ramp was accomplished to reacquire the uplink.

C. Mars Orbit Trim Number 1 (VO-2)

On August 9, Mars orbit trim number 1 (MOT-1) was successfully performed during the Goldstone DSS 14 view period. This trim refined the Orbiter 2 orbit and resulted in an orbit of 27.3 hours duration. The motor burn lasted 7 seconds. The burn was accomplished without the benefit of a roll, yaw, or roll turn by using the Sun-line reference technique. That is, the burn was timed for the point in the orbit in which the attitude of the Orbiter was corrected without a maneuver. This method preserved the attitude control gas supply. Although telemetry later indicated that the high-gain antenna had moved 0.4 degrees during the motor burn, due to backlash, no changes were observed in the "S" or "X" band downlinks.

D. Mars Orbit Trim Number 2 (VO-2)

On August 14, Australia DSS 43 supported MOT-2 for Viking Orbiter 2. DSS 63 provided backup support for the motor burn. This trim maneuver was to refine the orbit of Orbiter 2 with a motor burn of 3 seconds. No changes in link quantities were observed during this Sun-line maneuver. These first two maneuvers provided a new concept in site certification. Instead of synchronizing the spacecraft's periapsis with a precise point on the planet, the spacecraft was left out of sync so that its periapsis walked around the planet at 40-deg steps per day. This permitted a good examination of the 40- and 50-deg north latitude band and all proposed landing sites.

E. Mars Orbit Trim Number 3 (VO-2)

MOT-3 for Orbiter 2 took place during the DSS 14 pass on August 25, with motor burn at 17:08:45 GMT, lasting for 72 seconds. This was a zero-turn maneuver, and the telecommunications link remained in the high-rate mode, (2 kb/s and 8-1/3 b/s) during the maneuver. The only observed change during the burn was a decrease of about 0.25 dB on X-band, which would correspond to a 0.25-deg change in the high-gain antenna pointing angle. This maneuver stopped Viking 2's westward walk, changed the spacecraft's speed by 155 km/h (96 mi/h) and initiated a drift in the easterly direction toward precise coordinates for the landing site.

F. Mars Orbit Trim Number 4 (VO-2)

The resynchronization of Orbiter 2 over the Utopia landing site occurred on August 27 during the DSS 14 pass. MOT-4 again used the Sun-line maneuver procedure and no changes in the downlink were observed.

G. Viking Lander 2 Preseparation Checkout, Descent, and Landing

Network support of activities associated with the landing of Viking Lander 2 began on September 2 with DSS 43 supporting the separation minus 39-hour command update. This command load prepared the mated lander for the preseparation checkout. This command load

was supported using configuration code 15. Australia DSS 44 provided backup command support for DSS 43.

Approximately nine hours later, preseparation checkout began. Spain DSS 63 supported this checkout. A special configuration was designed for the DSS 63 pass. In as much as a Lander 1 direct link was to occur during the first part of DSS 63's view period, two configurations were required. The first configuration was the standard three-spacecraft configuration for Orbiter/Lander/Orbiter, Code 30. Following the Lander direct link, a configuration was needed that would assure the receipt of the Lander 2 checkout data at JPL. Figure 1 shows the configuration used for the second half of the DSS 63 pass. This configuration provided three processing channels for Lander checkout science data. Two of these data streams were output via the wideband data line while the third was output on the high-speed data line, providing dual transmission paths. In parallel with the Lander 2 checkout data, Orbiter 1 was outputting 4 kb/s science data. Since no data channel was available at DSS 63 to process these data, they were recorded on analog tape for postpass playback if required. During the checkout, the relay subsystems were turned on and performed normally. The 10-watt UHF transmitter output power measured 10.72 watts, which was 0.44 dB above the data base value of 9.68 watts.

The Lander 2 checkout proceeded normally during the DSS 63 pass. DSS 62 provided an uplink for Viking Orbiter 2.

Spain DSS 63 supported the separation minus 9.5- and 3.5-hour command updates and the separation "GO" command during their pass on the following day, September 3. Configuration code 24 was used to support this command activity. This configuration code provided two high-rate science data streams with channel 2 of telemetry and command processor alpha outputting data to the high-speed data line while channel 3 of the Telemetry and Command Processor Assembly (TCP) beta output data for wideband data line transmission. This same configuration code had been used for support of preseparation checkout of Lander 1.

The purpose of the "GO" command was explained in the previous article of this series.

All commands scheduled during the DSS 63 view period were successfully transmitted.

Spain DSS 62 provided backup command support for DSS 63.

Goldstone DSS 14 was prime for separation, descent, and landing support. DSS 11 acted as the backup command station for DSS 14.

Since all of the descent data were to be at 4000 b/s, configuration code 15 was specified. Both telemetry and command processor strings were initialized for Orbiter 2, providing dual processing channels with their outputs multiplexed onto one wideband data line.

Separation occurred at 19:39:59 GMT Earth received time on September 3. The landing sequence had been perfect up to this point; however, at 19:46:27 GMT, the X-band receiver showed a drop in received signal level and then went out of lock at 19:47:02 GMT. At the same time the S-band receivers were showing decreases in received AGC. These receivers all dropped lock at 19:47:52 GMT. Goldstone DSS 14 responded to the situation and regained S-band lock within 2 minutes at a received signal level of −169 dBm. Since this signal level was consistent with the low-gain antenna with the high-rate subcarrier on it was assumed that the signal was not coming from a mispointed high-gain antenna. At 20:08:34 GMT, approximately 19 minutes after the downlink reacquisition, commands were sent to assure the spacecraft was on the low-gain antenna, and to select the cruise mode at 8-1/3 b/s. A round trip light time later (41 minutes) telemetry lock was established and indicated that a switchover of the attitude control system had occurred and that the spacecraft had rolled off of Vega reference by some unknown amount. Engineering data also indicated that the descending Lander-to-Orbiter real-time relay link was working and that the Lander appeared to be in good health. This mode of operation was to continue through touchdown (22:58:20 GMT) on September 3 and until approximately 07:00:00 GMT the following day.

When it was determined the spacecraft had rolled off the Vega reference, a command designated "fly back and sweep" was sent. This command would cause the spacecraft to reacquire Vega if the star was within 5 degrees of the star tracker. Vega was not acquired, indicating a roll of more than 5 degrees. Shortly afterward, commands were sent to roll the spacecraft 360 degrees to obtain a roll attitude reading. The Canopus loss contingency plan identified in the previous article of this series was used to determine the spacecraft orientation in roll axis based on the point at which the X-band signal level reached a peak. Australia DSS 43 supported this effort and obtained a rapid X-band lock, making the star mapping possible. A peak was observed of −149.06 dBm proving two things: one, that the high-gain antenna was still working, and two, that the spacecraft had rolled about 22

degrees off Vega. The Orbiter was then rolled to Vega, the high-gain antenna selected, the high-rate subcarrier turned on, and the playback of the first two Lander pictures initiated. The pictures were received without further problems.

The second received picture, which was a 310-degree panoramic survey, showed a blemish on the Lander's high-gain X-band antenna that could have been caused during landing. Since the antenna dish is a very thin honeycomb design, it was vulnerable to damage while in the stowed position during landing if a substantial shock was experienced.

H. First Lander 2 Direct Link

The first Lander 2 direct S-band link occurred on September 5 with DSS 43 supporting. Configuration code 61 was used by DSS 43 for this pass and was to be used for the first 20 Lander 2 direct links. As identified in the previous article of this series, Code 61 provides 2 processing channels for Orbiter data and 4 processing channels for Lander direct link data.

During the DSS 43 precalibrations it was determined that channel 3 of TCP beta was inoperative. This channel was assigned to process Lander 250-b/s backup data and output via the wideband data line. A decision was made to use channel 2 of the DSS 42 TCP string for this 250 b/s backup data stream. The Viking configuration permits receiver number 2 located at DSS 43 to interface with Subcarrier Demodulator Assemblies 7 and 8 at DSS 42. Two hours prior to the scheduled Lander acquisition, a problem developed with a Helios spacecraft. Australia DSS 42 was assigned to track Helios with the 250-b/s backup stream being given up. Lander acquisition occurred at 03:30:00 GMT with a signal level of −151.5 dBm, very close to the predicted level. An examination of the telemetry data indicated that the uplink sweep had acquired both Lander transponders and that the uplink signal levels for low- and high-gain antennas were nominal. Since all data streams appeared to be nominal, an assumption was made that the damage to the high-gain antenna revealed by the second lander picture was either not severe enough to degrade the communication performance or that the assumption of damage was incorrect. Because the antenna dish faces upward while stowed, it was possible that some surface material could have been thrown up onto the dish during landing and that the apparent damage was really a discoloration caused by Martian dirt. This last theory seems to be the most popular. Since the high-gain antenna surface would never again be in a position in which it could be seen by the Lander cameras, a closer examination was not possible.

I. Mars Orbit Trim Number 7 (VO-1)

MOT-7 took place on September 11. This trim maneuver was supported by DSS 14. It broke the orbital synchronization of Orbiter 1 and caused it to be a walk around the planet. Lander 1 began a reduced-mission phase with continuing biological experiments, weather reporting, and picture acquisitions, but with both real-time and recorded data being transmitted via the Lander to Earth by direct link only. Viking Orbiter 1 began its walk at 12:24:34 on 11 September following an engine burn that lasted 16 seconds. The resulting orbit moved the spacecraft approximately 40 degrees east each day. The orbit was to carry VO-1 completely around the planet in 9 days continuing the walk to nearly half-way around the planet again until it reached a plane that would pass over the VL-2 location. The maneuver was successfully completed using the standard roll, yaw, roll, and burn sequence.

J. Mars Orbit Trim Number 8 (VO-1)

This trim took place on September 20 and was supported successfully by DSS 14. The burn occurred at 22:36:19 GMT Earth received time. It was a sunline maneuver with no changes observed in the downlink signal levels. This burn accomplished a fine adjustment to orbital statistics in preparation for the synchronization burn to occur on September 24.

K. Mars Orbit Trim Number 9 (VO-1)

MOT-9 synchronized VO-1 over VL-2 to permit VO-1 to become the relay station for Lander 2 data. The maneuver was completed using the Sun-line technique. One anomaly occurred during this maneuver. Upon switching to the low-gain antenna the downlink was observed to be about 1.5 dB low, with the uplink being at least 6 dB lower than predicted. Spain DSS 61 had not turned off range modulation at the required time and the observed degradation was the result of this modulation on the uplink. The trim was supported by DSS 63 and DSS 14 during an overlapping view period.

L. Pre-MOT-5 Test Burn Maneuver (VO-2)

This trim was accomplished for the primary purpose of testing VO-2's motors prior to MOT-5 to make absolutely sure everything was operational prior to MOT-5. The test trim was supported by DSS 43. Near the beginning of their pass, a hydraulic pump failure occurred preventing movement of the DSS 43 antenna. Goldstone's DSSs 12 and 14 passes were extended as long as possible, and, in addition, commands were sent to switch the spacecraft to cruise engineering only mode in the event DSS 43 could

not make repairs in time for the maneuver and DSS 44 would be required to track the downlink. Australia DSS 43 managed to recover prior to the main maneuver; however, the cruise mode of telemetry was maintained.

M. Mars Orbit Trim Number 5 (VO-2)

MOT-5's purpose was to modify VO-2's orbit plane so that it could begin observations of the Martian north polar cap. This maneuver differed from the standard in that a command must be transmitted and received at the spacecraft before the motor burn would take place. The spacecraft was first rolled, yawed, and rolled on the low-gain antenna, and then the high-gain antenna was selected. A measurement of the X-band received signal level was made. A measurement below the predicted level would have indicated that the spacecraft high-gain antenna was not properly aligned and that the burn should not be attempted. The spacecraft had been previously programmed to recover from the maneuver automatically should a "GO" command not be received. The X-band downlink was found to be within tolerance and the "GO" command was transmitted. Figure 2 shows the time line associated with MOT-5. The top line indicates the ground time for DSS initiated events. The middle line shows the events when they arrive at the spacecraft or events that originate at the spacecraft. The lower line shows events occurring a round-trip light time after a ground originated event or a one-way light time after a spacecraft event.

MOT-5 was performed flawlessly. The motor burn lasted 5 minutes and produced a velocity change of 343 m/s. It changed the orbit inclination from 55.3 degrees to 75 degrees. The walk will change 30 degrees per day with a planned resynchronization over VL-2 to take place after 16 revolutions on October 18. VO-1 will then be released to start a second walk during solar conjunction. It will resync over VL-1 sometime in mid-November.

IV. Conclusion

With two spacecraft in orbit and two spacecraft landed, all returning extremely large amounts of data daily, the Viking Mission would have to be considered one of the most successful on record. It is also gratifying to note that during this exceptionally high activity period, with the DSN being utilized to near 100 percent capability continuously, the loss of data due to network hardware failures has been insignificant. This has been made possible, to a large degree, by utilizing 64-meter DSS "failure mode" configurations that were designed to optimize the data processing capabilities at a station in the event of a single-point failure in any telemetry stream. These configurations were described in detail in previous articles in this series. Another factor that contributed to the excellent network performance was the use of the DSS Computer Assisted Countdown, which will be described in the next report.

Table 1. Viking Operations Activities

Date	Spacecraft	Activity
1. Aug. 3	Viking 1	Station keeping trim maneuver
2. Aug. 6	Vikings 1 & 2	First simultaneous tracking of 2 VOs by one DSS
3. Aug. 7	Viking 2	MOI
4. Aug. 9	Viking 2	MOT-1
5. Aug. 14	Viking 2	MOT-2
6. Aug. 25	Viking 2	MOT-3
7. Aug. 27	Viking 2	MOT-4
8. Sept. 2	Viking 2	Preseparation checkout
9. Sept. 3	Viking 2	Separation, descent & touchdown
10. Sept. 4	Viking 2	First direct link
11. Sept. 11	Viking 1	MOT-7
12. Sept. 18	Viking 1	First solar occultation
13. Sept. 20	Viking 1	MOT-8
14. Sept. 24	Viking 1	MOT-9
15. Sept. 25	Viking 1	Lunar occultation
16. Sept. 28	Viking 1	Ground Communications Facility 7.2 kb/s high-speed data line test
17. Sept. 29	Viking 2	Pre-MOT 5 test burn maneuver
18. Sept. 30	Viking 2	MOT-5

Table 2. Station support for Viking

DSS	Tracks[a]	Hours tracked	Commands transmitted
	August		
11	30	229:35	2
12	6	42:55	0
14	69	494:34	2248
42	27	242:53	1440
43	69	571:21	3094
44	7	56:55	0
61	31	305:24	3511
62	9	83:45	438
63	62	541:52	2318
Total (monthly)	310	2569:14	13,051
	September		
11	29	216:14	1430
12	6	45:24	6
14	72	486:59	1205
42	34	304:02	1532
43	69	584:59	2685
44	11	91:29	4
61	29	269:36	1028
62	7	98:29	332
63	81	536:10	1495
Total (monthly)	338	2633:22	9717
Report total	648	5202:36	22,768

[a]The number of tracks includ. the number of passes, each of which includes one, two, or three spacecraft simultaneously.

Table 3. IDR production

DSS	Total original	Delivered in 24 hours	Delivered late
14	127	126	1
43	128	122	6
63	139	130	9

Table 4. Viking Discrepancy Report summary, 1 January 1975–26 September 1976

Resolution	Deep Space Station										Deep Space Network	Ground Communication Facility	Network Data Processing Area	Network Operations Control Area	Total	%
	11	12	14	42	43	44	61	62	63	71						
Station Dependent	55	47	188	45	118	22	37	25	141	16	7	34	133	72	940	79.8
Station Independent	6	7	21	8	10	1	2	4	18	1	10	9	76	30	203	17.2
Other or Unavoidable	3	2	3	0	1	0	0	1	0	1	14	5	1	3	34	2.8
Total DRs Closed	64	56	212	53	129	23	39	30	159	18	31	48	210	105	1177	
Total DRs Generated	66	56	221	53	139	23	39	30	167	18	32	48	224	113	1229	
DRs Opened as of 26 Sept. 76	2	0	9	0	10	0	0	0	8	0	1	0	14	8	52	

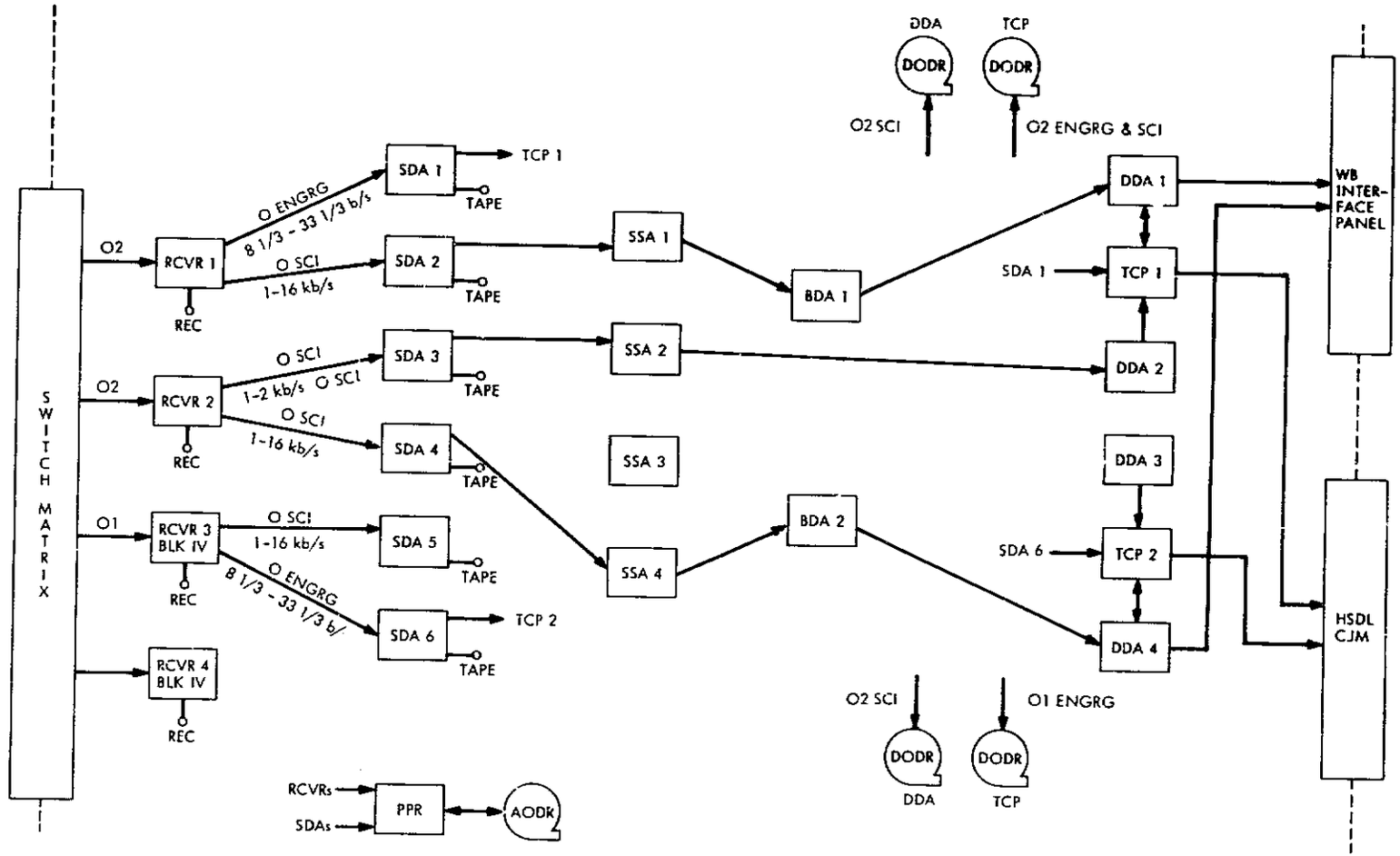

Fig. 1. DSS 63 VO-2 preseparation checkout configuration

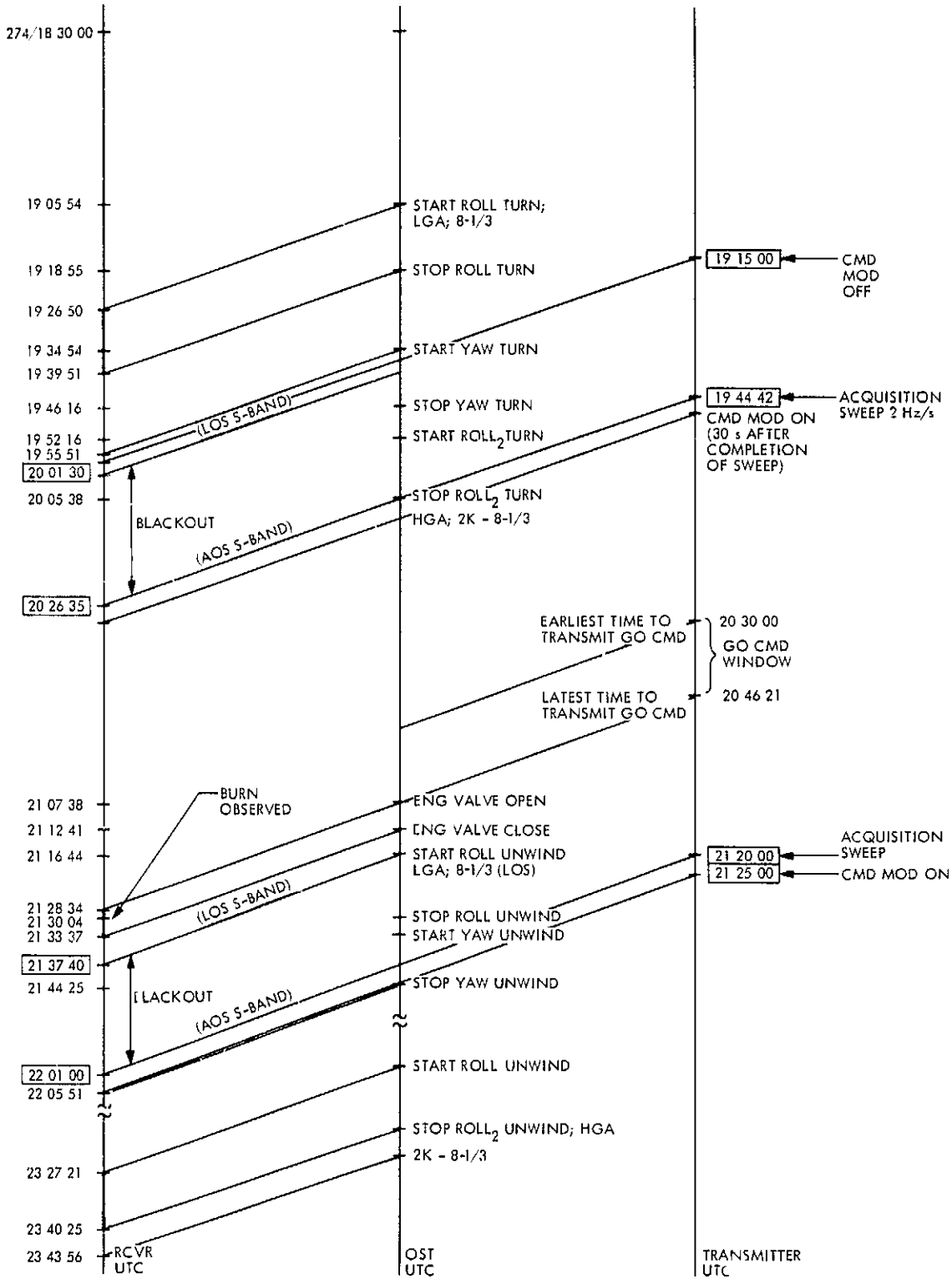

Fig. 2. VO-2 MOT-5 (plane change) summary

N77-14048

Pioneer Venus 1978 Mission Support

R. B. Miller
TDA Mission Support

The Tracking and Data Acquisition portion of the Ground Data System, which will support the Differential Long Baseline Interferometry Wind Measurement Experiment, is described.

I. Introduction

The Pioneer Venus Multiprobe Mission includes a Differential Long Baseline Interferometry (DLBI) Experiment, which will attempt to measure the wind velocities in the atmosphere of Venus as four probes descend through the atmosphere. The fundamentals of the experiment are described in Ref. 1. The experiment will be using interferometry techniques to measure the components of the wind velocity perpendicular to the line-of-sight (Earth–spacecraft direction), and established doppler techniques to measure the velocity components along the line-of-sight. Each pair of stations which comprise the interferometer resolve only one component of the velocity. In order to resolve both components of the wind velocity perpendicular to the line-of-sight and to provide some measure of redundancy, four stations will be equipped to support this experiment. The 64-meter DSN stations located at Goldstone, California, and Canberra, Australia, will be utilized, along with the 9-meter Space Flight Tracking and Data Network (STDN) stations located at Guam and Santiago, Chile.

The end product at each tracking station is a wideband-width digital recording covering the entire bandwidth of interest, which includes five spacecraft signals. Plans to summer 1976 had assumed that the deliverable to the experimenter, located at the Massachusetts Institute of Technology (MIT), would be the actual wideband recordings produced at these tracking stations. This plan involved the Project procuring for the experimenter recorders capable of playing back these wideband recordings, and required that the experimenter implement and operate a system to convert the wideband recordings into a useable computer-compatible form. Estimates by MIT of the resources required to implement and operate this conversion process turned out to be a very significant portion of the total processing costs at MIT for the experiment. This problem, coupled with a similar expensive processing cost for the initial bandwidth reduction of the Pioneer Venus Orbiter occultation radio science data, led the DSN to form a special team in May 1976 to see what the DSN might be capable of doing to help solve both of these problems for the Project. This activity culminated in a functional design and estimated resources required, which were approved by both the Project and the Office of Tracking and Data Acquisition in June 1976. The result will be a new occultation subsystem to be implemented in the 64-meter subnet (which will be described in a subsequent Pioneer Venus Progress Report

article), and the agreement of the DSN to provide (with Project financial assistance) equipment in Compatibility Test Area 21 (CTA 21) at JPL, Pasadena, necessary for reducing the bandwidth of the wideband digital recordings to produce standard computer-compatible recordings which will be the deliverable to the experimenter.

The total Ground Data System to support the DLBI Wind Measurement Experiment, therefore, now comprises four tracking stations located around the Pacific Basin in Australia, Guam, Chile, and California, a tape conversion facility located at JPL, Pasadena, and, finally, the actual science data processing to be performed at the Massachusetts Institute of Technology. The remainder of this article will describe the TDA-provided portions of this system: the tracking station configurations and the tape conversion facility at CTA 21.

II. Tracking Station DLBI Configuration

The key requirements for the tracking stations to support the DLBI experiment are described in Ref. 1. The details of the requirements had been conveyed in written material to the DSN through the flight project. In November 1975, a meeting was held at JPL with the experimenters and representatives of DSN Engineering and STDN Engineering for the purpose of clarifying the requirements face-to-face with the experimenters. After this meeting, the DSN then proceeded to produce a first cut at a functional design for the DSN stations. This functional design at a block diagram level was presented to the experimenter in mid-April 1976 in a teleconference. This teleconference and other informal exchanges between DSN Engineering and the experimenter then resulted in a final design for the DSN configuration which was formally reviewed and accepted by the experimenter on 22 June 1976 in a meeting at JPL. The resulting DSN design is shown at a functional level in the top part of Fig. 1. (A more detailed description of the receiver and calibrator design will be provided in a subsequent Progress Report article.) A key decision which was made in the design process was that the requirements for the DLBI experiment were sufficiently stringent and unique to warrant the DLBI requirement being met by a separate receiver dedicated to the experiment. The original concept had involved one of the open-loop receivers which will be provided for precarrier detection telemetry recovery including a second port 2 MHz wide to support the DLBI experiment. The final design involves a separate DLBI receiver which brings the total complement of open-loop receivers at Goldstone (DSS 14) and Australia (DSS 43) up to five per station for the Multiprobe entry.

The configuration involves a calibration tone generator which produces two tones, one above and one below the five spacecraft signals. The DSN configuration includes a switching capability to insert the calibration tones either before or after the low-noise amplifier. The tones will be inserted before the low-noise amplifier for testing purposes and for pre-pass checkout, but will have to be inserted after the low-noise amplifier to avoid possible interference with the recovery of the telemetry data from the probes during the actual entry event. The tones are also fed to a monitoring system which will strip the tones off the output of the receiver and compare them against the tones direct from the tone generator.

One of the most difficult parts of the actual receiver is the final mixer which must be flat from essentially dc to 1.8 MHz and have the images down at least 10 dB at the 1.8-MHz point. In order to meet the stringent relative phase stability requirements of the experiment, certain critical modules will be contained in temperature-stabilizing ovens. In addition, the cables carrying the tones from the control room up to the antenna will be actively stabilized as well as the cable carrying the reference frequency into the first mixer of the receiver. Redundant widebandwidth digital recorders will be provided at each station. For this experiment, the recorders will be operated at a 12-megabit per second rate operating at 76 cm (30 inches) per second.

It has been planned from the beginning that the STDN design would be derived by STDN Engineering based on whatever was the finalized design for the DSN stations. With the finalization of the DSN design on 22 June, STDN Engineering proceeded with the detailed design for the STDN stations, which culminated in a formal review of the STDN design on 16 September at Goddard wherein the experimenter did concur in the STDN design.

Notice in Fig. 1 that the functional design of the STDN stations is essentially identical to the DSN except that it is not required to have the calibration tones switchable between the input and output of the low-noise amplifier, since there will be no telemetry recovery from the STDN stations. STDN Engineering was able to take advantage of the functional commonality and produce a detailed design, which involves use of many common modules with the DSN configuration. The calibration tone generator will be a common design using common modules as well as the critical last mixer mentioned above. The plan is to have the DSN procure, with Goddard funding, the common modules for the STDN stations. The STDN receiver involves using the first local oscillator (first mixer) in the standard STDN operational receiver, the multiple-

frequency receiver. The analog-to-digital converter and recorder will be loaned to the STDN by the DSN as originally planned. The DSN is responsible for providing the necessary interface electronics to hook the recording subsystem up to the STDN Frequency and Timing Subsystem and power equipment. The interface of the STDN receiver to the recorder was to be a Goddard responsibility, but this engineering interface problem has been eliminated by STDN use of the same final mixer as in the DSN configuration.

III. Station Performance Validation

There will be several means of validating the proper performance of elements of the station configuration for testing purposes and for pre-pass checkout as well as during the actual event. The calibration tone monitor, comparing the tones as they go up to the input or output of the low-noise amplifier against the tones coming out of the rear-end of the receiver, will enable detection of several possible problems in the receiver chain. The recorders themselves are 18-track and have three indicator lights per track which are capable of detecting catastrophic failures in a particular track as well as the capability to do a bit error computation on a single track at a time. The micro controller on the recorder will be able to switch the bit error computation every 15 seconds from one track to another. This monitoring is possible on only one recorder at a time; however, the monitoring can be switched between the recorders without affecting the recording process during the period of interest.

For a total end-to-end system check at the DSN stations, it is planned at the current time to provide a spectrum analyzer type of device to operate on a full read-after-write output from the recorder in real-time. This will enable the detection of all signals of interest, or at least a single signal of interest, to show that the total end-to-end system is configured properly and that actual data are going to the recorder. The possibility of employing a similar process at the STDN stations has been discussed, and it appears feasible to provide a commercially available spectrum analyzer capable of detecting the bus signal using a digital-to-analog converter after the full read-after-write on the recorder. The advantage of this kind of approach for the STDN stations is that it would also be assuring that the station was actually on point. This is known automatically at the 64-meter stations because of the capability of detecting the telemetry in real-time. Other alternatives are being discussed for the STDN stations, such as the feasibility of tracking the Orbiter spacecraft using a regular closed-loop receiver just for the purpose of validating that the station is indeed on point. These monitor alternatives are still being evaluated by the STDN.

IV. The DLBI Tape Conversion Facility

The bottom part of Fig. 1 portrays the functional elements in the tape conversion facility to be provided at the Compatibility Test Area (CTA 21) at JPL, Pasadena. The process involves recovering one spacecraft signal at a time from the wideband recording by digitally mixing an estimate of that particular spacecraft signal with the output of the wideband tape recording and then digitally filtering the product so that the output is of sufficiently narrow bandwidth to be accommodated on a standard 9-track computer-compatible tape recording. The digital bandwidth reduction mixer and filter is envisioned to be a piece of special-purpose hardware (involving firmware), while the controller and formatter will be software written for a standard DSN minicomputer already available in CTA 21. The planned resulting bandwidth will be on the order of 1 kHz. Each of the five spacecraft signals (four probes and the bus) and the two calibration tones will each be independently processed. It will be Project responsibility to provide the DSN with the estimate of the frequency history of each of the five spacecraft signals.

V. DLBI Ground Data System Integration Plan

Figure 2 shows the overall major milestone schedule for the DLBI Wind Measurement Experiment of Pioneer Venus. For integrating the DSN and STDN elements, it is planned to do a trial installation in an STDN station located at Goldstone of all equipment required for the STDN configuration in mid-November 1977. This should enable solving any final integration and interface problems utilizing local engineering support. For interfacing with the experimenter, it is planned to provide on 1 October 1977 a computer-compatible tape that is correct in format, followed on 1 January 1978 by a computer-compatible tape which contains actual tones which have passed through the entire TDA portion of the Ground Data System. It is anticipated that the first computer-compatible recording containing actual signals (from the ALSEP or some other suitable spacecraft signal) will be available for the experimenter at the end of the first week of February 1978. At least two of the four stations should be ready in mid-February 1978 to start supporting some end-to-end system checkouts, with all four stations ready by mid-March 1978. It is planned to be fully operational by 1 April 1978, and to start supporting regular

interferometry observations (currently envisioned as ALSEP tracking) from that time until the actual entry event the first of December 1978. This will give at least eight months to shake out any remaining problems in the total system, including the equipment and software at MIT.

Reference

1. Miller, R. B., "Pioneer Venus 1978 Mission Support," in *The Deep Space Network Progress Report 42-31*, pp. 11–14, Jet Propulsion Laboratory, Pasadena, Calif., Feb. 15, 1976.

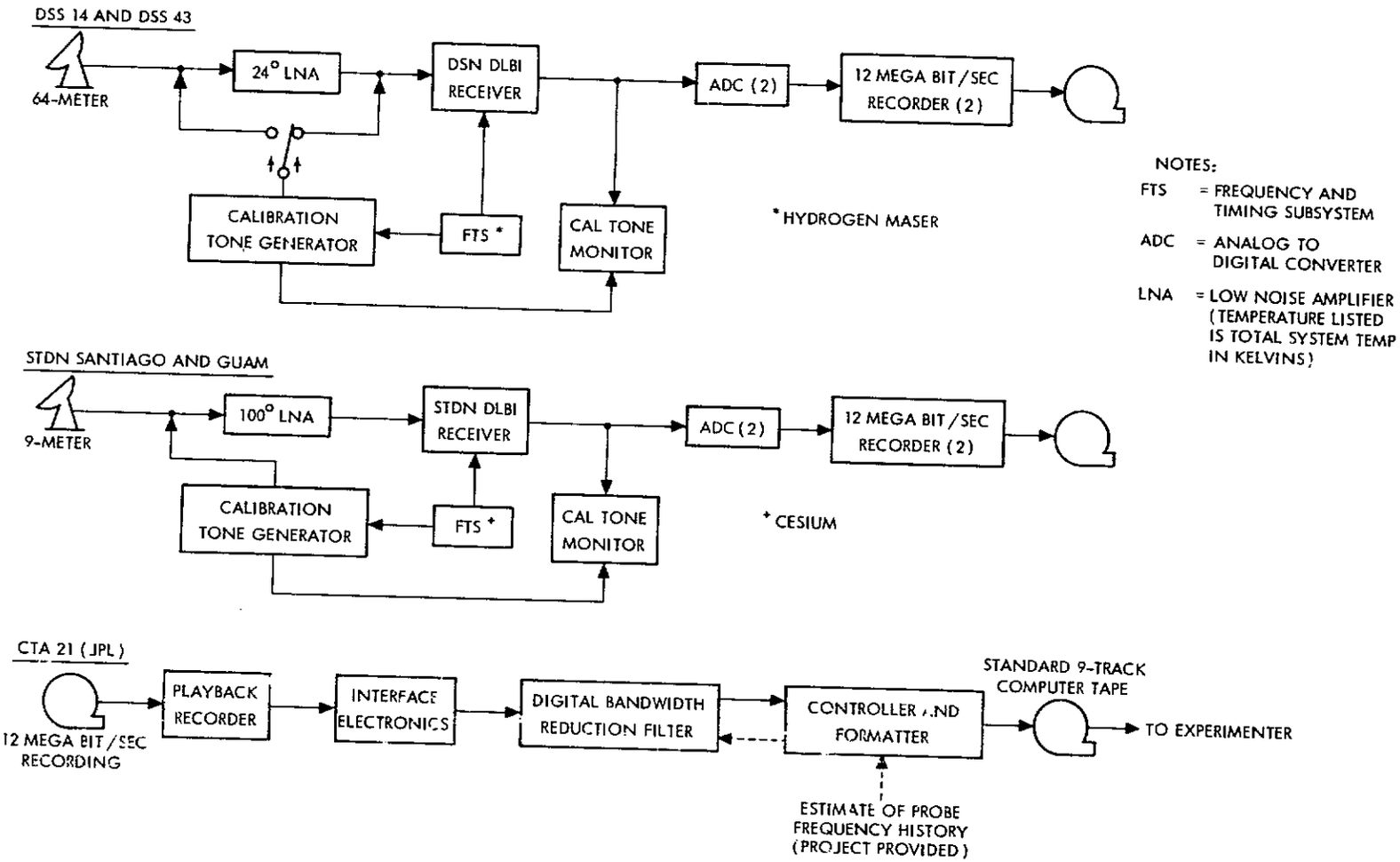

Fig. 1. Configuration for support of Pioneer Venus 1978 DLBI Wind Measurement Experiment

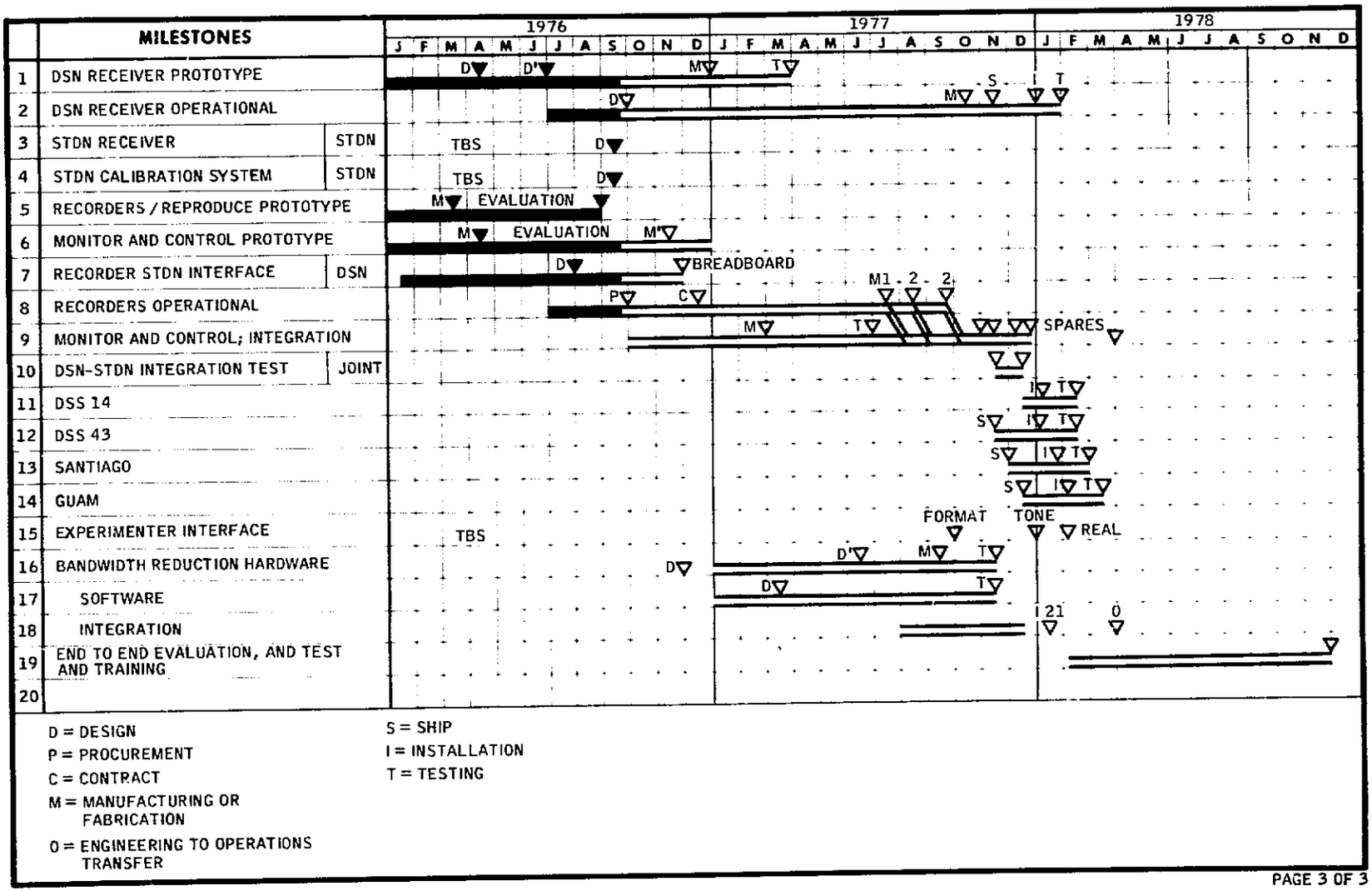

Fig. 2. Pioneer Venus 1978 major milestone schedule for DLBI Wind Measurement Experiment

N77-14049

Helios Mission Support

P. S. Goodwin
TDA Mission Support
E. S. Burke and R. E. Morris
DSN Network Operations Section

Operating beyond its 18-month design lifetime, the Helios-1 spacecraft continues to gather valuable scientific data. Having achieved its fourth perihelion, the Helios-1 spacecraft is being closely followed by Helios-2, as the latter emerges from a lengthy solar conjunction period, in which considerable scientific data were collected on Experiments 11 and 12 (Celestial Mechanics and Faraday Rotation). The scientific opportunities to compare the data from the two Helios spacecraft continue to add to man's knowledge of the sun's influence upon the inner solar system.

I. Introduction

This is the twelfth article in a series that discusses Helios-1 and -2 mission support. The previous article (Ref. 1) reported on a Helios-1 spacecraft power anomaly, Helios-2 occultation, STDN–DSN telemetry cross-support engineering-level tests, tracking coverage and DSN performance. This article covers the Helios-1 third solar occultation and fourth perihelion. A Helios-2 spacecraft emergency and third solar conjunction (occultation) are also discussed. Additional topics include STDN–DSN telemetry and command cross-support, Ground Data System tests, tracking coverage, plus DSN system performance for August and September 1976.

II. Mission Operations and Status

A. Helios-1 Operations

The Helios-1 spacecraft occulted the sun for a third time on September 23, 1976. The spacecraft was transmitting on traveling-wave tube amplifier 2 (TWTA-2), high-power mode, and stored experiment data on-board the spacecraft for memory readout later at a higher bit rate. As the probe cleared the "blackout" region, heading towards its fourth perihelion, the spacecraft team commanded TWTA-2 to medium power. The medium power mode was selected to reduce the risk of excessive traveling-wave tube (TWT) assembly temperature as the spacecraft approached the sun.

At 1907 GMT on Tuesday, October 5, 1976, the Helios-1 spacecraft successfully passed its fourth perihelion at a minimum distance of 0.309 AU (approximately 45 million km) from the sun. The maximum solar impact was equal to 10.445 solar constants. The overall performance of the spacecraft and its 10 scientific instruments, which had exceeded the design lifetime of 18 months, was excellent. All 10 experiments were fully configured for prime mission mode and delivering valuable science data.

Several members of the scientific team observed the perihelion passage from the German Space Operations Center (GSOC). The scientists are finding Helios-1 perihelion data very interesting since it provides a second unique opportunity of comparing measurements with Helios-2 (presently approaching its second perihelion, which is centered around October 20, 1976).

B. Helios-2 Operations

At 17:44:52 GMT on September 4, 1976, after transmission of a "ranging-on" command (at 1715 GMT), the downlink of the Helios-2 spacecraft was lost. This occurred during pass number 234 over DSS 11 (Goldstone). The failure was observed while attempting to acquire the ranging signal. Several commands were transmitted altering the spacecraft's RF configuration in an attempt to restore the downlink. This eventually resulted in reestablishing the Helios-2 spacecraft's downlink, but near threshold. To learn if the low signal was due to DSS 11 or the spacecraft, the services of DSS 42 (Australia) were attained from a scheduled Viking pass. DSS 42 was brought up as a Helios "follow-on" pass after DSS 11's loss of signal. Subsequent troubleshooting (altering the spacecraft configuration by commands) over DSS 42 tentatively restored the downlink signal at 1938 GMT in the following configuration: TWTA-1, high power, driver 1, and noncoherent mode. A spacecraft emergency was declared at 2254 GMT. After reconfiguring the spacecraft in the combination of TWTA-1, medium power, driver 1, coherent and medium-gain antenna, the DSS 42 receiver obtained lock. Switching to the spacecraft's high-gain antenna (HGA) resulted in a solid receiver and telemetry lock at 0121 GMT, September 5. The spacecraft configuration and health were verified, and the spacecraft emergency terminated at 0500 GMT on September 5.

After a few days in which to analyze the spacecraft anomaly, it was theorized that the loss of downlink was probably caused as a result of two commands: (1) ranging-on, and (2) TWTA-2 medium power. Pending further investigations it was recommended to (1) avoid ranging commands until after the second perihelion, and (2) stay on TWTA-1 in the medium-power mode.

Helios-2 experienced its third "blackout" (solar occultation) period during September 20–29, centered on September 26, 1976. All scientific data were read into memory on-board the spacecraft and later read-out when higher bit rates were available.

The Helios-2 spacecraft will pass its second perihelion around October 20, 1976. The results of this perihelion will be covered in the next progress report.

C. STDN–DSN Engineering Test and Support

Encouraged by the DSN engineering tests regarding STDN real-time telemetry and command cross-support completed during May–June 1976 (Refs. 1 and 2), the U. S. Helios Project Manager requested support for Helios-1 and -2 by the STDN Goldstone Station (GDS). This cross-support was requested for the October perihelions of Helios-1 and -2, thence continuing until November 15, when STDN GDS will temporarily be de-committed from all flight support for a scheduled equipment modification program.

Before the STDN–DSN real-time Helios cross-support could be considered operational, the link between STDN GDS and the DSN Goldstone inter-site microwave system needed more permanency. The interface installed for the engineering tests in June was a one-way temporary coaxial cable.

After considering available options, it was decided that the most suitable and economical method of providing a full duplex interconnection between STDN GDS and DSS 11 was to reestablish the old Project Apollo microwave link between STDN GDS and DSS 14. There it could join the DSN Goldstone inter-site microwave system. The Apollo-era equipment was reinstalled and successfully tested by September 30, 1976.

The plan was to first send real-time spacecraft telemetry over the newly established microwave link (Fig. 1) from STDN GDS to DSS 11 (via DSS 14 and GCF 10, both at Goldstone) where it would be processed by the back-up TCP string and sent to JPL. The uplink-lock and command tests would be conducted a week later followed by a telemetry and command demonstration pass. Upon successful completion of this demonstration pass, the STDN–DSN Helios cross-support configuration would be committed for operational support.

The first real-time Helios spacecraft telemetry was processed over the new STDN–DSN configuration (see Figs. 1 through 3) on October 1, 1976, during a demonstration pass. Data from two other STDN–DSN Helios cross-support passes were accumulated on October 15 and 16. The results are shown in Table 1.

The STDN–DSN Helios command configuration was successfully tested during the week of October 11, 1976. Several spacecraft uplink acquisitions and commanding sequences were conducted for STDN (GDS) operator training during this week. With the successful STDN–DSN Helios Telemetry and Command cross-support demonstration track performed on October 18, 1976, the STDN–DSN cross-support configuration was declared operational for Helios Project support.

Although the data from this cross-support configuration were degraded (approximately 3.5 dB) when compared to a DSN 26-meter station, the data received from Helios at perihelion and distances less than 1 AU are excellent.

D. Ground Data System Tests

1. High-Speed Data Line Change to 7.2 kb/s. The Deep Space Network (DSN) plans to convert all high-speed data terminals to 7.2 kb/s on December 1, 1976. This conversion will standardize DSN high-speed data line rates with NASA Communications (NASCOM) standards. On September 27, 1976, during Helios-1 pass 658 over DSS 12 (Goldstone), a special Ground Communications Facility (GCF) test was performed to verify that the DSN GCF conversion to a 7.2-kb/s high-speed data line (HSDL) rate was compatible with mission-dependent Mission Control and Computing Center (MCCC) software programs and hardware. The test consisted of sending parallel data streams on standard 4.8-kb/s HSDL and the new 7.2-kb/s HSDL to MCCC for Model 360-75 computer processing (monitor and tracking data were not tested at this time). Although one command anomaly did occur, there were no problems attributable to the 7.2-kb/s interface during the test. The planned changeover to the 7.2-kb/s HSD system on December 1, 1976 should be essentially "invisible" to the MCCC data system and to DSN–MCCC operations.

2. New Telemetry Capability at the German Weilheim Station. In April 1976, the German Helios Project Office received word that their request to modify the Telecommand Station at Weilheim to include a telemetry data receiving capability had been approved. Conversion was planned for late 1976 (Ref. 2). By August the conversion was progressing quite satisfactorily. The telemetry receiving equipment had been transported from the 100-meter Effelsberg Station to Weilheim. After internal (German) engineering tests were completed, internetwork interface tracking validation tests were scheduled involving Weilheim and DSS 62 (Spain). The DSN supported two of these tests—the first on September 13 and the second on September 17, 1976. These tests were highly successful, and the Weilheim Telemetry/Command Station (67/68) became operational on September 20, 1976.

E. Actual Coverage Versus Scheduled Coverage

This report covers tracking activities for a 63-day period from August 9 through October 10, 1976. Operations for this period include Helios-1 cruise, solar occultation, and fourth perihelion. Helios-2, still in solar conjunction phase, occulted the sun for the third time. Total tracks for both spacecraft were 101 for a total of 862.7 hours. Although this represents only 82 percent of the passes taken last period, there were 61 more hours of coverage. The Helios spacecraft received 41.4 percent of the DSN tracking time allotted to both Pioneer and Helios, after Viking requirements were satisfied. Helios-1 was tracked 50 times for a total of 441.4 hours; Helios-2 was tracked 51 times for 421.6 hours. The average pass time was 8.8 hours for Helios-1 and 8.2 hours for Helios-2. This compares with the last report period of 7.03 and 5.5 hours, respectively. Only 25 hours of 64-meter subnet support was allocated for the Helios spacecraft during this period due to Viking support requirements. As the Helios-1 and -2 spacecraft trajectories approach Earth, only the 26-meter subnet will be required for tracking, with the exception of ranging at DSS 14. DSN tracking support is expected to continue at its present level throughout the next report period.

III. DSN System Performance

A. Command System

The Helios extended mission command activity continued at a low level during August and September for both spacecraft. A total of 2461 commands were radiated to both Helios-1 and -2 spacecraft. This compares to 2910 commands radiated during the last reporting period. This low activity is due to two reasons: (1) the Helios-2 spacecraft spent the greater portion of this time in solar conjunction (sun–Earth–probe (SEP) angle less than 5 degrees), and (2) heavy Viking activities resulting in relatively few tracks for Helios. The cumulative command totals through September are 40,792 for Helios-1 and 14,345 for Helios-2.

There were three command system aborts during August and September—all with Helios-1. Two of the aborts were caused by DSS transmitter failures and the third by a fault in a DSS Command Modulator Assembly (CMA). Helios-2 experienced no command aborts. The cumulative command system abort count was raised to 13 for Helios-1 and remained at 3 for Helios-2.

Total command system downtime for the months of August and September rose to 12 hours and 50 minutes (almost twice the figure for the previous 2 months). Approximately one-half (5.3 hours) of the reported downtime for this period was caused by one failure at DSS 44 (a faulty circuit breaker). Of the 10 failures recorded, 5 were transmitter associated.

B. Tracking System

As the Helios spacecraft speed toward their even-numbered (in-bound) perihelions, their velocity with respect to Earth causes a negative doppler shift which exceeds the capability of the standard doppler extractor. To compensate for this condition, an additional 1-megahertz bias is added to the standard doppler bias at the 26-meter stations for a total bias of 2 megahertz. (Stations with Block IV receivers (64-meter) are able to select a minus 1-MHz bias.) The bias shift is required to avoid ambiguous doppler counts when the negative doppler approaches or exceeds the amount of positive doppler fixed bias.

The Network Operations Analysis Group (Tracking) computes the dates to add this special bias into the systems for each spacecraft. This doppler "offset" bias will be required for Helios-1 from September 29 through October 26 and for Helios-2 from October 6 through November 7, 1976.

Also affected are the transmit and receive frequencies at the Helios-supporting DSN stations. Because of this negative doppler frequency, a ground station must transmit at a lower than normal frequency and receive a higher than normal frequency to maintain relative constant frequencies at the spacecraft receiver. On September 23 the DSN stations supporting Helios-1 began operating on voltage-controlled oscillator (VCO) transmit S-band channel 20-b and receive S-band channel 22-a, as opposed to channels 21-a and 21-b, which are normally used. This will continue until November 2, 1976. Helios-2 VCO change to 14-b and 16-a for transmit and receive, respectively, will be required between September 27 and November 14, 1976. The times to switch to these frequencies are computed by the Network Operations Analysis Group.

The Helios-1 spacecraft's ranging transponder began to operate once more on July 14, 1976, when its temperature again came within operable limits (Ref. 3). Good ranging points are now possible with Helios-1 until about October 20 when it is predicted that the temperature of the ranging unit will again slip into the non-operational range (5°C to 18°C).

Ranging with the Helios-2 spacecraft has not been attempted since the spacecraft emergency on September 4, 1976. Because a ranging command was thought to be partially to blame for the loss of spacecraft downlink, it was agreed that ranging would not be tried again with Helios-2 until after the second perihelion on October 17, 1976, when better link conditions would exist.

C. Telemetry System

During the Helios-1 and -2 superior conjunction periods, two types of data have been routinely collected for internal DSN use. The first type of data consists of hourly readings from the system-noise-temperature (SNT) recordings. The second type was spectral broadening test data. These data are being used to expand a data base that will be used later to improve telemetry predict values at small SEP angles.

Telemetry support for Project Helios has been rather routine—broken only with special downlink signal predictions for the STDN-DSN cross-support configuration. DSN telemetry predicts have been within 0.6 dB in automatic gain control (AGC) and 0.8 dB in signal-to-noise ratio (SNR) for Helios-1. Helios-2 figures are not so readily computed since tracking has been minimal during this period, caused by extremely small SEP angles.

IV. Conclusions

Emerging from a relatively quiet cruise phase, the Helios-2 spacecraft experienced its third solar occultation on September 23, 1976. Spacecraft ranging was again possible as the spacecraft ranging assembly temperature rose above 18 degrees Celsius. On October 5, 1976, the Helios-1 spacecraft passed within 0.309 AU (approximately 45 million km) of the sun as its instruments recorded the fourth perihelion. The spacecraft's health is good as it continues its trajectory which will bring it closer to Earth.

Overcoming a spacecraft emergency on September 4, 1976, the Helios-2 spacecraft passed its third solar occultation on September 26, 1976. Owing to the nature

of the spacecraft emergency, the spacecraft team is cautiously delaying, until after the second perihelion (October 20, 1976), any further attempt at spacecraft ranging.

The awaited decision confirming STDN–DSN Helios cross-support for Project Helios came in mid-September 1976. An STDN–DSN Helios cross-support configuration was verified and placed into operation on October 18, 1976. This telemetry and command configuration utilizes the facilities shown in Figs. 1 through 3.

The DSN is continuing plans to convert to the 7.2-kb/s high-speed data terminals. One of the tests performed to verify hardware/software compatibility was run during Helios-1 pass 658 in September. All equipment performed well.

The German Helios command station at Weilheim was modified to include telemetry and command capabilities (telemetry added) and began operations on September 20, 1976. The German Effelsberg 100-meter radio telescope is no longer supporting Helios.

The Helios-1 and -2 spacecraft tracking activities remained at about the same level as in the previous period. This was primarily because the Helios-2 spacecraft remained in solar conjunction for most of this time period. Tracking coverage should increase during the next period owing to both spacecraft passing perihelion and approaching closer to Earth.

Although the number of commands sent to the Helios spacecraft decreased, there were three command system aborts during this report period (all on Helios-passes). Except for transmit and receive frequency changes and added doppler bias to compensate for the high doppler rate at this point in the trajectories of the spacecraft, the performance of the Telemetry and Tracking Systems remained fairly routine.

Acknowledgments

The authors wish to thank the following members of the Network Operations Analysis Group for their contribution of periodic Network Performance Reports.

Tracking:	A. L. Berman, R. S. Schlaifer, L. Bright
Command:	R. Gillette, W. L. Tucker
Telemetry:	R. Allis, H. G. Lemasters
Monitor and RFI:	P. Low, C. Lunde

References

1. Goodwin, P. S., Meeks, W. G., and Morris, R. E., "Helios Mission Support," in *The Deep Space Network Progress Report 42-35*, pp. 24–27, Jet Propulsion Laboratory, Pasadena, Calif., Oct. 15, 1976.
2. Goodwin, P. S., Meeks, W. G., and Morris, R. E., "Helios Mission Support," in *The Deep Space Network Progress Report 42-34*, pp. 21–26, Jet Propulsion Laboratory, Pasadena, Calif., Aug. 15, 1976.
3. Goodwin, P. S., Meeks, W. G., and Morris, R. E., "Helios Mission Support," in *The Deep Space Network Progress Report 42-33*, pp. 26–31, Jet Propulsion Laboratory, Pasadena, Calif., June 15, 1976.

Table 1. STDN–DSN Helios cross-support engineering test results

Day of year (1976)	Bit rate	Predicted (DSN), dB	STDN		DSN vs STDN	
			Block III, dB	MFR, dB	Block III difference, dB	MFR difference, dB
275 (Oct 1)	32	9.8	6.2	4.8	3.6	5.0
	64	8.5	4.0	2.6	4.5	5.9
289 & 290 (Oct 15, 16)	128	8.1	5.3	N/A	2.8	N/A

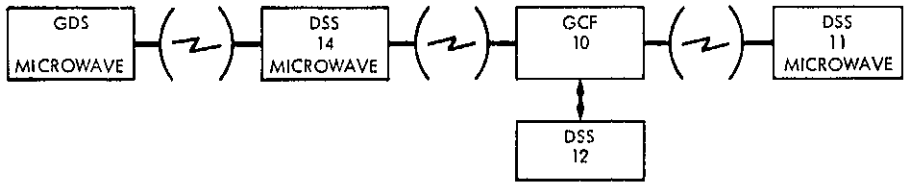

Fig. 1. STDN (GDS)-DSS microwave configuration

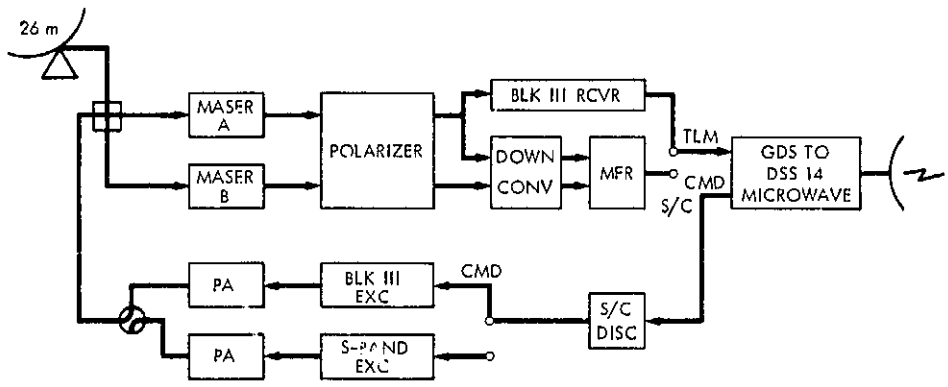

Fig. 2. STDN (GDS) cross-support configuration

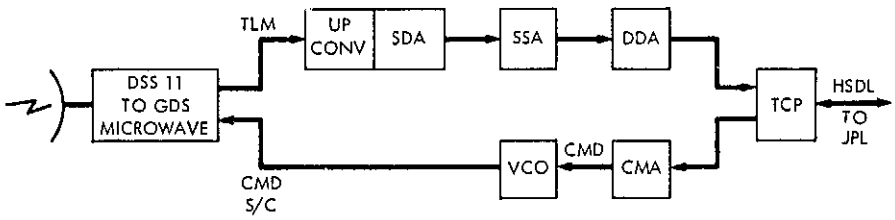

Fig. 3. DSS cross-support configuration

N77-14050

Terminology of Ranging Measurements and DSS Calibrations

T. Komarek
Telecommunications Systems Section

T. Otoshi
Radio Frequency and Microwave Subsystems Section

This article presents a proposed set of basic terminology related to deep space ranging measurements. Calibration equations are derived for the "dish-mounted zero delay device" method for 26-m antenna systems and the "translator" method for 64-m antenna systems.

I. Introduction

Data produced by the ranging system can be used in many ways: spacecraft orbit determination, space plasma measurements, earthquake detection, etc. Whatever the objective is, the basic element is always the measurement of the time elapsed between transmission and reception of a ranging code by an Earth-bound Deep Space Station (DSS). The ranging code is modulated on a RF carrier transmitted from a DSS to a distant spacecraft (S/C), where it is demodulated and retransmitted back to Earth. The time delay measured, therefore, necessarily includes the DSS and spacecraft hardware delays, as well as medium effects due to tropospheric refraction and "deceleration" in the ionosphere and space plasma.

This article addresses terminology of ranging measurements with obvious emphasis on DSS delay calibrations since this is the most complicated part of the ranging telecommunication link. To make the semantics meaningful, it is useful to recognize the following "axioms:"

(1) Range is always one-way; it is measured in units of length.

(2) Delay is measured in time units (whatever they are).*

(3) "Light time" corresponds to propagation with the velocity of light in vacuum.

This article was originally a response to the immediate needs of the Viking Radio Science Team. It is suggested, however, that the terminology presented would be con-

*The "range unit" is a time unit since it is an integer fraction of the time period of the DSS master oscillator.

sidered for acceptance by the Ranging Accuracy Team and, through this body, acceptance by other organizations involved, i.e., DSN, Spacecraft Telecommunications, Navigation, and Mission Control.

II. Definitions and Explanations

The following definitions apply to the general case ranging system geometry shown in Fig. 1:

Topocentric range ρ, in meters, is the distance between the DSS and spacecraft reference locations.

Reference locations are the spacecraft antenna aperture plane, DSS antenna axis crossing for the azimuth-elevation (az-el) mount, and the intersection of the polar axis with the hour angle (HA) plane for the hour angle-declination (HA-Dec) mount.

Round trip light time, in seconds, is

$$RTLT = 2\,\rho/c$$

where c is the velocity of light in vacuum.

Round trip propagation time is the time for the ranging modulation to propagate from the *DSS reference location* through the propagation media (planetary atmosphere, space plasma, . . .) to the *S/C reference location* and back, as measured by a correlation-type ranging machine.

$$RTPT = RTLT + BIAS_{MEDIA}$$

Delay to spacecraft, $D_{S/C}$, in seconds, is the total delay measured by a ranging machine when ranging to a spacecraft. It is related to *RTPT* by

$$RTPT = D_{S/C} - BIAS_{S/C} - BIAS_{DSS} + Z_{CORRECTION} \tag{1}$$

where all entries are in seconds, and

$BIAS_{S/C}$ = spacecraft turnaround delay

$BIAS_{DSS}$ = 2-way DSS delay pre- and post-track measured from the ranging machine to a DSS turnaround device (either ZDD or translator) and back.

$Z_{CORRECTION}$ = 2-way ground station delay correction which must be made to account for the

(a) difference in the DSS turnaround device path and the ranging-to-spacecraft path up to the DSS aperture plane.

(b) difference between the DSS antenna aperture plane and the DSS reference location.

III. DSS Calibrations

A. Dish-Mounted Zero-Delay-Device Method

Station delay calibrations by means of a dish-mounted zero delay device (ZDD) are presently used by the 26-m DSS subnets. This technique (Fig. 2) uses the geometric optics principle in which, for a large antenna with a parabolic geometry (including Cassegrain S/X reflex feed systems), the distance for any ray path from the primary feed phase center to the paraboloid aperture plane via the microwave optics airpath is a constant. Under this assumption, the time delay for any ray propagating along the microwave optics path from the feed horn phase center to the aperture plane is the same as that for any other ray path between these two points (going from the feed horn phase center to the aperture plane or from the aperture plane to the feed horn phase center via the microwave optics ray paths).

Assuming that the internal delay of the ZDD is negligible, it can be seen from Fig. 2 that when ranging to a spacecraft

$$D_{S/C} = D_{ZDD} + \tau_X + \tau_{R,up} + BIAS_{S/C} + \tau_{R,\,down} + \tau_X \tag{2}$$

where D_{ZDD} is the round trip delay from the ranging machine to the ZDD located on the dish surface and back to the ranging machine. It includes transmitter and receiver delays as well as round trip airpath delays within the antenna structure.

It can also be seen from Fig. 2 that

$$RTPT = \tau_b + \tau_h + \tau_X + \tau_{R,up} + \tau_{R,down} + \tau_X + \tau_h + \tau_b \tag{3}$$

Solving for $(\tau_{R,up} + \tau_{R,down})$ from (2) and substitution into (3) gives

$$RTPT = D_{S/C} - BIAS_{S/C} - D_{ZDD} + 2\tau_h + 2\tau_b \quad (4)$$

Comparison of (4) with (1) gives

$$BIAS_{DSS} = D_{ZDD} \quad (5)$$

$$Z_{CORRECTION} = 2\tau_h + 2\tau_b \quad (6)$$

where, from the geometry of Fig. 2, the one-way airpath delays τ_h and τ_b (in seconds) are

$$\tau_h = \frac{h}{c} \quad (7)$$

$$\tau_b = \frac{b}{c}\cos\delta \quad (8)$$

and where

h = distance in meters between two planes parallel to the aperture plane. The first plane intersects the ZDD and the second plane contains the declination (secondary) axis.

b = perpendicular distance in meters between the hour-angle (primary) and declination (secondary) axes. This distance in JPL antenna drawings is shown to be 6.7056 meters (22.0 ft).

c = speed of electromagnetic wave in vacuum (2.997925×10^8 m s^{-1})

δ = spacecraft declination angle

The values of D_{ZDD} given by (5) are reported for pre- and post-track on the "DSS Post-Track Report." The $Z_{CORRECTION}$ given by (6) depends not only on the physical location of the ZDD on the dish surface but also on the spacecraft declination angle δ. Values of h and b are obtained at each 26-m DSS from physical measurements and are the constants supplied by the DSN. These constants together with the declination angle information should be used by the Orbit Determination Software to determine the $Z_{CORRECTION}$ from (6) for the appropriate tracking pass.

B. Translator Method

The DSS calibration method using the dish-mounted ZDD suffers by multipath errors due to multiple reflections from the antenna structure. For 64-m stations, where the multipath error can be several meters, another calibration method was developed using the Block IV translator (Fig. 3). In this method, only a portion of the DSS hardware delays is pre- and post-track measured. The rest of the hardware delays (including antenna and cabling) is calculated from geometrical dimensions (in the case of waveguide and airpath) and precalibrated (in the case of complex components such as diplexers and filters).

When ranging to a spacecraft, the ranging machine measures $D_{S/C}$, the total two-way delay-to-spacecraft. $D_{S/C}$ contains the propagation delays and both DSS and S/C biases. From Fig. 3, using τ to denote one-way delay, it can be seen that

$$D_{S/C} = \tau_1 + \tau_3 + \tau_{C,up} + \tau_{R,up} + BIAS_{S/C} + \tau_{R,down} + \tau_{C,down} + \tau_4 + \tau_2 \quad (9)$$

where

all entries are in time units

$\tau_1, \tau_2, \tau_3, \tau_4$ = DSS hardware delays shown in Fig. 3.

τ_R = propagation delay (including medium effects) from the DSS antenna aperture plane to the S/C reference location.

τ_C = one-way delay from feedhorn phase center to aperture plane of the DSS antenna via the microwave optics airpath. The S-band airpath includes points on the ellipsoidal reflector, dichroic plate, hyperboloidal subreflector, and the main paraboloidal reflector surface.

τ_D = one-way delay between the aperture plane and DSS reference location

Both τ_C and τ_D are constants for a given DSS, independent of the point on the dish surface where reflection takes place, due to the parabolic geometry of DSS antenna dishes and Cassegrain design.

Also from Fig. 3, it can be seen that the round trip propagation time is

$$RTPT = \tau_D + \tau_{R,up} + \tau_{R,down} + \tau_D \quad (10)$$

But from (9)

$$\tau_{R,up} + \tau_{R,down} = D_{S/C} - \sum_{i=1}^{4}\tau_i - \tau_{C,up} - \tau_{C,down} - BIAS_{S/C} \quad (11)$$

Substituting (11) into (10) gives

$$RTPT = 2\tau_D + D_{S/C} - \sum_{i=1}^{4} \tau_i - \tau_{C,up} - \tau_{C,down} - BIAS_{S/C} \quad (12)$$

Defining one-way delays τ_5 and τ_6 as

$$\tau_5 \triangleq \tau_{C,up} - \tau_D$$

$$\tau_6 \triangleq \tau_{C,down} - \tau_D,$$

then substituting into (12) leads to the RTPT expression when ranging to spacecraft of

$$RTPT = D_{S/C} - BIAS_{S/C} - \sum_{i=1}^{6} \tau_i \quad (13)$$

When ranging to translator, the ranging machine measures D_{XLATOR}, the two-way delay-to-translator.

From Fig. 3

$$D_{XLATOR} = \tau_1 + \tau_{XLATOR} + \tau_2 \quad (14)$$

where

τ_{XLATOR} = one-way delay from the uplink sample point through the translator to the downlink sample point. This delay is calibrated by a portable ZDD.

From (13) and (14)

$$RTPT = D_{S/C} - BIAS_{S/C} - D_{XLATOR} - \sum_{i=3}^{6} \tau_i + \tau_{XLATOR} \quad (15)$$

Comparing (15) with (1) we get the DSS calibrations for the translator method:

$$BIAS_{DSS} = D_{XLATOR} \quad (16)$$

$$Z_{CORRECTION} = \tau_{XLATOR} - \sum_{i=3}^{6} \tau_i \quad (17)$$

or from substitutions of τ_5 and τ_6

$$Z_{CORRECTION} = \tau_{XLATOR} + 2\tau_D - \tau_3 - \tau_4 - \tau_{C,up} - \tau_{C,down} \quad (17a)$$

where all terms are defined in Fig. 3.

The $Z_{CORRECTION}$ does not require knowledge of τ_h as in the case of a dish-mounted ZDD. Except for τ_{XLATOR}, which is a calibrated value obtained through measurement, most of the terms in $Z_{CORRECTION}$ are calculated quantities, which is a major drawback of this calibration method. The station bias (D_{XLATOR}) is a measured delay, reported by a station pre- and post-track. Values of τ_D,($\tau_{C,up}$) and ($\tau_{C,down}$) for the S/X reflex feed configuration for 64-m antenna systems have been determined by Batelaan and are reported in Ref. 1.

Reference

1. Otoshi, T. Y., ed., *A Collection of Articles on S/X-Band Experiment Zero Delay Ranging Tests*, Technical Memorandum 33-747, Vol. 1, Jet Propulsion Laboratory, Pasadena, Calif., Nov. 1975, p. 50.

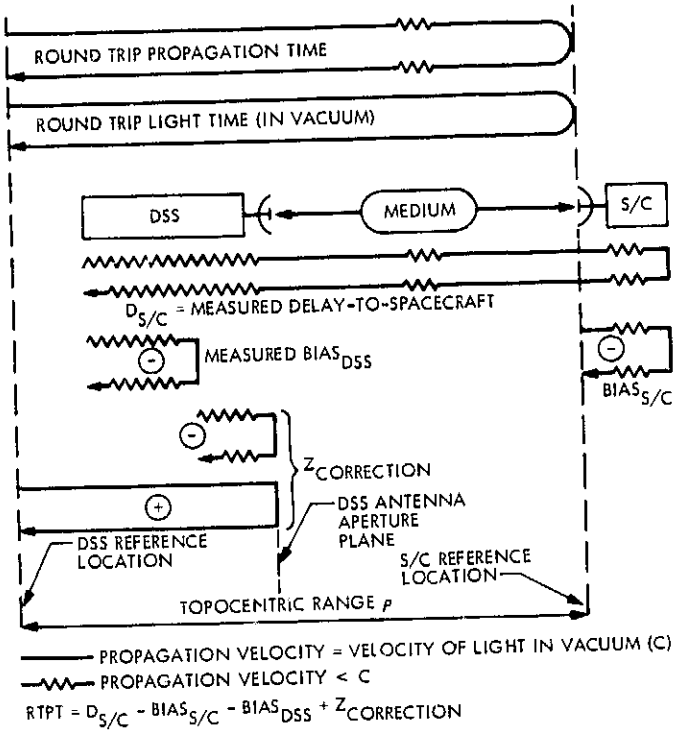

Fig. 1. Ranging measurement definitions

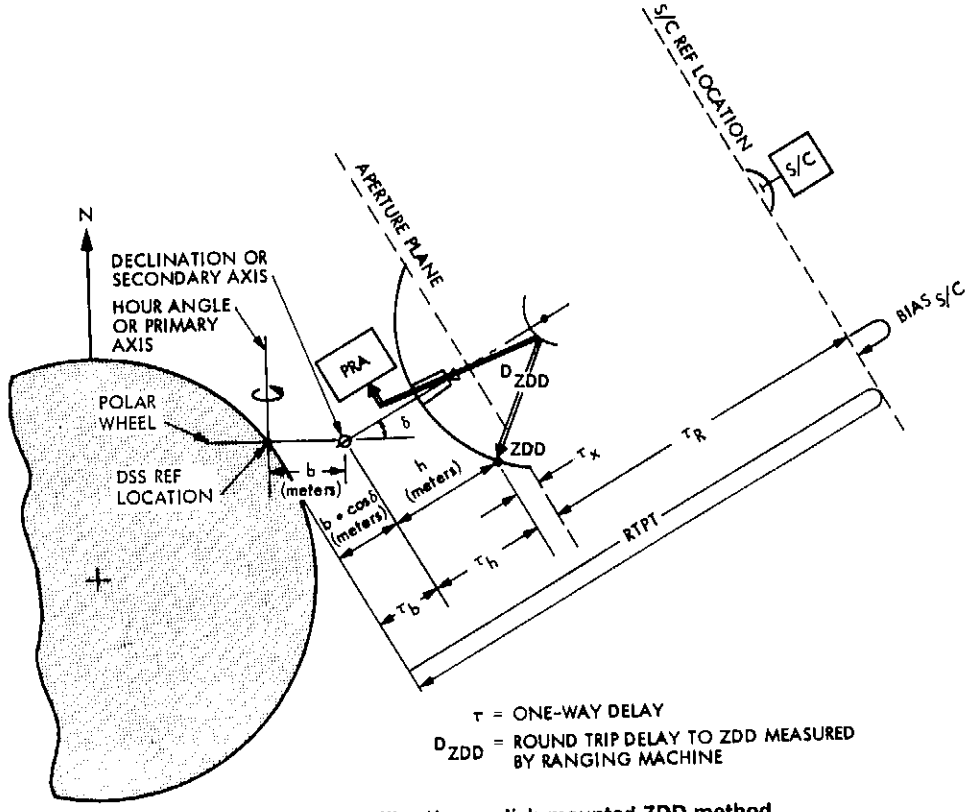

Fig. 2. DSS calibration — dish-mounted ZDD method

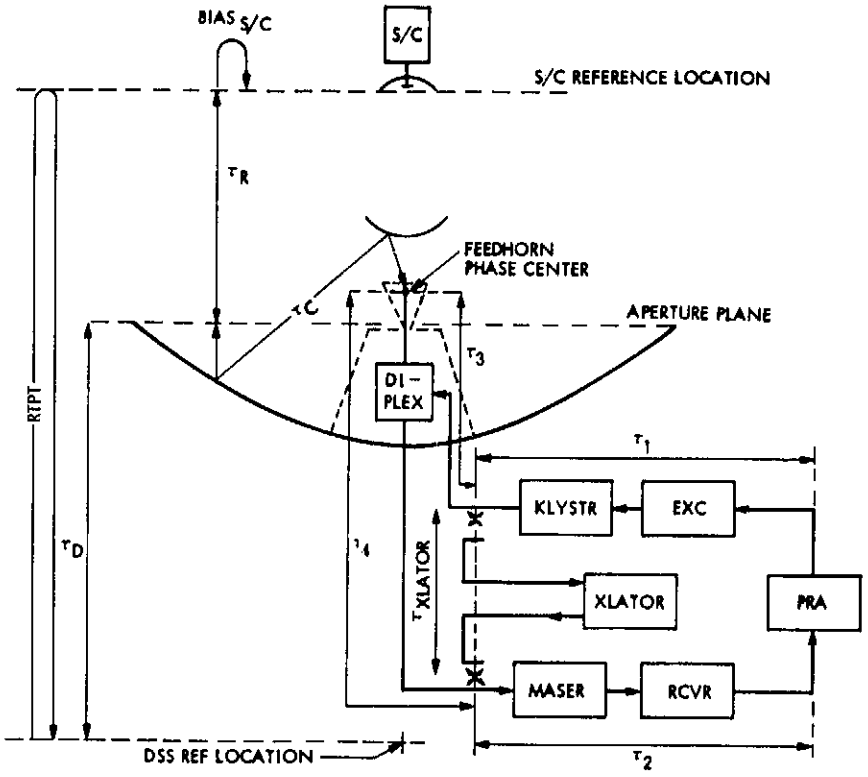

Fig. 3. DSS calibration — translator method

N77-14051

Magnitude of 64-m Elevation Axis Movements Due to Alidade Temperature Changes

N. t. Hung, H. Phillips, and R. Zanteson
DSN Engineering Section

In projected very-long baseline interferometry (VLBI) work a reference point for 64-m antennas is the intersection of the elevation and azimuth axes. This report describes a minimum-level effort at DSS 14 to determine the magnitude of the effect of diurnal changes in the temperature of the alidade legs on the height of the elevation axis. The thermal expansion between the lowest recorded temperature −3°C (27°F) and the highest, 36°C (97°F), over the period covered was 8.9 mm (0.35 in.).

I. Introduction

In projected VLBI work a reference point for 64-m antennas is the intersection of the elevation and azimuth axes. This report describes a minimum level effort at DSS 14 to determine the magnitude of the effect of diurnal changes in the temperature of the alidade legs on the height of the elevation axis. The results, over a period from March through September, 1976, show an average height change of 1.70 mm (0.07 in.) during a day, with a range from 0.1 mm (0.004 in.) to 3.5 mm (0.14 in.) for the period covered. The thermal expansion between the lowest recorded temperature −3°C (27°F) and the highest, 36°C (97°F), over the period covered was 8.9 mm (0.35 in.).

II. Test Instrumentation

Alidade temperature measurements were made using surface thermometers placed on an inner surface (to avoid direct sunlight) of the front alidade legs (Figs. 1 and 2). Initially, thermometers were placed on the right front leg. After one month's data were taken, one of the thermometers was moved to the left leg to determine if the temperatures there were significantly different.

The alidade leg and ambient temperature readings were recorded three times each day by maintenance personnel, generally at 0600, 1200, and 2000 hours. The temperature readings for the right leg were averaged, and the differences between the high and low reading for

these data and for the left leg and ambient temperatures were tabulated. The results were then reduced statistically, and are shown for each month in Table 1. The dimensional change is based on a length of 20.96 m (835 in.), the distance from the elevation bearing to the machinery deck level, and a coefficient of thermal expansion of 1.08×10^{-5}/°C (6×10^{-6}/°F).

III. Conclusions

The maximum elevation change of the elevation axis measured during one day was 3.5 mm (0.14 in.). The maximum change over the period of record was 8.9 mm (0.35 in.). These numbers may be useful in evaluating methods for monitoring the position of the axis intersection.

The precision of the results obtained is seriously limited by the limited number of data points for each day. The use of continuous recording equipment would provide much more accurate information, but at a considerable cost in instrumentation and data reduction. The need for this must be defined before such a program is undertaken.

An accurate correlation between temperature measurements and elevation position was beyond the scope of this effort. The use of temperature measurements as an element in determining the position of the elevation axis would require considerable development effort, if practical.

Table 1. Changes in alidade leg temperature, length, and ambient temperature

Month, 1976	Right leg		Left leg		Ambient
	ΔT, °C (standard deviation)	Δh, mm (for average Δt)	Average ΔT, °C (standard deviation)	Δh, mm (for average Δt)	ΔT, °C (standard deviation)
Mar.	7.58 2.83	0.017			
Apr.	7.82 3.46	0.018	6.50 3.73	0.15	
May	8.54 3.57	0.20	7.82 3.23	0.18	9.77 4.70
Jun.	7.62 3.31	0.17	5.96 3.50	0.14	9.59 3.94
Jul.	7.51 3.23	0.17	5.69 2.88	0.13	9.82 4.46
Aug.	8.31 3.07	0.19	6.91 2.35	0.16	10.80 3.28
Sep.	5.08 2.81	0.12	4.55 2.44	0.10	7.65 3.27

Fig. 1. Thermometer locations on alidade leg

Fig. 2. Typical thermometer location

N77-14052

An Improved Upper Bound on the Block Coding Error Exponent for Binary Input Discrete Memoryless Channels

R. J. McEliece
Communications Systems Research Section

J. K. Omura
University of California at Los Angeles

For coded telemetry systems it is important to know the tradeoff between the error probability and the complexity of implementation. For systems using block codes, the block coding error exponent is a good way to estimate this tradeoff. In this article we show how the new upper bounds on the minimum distance of binary codes obtained by McEliece et al. result in improved upper bounds on the coding error exponents for binary input memoryless channels.

Consider a binary-input memoryless channel with input alphabet $A = \{0,1\}$ output alphabet B, and transition probabilities $\{p(y|x) : x \in A, y \in B\}$. Let $C = \{\mathbf{x}_1, \mathbf{x}_2 \cdots, \mathbf{x}_M\}$ be a binary code of length n and rate $R = n^{-1} \log_2 M$ for this channel, and assume that each of the M codewords is sent with probability $1/M$. Let $d_{min}(C)$ denote the minimum Hamming distance between distinct codewords, and let $P_e(C)$ denote the probability of maximum-likelihood decoder error when the code C is used on the given channel.

Now define

$$\delta(n,R) = \frac{1}{n} \max d_{min}(C) \tag{1}$$

$$P_e(n,R) = \min P_e(C) \tag{2}$$

where the maximum and minimum in (1) and (2) are taken over the set of all codes of length n and rate $\geq R$. And finally define[1]

$$\delta(R) = \lim_{n \to \infty} \delta(n,R) \tag{3}$$

$$E(R) = \lim_{n \to \infty} -\log_2 P_e(n,R). \tag{4}$$

The maximum minimum distance $\delta(R)$ is unknown except at the points $R = 0, 1 : \delta(0) = 1/2, \delta(1) = 0$. The block coding error exponent $E(R)$ is known only for $R = 0$ and

[1]These limits are not known to exist. However, in what follows every upper bound is an upper bound on the corresponding lim sup's, and the lower bounds are lower bounds on the lim inf's, so there is no harm in pretending the limits exist.

$R \geq R_{crit}$, R_{crit} being a number to be defined below. We shall now briefly survey the known upper and lower bounds on $E(R)$, and indicate how the new upper bound $\delta^*(R)$ on $\delta(R)$ obtained in Ref. 1 can be used to improve the known upper bounds on $E(R)$ for small values of R.

First, the *sphere-packing* bound $E_{sp}(R)$ and the *random coding* bound $E_r(R)$, valid for all rates R less than channel capacity (Refs. 2, 3):

$$E_r(R) \leq E(R) \leq E_{sp}(R). \tag{5}$$

The two bounds in (5) are equal for sufficiently large R, and in fact the number R_{crit} cited above is the point where these two bounds meet. (Formulas for E_r and E_{sp} for binary symmetric and binary erasure channels are given in the Appendix.)

Next, we have bounds which depend on the *Bhattacharyya* parameter (Refs. 4, 5) for the channel, which is defined by

$$\alpha = -\log_2 \sum_{y \in b} (p(y|0)p(y|1))^{1/2}.$$

These bounds are

$$\alpha D \leq E(R) \leq \alpha\delta(R) \tag{6}$$

where $0 \leq D \leq 1/2$ is defined implicitly by $R = 1 - H_2(D)$, where $H_2(x)$ is the binary entropy function. (The lower bound in (6) is called the *expurgated* bound $E_{ex}(R)$; it is only valid for $0 \leq R \leq R'$, where R' is the rate at which the expurgated bound meets the random coding bound.) As mentioned, the function $\delta(R)$ is unknown, so the upper bound in (6) is ineffective. However, by using the bound $\delta(R) \leq \delta^*(R)$ obtained in Ref. 1 (for numerical values of $\delta^*(R)$, see Table 1 in Ref. 1), we obtain an upper bound

$$E(R) \leq \alpha\delta^*(R) \tag{7}$$

which can be evaluated, and which is already better than any previously known upper bound for small values of R.

Finally, Shannon et al. (Ref. 3) have shown that if $E_0(R)$ is any upper bound to $E(R)$, then so is the convex hull of the curves $E_0(R)$ and $E_{sp}(R)$. In particular, by taking $E_0(R) = (1/2)\alpha$ (from (6) and the fact that $\delta(0) = 1/2$), we see that $E(R)$ is bounded from above by the line passing through the point $(0,(1/2)\alpha)$ which is tangent to $E_{sp}(R)$. This bound is called the *straight-line* bound $E_{sl}(R)$. However by taking $E_0(R) = \alpha\delta^*(R)$ (cf. (7)) we can obtain an upper bound which is significantly better than $\min(E_{sl}(R), E_{sp}(R))$ for a considerable range of R's. We illustrate this in Fig. 1 with a binary symmetric channel with crossover probability $\epsilon = 0.01$, $\alpha = -\log_2 \sqrt{4\epsilon(1-\epsilon)} = 2.329$, and in Fig. 2 with a binary erasure channel with erasure probability $\epsilon = 0.01$, $\alpha = -\log_2 \epsilon = 6.644$. In both figures the unknown region for $0 \leq R \leq R_{crit}$ in which $E(R)$ lies is shaded. A final point worth mentioning is that the new upper bound (7) on $E(R)$ always matches the expurgated bound $E_{ex}(R)$ in slope at $R = 0$. (Both slopes are $-\infty$; this is well known for the expurgated bound, and follows for the bound (7) from the results of Ref. 1.) This fact supports the conjecture that $E(R) = E_{ex}(R)$ for $R \leq R_{crit}$ for binary input channels.

References

1. McEliece, R. J., Rodemich, E. R., Rumsey, H., Jr., and Welch, L. R., "New upper bounds on the rate of a code via the Delsarte–MacWilliams inequalities," *IEEE Trans. Inform. Theory*, Vol. IT-23, Mar. 1977 (in press).
2. Gallager, R. G., "A simple derivation of the coding theorem and some applications," *IEEE Trans. Inform. Theory*, Vol. IT-11, pp. 3–18, Jan. 1965.
3. Shannon, C. E., Gallager, R. G., and Berlekamp, E. R., "Lower bounds to error probability for coding on discrete memoryless channels," *Inform. Contr.*, Vol. 10, pp. 65–103 (Part I), pp. 522–552 (Part II), Jan. 1967.
4. Omura, J. K., "Expurgated bounds, Bhattacharyya distance, and rate distortion functions," *Inform. Contr.*, Vol. 24, pp. 358–383, Apr. 1974.
5. Omura, J. K, "On general Gilbert bounds," *IEEE Trans Inform. Theory*, Vol. IT-19, pp. 661–665, Sept. 1973.

Appendix

$E_r(R)$ and $E_{sp}(R)$ for Binary Symmetric and Binary Erasure Channels

For a binary symmetric channel with crossover probability ϵ, the random coding exponent is given by

$$E_r(R) = \begin{cases} 1 - R - \log_2(1 + \sqrt{4\epsilon(1-\epsilon)}) & 0 \le R \le 1 - H_2(\sqrt{\epsilon}/(\sqrt{\epsilon} + \sqrt{1-\epsilon})) \\ T_\epsilon(D) - H_2(D) & 1 - H_2(\sqrt{\epsilon}/(\sqrt{\epsilon} + \sqrt{1-\epsilon})) \le R \le 1 - H_2(\epsilon) \end{cases}$$

where $T_\epsilon(D) = -D\log_2\epsilon - (1-D)\log_2(1-\epsilon)$, and D satisfies (7). The sphere packing exponent is

$$E_{sp}(R) = T_\epsilon(D) - H_2(D) \qquad 0 \le R \le 1 - H_2(\epsilon).$$

(Hence $R_{crit} = 1 - H_2(\sqrt{\epsilon}/(\sqrt{\epsilon} + \sqrt{1-\epsilon}))$ and $E(R) = E_r(R) = E_{sp}(R)$ for $R \ge R_{crit}$.) For the binary erasure channel with erasure probability ϵ:

$$E_r(R) = \begin{cases} 1 - R - \log_2(1+\epsilon) & 0 \le R \le 1 - 2\epsilon/(1+\epsilon) \\ E_{sp}(R) & 1 - 2\epsilon/(1+\epsilon) \le R \le 1 - \epsilon, \end{cases}$$

where

$$E_{sp}(R) = \frac{\rho\epsilon 2^\rho}{(1-\epsilon) + \epsilon 2^\rho} - \log_2((1-\epsilon) + \epsilon 2^\rho),$$

where ρ is determined by $R = 1 - \epsilon 2^\rho/(1 - \epsilon + \epsilon 2^\rho)$.

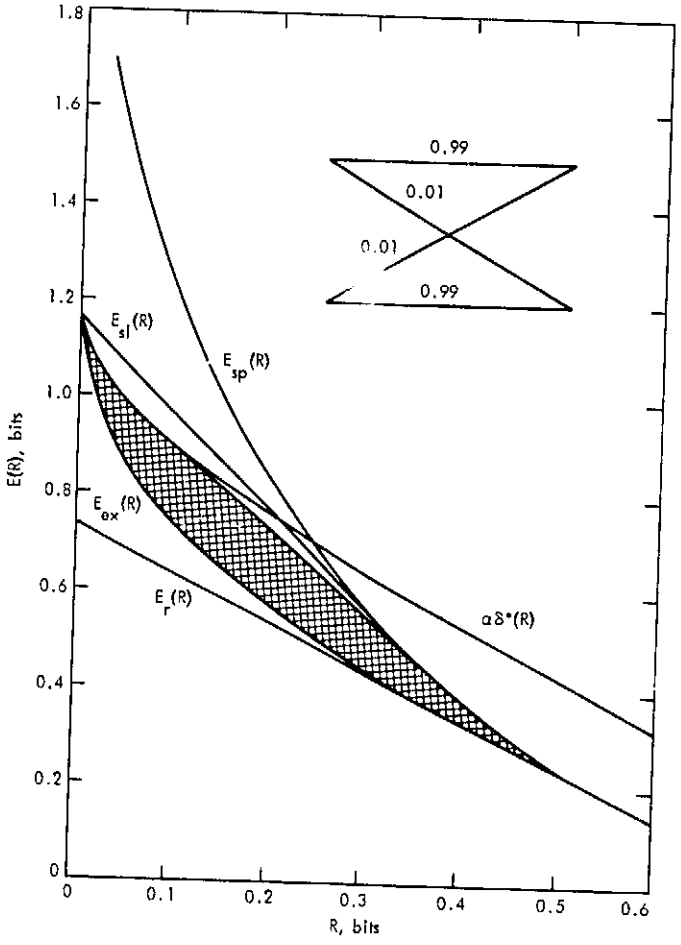

Fig. 1. A binary symmetric channel

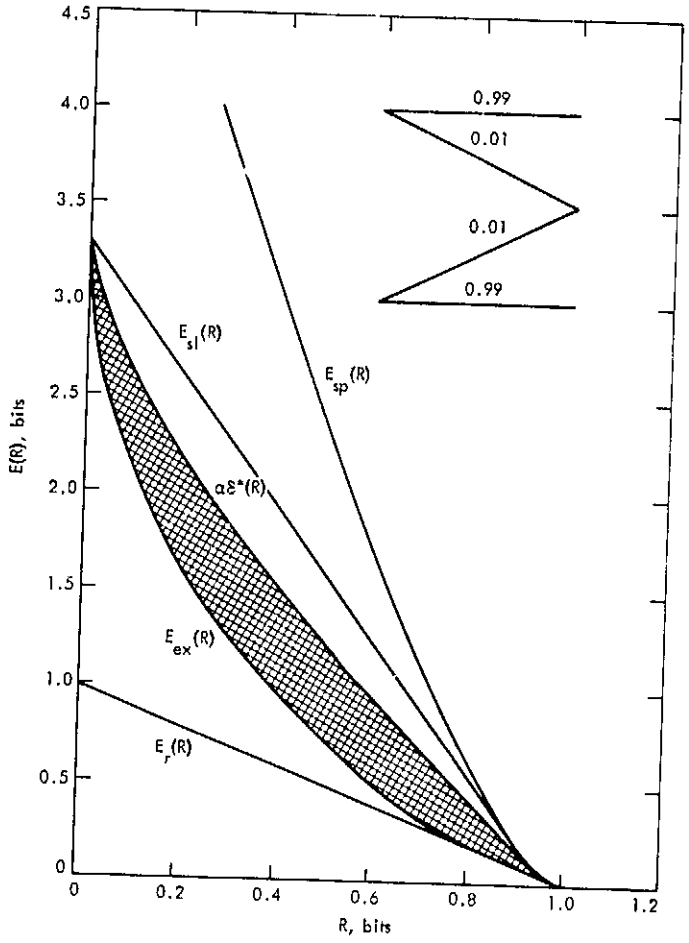

Fig. 2. A binary erasure channel

N77-14053

A Radar Study of the Backup Martian Landing Sites

G. S. Downs, R. R. Green, and P. E. Reichley
Communications Systems Research Section

The Goldstone radar system at DSS 14 was used to probe the Martian surface at 8495 MHz in a narrow strip between −6 deg and −2 deg latitude. The Viking C landing sites lie in this strip, and their altitudes, rms surface slope, and reflectivity are presented here.

The latest Martian opposition (condition of closest approach) occurred on December 9, 1975. At that time the sub-Earth point on Mars was at a latitude of −1 deg, traveling south to a minimum of −6 deg in mid-January, 1976. Turning northward, the sub-Earth point reached a latitude of 24 deg by July 1976 (the planned time of the first Viking landing). The backup landing sites, to be considered in the event of a failure on the first landing, were in a narrow strip just south of the Martian equator. The region contained possible landing sites that could be probed by radar at a time when the sensitivity of Earth-based radars was near a maximum (the sensitivity decreases as the fourth power of the distance).

These backup sites, known as "C" sites, were probed at a frequency of 8495 MHz. The R&D X-band transmitter at DSS 14, Goldstone, California, was used as a signal source. The 64-m antenna at DSS 14 was used for transmission and reception. Small cells 25 km E–W by 150 km N–S were isolated on the Martian surface. This isolation was accomplished by (1) phase modulating a CW signal with a pseudorandom sequence upon transmission, thereby facilitating differential range measurements; (2) Fourier analyzing the output of each of 32 range gates to produce a 64-point spectrum every 65 ms. About 461 spectra were combined to produce an average spectrum every 30 seconds. The basic bit length of the phase modulation was 8 μs. The maximum doppler shift (due to the rotation of Mars) measurable was 984 Hz, so the maximum resolution was 15.6 Hz. This corresponds to an E–W resolution of 0.07 deg in longitude along the doppler equator within 10 deg of the sub-Earth point. The resolution was dropped to 0.5 deg throughout the data analysis to decrease the effects of receiver noise. The N–S resolution, determined by the modulation bit length, was about 2.5 deg. These resolutions correspond to the cell size quoted above.

The 30-second data frames collected during a particular observing run were combined to yield backscatter functions (reflected power versus the angle of incidence) for each 0.5-deg region located along the doppler equator. Each function was analyzed to determine residual range,

the roughness parameter C, and the reflectivity ρ. The parameters C and ρ are referred to as the scattering parameters. The manner in which the cells are isolated on the Martian surface and the techniques of determining range and the scattering parameters are described in detail in Refs. 1 and 2.

Observation runs were made between 20 December 1975 and 25 February 1976 for the purpose of studying the Viking C sites. The results of 12 runs are condensed here by combining results within three latitude bands, each 2 deg wide. The bands are centered at latitudes of −6 deg, −4 deg, and −2 deg. All numerical results at a particular longitude, pertaining to a particular parameter and located within 1 deg in latitude of the center of the strip, were averaged together. The results are presented in Figs. 1 and 2. Figure 1 corresponds to the strip 2 deg wide N–S centered at −6 deg latitude, while Fig. 2 corresponds to the strip centered at −4 deg, with one exception: all data in Fig. 2 for longitudes greater than 300 deg apply to the strip centered at −2 deg latitude. The residual ranges have been converted to altitude in km. The reference surface corresponding to 0-km altitude is the ellipsoid of Standish (Ref. 3) with a radial scale of 3397.515 km. The Martian ephemeris used for the final analysis was obtained from the JPL ephemeris DE 96, modified by a small range polynomial determined by M. Standish using, in part, the observations described herein. The roughness parameter C has been converted to θ_r, the estimate of the rms slope of the surface, where $\theta_r = C^{-1/2}$ radians. The one-standard-deviation uncertainty in altitude is less than 0.5 km. The plot of each θ_r and ρ in Figs. 1 and 2 is a vertical bar. The middle of the bar represents the estimate of the parameter. The length of the bar represents one standard deviation above and below the estimate. (Any bar exceeding 8 deg or 12 percent is truncated). Hence there is a 68-percent probability that the true value of the parameter lies on the bar.

The positions of the seven C sites are marked on the appropriate figures. The site nomenclature and position are those in use as of 22 April 1976. In some cases the site is actually a region and is marked at two longitudes or latitudes.

Acknowledgement

The authors are greatly indebted to W. Hudson, C. Franck, R. Genzmer, and D. Rife for their long vigils to collect the data; to C. Kodak, R. Smith, R. Leu, T. Tesarek, and K. Hansen for many hours spent with the transmitter, and to the operations personnel at DSS 14 for their assistance with the operations.

References

1. Downs, G. S., and Reichley, P. E., "Radar Ranging of the Planet Mars at 8495 MHz," in *The Deep Space Network Progress Report 42-29*, pp. 95–106, Jet Propulsion Laboratory, Pasadena, California, Oct. 15, 1975.

2. Downs, G. S., Goldstein, R. M., Green, R. R., Morris, G. A., and Reichley, P. E., "Martian Topography and Surface Properties as seen by Radar: The 1971 Opposition," *Icarus*, 18, pp. 8–21, 1973.

3. Standish, E. M., "The Figure of Mars and its Effect on Radar Ranging," *Astron. Astrophys*, 26, pp. 463–466, 1973.

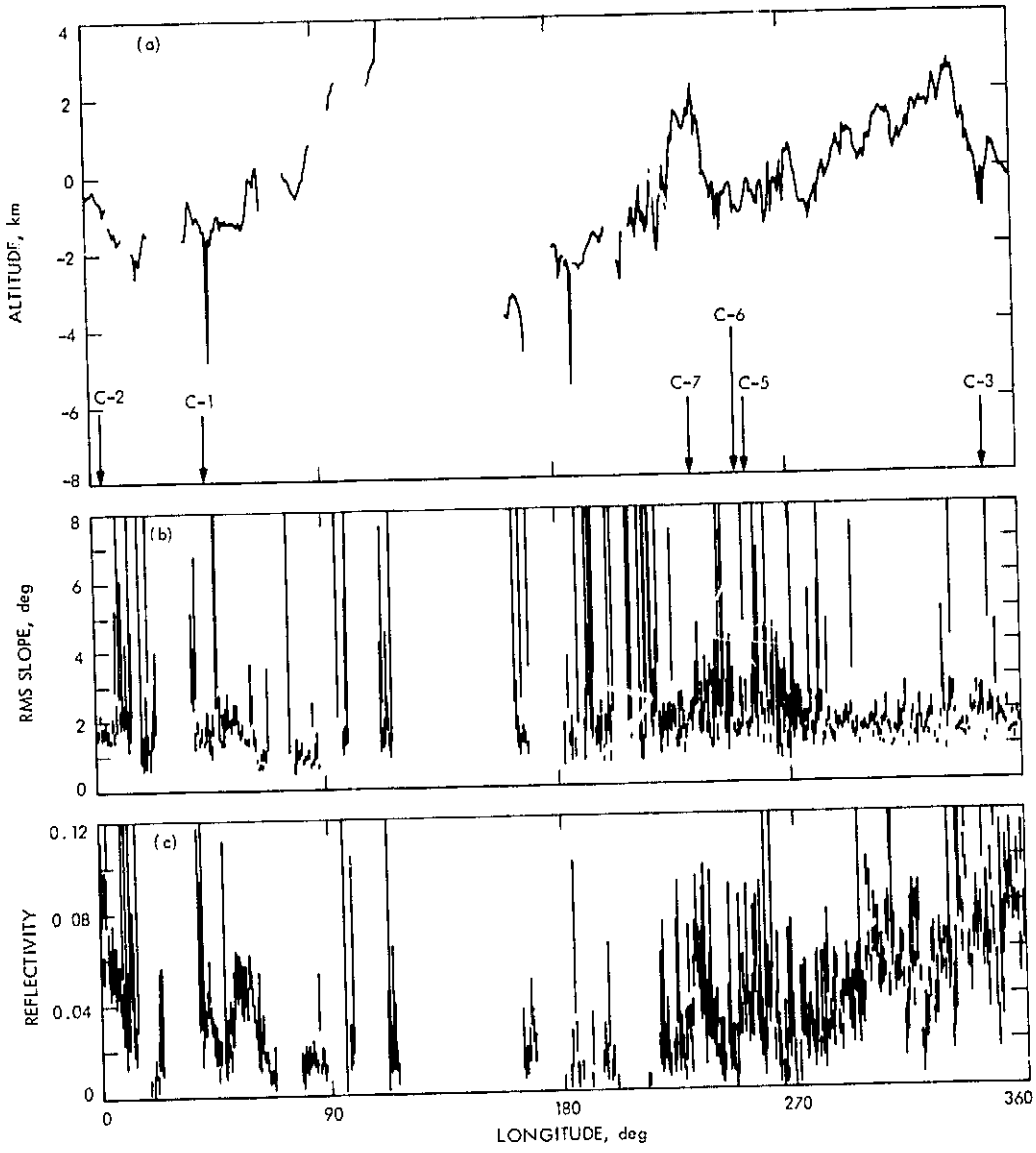

Fig. 1. Martian radar surface properties as seen by radar at 8495 MHz, −6 deg latitude: (a) altitude, (b) rms slope, and (c) reflectivity. Longitudes of the C sites are marked

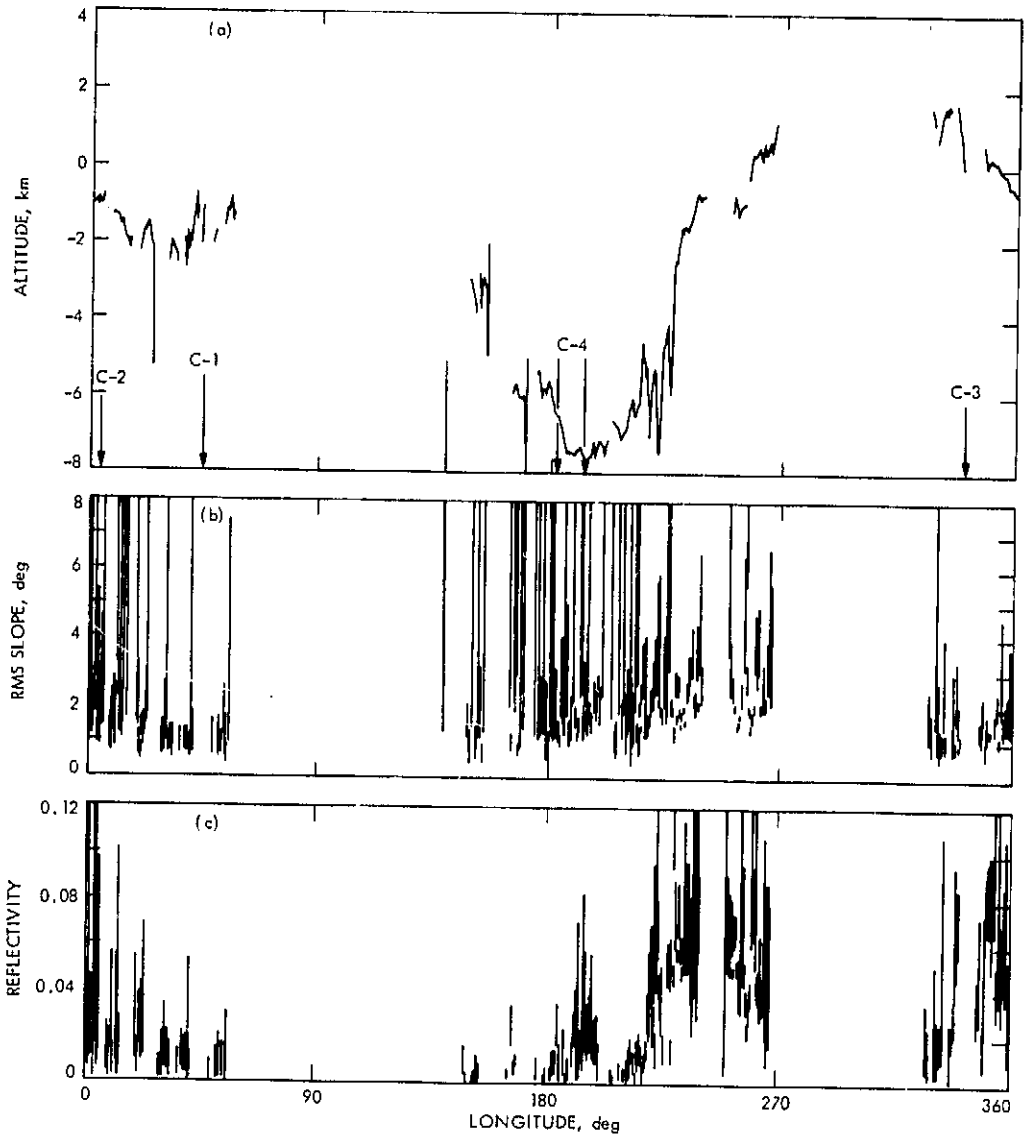

Fig. 2. Martian radar surface properties as seen by radar at 8495 MHz, −4 deg latitude, or −2 deg latitude (longitude > 300 deg): (a) altitude, (b) rms slope, and (c) reflectivity. Longitudes for the C sites are marked

N77-14054

The Effect of Direct Current Bias in the Computation of Power Spectra

E. R. Rodemich
Communications Systems Research Section

We determine the effect of dc bias in the approximate computation of spectra of Gaussian processes by hard limiting.

I. Introduction

The spectral density $S(\omega), |\omega| \leq \pi$, of a stationary Gaussian process $\{x_k\}$, $-\infty < k < \infty$, of mean zero, can be expressed in terms of the covariances $R_x(k) = E(x_n x_{n+k})$ by

$$S(\omega) = R_x(0) + 2\sum_{k=1}^{\infty} R_x(k)\cos k\omega. \tag{1}$$

If we put

$$y_i = \begin{cases} +1, x_i \geq 0, \\ -1, x_i < 0, \end{cases} \tag{2}$$

Then it is known (Ref. 1) that $R_y(k) = E(y_n y_{n-k})$ satisfies the relation

$$R_x(k) = R_x(0)\sin\left[\frac{\pi}{2} R_y(k)\right]. \tag{3}$$

In practice, the series in (1) is truncated, and the correlations $R_y(k)$ are estimated from samples of finite size, which leads to random errors in the evaluation of $S(\omega)$. These errors will not be considered here. Neglecting them, we use the variables $\{y_k\}$ to estimate $R_y(k)$, then apply (3) and (1) to get $S(\omega)$. This leads to a saving in computation time over the direct estimation of $R_x(k)$ from $\{x_k\}$, since these estimates require a large

number of arithmetic operations. The variance $\sigma^2 = R_x(0) = E(x_k^2)$, if needed, must be estimated separately. This variance, which enters $S(\omega)$ as a scale factor, is often unimportant, because it can be affected by many extraneous factors.

We consider the following problem: Suppose that an unknown bias a is added to the Gaussian process $\{x_k\}$, so that we get $\{x_k + a\}$, $-\infty < k < \infty$. The formula (2) cannot be applied if a is unknown. However, we can take

$$y_i = \begin{cases} +1, x_i + a \geq 0, \\ -1, x_i + a < 0. \end{cases} \tag{4}$$

Then we can estimate the numbers $E_k = E(y_n y_{n+k})$ (no longer correlations) take

$$R_x^*(k) = \sin\left(\frac{\pi}{2} E_k\right), \tag{5}$$

in analogy with (3), and form

$$S^*(\omega) = R_x^*(0) + 2\sum_{k=1}^{\infty} R_x^*(k) \cos k\omega. \tag{6}$$

If $a = 0$, $S^*(\omega)$ is $S(\omega)/\sigma^2$. If $a \neq 0$, $S^*(\omega)$ approximates $S(\omega)$ in some sense. We shall investigate how close this approximation is.

To find $S(\omega)$ exactly, (3) needs to be replaced by a formula involving a non-elementary function which depends on a/σ. This is not practical for real-time computations. Hence we consider the above approximation.

II. Formulas

Let the Gaussian random variables x_k have variance σ^2. Then the value of $E_k = E(y_n y_{n+k})$ depends only on $\rho_k = R_x(k)/\sigma^2$, and can be written as

$$E_k = f(\rho_k), \tag{7}$$

where

$$f(z) = \frac{1}{2\pi\sqrt{1-z^2}} \times \int_{-\infty}^{\infty}\int_{-\infty}^{\infty} y(t_1)y(t_2) \exp\left[\frac{t_1^2 + t_2^2 - 2zt_1t_2}{2(1-z^2)}\right] dt_1\, dt_2, \tag{8}$$

with

$$y(t) = \begin{cases} +1, t \geq -a/\sigma, \\ -1, t < -a/\sigma. \end{cases}$$

This follows if we evaluate E_k directly as the expectation of a function of x_n and x_{n+k}, by integrating over the bivariate Gaussian distribution (Ref. 2).

If we differentiate (8) with respect to z, the resulting integral can be simplified by integration by parts, and we get

$$f'(z) = \frac{2}{\pi\sqrt{1-z^2}} \exp\left(-\frac{a^2/\sigma^2}{1+z}\right).$$

Integrate this equation from 0 to z. Using the variable of integration $u = \sin^{-1}z$,

$$f(z) - f(0) = \frac{2}{\pi}\int_0^{\sin^{-1}z} \exp\left(-\frac{a^2/\sigma^2}{1+\sin u}\right) du. \tag{9}$$

To evaluate $f(0)$, note that at $z = 1$, the distribution in (8) is concentrated on the line $t_1 = t_2$. Then $f(1) = E(y(t_1)^2) = 1$. Hence, putting $z = 1$ in (9),

$$1 - f(0) = \frac{2}{\pi}\int_0^{\pi/2} \exp\left(-\frac{a^2/\sigma^2}{1+\sin u}\right) du. \tag{10}$$

By numerical integration of the integral in (9), going from $z = 0$ to $z = 1$ and to $z = -1$, tables of $f(z)$ were obtained for various values of a/σ. Some of these are plotted in Fig. 1.

If we plot $[\sin(\pi/2)f(z)]$ instead of $f(z)$, the curve for $a = 0$ becomes a straight line, and the other curves are also modified, but they do not come significantly closer to the line for $a = 0$. The separation between the curves is the error in this method of approximating $R_x(k)/\sigma^2$, so at first glance this method does not look too promising.

However, instead of $R_x^*(k)$, we should be considering

$$\overline{R_x}(k) = \frac{\sin\left[\frac{\pi}{2}E_k\right] - \sin\left[\frac{\pi}{2}f(0)\right]}{\sin\left[\frac{\pi}{2}f(1)\right] - \sin\left[\frac{\pi}{2}f(0)\right]} = C_1[R_x^*(k) - C_2], \tag{11}$$

where

$$C_2 = \sin\left[\frac{\pi}{2} f(0)\right],$$

and

$$C_1 = (1 - C_2)^{-1}.$$

$\overline{R}_x(k)$ is plotted as a function of $R_x(k)/\sigma^2$ in Fig. 2. We see that $\overline{R}_x(k)$ is a good approximation to $R_x(k)/\sigma^2$ if $R_x(k)/\sigma^2$ is not too close to -1 (which is usually true).

Forming the numbers $\overline{R}_x(k)$ requires knowing something about the function $f(z)$. However, they are only wanted to construct the function

$$\overline{S}(\omega) = 1 + 2\sum_{k=1}^{\infty} \overline{R}_x(k) \cos k\omega. \tag{12}$$

This function can be found more directly as

$$\overline{S}(\omega) = C_1[S^*(\omega) - C_2\delta(\omega)]. \tag{13}$$

The presence of a dc component in $\{y_k\}$ causes a spike in the spectrum $S^*(\omega)$ at $\omega = 0$. This can be removed by inspection, which is the significance of the term $-C_2\delta(\omega)$ in (13). Then the multiplier C_1 can be adjusted to give whatever scale is desired for the spectrum. Thus we get $\overline{S}(\omega)$, defined by (12), without any particular knowledge about a or the function f(z)

The error $\overline{R}_x(k) - R_x(k)/\sigma^2$ is negative for $R_x(k) > 0$, with a minimum near $R_x(k) = 0.44\sigma^2$ for all values of a/σ between 0 and 1. For $R_x(k) < 0$, the error is positive, increasing as $R_x(k)/\sigma^2$ goes from 0 to -1. These errors are given at $R_x(k)/\sigma^2 = 0.44$ and -0.30 for several values of a/σ in Table 1.

Another method which we can consider for comparison is to first compute the correlation

$$R_y(k) = \frac{E_k - f(0)}{1 - f(0)},$$

then take

$$\widetilde{R}_x(k) = \sin\left[\frac{\pi}{2} R_y(k)\right]$$

and

$$\widetilde{S}(\omega) = 1 + 2\sum_{k=1}^{\infty} \widetilde{R}_x(k) \cos k\omega.$$

This method is suggested by the original relation (3). Curves for $\widetilde{R}_x(k)$ as a function of $R_x(k)/\sigma^2$, similar to the curves of Fig. 2, can be plotted. These curves have the same general appearance, but they range farther from the line for $a = 0$. Values of the error $\widetilde{R}_x(k) - R_x(k)/\sigma^2$ are given in Table 1 for comparison. We see that this method is not as good, as well as being harder to implement.

References

1. Goldstein, R. M., "Radar Exploration of Venus," Thesis, California Institute of Technology, 1962.
2. Feller, W., *An Introduction to Probability Theory and Its Applications*, Vol. 2, 2nd edition, Wiley, New York, 1961.

Table 1. The errors in $R_x(k)$ and $R_x(k)$ for $R_x(k)/\sigma^2 = 0.44$ (upper number) and -0.30 (lower number)

a/σ	0.2	0.5	1.0
$\overline{R_x}(k) - R_x(k)/\sigma^2$	-0.0001 $+0.0003$	-0.0031 $+0.0093$	-0.0342 $+0.0822$
$\widetilde{R}_x(k) - R_x(k)/\sigma^2$	-0.0031 $+0.0064$	-0.0192 $+0.0378$	-0.0738 $+0.1261$

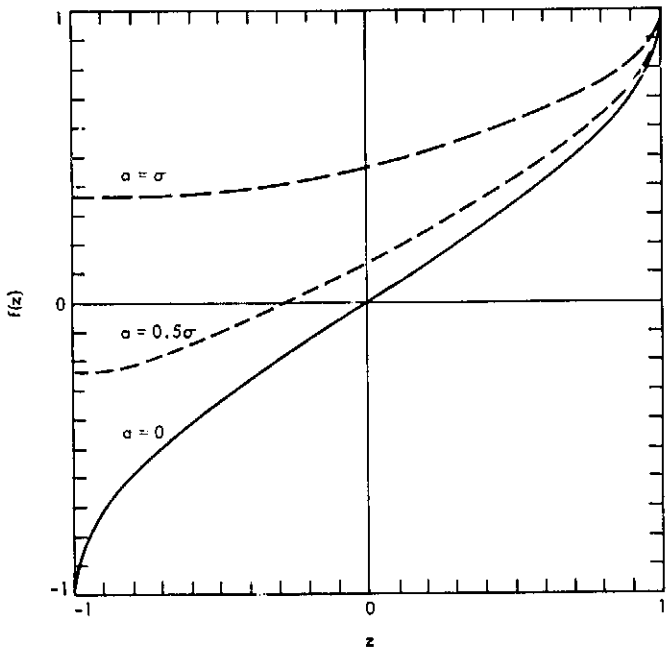

Fig. 1. The function $f(z)$ for various values of a/σ

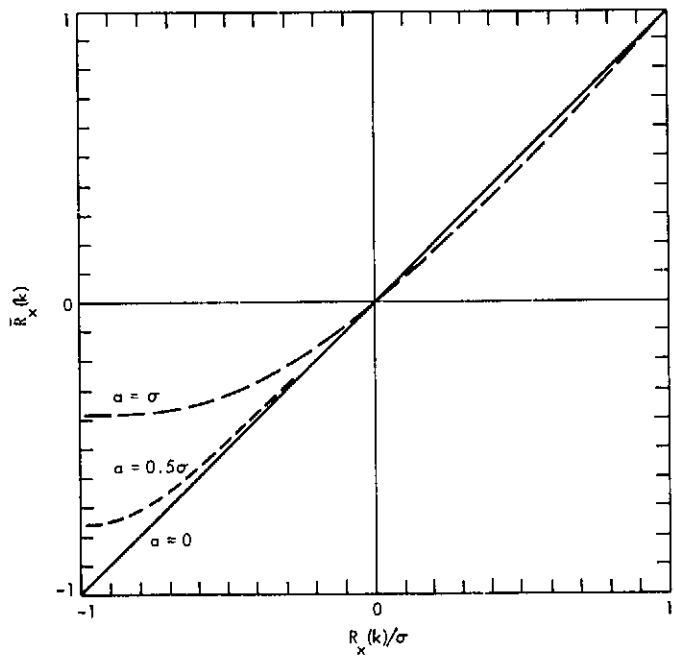

Fig. 2. $\overline{R_x}(k)$ as a function of $R_x(k)/\sigma^2$, for various values of a/σ

N77-14055

Standard Random Number Generation for MBASIC

R. C. Tausworthe
DSN Data Systems Section

This article presents and analyzes a machine-independent algorithm for generating pseudorandom numbers suitable for the standard MBASIC system. The algorithm used is the "polynomial congruential" or "linear recurrence modulo 2" method devised by the author in 1965. Numbers, formed as nonoverlapping, adjacent 28-bit words taken from the bit stream produced by the formula $a_{m+532} = a_{m+37} + a_m$ *(modulo 2), will not repeat within the projected age of the solar system, will show no ensemble correlation, will exhibit uniform distribution of adjacent numbers up to 19 dimensions, and will not deviate from random runs-up and runs-down behavior.*

I. Introduction

The first MBASIC random number generator (Ref. 1), implemented on the Univac 1108, used a linear congruential method, $x_{n+1} = 5^{15}x_n \pmod{2^{35}}$, followed by normalization to the range (0,1). This generator was used probably because it was already available in the U1108 statistics package. Empirical tests by users, however, later proved that the generator possesses very nonrandom correlation properties indeed, especially unless great care is taken in specifying the initial "start" value.

The canned-in default starting value, or "seed," ($x_0 = 5^{15}$) had been selected because theoretical results (Ref. 2) claimed that the longest nonrepeating sequences are obtained when x_0 is an odd power of 5. Unfortunately, the particular x_0 chosen, while perhaps generating a long sequence, does not seem to produce numbers with very good randomness properties.

This article describes an alternate generator of a type whose randomness has been theoretically shown to be vastly superior and which can be implemented on any computer, despite word length restrictions (the U1108 algorithm was tailored to 36-bit words). It is a machine-independent algorithm.

The generation method is almost as fast as the linear congruential method, but not quite. The ratio of speeds is about 3:1.

II. The Linear Recurrence Modulo 2 Method

In 1965, the author (Ref. 3) showed that numbers produced as successive binary words of length s taken L bits apart ($s \leq L$) from a linear (shift-register) bit-stream recursion of the form

$$a_n = c_1 a_{n-1} + \cdots + c_{p-1} a_{n-p+1} + a_{n-p} \quad \text{(modulo 2)}$$

form a pseudorandom sequence whenever the polynomial $f(x) = x^p + c_{p-1}x^{p-1} + \cdots + c_1 x + 1$ is primitive over $GF(2)$. The algebraic structure of these pseudorandom numbers provided a way of proving that, over randomly chosen starting values $a_0, \cdots, a_{p-1}$ in the numeric sequence, the correlation between numbers is essentially zero, being ostensibly equal to -2^{-p}, for all numbers in the sequence separated by less than $(2^p - s - 1)/L$, subject to the restriction $(L, 2^p - 1) = 1$. The author further showed that adjacent k-tuples of such numbers were uniformly distributed for $1 \leq k \leq (p/L)$.

The algorithm for computing the numbers is simple, especially when $f(x)$ is a primitive trinomial, say $x^p + x^q + 1$, where $q < p/2$. An even greater simplification is possible, as is shown in this article, when p is an even multiple of L, as is the case for the trinomial $x^{532} + x^{37} + 1$ (from Zierler and Brillhard (Ref. 4). The generator based on this polynomial has period 1.4×10^{160}, has virtually no (average) correlation between any numbers separated by less than 5×10^{158}, has 28-bit precision numbers available, and has adjacencies up to 19 dimensions uniformly distributed. Runs-up and -down statistics up to length 16 are impeccable. The period and maximum correlation distance are, in fact, so great that the generator would have to produce numbers at a nanosecond rate for more than 10^{142} years before nonrandom distribution or correlation effects would be noticeable as nonrandom. Almost 4×10^{11} numbers would have to be examined to detect deviations in runs-up and runs-down statistics as nonrandom.

These pseudorandom number generators have been widely studied (Refs. 5–8) since 1965, both theoretically and empirically, and have been "promoted to pride of place in the field of pseudorandom number generation (Ref. 7)."

Tootill (Ref. 8) has even discovered generators of this type for which "there can exist no purely empirical tests of the sequence as it stands capable of distinguishing between it and [truly random sequences]." For reasons having to do with computer storage and precision, the generator of this article is, unfortunately, not one of these. Nevertheless, the generator described is vastly superior to any linear congruential generator in existence.

III. The Method

The algorithm for producing the succeeding p bits from the current set of p bits in the $x^p + x^q + 1$ generator is,

(1) Left-shift the p bit string by q bits, inserting q zeros on the right, dropping q bits on the left.

(2) Add modulo 2 (exclusive-or) the original and shifted p bits.

(3) Right-shift this result by $p - q$ bits, supplying $p - q$ zeros on the left, and dropping $p - q$ bits on the right.

(4) Add the results of 2 and (3) above modulo 2 to give the next p bits.

The proof that this algorithm works is very simple, and the reader is invited to apply the algorithm to the bit string $a_1 a_2 \cdots a_p$ and use the reduction formula $a_{p+m} = a_{q+m} + a_m$ (try it with $a_1 a_2 a_3 a_4 a_5$ with $a_{5+m} = a_{2+m} + a_m$ to see what is happening).

Note in the method that the number of computations required for generating the next p bits grows at most linearly in p. Assuming $p >> L$, then partitioning the p generator bits into words of length L produces a number of words that also increases in proportion to p. Therefore, the number of computations for L bit precision random numbers, to first-order effects, is independent of the recursion degree p. Making p large, however, has advantages in increasing randomness properties.

It is true that as p increases, more and more registers are required to compute each new set of p bits, and shifting many registers at once presents a small inconvenience in most computer languages. These factors place a small speed and storage overhead on the generation process; but as we shall see, even this is not extreme due to the particular trinomial chosen.

The trinomial $x^{532} + x^{37} + 1$ ($p = 532$, $q = 37$) has several things to recommend it: (1) 532 is factorable into $28 \cdot 19$, which means that 19 words each having 28 bits precision can be generated all at once by the algorithm; (2) up to and including 19-tuples of adjacently produced

random numbers will be uniformly distributed; (3) 28 and 19 are both relatively prime to the period $(2^{532} - 1)$, so no ill effects occur as a result of beginning new words every 28 bits; (4) the period and correlation distance are so great as never to be witnessed in the lifetime of the universe; and (5) the $q = 37$ value produces good runs-up and runs-down statistics (Ref. 8), up to runs of length 16.

On converting 28-bit fixed-point mantissas to real numbers, 8-digit precision results. Some machines, such as the 1108, may have to reduce this precision in order to fit the floating-point exponent field into the word (the UI108 has only 27-bit mantissa precision). In such cases, the most significant bits of the generated words may always be retained without losing randomness qualities, so that all implementations produce essentially identical results, within machine precision. This philosophy is present in the algorithm which follows in Section IV.

The RANDOMIZE function which initializes the generator uses a multiplicative linear congruential algorithm to generate the first 19-number "seed," from which the rest of the generated numbers grow. The particular value for the multiplicator a in the algorithm

$$x_{n+1} \equiv ax_n \pmod{2^L}$$

was chosen as $41{,}475{,}557_{10}$ for the $L = 28$ case from theoretical results published in Ahrens and Dieter (Ref. 9), who show that good randomness results when

$$a \equiv 5 \pmod 8$$
$$a \approx 2^{L-2}\xi$$

where $\xi = (5^{1/2} - 1)/2$ (the "golden section number").

IV. The Algorithm

Managing the 532-bit shift-register is the main trick in implementing the method of the previous section. The algorithm given in this section utilizes an array W_i, $i = 0, \cdots, 18$ of b-bit computer words ($b \geq 28$) sufficient to encompass the $p = 532$ span of bits to be operated on (and retained), and delivered in 28-bit chunks whenever the RANDOM function is invoked.

On machines having word sizes smaller than 28 bits, double words will have to be used for each word in the algorithm below. Two values of the RANDOMIZE argument that round to the same internal fixed-point representation will produce the same random sequence; conversely, every unique fixed-point representation of the argument produces a unique random sequence. In addition, so long as the value of the argument is the same and stays within the precisions of two differing machines, the sequences produced on each will be the same, within machine precision.

Counting the number of elemental operations (load, store, shift, etc.) for the algorithm, one finds about $10 + f$ operations per number generated, where f is the number of operations in "floating" the fixed-point number. The linear congruential algorithm requires only about $3 + f$ such operations, so the ratio of speeds is approximately 3:1.

The RANDOM function is about $23 + f$ operations long, as compared to $3 + f$ for its linear congruential form, and data storage is 21 words vs 2. However, even though the program requires perhaps 7 times as much core as the linear congruential form, the total is still probably under 50 locations, of negligible concern in most installations. The asymptotically random sequence of Tootill (Ref. 8) requires 607 words to store the array W_i alone. (This, coupled with the fact that only 23-bit precision was available in that generator, is why it was not considered here.)

The two functions, described in CRISP-PDL syntax (Ref. 10), are as follows:

```
Function:  RANDOMIZE(starter:universal real)
           <* This function declares and initializes a 19-element
           <* array, W0,...,W18 with random numbers generated
           <* by a linear congruential method. An integer I is
           <* set to zero to enable RANDOM to select W0 as the
           <* first random number. W and I are permanent data
           <* structures, accessed only by RANDOMIZE and RANDOM
```

```
.1      constant multiplier:integer = 41475557
.2      variable j:integer, I:integer,
          W:array [0..18] of universal integer
.3      if    (starter<0) <*MBASIC manual specifications*>
.4      :       starter:=clocktime <*returns current time of day as integer*>
.5      :-->(starter=0)
.6      :       starter:=multiplier
        :-->(else) <*starter>0*>
.7      :       starter:=fix(starter)<*floating-to-integer conversion*>
        :..endif
.8      W0:=starter
.9      loop for j:=1 to 18
.10     ↑ Wj:=(Wj-1*multiplier) modulo 2**28
.11     ←←repeat with next j
.12     I:=0 <*set up to pick W0 as first random number*>
        endfunction
```

Function: RANDOM:real

```
        <* This algorithm makes use of a 19-word array,
        <* W0,...,W18, each with b≥28 bits. Each word contains
        <* 28 bits of the generator, right justified. An
        <* integer variable I on entry contains the index of
        <* the word array next to be returned as the random value.
        <* Both W and I are permanent data structures, accessed
        <* only by RANDOM and RANDOMIZE. The latter of these
        <* initializes I to zero and W to the seed.

.1      variable j:integer
.2      if (I  19) <*all words have been used up*>
.3      :   I:=0 <*reset to first element in array*>
.4      :   loop for j:=0 to 16 <*exclude last two words*>
.5      :   ↑ load Wj+1,Wj+2 into A0,A1
.6      :   ↑ left shift A1 by b-28 <*join bits in stream*>
.7      :   ↑ left shift A0,A1 by 9 <*q=37 is 28+9*>
.8      :   ↑ Wj:=(Wj XOR A0) <*the recursion formula*>
.9      :   ←←repeat with next j
.10     :   load W18,W0 into A0,A1 <*now compute W17:*>
.11     :   left shift A1 by b-28 <*join W18, W0 bit streams*>
.12     :   left shift A0,A1 by 9 <*A0 now has final 19 bits of W18*>
.13     :   W17:=W17 XOR A0 <*and first 9 bits of stream shifted 495*>
.14     :   load W0,W1 into A0,A1 <*do similarly for W18*>
.15     :   left shift A1 by b-28
.16     :   left shift A0,A1 by 9
.17     :   W18:=(W18 XOR A0)
        :..endif
.18     RANDOM   float(Wj)/2**28 <*convert to real*>
.19     I:=I+1
        endfunction
```

V. Conclusion

The algorithm given has been implemented as the RANDOM function in the MBASIC processor currently on the Caltech PDP-10 computer. All tests so far run on it validates the randomness properties claimed by the theory. In that theory, by the way, the only factor left to chance is the specification of the initial "seed." The stated uniformity, zero-correlation, and runs statistics are all based on the single assumption that the seed be chosen randomly. Of course, the default value canned in was not randomly chosen, but chosen specifically to look random except for the first word, and certainly, to the extent of our tests, this appears to have worked beautifully.

We have demonstrated that the generator is also capable (as is every known random number generator) of producing numbers with 3σ variations from randomness over a few thousand samples when the wrong seed is supplied.

References

1. MBASIC, Vol. I — Fundamentals, Jet Propulsion Laboratory, Pasadena, Calif., p. 188.
2. Knuth, D. E., *The Art of Computer Programming*, Vol. 2 — Seminumerical Algorithms, Addison-Wesley Co., Reading, Mass., 1969.
3. Tausworthe, Robert C., "Random Numbers Generated by Linear Recurrence Modulo Two," *Math Comp*, Vol. XIX, No. 90, Apr., 1965, pp. 201–208.
4. Zierler, N., and Brillhart, J., "On Primitive Trinomials (Mod 2), II," *Inform. Contr.*, Vol. 14, No. 6., June 1969, pp. 566–569.
5. Whittlesey, J. R. B., "A Comparison of the Correlational Behavior of Random Number Generators for the IBM 360," *Comm. ACM*, Vol. 11, No. 9, Sept., 1968, pp. 641–644.
6. Neuman, F., and Martin, C. F., "The Autocorrelation Structure of Tausworthe Pseudorandom Number Generators," *IEEE Trans. Comp.*, Vol. C-25, No. 5, May 1976, pp. 460–464.
7. Tootill, J. P. R., et. al., "The Runs-Up and -Down Performance of Tausworthe Pseudorandom Number Generators," *ACM J.*, Vol. 18, No. 3, July, 1971, pp. 381–399.
8. Tootill, J. P. R., et al., "An Asymptotically Random Tausworthe Sequence," *ACM J.*, Vol. 20, No. 3, July 1973, pp. 469–481.
9. Ahrens, J. H., et al., "Pseudorandom Numbers: A New Proposal for the Choice of Multiplicators," *Computing*, No. 6, Springer-Verlag, 1970, pp. 121–138.
10. Tausworthe, R. C., *Standardized Development of Computer Software*, SP 43-29, Jet Propulsion Laboratory, Pasadena, Calif., July 1976.

N77-14056

The Fast Decoding of Reed-Solomon Codes Using Fermat Theoretic Transforms and Continued Fractions

L. R. Welch and I. S. Reed
University of Southern California

T. K. Truong
TDA Engineering Office

It is shown that Reed–Solomon (RS) codes can be decoded by using a fast Fourier transform (FFT) algorithm over finite fields $GF(F_n)$, where F_n is a Fermat prime, and continued fractions. This new transform decoding method is simpler than the standard method for RS codes. The computing time of this new decoding algorithm in software can be faster than the standard decoding method, for RS codes.

I. Introduction

Recently, Gore (Ref. 1) proposed the usage of a finite field transform over $GF(q^n)$, where q is a prime number and n is an integer, for decoding RS codes. Michelson (Ref. 2) has implemented Mandelbaum's algorithm (Ref. 3) and showed that the decoder, using a transform over $GF(q^n)$, is faster than a more standard decoder (Ref. 4). The disadvantage of this transform method is that the code length is such that the most efficient FFT algorithms cannot be used to yield fast transform decoders.

Rader (Ref. 5) proposed transforms over rings of integers modulo Fermat numbers. Such transforms can be used to compute error-free convolutions of real integer sequences. Agarwal and Burrus (Ref. 6) extended Rader's Fermat number theoretic transform by using the generator $\alpha = \sqrt{2}$ for the transform rather than $\alpha = 2$. If $\sqrt{2}$ is the generator of the transform, the transform has an FFT algorithm which can be used to calculate transforms with as many as 2^{n+2} points of integer data. This transform was extended to residue classes of quadratic integers $I_{F_n}(\sqrt[2]{2})$, where $\sqrt{2}$ is a root of $x^2 - 2 = 0$, F_n is a Fermat number and I_{F_n} denotes the set of integers mod F_n (Ref. 7). McClellan (Ref. 8) has realized recently the hardware for the Fermat prime theoretic transforms. He showed that the arithmetic used to perform these transforms required only integer additions and circular shifts.

Recently, Justesen (Ref. 9) proposed that transforms over $GF(F_n)$, where $F_n = 2^{2^n} + 1$ for $n = 1,2,3,4$ is a Fermat prime, can be used to define RS codes and to improve the decoding efficiency of these codes.

Recently, the authors (Ref. 10) extended the transform to the finite field of type $I_{F_n}(\sqrt{2})$ (isomorphic to $GF(F_n)$), where $\sqrt{2}$ is a root of the polynomial $P(x) = x^2 - 2$ over $GF(F_n)$, and I_{F_n} denotes the set of integers modulo F_n. Again the arithmetic used to perform this transform requires only integer additions, circular shifts, and a minimum number of integer multiplications by powers of $\sqrt{2}$. An FFT over the finite field of type $I_{F_n}(\sqrt{2})$ can be used to encode and decode RS codes of as many as 2^{n+1} symbols for $n \geq 3$,4. Encoding and decoding can be accomplished faster and more simply than any other known standard decoder for RS codes of the same symbol range. It was also shown (Ref. 10) that the FFT over $GF(K \cdot 2^n + 1)$, where K and n are integers, can be used to encode and decode a class of RS codes. A special case of the radix—8 FFT over $GF(q^2)$, where $q = 2^p - 1$ is a Mersenne prime, was developed to encode and decode another class of RS codes.

The decoding of systematic Reed–Solomon codes using the transform over $GF(F_n)$ was composed of the following three steps (Ref. 10).

(1) Compute the FFT over $GF(F_n)$ of the received code N-tuple; i.e.,

$$S_K = \sum_{m=0}^{N-1} \gamma_m \alpha^{mK}$$

where $\gamma_m \epsilon GF(F_n)$ and α is an element of order N.

(2) Use Berlekamp's iterative algorithm (Ref. 11) to determine σ_i from the known $S_j = E_j$ for $i = 1,2,\cdots,t$ and $j = 1,2,\cdots,2t$. Then compute the remaining transform error E_j.

(3) Compute the inverse of the transform over $GF(F_n)$ of $S_K - E_K$ to obtain the corrected code.

An advantage of this transform decoding algorithm over other methods is that a FFT over $GF(F_n)$ can be used to compute the syndromes and error magnitudes. In this paper, Berlekamp's iterative algorithm can be modified by using continued fractions in $GF(F_n)$. This modified Berlekamp's algorithm can be easily implemented on a digital computer.

II. New Approach to Decode Reed–Solomon Code Using the Transform Over $GF(F_n)$

In this section, a new approach is developed to define and decode RS codes. The following theorem and definitions are needed.

Theorem 1: Let q be a prime number. Also let $A(x)$ be the formal power series of form

$$A(x) = \sum_{i=0}^{\infty} a_i x^{d-i} \tag{1}$$

where $a_i \epsilon GF(q)$, the degree of $A(x)$,d, is a real integer, and $a_0 \neq 0$. Define the set

$$F = \left\{ \sum_{i=0}^{\infty} a_i x^{d-i} \,\middle|\, a_i \epsilon GF(q) \text{ and } d \text{ is an integer} \right\}$$

such that addition is given by

$$G(x) = B(x) + C(x) = \sum_{i=0}^{\infty} b_i x^{e-i} + \sum_{i=0}^{\infty} c_i x^{f-i},\ e \geq f$$

$$= \sum_{i=0}^{\infty} g_i x^{e-i}$$

where

$$g_i = \begin{cases} b_i, & i < e - f \\ b_i + c_{i-(e-f)}, & i \geq e - f \end{cases}$$

and multiplication is given by

$$H(x) = B(x) \cdot C(x) = \left(\sum_{i=0}^{\infty} b_i x^{e-i} \right) \left(\sum_{i=0}^{\infty} c_i x^{f-i} \right)$$

$$= \sum_{i=0}^{\infty} h_i x^{e+f-i}$$

where

$$h_i = \sum_{j=0}^{i} b_j c_{i-j}$$

Then R is an infinite field.

Proof: It is evident that R satisfies the postulates of a commutative ring with unity element. An additive identity element and a multiplicative unit element in this ring are

$$D(x) = \sum_{i=0}^{\infty} d_i x^{d-i},\ d_i = 0 \text{ for } i = 0,1,2,\cdots,\infty$$

and

$$F(x) = \sum_{i=0}^{\infty} f_i x^{d-i},\ d = 0, f_0 = 1, f_j = 0 \text{ for } j > 0$$

Every nonzero element of F, i.e.,

$$A(x) = \sum_{i=0}^{\infty} a_i x^{e-i}$$

has an inverse element $B(x)$ defined by

$$B(x) = A(x)^{-1} = \sum_{i=0}^{\infty} b_i x^{-e-i}$$

where

$$b_0 = a_0^{-1}$$

$$b_i = a_0^{-1}\left(\sum_{j=1}^{i-1} a_j b_{i-j}\right) \text{ for } (i = 1,2,\cdots)$$

Hence F is a field.

If the set R is composed of all power series not containing negative powers of x, i.e.,

$$R = \left\{\sum_{i=0}^{d} a_i x^{d-i} \,\middle|\, a_i \epsilon GF(q),\ d \text{ is a positive integer}\right\} \subset F \tag{2}$$

then it is evident that R is a subring of F. The integer part $[A(x)]$ of $A(x)$ in (1) is defined by

$$[A(x)] = \sum_{i=0}^{d} a_i x^{d-i}$$

Let $p(x)$ be the ratio of elements in R, i.e., a rational fraction form of type,

$$p(x) = \frac{\sum_{i=0}^{e} a_i x^{e-i}}{\sum_{i=0}^{f} b_i x^{f-i}}$$

where

$$\sum_{i=0}^{e} a_i x^{e-i}, \sum_{i=0}^{f} b_i x^{f-i} \epsilon R \subset F$$

By theorem 1, it can be proved that $p(x)$ is an element in the field F. An element in F of form $p(x)$ is called a rational element.

Let $GF(F_n)$ be the finite field, where $F_n = 2^{2^n} + 1$ is a Fermat prime for $n = 1,2,3,4$. It was shown in Ref. 10 that the field of type $I_{F_n}(\sqrt[4]{2})$ is isomorphic to $GF(F_n)$ for $n = 3,4$ and that $\alpha = \sqrt[4]{2} \epsilon GF(F_n)$ is an element of order 2^{n+4}. In these fields a systematic RS code can be specified in $GF(F_n)$ as follows:

Assume the code length for the RS code is $N = 2^{n+4}$. Let a code word be represented by $f(x)$, a polynomial of degree $N - 1$ over $GF(F_n)$. The generator polynomial of $g(x)$ is defined as

$$g(x) \quad \sum_{i=1}^{d-1} (x - \alpha^i)$$

where

$$d = 2^K < N = 2^{n+4}$$

and $\alpha = \sqrt[4]{2}, \alpha^2 = (\sqrt[4]{2})^2, \cdots, \alpha^d = (\sqrt[4]{2})^d$ are the roots of $g(x)$ in $GF(F_n)$. The resultant RS code with N symbols, which is a multiple of the generator polynomial, is composed of $d - 1$ parity check symbols and $N - (d - 1)$ information symbols, where d is the minimum distance of the RS code. If t is the number of errors, the code will correct, then $d = 2t + 1$.

Suppose that the code word $f(x) = f_0 + f_1 x + \cdots + f_{N-1}x^{N-1}$ is transmitted over a noisy channel. The received code word $R(x) = \gamma_0 + \gamma_1 x + \cdots + \gamma_{N-1}x^{N-1}$ is composed of the original code word with the addition of possible errors, i.e.,

$$\gamma(x) = f(x) + e(x)$$

where $e(x) = e_0 + e_1 x + e_2 x^2 + \cdots + e_{N-1}x^{N-1}$ is an error polynomial.

Upon receiving the message $\gamma(x)$, the first step in the decoding process is to take the FFT of the message in $I_{F_n}(\sqrt[4]{2})$. The transform is taken of the received N-tuple message $(\gamma_0, \gamma_1, \cdots, \gamma_{N-1})$, the coefficients of the polynomial $\gamma(x)$. This transform is

$$\begin{aligned} S_K &= \sum_{n=0}^{N-1} \gamma_n (\sqrt[4]{2})^{Kn} \\ &= \sum_{n=0}^{N-1} (f_n + e_n)(\sqrt[4]{2})^{Kn} \\ &= \sum_{n=0}^{N-1} f_n (\sqrt[4]{2})^{Kn} + \sum_{n=0}^{N-1} e_n (\sqrt[4]{2})^{Kn} \\ &= F_K + E_K \text{ for } K = 0,1,\cdots,N-1 \end{aligned}$$

Since $f(x)$ is a multiple of $g(x)$, $f(\alpha^i) = 0$ $i = 1,2,\cdots,d-1$.

Hence,

$$S_K = E_K = e(\sqrt[N]{2})^K = \sum_{n=0}^{N-1} e_n(\sqrt[N]{2})^{Kn}$$

$$= \sum_{n=0}^{N-1} e_n[(\sqrt[N]{2})^n]^K \text{ for } k = 1,2,\cdots,d-1 \tag{3}$$

where $E_K \epsilon GF(F_n)$ is periodic with N. Let Y_i and X_i be the ith error magnitudes and the ith error location, respectively. Then the syndrome in (3) becomes

$$S_K = E_K = \sum_{i=1}^{t} Y_i X_i^K \text{ for } k = 1,2,\cdots,d-1 \tag{4}$$

The generating function of the sequence (E_K) is defined as a formal power series. That is,

$$E(x) = E_1x^{-1} + E_2x^{-2} + E_3x^{-3} + \cdots = \sum_{K=1}^{\infty} E_K x^{-K} \tag{5}$$

where

$$E_K \epsilon GF(F_n)$$

Substituting (4) into (5), one gets

$$E(x) = \sum_{K=1}^{\infty} \sum_{i=1}^{t} Y_i X_i^K x^{-K}$$

$$= \sum_{i=1}^{t} Y_i \sum_{K=1}^{\infty} (X_i x^{-1})^K$$

$$= \sum_{i=1}^{t} Y_i \frac{X_i x^{-1}}{1 - X_i x^{-1}}$$

Thus

$$E(x) = E_1x^{-1} + E_2x^{-2} + E_3x^{-3} + \cdots$$

$$= \sum_{i=1}^{t} Y_i \frac{X_i}{x - X_i} = \frac{P(x)}{\sigma(x)} \tag{6}$$

where

$$P(x) \text{ and } \sigma(x) = \prod_{i=1}^{t} (x - X_i) \epsilon R$$

Note that $E(x)$ is a rational element in F. Since

$$\sigma(x) = x^t - \sigma_1 x^{t-1} + \sigma_2 x^{t-2} + \cdots + (-1)^t \sigma_t, \text{ then}$$

$$\sigma(X_i) = 0 = X_i^t - \sigma_1 X_i^{t-1} + \sigma_2 X_i^{t-2} + \cdots + (-1)^t \sigma_t, \text{ for } i = 1,2,\cdots,t$$

Multiplying the above equation by $Y_i X_i^j$, one gets,

$$Y_i X_i^{j+t} - \sigma_1 X_i^{j+t-1} + \sigma_2 Y_i X_i^{j+t-2} + \cdots + (-1)^t \sigma_t Y_i X_i^j$$

Summing on i for $i = 1,2,\cdots,t$, then

$$\sum_{i=1}^{t} Y_i X_i^{j+t} - \sigma_1 \sum_{i=1}^{t} Y_i X_i^{j+t-1} + \cdots + (-1)^t \sigma_t \sum_{i=1}^{t} Y_i X_i^j = 0$$

Using (4), we have,

$$S_{j+t} - \sigma_1 S_{j+t-1} + \cdots + (-1)^t \sigma_t S_j = 0, \qquad \text{for } j \leq t$$

and

$$E_{j+t} - \sigma_1 E_{j+t-1} + \cdots + (-1)^t \sigma_t E_j = 0 \qquad \text{for } j > t \tag{7}$$

It will be shown in the next section that $\sigma(x)$ in (6) can be calculated by using continued fraction approximations when only the first $2t$ coefficients of $E(x)$, i.e., $S_1, S_2, \cdots, S_{d-1}$ are known. If the coefficients of $\sigma(x)$, i.e., σ_i for $i = 1,2,\cdots,t$, are known, then Eq. (7) is used to obtain $E_0, E_1, E_{d-1}, \cdots, E_{N-1}$, and the transform of the N-tuple error pattern i.e., $(E_0, E_1, E_2, E_3, \cdots, E_{N-1})$ is obtained. Thus, the N-tuple error pattern $(e_0, e_1, \cdots, e_{N-1})$ is found by taking the inverse transform over I_{F_n} $(\sqrt[N]{2})$ of E_K for $k = 0, 1, \cdots, N-1$. Finally, the original N-tuple code word can be computed by subtracting e_n from the received code word r_n.

III. Implementing Berlekamp's Algorithm by Using Continued Fraction Approximations

It was shown in the previous section that $E(x) = P(x)/\sigma(x)$ in (6) is a rational element in the field of all formal power series F. Thus, using a procedure precisely similar to that used for rational elements in the real number field, described in Appendix A, it is possible to use continued fractions to develop a finite sequence of rational approximations to $E(x)$. That is, the recursive formula on convergents is given by.

$$E_r(x) = \frac{q_S(x)P_{S-1}(x) - P_{S-2}(x)}{q_S(x)\sigma_{S-1}(x) + \sigma_{S-2}(x)} = \frac{P_S(x)}{\sigma_S(x)} \tag{8}$$

where

$$P_1(x) = q_1(x), P_0(x) = 1, \sigma_0(x) = 0, \sigma_1(x) = 1.$$

The partial quotients $q_s(x)$ in (8) can be computed by the following formula recursively,

$$R_{s-2}(x) = q_s(x)R_{s-1}(x) + R_s(x) \tag{9}$$

where $R_{-1}(x) = E(x)$, $R_0(x) = 1$ and $q_s(x)$ is obtained as the "integer part" of $R_{s-2}(x)/R_{s-1}(x)$ and $R_s(x)$ is the "remainder"; and

$$(-1)^s R_s(x) = \sigma_s(x)E(x) - P_s(x) \tag{10}$$

where $\sigma_s(x)$ and $P_s(x)$ also satisfy the recursion in Eq. (9) with the initial values given in Eq. (8). By applying Euclid's algorithm to the rational element $E(x)$ in F, observe that $E(x) - P_s(x)/\sigma_s(x)$ will be terminated when $R_s(x) = 0$.

The norm of $A(x) \epsilon F$ will be used below in the proofs of theorem 2. This norm is defined as follows:

Definition

The norm of $A(x) = \sum_{i=0}^{\infty} a_i x^{d-i}$, $\|A(x)\|$, is defined by $\|A(x)\| = 2^d$

where d is a degree of $A(x)$

The properties of norm $\|A(x)\|$ are

a) $\|AB\| = \|A\| \cdot \|B\|$

b) $\|A\| > 0$ and $\|A\| = 0$ if $A = 0$

c) $\|A^{-1}\| = \dfrac{1}{\|A\|}$

d) $\|A \pm B\| \leq \max(\|A\|, \|B\|)$ if $\|A\| = \|B\|$ and $\|A \pm B\| = \max(\|A\|, \|B\|)$ if $\|A\| \neq \|B\|$

Lemma 1: Let n be the smallest finite integer such that $R_n(x) = 0$, where $R_s(x)$ is defined in (10); i.e., $E(x) = P_n(x)/\sigma_n(x)$. Then $\|R_s(x)\|$ is a monotone decreasing sequence for $s = 0,1,2,\cdots,n$ and $\|\sigma_s(x)\|$ is a monotone increasing sequence for $s = 0,1,2,\cdots,n$.

Proof:

By (9), one gets,

$$R_{s-2}(x) = q_s(x)R_{s-1}(x) + R_s(x)$$

where $\deg R_s(x) < R_{s-1}(x)$. This implies $\|R_s(x)\| < \|R_{s-1}(x)\|$ for $n = 1,2,\cdots,n$. Furthermore, since $\sigma_1(x) = 1$ and $\sigma_0(x) = 0$, then $\|\sigma_1(x)\| > \|\sigma_0(x)\|$. Assume $\|\sigma_{s-1}(x)\| > \|\sigma_{s-2}(x)\|$ for all $s \leq n$. By (8),

$$\sigma_s(x) = q_s(x)\sigma_{s-1}(x) + \sigma_{s-2}(x)$$

It follows from the norm properties that

$$\begin{aligned}\|\sigma_s(x)\| &= \|q_s(x)\sigma_{s-1}(x) + \sigma_{s-2}(x)\| \\ &= \|q_s(x)\sigma_{s-1}(x)\| = \|q_s(x)\|\|\sigma_{s-1}(x)\|\end{aligned} \tag{11}$$

But, by (9),

$$\begin{aligned}\|q_s(x)R_{s-1}(x)\| &= \|R_s(x) - R_{s-2}(x)\| \\ &= \|R_{s-2}(x)\| \\ \|q_s(x)\| &= \frac{\|R_{s-2}(x)\|}{\|R_{s-1}(x)\|} > 1\end{aligned}$$

Thus, (11) becomes

$$\|\sigma_s(x)\| > \|\sigma_{s-1}(x)\| \qquad \text{for } 1 \leq s \leq n.$$

To compute the norm of the difference $E(x) - P_s(x)/\sigma_s(x)$, we observe that

$$\left\| E(x) - \frac{P_s(x)}{\sigma_s(x)} \right\| = \frac{\|S(x)\sigma_s(x) - P_s(x)\|}{\|\sigma_s(x)\|} = \frac{\|R_s(x)\|}{\|\sigma_s(x)\|}$$

Then, by lemma 1,

$$\left\| E(x) - \frac{P_s(x)}{\sigma_s(x)} \right\| < \left\| E(x) - \frac{P_{s+1}(x)}{\sigma_{s+1}(x)} \right\|, \qquad \text{for } 0 \leq s \leq n-1 \tag{12}$$

For decoding RS codes over $GF(F_n)$, we only know the first $2t$ coefficients of $E(x)$ in (6). That is,

$$E(x) = E_1x^{-1} + E_2x^{-2} + \cdots E_{-t}x^{-2t} \underbrace{+ Xx^{-2t-1} + \cdots}_{X(x)}$$

where $X(x)$ is an unknown element in F. The following theorem is developed to recover the rational element $E(x)$ in F precisely when only the first $2t$ coefficients of $E(x)$ in (6) are known.

Theorem 2: Let $E(x) = P(x)/\sigma(x)$ in (6) be a rational element in F defined by theorem 1, where $P(x)$ and $\sigma(x) \epsilon R$ are defined in (2) and $\|E(x)\| < 1$. Let $X(x)$ be an unknown element in F such that $\deg X(x) < -2 \deg \sigma(x)$. If the first $\deg X(x) + 1$ coefficients of $E(x)$ are known, i.e.,

$$E(x) + X(x) = E_1x^{-1} + E_2x^{-2} + \cdots + E_{\deg X(x)+1}x^{\deg X(x)+1} + Xx^{\deg X(x)} + \cdots$$

where

$$X(x) = Xx^{\deg X(x)} + \cdots$$

Then $E(x)$ can be obtained by using the continued fraction algorithm operating on $E(x) + X(x)$.

Proof: By (10), we know that

$$\begin{aligned}(-1)^S R_S(x) &= \sigma_S(x)[E(x) + X(x)] - P_S(x)\\ &= (\sigma_S(x)E(x) - P_S(x)) + \sigma_S(x)X(x)\end{aligned}$$

where $\sigma_S(x)X(x)$ indicates the location of the unknown coefficients in $R_S(x)$.

We see that following the Euclidean division of $R_{S-2}(x)$ by $R_{S-1}(x)$, it follows immediately that $q_S(x)$, which is independent of $X(x)$, can be determined if and only if

$$\begin{aligned}&\deg R_{S-1}(x) - \deg \sigma_{S-1}(x)X(x) > \deg R_{S-2}(x)\\ &\quad - \deg R_{S-1}(x) = \deg q_S(x) \text{ for } S \geq 2 \qquad (13)\end{aligned}$$

(Note that the left side of (13) indicates the number of known coefficients in the divisor and the right side of (13) indicates the degree of the partial quotient $q_S(x)$.) It follows from (13) that

$$2^{2\deg R_{S-1}(x)} > 2^{\deg R_{S-2}(x) - \deg \sigma_{S-1}(x)X(x)}$$

By the properties of norm, (13) becomes

$$\| R_{S-1}(x) \|^2 > \| R_{S-2}(x) \|^2 \cdot \| \sigma_{S-1}(x) \|^2 \cdot \| X(x) \| \qquad (14)$$

But, by (11) in the proof of the lemma 1, one has,

$$\| \sigma_S(x) \|^2 = \| q_S(x) \|^2 \cdot \| \sigma_{S-1}(x) \| \qquad (15)$$

Since, by (9),

$$\| R_{S-2}(x) \|^2 = \| q_S(x)R_{S-1}(x) + R_S(x) \|^2 \qquad (16)$$

Then, by the lemma 1, (16) becomes

$$\| R_{S-2}(x) \| = \| q_S(x)R_{S-1}(x) \| = \| q_S(x) \| \cdot \| R_{S-1}(x) \| \qquad (17)$$

From (8), one gets

$$\| \sigma_1(x) \| = 1 \qquad (18)$$

and

$$\| R_0(x) \| = 1$$

Thus, from (15), (17), (18), we have

$$\| \sigma_{S-1}(x) \| = \| R_{S-2}(x) \|^{-1} \qquad (19)$$

Substituting (19) into (14), one obtains

$$\| R_{S-1}(x) \|^2 > \| X(x) \|$$

Hence $q_S(x)$, which is independent of $X(x)$, is obtained by the Euclidean division of $R_{S-2}(x)$ by $R_{S-1}(x)$ if and only if

$$\| R_{S-1}(x) \|^2 > \| X(x) \| \qquad (20)$$

Let $q_n(x)$ be the last partial quotients such that $q_n(x)$, which is independent of $X(x)$, can be determined by the Euclidean division algorithm. It follows from (20) that

$$\| R_n(x) \|^2 \leq \| X(x) \| \qquad (21)$$

By (19), (21) becomes

$$\| \sigma_{n-1}(x) \|^{-2} \leq \| X(x) \|$$

This implies

$$\| X(x) \|^{-1} \leq \| \sigma_{n+1}(x) \|^2 \qquad (22)$$

Since $\| \sigma(x) \|^2 < \| X(x) \|^{-1}$, thus (22) becomes,

$$\| \sigma(x) \|^2 < \| \sigma_{n+1}(x) \|^2 \qquad (23)$$

Consider either

$$\left\| E(x) - \frac{P_n(x)}{\sigma_n(x)} \right\| = \left\| E(x) - \frac{P(x)}{\sigma(x)} \right\|$$

or

$$\left\| E(x) - \frac{P_n(x)}{\sigma_n(x)} \right\| > \left\| E(x) - \frac{P(x)}{\sigma(x)} \right\|$$

If

$$\left\| E(x) - \frac{P_n(x)}{\sigma_n(x)} \right\| = \left\| E(x) - \frac{P(x)}{\sigma(x)} \right\| = 0$$

then

$$E(x) = \frac{P(x)}{\sigma(x)} = \frac{P_n(x)}{\sigma_n(x)}.$$

If

$$\left\| E(x) - \frac{P_n(x)}{\sigma_n(x)} \right\| > \left\| E(x) - \frac{P(x)}{\sigma(x)} \right\| = 0,$$

then

$$\left\| E(x) - \frac{P_n(x)}{\sigma_n(x)} \right\| = \left\| \left(E(x) - \frac{P_{n+1}(x)}{\sigma_{n+1}(x)} \right) + \left(\frac{P_{n+1}(x)}{\sigma_{n+1}(x)} - \frac{P_n(x)}{\sigma_n(x)} \right) \right\| \leq \max \left(\left\| E(x) - \frac{P_{n+1}(x)}{\sigma_{n+1}(x)} \right\|, \left\| \frac{P_{n+1}(x)}{\sigma_{n+1}(x)} - \frac{P_n(x)}{\sigma_n(x)} \right\| \right) \quad (24)$$

By (12), (24) becomes either

$$\left\| E(x) - \frac{P_n(x)}{\sigma_n(x)} \right\| = \left\| E(x) - \frac{P_{n+1}(x)}{\sigma_{n+1}(x)} \right\|$$

or

$$\left\| E(x) - \frac{P_n(x)}{\sigma_n(x)} \right\| \leq \left\| \frac{P_{n+1}(x)}{\sigma_{n+1}(x)} - \frac{P_n(x)}{\sigma_n(x)} \right\|.$$

If

$$\left\| E(x) - \frac{P_n(x)}{\sigma_n(x)} \right\| = \left\| E(x) - \frac{P_{n+1}(x)}{\sigma_{n+1}(x)} \right\|,$$

this implies $R_n(x) = R_{n+1}(x) = 0$. If

$$\left\| E(x) - \frac{P_n(x)}{\sigma_n(x)} \right\| \leq \left\| \frac{P_{n+1}(x)}{\sigma_{n+1}(x)} - \frac{P_n(x)}{\sigma_n(x)} \right\| = \frac{\| P_{n+1}(x)\sigma_n(x) - \sigma_{n+1}(x)P_n(x) \|}{\| \sigma_{n+1}(x) \| \cdot \| \sigma_n(x) \|} \quad (25)$$

By the same procedure used in the derivation of (A-10) in Appendix A, (25) becomes

$$\left\| \frac{P(x)}{\sigma(x)} - \frac{P_n(x)}{\sigma_n(x)} \right\| \leq \frac{1}{\| \sigma_{n+1}(x) \| \| \sigma_n(x) \|} \quad (26)$$

Multiplying (26) by $\| \sigma(x) \| \| \sigma_n(x) \|$ gives

$$\| P(x)\sigma_n(x) - P_n(x)\sigma(x) \| \leq \frac{\| \sigma(x) \|}{\| \sigma_{n+1}(x) \|}$$

By (23), this yields,

$$\| P(x)\sigma_n(x) - P_n(x)\sigma(x) \| < 1,$$

which implies

$$\| P(x)\sigma_n(x) - P_n(x)\sigma(x) \| = 0$$

Then

$$\frac{P(x)}{\sigma(x)} = \frac{P_n(x)}{\sigma_n(x)}$$

Hence the theorem is proved.

A simple example of theorem 2 for decoding a RS code in $GF(F_n)$ is now presented.

Example: Let $GF(2^{2^2} + 1)$ be the field of integers modulo the Fermat prime $F_2 = 17$. We consider a 2-error correcting 8-tuple RS in $GF(17)$. (Note that this example is the same example in Ref. 10.)

Assume the information symbols are $1,2,3,2 \epsilon GF(17)$; i.e., $I(x) = 1x^7 + 2x^6 + 3x^5 + 2x^4$. By the example in (Ref. 10), the encoding of $I(x)$ is the polynomial

$$b(x) = 1x^7 + 2x^6 + 3x^5 + 2x^4 + 15x^3 + 12x^2 + 2x + 5$$

Suppose that two errors occur in the received words, i.e.,

$$\gamma(x) = 5 + 2x + 9x^2 + 15x^3 + 2x^4 + 1x^5 + 2x^6 + 1x^7$$

By the example in (Ref. 10), the syndrome can be calculated, using a FFT over $GF(F_n)$. That is,

$$S_K = E_K = \sum_{n=0}^{8-1} \gamma_n 2^{nK} \qquad \text{for } k = 1,2,3,4$$

Hence,

$$S_1 = E_1 = -8$$
$$S_2 = E_2 = -5$$
$$S_3 = E_3 = 11$$
$$S_4 = E_4 = -1$$

By (6)

$$E(x) = -8x^{-1} - 5x^{-2} + 11x^{-3} - x^{-4} + \underbrace{Xx^{-5} + \cdots}_{X(x)} = \frac{P(x)}{\sigma(x)} \quad (27)$$

where

$$\sigma(x) = \prod_{i=1}^{2} (x - x_i) = x^2 - \sigma_1 x + \sigma_2,$$

and X denotes the first unknown coefficient of $X(x)$. Since the deg $X(x) <$ deg $\sigma(x) = -2t = -4$ in (27) then, by Theorem 2, $\sigma(x)$ can be determined by the use of a continued fraction which is given below in tabular form.

S	$R_{S-2}(x) = q_S(x)R_{S-1}(x) + R_S(x)$	$q_S(x)$	$R_S(x)$	$\sigma_S(x) = q_S(x)\sigma_{S-1}(x) + \sigma_{S-2}(x)$
-1				1
0				0
1	0 $1\overline{)\ -8x^{-1} - 5x^{-2} + 11x^{-3} - x^{-4} + Xx^{-5} + \cdots}$ $0x^{-1} + 0x^{-2} + 0x^{-3} + 0x^{-4} + \cdots$ $-8x^{-1} - 5x^{-2} + 11x^{-3} - x^{-4} + Xx^{-5} + \cdots$	0	$-8x^{-1} - 5x^{-2} + 11x^{-3}$ $- x^{-4} + Xx^{-5} + \cdots$	$\sigma_1(x) = 0 \cdot 0 + 1 = 1$
2	$2x + 3$ $-8x^{-1} - 5x^{-2}$ $+ 11x^{-3} - x^{-4}$ $+ Xx^{-5} + \cdots$ $1\overline{)\ 1 - 10x^{-1} + 5x^{-2} - 2x^{-3} + Xx^{-4} + \cdots}$ $10x^{-1} - 5x^{-2} + 2x^{-3} + Xx^{-4} + \cdots$ $10x^{-1} - 15x^{-2} - x^{-3} + \cdots$ $10x^{-2} + 3x^{-3} + Xx^{-4} + \cdots$	$2x + 3$	$10x^{-2} + x^{-3}$ $+ Xx^{-4} + \cdots$	$\sigma_2(x) = (2x + 3) \cdot 1 + 0$ $= 2x + 3$
3	$6x - 4$ $-7x^{-2} + 3x^{-3}$ $+ Xx^{-4} + \cdots$ $-8x^{-1} - 5x^{-2} + 11x^{-3} - x^{-4} + Xx^{-5} + \cdots\ \overline{)\ -8x^{-1} + x^{-2} + Xx^{-3} + \cdots}$ $-6x^{-2} + Xx^{-3} + \cdots$ $-6x^{-2}$ $0x^{-2} + Xx^{-3}$	$6x - 4$	$0 + Xx^{-3} + \cdots$	$\sigma_3 = (6x - 4)(2x + 3)$ $+ 1$ $= x^2 - 2x + 9$

From the above tabular form, observe that $R_3 = 0 + Xx^{-3}$. Hence, $\sigma(x) = \sigma_3(x) = x^2 - 2x + 9$ where $\sigma_1 = 2$ and $\sigma_2 = 9$. By (7), one gets

$$E_{j+2} - 2E_{j+1} + 9E_j = 0 \qquad \text{for } j > 2 \tag{28}$$

From (28), the rest of the transform E_j of the error pattern is $E_5 = 1$, $E_6 = 11$, $E_7 = 13$, $E_8 = E_9 = 12$. By example in Ref. 10, the inverse FFT over $GF(2^{2^2} + 1)$ of the E_j for $j = 0,1, \cdots, 7$ is given by

$$(e_0,e_1,e_2,e_3,e_4,e_5,e_6,e_7) = (0,0,14,0,0,15,0,0)$$

The corrected code word is

$$b(x) = \gamma(x) - e(x) = (5,2,9,15,2,1,2,1) - (0,0,14,0,0,15,0,0) = (5,2,12,15,2,3,2,1)$$

Appendix

The Computation of Continued Fractions by Using Euclid's Algorithm

Let S be an irreducible rational element S in the field of real numbers. In this Appendix, it will be shown that a finite sequence of rational approximations to S can be constructed by using continued fractions.

Let $S = a/b$, where a and b are integers, be an irreducible rational element in the field of real numbers. Using Euclid's algorithm, one gets,

$$\begin{aligned} a &= bq_1 + \gamma_1 \\ b &= \gamma_1 q_2 + \gamma_2 \\ \gamma_1 &= \gamma_2 q_3 + \gamma_3 \\ &\vdots \\ \gamma_{k-2} &+ \gamma_{K-1} q_K + \gamma_K \\ &\vdots \\ \gamma_{n-3} &= \gamma_{n-2} q_{n-1} + \gamma_{n-1} \\ \gamma_{n-2} &= \gamma_{n-1} q_n + \gamma_n = \gamma_n q_n \end{aligned} \tag{A-1}$$

or

$$\begin{aligned} \frac{a}{b} &= q_1 + \frac{\gamma_1}{b} \\ \frac{b}{\gamma_2} &= q_2 + \frac{\gamma_2}{\gamma_1} \\ \frac{\gamma_1}{\gamma_2} &= q_3 + \frac{\gamma_3}{\gamma_2} \\ &\vdots \\ \frac{\gamma_{K-2}}{\gamma_{K-1}} &= q_K + \frac{\gamma_K}{\gamma_{K-1}} \\ &\vdots \\ \frac{\gamma_{n-3}}{\gamma_{n-2}} &= q_{n-1} + \frac{\gamma_{n-1}}{\gamma_{n-2}} \\ \frac{\gamma_{n-2}}{\gamma_{n-1}} &= q_n \end{aligned}$$

By (A-1), $S = a/b$ can be developed by a continued fraction, as follows:

$$S = \frac{a}{b} = q_1 + \cfrac{1}{q_2 + \cfrac{1}{q_3 + \ddots + \cfrac{1}{q_K + a_K}}}, \quad k < n \tag{A-2}$$

or

$$= q_1 + \cfrac{1}{q_2 + \cfrac{1}{q_3 + \ddots + \cfrac{1}{q_n}}} \tag{A-3}$$

where q_K for $k = 1,2,\cdots,n$ are called the partial quotients.

Let us define the convergents S_K for $k = 1,2,\cdots,n$ as follows

$$\begin{aligned} S_1 &= q_1 \\ S_2 &= q_1 + \frac{1}{q_2} \\ S_3 &= q_1 + \cfrac{1}{q_2 + \cfrac{1}{q_3}} \\ &\vdots \\ S_n &= \frac{a}{b} = q_1 + \cfrac{1}{q_2 + \cfrac{1}{q_3 + \ddots + \cfrac{1}{q_n}}} \end{aligned}$$

From (A-1), we observe that S_K is a finite sequence. In other words, S_1, S_2, $\cdots$, S_K, $\cdots$ will be terminated when $\gamma_n = 0$. Thus, $S_n = a/b$, where n is a finite number.

A recursive formula for convergents is generated as follows. Let $P_0 = 1$ and $Q_0 = 0$. Then set

$$S_1 = \frac{q_1}{1} = \frac{P_1}{Q_1}$$

$$S_2 = q_1 + \frac{1}{q_2} = \frac{q_2 q_1 + 1}{q_2 \cdot 1 + 0} = \frac{q_2 P_1 + P_0}{q_2 Q_1 + Q_0} = \frac{P_2}{Q_2}$$

$$S_3 = q_1 + \cfrac{1}{q_2 + \cfrac{1}{q_3}} = \frac{\left(q_2 + \frac{1}{q_3}\right) P_1 + P_0}{\left(q_2 + \frac{1}{q_3}\right) Q_1 + Q_0}$$

$$= \frac{q_2 P_1 + P_0\left(\frac{1}{q_3}\right) q_3}{(q_2 Q_1 + Q_0) + \frac{P_1}{Q_1}} = \frac{q_3 P_2 + P_1}{q_3 Q_2 + Q_1} = \frac{P_3}{Q_3}$$

The recursive convergents are defined as

$$S_K = \frac{q_K P_{K-1} + P_{K-2}}{q_K Q_{K-1} + Q_{K-2}} = \frac{P_K}{Q_K} \tag{A-4}$$

where $P_1 = q_1$, $P_0 = 1$, $Q_0 = 0$, $Q_1 = 1$, for $k = 2,3,\cdots,n$.

(A-4)

In order to calculate Eq. (A-4), it is necessary to compute the partial quotients. To do this, by the same procedure used in the derivation of (A-4), we can show first that S in (A-2) can be expressed in the following form:

$$S = \frac{(q_K + \alpha_K)P_{K-1} + P_{K-2}}{(q_K + \alpha_K)Q_{K-1} + Q_{K-2}}, \text{ where } \alpha_K \text{ is defined in (A-2)}$$

If S has this form, then

$$(q_K + \alpha_K)(P_{K-1} - SQ_{K-1}) = S\,Q_{K-2} - P_{K-2}$$

and,

$$\frac{1}{\alpha_{K-1}} = q_K + \alpha_K = -\frac{P_{K-2} - Q_{K-2}S}{P_{K-1} - Q_{K-1}S} = -\frac{R'_{K-2}}{R'_{K-1}} \tag{A-5}$$

where $R'_K = P_K - Q_K S$. It follows that

$$q_K R'_{K-1} + R'_{K-2} = -\alpha_K R_{K-1} = -\left(-\frac{R'_K}{R'_{K-1}}\right) \cdot R'_{K-1} = R'_K$$

Finally,

$$R'_K = q_K R'_{K-1} + R'_{K-2} \tag{A-6}$$

By (5-A), the initial condition of R'_K for $K = 0,1$, is given by

$$R'_{-1} = P_{-1} - Q_{-1}S = -S$$

$$R'_0 = P_0 - Q_0 S = 1 - 0 \cdot S = 1$$

Define a new function R_K in forms of R'_K by $R'_K = (-1)^K R_K$. Then (A-6) becomes

$$-(-1)^{K-2}R_{K-2} = q_K(-1)^{K-1}R_{K-1} - (-1)^K R_K$$

It is evident that

$$R_{K-2} = q_K R_{K-1} + R_K \text{ for both even and odd } k$$

Hence

$$R_{K-2} = q_K R_{K-1} + R_K \tag{A-7}$$

with

$$R_{-1} = (-1)^{-1}R'_{-1} = S$$

$$R_0 = (-1)^0 R'_0 = 1$$

and by (A-5)

$$(-1)^K R_K = Q_K S = P_K \tag{A-8}$$

To show that $S_K = (P_K/Q_K)$, which is computed by using a continued fraction, is an irreducible fraction, i.e., $(P_K,Q_K) = 1$, consider the difference between S_K and S_{K-1} for $K > 1$. That is,

$$S_K - S_{K-1} = \frac{P_K}{Q_K} - \frac{P_K}{Q_{K-1}} = \frac{P_K Q_{K-1} - Q_K P_{K-1}}{Q_K Q_{K-1}} \tag{A-9}$$

Let $I_K = P_K Q_{K-1} - Q_K P_{K-1}$. By (A-4),

$$\begin{aligned} I_K = P_K Q_{K-1} - Q_K P_{K-1} &= (q_K P_{K-1} + P_{K-2})Q_{K-1} \\ &\quad - (q_K Q_{K-1} + Q_{K-2})P_{K-1} \\ &= -(P_{K-1}Q_{K-2} - Q_{K-1}P_{K-2}) \\ &= -I_{K-1} \end{aligned} \tag{A-10}$$

Since $I_1 = P_1 Q_0 - Q_1 P_0 = q_1 \cdot 0 - 1 \cdot 1 = -1$, one has, by (A-10), $I_2 = -I_1 = 1$. With the above result, one has $I_K = (-1)^K$. It follows that

$$S_K - S_{K-1} = \frac{P_K}{Q_K} - \frac{P_{K-1}}{Q_{K-1}} = \frac{(-1)^K}{Q_K Q_{K-1}} \qquad \text{for } k > 1$$

or

$$P_K Q_{K-1} - Q_K P_{K-1} = (-1)^K \qquad \text{for } k > 1 \tag{A-11}$$

If $(P_K,Q_K) = d_K$, then, by (A-11), $d_K | (-1)^K$. This implies that $d_K = 1$. Hence $(P_K,Q_K) = 1$.

A simple example, showing how to compute the rational approximations to an irreducible rational number, is presented in the following tabular form. For this example, S is the fraction 38/105.

s	$R_{s-2} = q_s R_{s-1} + R_s$	q_s	R_s	$P_s = q_s P_{s-1} + P_{s-2}$	$Q_s = q_s Q_{s-1} + Q_{s-2}$	$S_s = \frac{P_s}{Q_s}$
-1				0	1	
0				1	0	
1	$\frac{38}{105} = 0 \cdot 1 + \frac{38}{105}$	0	$\frac{38}{105}$	$P_1 = 0 \cdot 1 + 0 = 0 = q_1$	$Q_1 = 0 \cdot 0 + 1 = 1$	$S_1 = 1$
2	$1 = 2 \cdot \frac{38}{105} + \frac{29}{105}$	2	$\frac{29}{105}$	$P_2 = 2 \cdot 0 + 1 = 1$	$Q_2 = 2 \cdot 1 + 0 = 2$	$S_2 = \frac{1}{2}$
3	$\frac{38}{105} = 1 \cdot \frac{29}{105} + \frac{9}{105}$	1	$\frac{9}{105}$	$P_3 = 1 \cdot 1 + 0 = 1$	$Q_3 = 1 \cdot 2 + 1 = 3$	$S_3 = \frac{1}{3}$
4	$\frac{29}{105} = 3 \cdot \frac{9}{105} + \frac{2}{105}$	3	$\frac{2}{105}$	$P_4 = 3 \cdot 1 + 1 = 4$	$Q_4 = 3 \cdot 3 + 2 = 11$	$S_4 = \frac{4}{11}$
5	$\frac{9}{105} = 4 \cdot \frac{2}{105} + \frac{1}{105}$	4	$\frac{1}{105}$	$P_5 = 4 \cdot 4 + 1 = 17$	$Q_5 = 4 \cdot 11 + 3 = 47$	$S_5 = \frac{17}{47}$
6	$\frac{2}{105} = 2 \cdot \frac{1}{105} + 0$	2	0	$P_6 = 2 \cdot 17 + 4 = 38$	$Q_4 = 2 \cdot 47 + 11 = 105$	$S_6 = \frac{38}{105}$

From the tabular form when $s = n = 6$, one observes $R_6 = 0$. By (A-8),

$$S = S_6 = \frac{P_6}{Q_6} = \frac{38}{105}$$

For a more detailed discussion of the relation of Euclid's algorithm to the continued fraction associated with a rational element in the field of real numbers, see Ref. 12.

Acknowledgment

The authors wish to thank Mr. B. Mulhall and Dr. B. Benjauthrit of JPL for supporting and encouraging the research that led to this paper. The authors also wish to thank Prof. R. Scholtz of USC for many helpful suggestions and for providing his class notes on algebraic coding.

References

1. Gore, W. C., "Transmitting Binary Symbols with Reed–Solomon Code," Johns Hopkins EE Report No. 73-5, Apr. 1973.

2. Michelson, A., "A New Decoder for the Reed–Solomon Codes Using a Fast Transform Technique," Systems Engineering Technical Memorandum No. 52, Electronic Systems Group, Eastern Division GTE Sylvania, Aug. 1975.

3. Mandelbaum, D., "On Decoding Reed–Solomon Codes," *IEEE Trans. Inform. Th.*, Vol. IT-17, No. 6, pp. 707-712, Nov. 1971.

4. Peterson, W. W., *Error-Correcting Codes*, MIT Press, Cambridge, Mass., 1961, pp. 168–169.

5. Rader, C. M., "Discrete Convolution Via Mersenne Transforms," *IEEE Trans. Comput.*, Vol. C-21, No. 12, Dec. 1972, pp. 1269–1273.

6. Agarwal, R. C., and Burrus, C. S., "Number Theoretic Transform to Implement Fast Digital Convolution," *Proc. IEEE*, Vol. 63, No. 4, Apr. 1975.

7. Reed, I. S., and Truong, T. K., "Convolutions over Residue Classes of Quadratic Integers," *IEEE Trans. Inform. Th.*, July 1976.

8. McClellan, J. H., "Hardware Realization of a Fermat Number Transform," *IEEE Trans. Acoustics, Speech, and Signal Processing*, Vol. Assp. 24, No. 3, June 1976, pp. 216–225.

9. Justesen, J., "On the Complexity of Decoding of Reed–Solomon Codes," *IEEE Trans. Inform. Th.*, Vol. IT-22, Mar. 1976, pp. 237–238.

10. Reed, I. S., Truong, T. K., and Welch, L. R., "The Fast Decoding of Reed–Solomon Codes Using Number Theoretic Transforms," to *The Deep Space Network Progress Report 42-35*, pp. 64–78, Jet Propulsion Laboratory, Pasadena, Calif., Oct. 15, 1976.

11. Berlekamp, E. R., *Algebraic Coding Theory*, McGraw-Hill, New York, 1968, Chapter 7.

12. Vinogrodov, I. M., *Elements of Number Theory*, Dover Publications, New York, 1954, Chapter 1.

N77-14057

The Fast Decoding of Reed-Solomon Codes Using High-Radix Fermat Theoretic Transforms

K. Y. Liu and I. S. Reed
University of Southern California

T. K. Truong
TDA Engineering Office

Fourier-like transforms over $GF(F_n)$, where $F_n = 2^{2^n} + 1$ is a Fermat prime, have found application in decoding Reed–Solomon codes. It is shown here that such transforms can be computed using high-radix fast Fourier transform (FFT) algorithms requiring considerably fewer multiplications than the more usual radix 2 FFT algorithm. A special 256-symbol, 16-symbol-error-correcting, Reed–Solomon (RS) code for space communication-link applications can be encoded and decoded using this high-radix FFT algorithm over $GF(F_5)$.

I. Introduction

Recently, Justesen (Ref. 1) and Reed, Truong, and Welch (Refs. 2, 3) proposed that transforms over $GF(F_n)$ (Refs. 4, 5) can be used to define Reed-Solomon (RS) codes (Ref. 6) and to improve the decoding efficiency of these codes. The transform over $GF(F_n)$ is of the form

$$A(f) = \sum_{t=0}^{d-1} a(t)\,\gamma^{ft} \qquad \text{for } 0 \le f \le d-1 \qquad (1)$$

where $F_n = 2^{2^n} + 1$ is a Fermat prime for $n \le 4$. In (1) the transform length d divides $F_n - 1$, $a(t) \in GF(F_n)$, and γ is a primitive dth root of unity which generates the d element cyclic subgroup

$$G_d = \{\gamma, \gamma^2, \cdots, \gamma^{d-1}, 1\}$$

in the multiplicative group of $GF(F_n)$. The inverse transform of (1) is

$$a(t) = (d)^{-1} \sum_{f=0}^{d-1} A(f)\,\gamma^{-ft} \qquad \text{for } 0 \le t \le d-1 \qquad (2)$$

where (d) denotes the residue of d modulo F_n and $(d)^{-1}$ is the inverse of (d) in $GF(F_n)$.

To transform longer integer sequences over $GF(F_n)$, from Ref. 5, one can use the fact that $\gamma = 3$ is a primitive element in $GF(F_n)$. Such a γ gives a maximum transform length of 2^{2^n}.

In space communication links, it was shown in Ref. 7 that in the concatenated $E = 16$-error-correcting, 255-symbol RS code, each symbol with 8 bits and a $K = 7$, rate $= {}^1/_2$ or ${}^1/_3$, Viterbi decoded convolutional code, can be used to reduce the value of E_b/N_0 required to meet a specified bit-error rate P_b, where E_b is the received energy for each bit, and N_0 is the noise power spectral density at the receiver input.

Figure 1 presents a curve of concatenated code bit probability of the error bound vs E_b/N_0 for a $K = 7$, $R = {}^1/_2$, convolutional code with 8 bits per RS symbol.

Since 3 is an element of order 2^{2^n} in $GF(F_n)$ (Ref. 5), an RS code of as many as 2^8 symbols of 9 bits each can be generated in $GF(F_3)$. Hence, by Ref. 2, the Fermat theoretic transform over $GF(F_3)$ can be used to decode an RS code of 2^8 symbols. For a given 223 information symbols, each of 8 bits, as mentioned above by Ref. 2, 224 information symbols in $GF(F_3)$, i.e., $S_1 = 0, S_2, \cdots, S_{224}$, can be represented in the range from 0 to $2^{24} - 1$. After encoding the information symbols, the parity check symbols in the 256-symbol RS code may occur in the range between 0 and 2^{24}. If 2^{24} is observed as a parity check symbol, deliberately change this value to 0, now an error. The transform decoder will correct this error automatically. Hence, the RS code generated in $GF(F_3)$ can be used to concatenate with a $K = 7$, rate ${}^1/_2$ or ${}^1/_3$ convolutional code.

The arithmetic used to perform these transforms over $GF(F_n)$ requires integer multiplications by powers of 3 and integer additions modulo F_n. However, integer multiplications by powers of 3 modulo F_n are not as simple as multiplications by powers of $\sqrt{2}$ modulo F_n, which can be implemented by circular shifts (Ref. 5). To remedy such a problem, it is shown here that high-radix fast Fourier transform (FFT) algorithms can be used to reduce the number of multiplications required for transforming integer sequences in $GF(F_n)$.

II. High-Radix FFT Algorithms Over $GF(F_n)$, Where F_n Is a Fermat Prime

In order to develop high-radix FFT algorithms over $GF(F_n)$, it is desirable, as we shall see, that multiplications involving the 2^ith roots of unity in $GF(F_n)$ be simple operations. This is made possible from the fact that the 2^ith roots of unity over $GF(F_n)$, where $2 \le i \le n + 1$ are plus or minus power of 2 mod F_n.

To see this, note that if $2|s$, then

$$(\pm 2^{s/2})^2 \equiv 2^s \mod F_n$$

and

$$[\pm 2^{(2^n+s)/2}]^2 = 2^{2^n} \cdot 2^s \equiv -2^s \mod F_n$$

Hence, by theorem 2.20 of Ref. 8, the congruences

$$x^2 \equiv 2^s \mod F_n \tag{3}$$

and

$$x^2 \equiv -2^s \mod F_n \tag{4}$$

have exactly two solutions given by

$$x \equiv \pm 2^{s/2} \mod F_n \tag{5}$$

and

$$x \equiv \pm 2^{(2^n+s)/2} \mod F_n \tag{6}$$

respectively. Now let γ be a primitive dth root of unity in $GF(F_n)$, where $d = 2^t$ with $1 \le t \le 2^n$. Then by theorem 1 of Ref. 9,

$$\gamma^{d/2} = (\gamma^{d/4})^2 = -1 \mod F_n$$

Also by (6),

$$\gamma^{d/4} = (\gamma^{d/8})^2 = \pm 2^{2^n-1} \mod F_n$$

Combining (5) and (6), one obtains

$$\gamma^{d/8} = (\gamma^{d/16})^2 = \pm 2^{k2^n-2} \mod F_n$$

where $k = 1, 3$. By repeatedly applying (5) and (6) in this manner, one has finally

$$\gamma^{d/2^i} = \pm 2^{k2^{n-i+2}} \mod F_n \tag{7}$$

where $2 \le i \le n + 1$ and $k = 1, 3, 5, \cdots, 2^{i-1} - 1$.

The high-radix FFT algorithms over $GF(F_n)$ are similar to those over the field of complex numbers (Refs. 10, 11). The following example illustrates the radix 16, decimation-in-frequency, twiddle-factor FFT over $GF(F_3)$.

Example. Let $F_3 = 2^{2^3} + 1 = 257$, $d = 16^2 = 256$. The radix 16, decimation-in-frequency, twiddle factor, FFT algorithm over $GF(F_3)$ is described as follows.

Let f and t in (1) be expressed as

$$f = f_1 \cdot 16 + f_0 \tag{8}$$

$$t = t_1 \cdot 16 + t_0 \tag{9}$$

where

$$f_i, t_i = 0, 1, 2, 3, \cdots, 15$$

Substituting (8) and (9) into (1), one has

$$A(f) = \sum_{t_0=0}^{15} \sum_{t_1=0}^{15} a(t_1 \cdot 16 + t_0)\gamma^{(f_1 \cdot 16+f_0)(t_1 \cdot 16+t_0)} \tag{10}$$

Since $\gamma^d = \gamma^{16^2} \equiv 1 \bmod F_3$, (10) becomes

$$A(f) = \sum_{t_0=0}^{15} \sum_{t_1=0}^{15} a(t_1 \cdot 16 + t_0)\gamma^{f_1 t_0 \cdot 16 + f_0 t_1 \cdot 16 + f_0 t_0}$$

$$= \sum_{t_0=0}^{15} \left[\left[\sum_{t_1=0}^{15} a(t_1 \cdot 16 + t_0)\gamma^{f_0 t_1 \cdot 16} \right] \gamma^{f_0 t_0} \right] \gamma^{f_1 t_0 \cdot 16}$$

Let

$$B_1(f_0 \cdot 16 + t_0) = \left[\sum_{t_1=0}^{15} a(t_1 \cdot 16 + t_0)\gamma^{f_0 t_1 \cdot 16} \right] \gamma^{f_0 t_0}$$

$$B_2(f_0 \cdot 16 + f_1) = \sum_{t_0=0}^{15} B_1(f_0 \cdot 16 + t_0) \cdot \gamma^{f_1 t_0 \cdot 16}$$

The radix 16, 256-point, FFT algorithm over GF(F_3) is then composed of the following stages:

Stage 1:

$$B_1(f_0 \cdot 16 + t_0) = \left[\sum_{t_1=0}^{15} a(t_1 \cdot 16 + t_0)\, \gamma^{f_0 t_1 \cdot 16} \right] \gamma^{f_0 t_0} \tag{11}$$

Stage 2:

$$B_2(f_0 \cdot 16 + f_1) = \left[\sum_{t_0=0}^{15} B_1(f_0 \cdot 16 + t_0)\gamma^{f_1 t_0 \cdot 16} \right] \tag{12}$$

From (7),

$$\gamma^{16} = \gamma^{d/16} \equiv \pm 2^k \qquad \bmod F_3$$

where $k = 1, 3, 5, 7$. It is shown in Ref. 9 that if γ is a primitive element in $GF(q)$, where q is a prime, then γ^m is also a primitive element in $GF(q)$, where $m = 3, 5, \cdots, q-2$. It is well known (Ref. 5) that 3 is a primitive element in $GF(F_n)$. Thus 3^m is also a primitive element in $GF(F_n)$ for $m = 3, 5, \cdots 2^{2^n} - 1$.

Now the choice of $\gamma = 3^3$ gives

$$\gamma^{16} = (3^3)^{16} = (3^{16})^3 = (-2^3)^3 \equiv 2 \qquad \bmod F_3$$

since $3^{16} \equiv -2^3 \pmod{F_3}$ and $2^9 \equiv -2 \pmod{F_3}$. Hence, $\gamma^{f_0 t_1 \cdot 16}$ in (11) can take on only the values ± 1 or a power of 2.

Since multiplications by ± 1 involve only sign change and since multiplications involving powers of 2 mod F_3 can be achieved by circular shifts, the 16-point discrete Fourier transform in the brackets of (11) can be evaluated without multiplications. These results are then referenced by multiplying by the so-called twiddle factor $\gamma^{f_0 t_0}$. Using a similar argument, (12) can also be evaluated without multiplications.

The number of operations required to perform a FFT of 256 points using the radix 2, the radix 4, and the radix 16 FFT algorithms over $GF(F_n)$ is shown in Table 1. From this table, one can see that the radix 4 and the radix 16 FFT algorithms require 30% and 70% fewer multiplications, respectively, than the more usual radix 2 FFT algorithm.

In the above example, it was shown that one can find a power of 3 for γ such that

$$\gamma^{d/2^{n+1}} \equiv 2 \qquad \bmod F_n$$

For this γ, one has

$$\gamma^{d/2^{n+2}} = \pm\sqrt{2} \qquad \bmod F_n$$

From Ref. 5,

$$\sqrt{2} = 2^{2^{n-2}}(2^{2^{n-1}} - 1) \qquad \bmod F_n$$

Hence multiplications involving integral powers of $\gamma^{d/2^{n+2}}$ can be accomplished either by circular shifts or a circular shift followed by a subtraction, depending on whether an even or an odd power of $\sqrt{2}$ is involved. As a consequence, a high radix FFT up to 2^{n+2} also could be developed. For example, the 256-point FFT over $GF(F_3)$ could be computed using a mixed radix FFT of radix 32 and radix 8.

In light of the above discussion, when transforming long integer sequences in $GF(F_n)$, it is desirable to perform as many high-radix FFT iterations as possible to reduce the required multiplications.

Acknowledgment

The authors wish to thank Mr. B. Mulhall and Dr. B. Benjauthrit of JPL for supporting and encouraging the research that led to this paper.

References

1. Justesen, Jorn, "On the Complexity of Decoding Reed–Solomon Codes," *IEEE Trans. Inform. Th.*, Vol. IT-22, March 1976, pp. 237–238.

2. Reed, I. S., Truong, T. K., and Welch, L. R., "The Fast Decoding of Reed–Solomon Codes Using Number Theoretic Transforms," *The Deep Space Network Progress Report 42-35*, pp. 64–78, Jet Propulsion Laboratory, Pasadena, Calif., Oct. 15, 1976.

3. Reed, I. S., Truong, T. K., and Welch, L. R., "The Fast Decoding of Reed–Solomon Codes Using Fermat Theoretic Transforms and Continued Fractions" (this volume).

4. Rader, C. M., "Discrete Convolutions via Mersenne Transforms," *IEEE Trans. Comput.*, Vol. C-21, pp. 1269–1273, Dec. 1972.

5. Agarwal, R. C., and Burrus, C. S., "Fast Convolution Using Fermat Number Transforms with Applications to Digital Filtering," *IEEE Trans. on Acoustics, Speech, and Signal Processing*, Vol. Assp-22, No. 2, Apr., 1974, pp. 87–97.

6. Reed, I. S., and Solomon, G., "Polynomial Codes over Certain Finite Fields," *SIAM J. Appl. Math.*, Vol. 8, June 1960, pp. 300–304.

7. Odenwalder, J., et al., "Hybrid Coding Systems Study Final Report," Linkabit Corp., NASA CR 114,486, Sept. 1972.

8. Niven, I., and Zuckerman, H. S., *An Introduction to the Theory of Numbers*, New York, Wiley, 1966.

9. Reed, I. S., and Truong, T. K., "The Use of Finite Fields to Compute Convolutions," *IEEE Trans. Inform. Th.*, Vol. IT-21, No. 2, Mar. 1975, pp. 208–212.

10. Bergland, G. D., "A Fast Fourier Transform Algorithm Using Base 8 Iterations," *Math. Comput.*, Vol. 22, No. 102, Apr. 1968, pp. 275–279.

11. Singleton, R. C., "An Algorithm for Computing the Mixed Radix Fast Fourier Transform," *IEEE Trans. Audio Electroacoust.*, Vol AU-17, pp. 93–103, June 1969.

Table 1. Number of operations required to transform $d = 256$ points FFT over $GF(F_n)$, where $n = 3, 4$.

Algorithm	Mod F_n multiplications	Mod F_n additions	Circular shifts
Radix 2 ($d = 2^8$)	769	2048	0
Radix 4 [$d = (2^4)^2$]	513	2048	256
Radix 16 [$d = (2^4)^2$]	225	2048	544

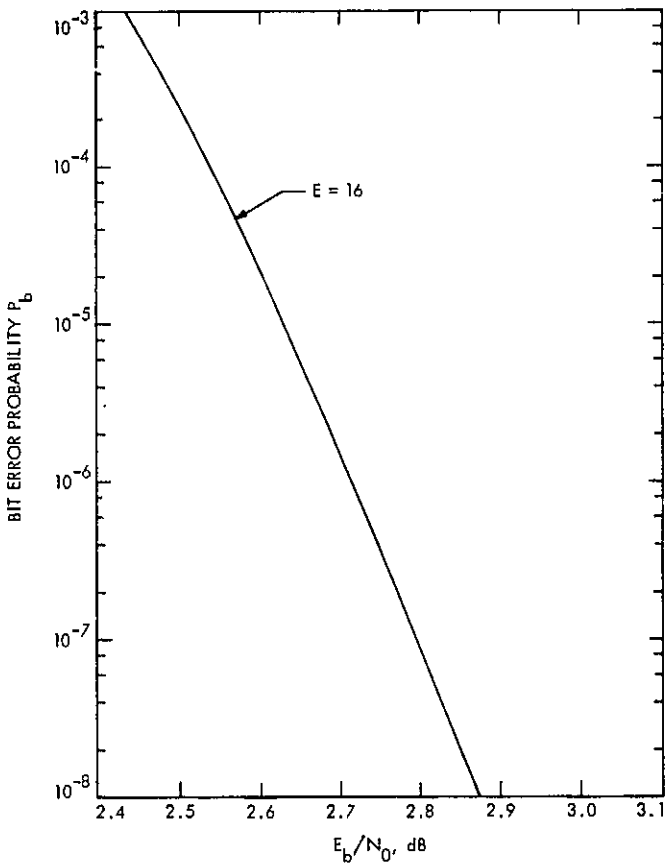

Fig. 1. Concatenated coding performance with a $K = 7$, $R = 1/2$ inner code and 8 bits/RS symbol

N77-14058

DSN Telemetry System Performance With Convolutionally Coded Data Using Operational Maximum-Likelihood Convolutional Decoders

B. Benjauthrit and B. D. L. Mulhall
TDA Engineering Office

B. D. Madsen
Telecommunications Systems Section

M. E. Alberda
DSN Data Systems Section

This article describes the DSN telemetry system performance with convolutionally coded data using the operational maximum-likelihood convolutional decoder (MCD) being implemented in the Network. The report covers data rates from 80 bps to 115.2 kbps and both S- and X-band receivers. The results of both one- and two-way radio losses are included.

I. Introduction

DSN telemetry system performance with convolutionally coded data at low data rates was presented in Ref. 1. In that article, real-time telemetry data obtained from the Compatibility Test Area (CTA 21) were processed by a simulated Viterbi decoding computer program to measure the system performance. The results covered the data rates ranging from 8 to 2048 bps, which will be useful in the design of telecommunication links for future spacecraft such as the Mariner Jupiter-Saturn (MJS), to be launched in 1977. Since such spacecraft will also employ higher data rates, the work described in this article covering data rates from 80 bps to 115.2 kbps was undertaken.

The article has a threefold purpose. The first is to give overall MCD acceptance test data received from the manufacturer. The second and third are to describe the test purposes, test setups, and test results from CTA 21 and from the Telecommunication Development Laboratory (TDL). The tests concentrate mainly on the Block IV receiver, high-data-rate, X-band carrier frequency with some S-band results to allow S- and X-band performance comparison. The effects of using different receiver bandwidths and subcarrier demodulator assembly (SDA) bandwidths are also investigated.

All 32 MCD production units were acceptance-tested, and their required performance was verified at the highest

data rate, 250 kbps, before delivery. They were also checked with the telemetry processing assembly (TPA) for proper interface prior to installation.

Since the actual operational software for the TPA was not ready when this project was underway, a special real-time computer program, called MCD Performance Evaluation Program (MCDPEP), was written in assembly language for collecting decoded data and formatting them into an appropriate compressed form on disc. The MCD status and symbol error information from the symbol synchronizer assembly (SSA) was also recorded. The recorded data were then processed by an off-line MCD Data Analysis Program (MDAP), also written in assembly language, to provide bit error rate (BER), symbol error rate (SER), burst error statistics, and MCD normalization rate (NR). The burst error statistics are expressed in terms of error-free runs (EFR) and burst length sample distributions.

The two-way radio losses of the DSN telemetry system were also examined for various values of carrier loop signal-to-noise ratio margin. These latter test results were obtained at TDL.

At present, only certain tests at data rates 44.8, 67.2 and 115.2 kbps are available from CTA 21. However, the test results from TDL cover a larger data range from 80 bps to 115.2 kbps. Additional tests will be accomplished in CTA 21 and in Spain, at DSS 62, by DSN Madrid Engineering. This will allow station-to-station comparison.

II. MCD Acceptance Test Data

Before delivery, each production MCD was verified to satisfy the functional requirements. The telemetry test data used were assumed corrupted by additive white Gaussian noise, and the tests performed at the highest allowable data rate, 250 kbps.

The acceptance tests consisted in part of BER performance, MCD symbol synchronization recovery interval, and channel error rate performance. These were accomplished for both code rates ½ and ⅓. Table 1 summarizes an average performance in terms of bit signal-to-noise ratio (ST_B/N_0), BER, and channel error rate. The table includes the corresponding standard deviation figures which are noticeably small. The functional requirements, lower and upper bounds, are also given in Table 1.

The verification of MCD symbol resynchronization recovery interval was done at ST_B/N_0 = 3 dB. For each MCD, ten observations were made for each code rate. This gives rise to 320 observations in all. The histogram plots of both code rates are depicted in Fig. 1. The figure indicates that the MCD time in symbols to resynchronization remains well below the functional requirements, i.e., 2000 symbols for rate ½ and 3000 symbols for rate ⅓.[1] The corresponding cumulative distribution plots of Fig. 1 are given in Fig. 2.

III. Performance Tests at CTA 21

The purpose of the test investigation at CTA 21 is to obtain telemetry system performance for medium to high data rates under the Mark III-1977 DSN telemetry system configuration. Emphasis is placed on the X-band Block IV receiver with corresponding results for the S-band, Block III receiver. Effects of receiver and SDA bandwidth are also examined. Another objective is to determine an optimum modulation index for each data rate.

The equipment used is a typical telemetry string (receiver, SDA, SSA, MCD, and TPA), along with symbols provided by the SCA via a radio frequency link. The SCA provides a cyclical repetitive 2047-bit pseudo random noise (PN) sequence encoded by a 7; ½ (or ⅓) convolutional encoder (with alternate symbols inverted) at the desired symbol rate and modulation index value. The MCD receives the noisy quantized (5-bit parallel) symbols from the SSA, performs its decoding function, and outputs decoded data to the TPA. The SSA, after proper initialization from the TPA via commands transmitted by the 920 emulator, periodically (once every 10^6 symbols) outputs symbol error count (SEC) to the TPA via the SSA/TPA coupler. Thus, MCD decoding performance is obtained from output SSA SER and output MCD BER.

The MCDPEP (resident in the TPA) stores and evaluates all MCD output data in real-time. Data are received in 8-bit bytes and sequentially stored in two alternate memory blocks (200 16-bit words/block), using the external direct memory processor (DMP) in the data chaining mode. Data are processed from one block while the other block is being accumulated. Data processing starts by searching the stored data to find frame synchronization within the known 2047-bit PN sequence, consisting of 11 consecutive 1's. Normal data, and inverted data if necessary, are searched. After finding frame sync, every stored data bit is compared with the corresponding known

[1]This assumes a nominal bit transition density (1/40 - 1/2 at 3 dB and greater). For low bit transition densities, the result may not be valid; see Ref. 2.

PN bit, being done 8 bits (one byte) at a time. Every byte containing one or more erroneous bits is stored in an output error list (OEL), and periodically transferred from core to disc in 50-word blocks, 32 bits/word.

The exclusive-OR byte pattern is stored, with 1's indicating error bits and 0's indicating correct bits. The corresponding good byte count (GBC) is also stored in the same entry, providing the number of consecutive correct bytes since the last previous error byte.

The 32-bit word format used for each OEL entry is shown below.

GBC (16 bits)	XOR (8 bits)	NR (7 bits)	1 bit
Good Byte Count	Byte Error Pattern	MCD Average NR	MCD Sync Change

An entry is made in the OEL whenever one of the following events occurs:

(1) GBC Full Count. An entry is made any time this counter reaches full-scale value, which is 8×2^{16} or 524,288 consecutive correct bits.

(2) MCD BER. Once every DMP block (or 3200 bits) the MCD is commanded to output its 4-bit NR word. This number is derived from the MCD internal normalization rate. It is related to the input SER and consequently the output BER. These NR outputs are stored and averaged (over 31 outputs), and the average value is entered in the OEL in the 7 bits provided (4-bit whole number plus 3-bit fractional number) once every 99,200 data bits. For these NR entries, the GBC value is shown as 0, although the actual value is retained and continues to be accumulated.

(3) MCD Node Sync Change. When a node sync change occurs, the MCD outputs its own status and an entry is made in the OEL, with the least significant bit equal to 1. If the MCD had previously achieved symbol sync, and then a sync change occurs; this means that the MCD output data are temporarily not valid and the program reverts to its frame sync search mode. When frame sync is again found, this implies that the MCD has regained symbol sync and the output data are again valid.

The MCD generates a node sync change when its input symbols are uncorrelated. To resync, the MCD attempts to find an acceptable level of symbol correlation by regrouping the incoming symbols.

The OEL continues to accumulate and is stored on disc for the test duration, nominally 10^7 bits. At the same time, another list is output on the Terminet printer containing every other average NR value, or once every 198,400 bits. When this list has reached the desired length, the test is manually terminated by actuating a switch on the TPA console, after which the stored SEC list is printed on the Terminet, with one entry every 10^6 symbols (or any other power-of-ten number of symbols available).

MDAP is an off-line program for use to complete the MCD data analysis phase. The program converts the OEL entries produced and recorded on disc by MCDPEP into a sequence of EFR's, classifies them, and generates their sample distributions. It also generates average BER and average NR at every 99,200 decoded bits. At the end of each run, the following are printed:

Total number of decoded bits

Total number of bit errors

Average bit error rate

Total number of EFRs

Total number of bit bursts

Total number of normalization rates

Average bit errors per burst

Average burst length in bits

EFR sample distribution

Number of distinct EFRs

Burst length sample distribution

Number of distinct burst lengths

Symbol error rate

When a sync change bit is detected, MDAP outputs the entire data statistics, reinitializes program parameters, and restarts to process the remaining data again.

Figure 3 gives an overall view of the test configuration. (A more detailed configuration is given in Fig. 7 which will be discussed later). The ST_B/N_0 used in describing the system performance is obtained from the average SER accumulated for each run via an uncoded performance

curve. The MCD error rate calibration curve (MCD input ST_B/N_0 in dB vs MCD normalization rate indication) for each rate is also obtained from the program printout, as shown in Fig. 4.

A. Optimization of Modulation Index

The signal energy per bit (which determines the bit error probability of a telemetry channel) of any modulation system is related to the total received power P_T as follows:

$$\frac{ST_B}{N_0} = \frac{P_T}{N_0}\frac{P_D}{P_T}T_B\,\eta_{WDL}\,\eta_S \tag{1}$$

where

P_D = sideband power available for data

N_0 = single-sided noise spectral density, W/Hz

T_B = bit time in seconds

η_{WDL} = subcarrier waveform distortion loss

η_S = system efficiency

= $\eta_{RL} + \eta_{SDL} + \eta_{BSDL}$, dB, where

η_{RL} = radio loss, dB

η_{SDL} = subcarrier demodulation loss, dB

η_{BSDL} = bit sync and detection loss, dB

One way to optimize the performance of the telemetry system is to maximize the data rate. To achieve this, the values of P_T/N_0 and ST_B/N_0 must be specified. Then the parameters P_D/P_T and η_S are adjusted to obtain the maximum data rate. Another way is to specify the values of the data rate, ST_B/N_0, and adjust the parameters P_D/P_T and η_S to minimize the required P_T/N_0.

The easiest parameter to adjust in the telemetry system is the modulation index. This parameter determines the allocation of power in the various sidebands and strongly affects the magnitude of the system losses.

For a single channel, a square-wave subcarrier, P_D/P_T, is $\sin^2\theta$, where θ denotes the system modulation index. Since η_{WDL} is usually small ($\eta_{WDL} \simeq 0$ dB), Eq. (1) may be rewritten as

$$\frac{ST_B}{N_0} = \frac{P_T}{N_0}\frac{\eta_S}{BPS}\sin^2\theta,\ BPS = 1/T_B \tag{2}$$

If the values of P_T/N_0, η_S, and BPS are known, the plot of ST_B/N_0 vs θ can be obtained from Eq. (2). Such plots for various values of P_T/N_0 from 51.45 to 54.58 dB are given in Fig. 5. They are for 10- and 30-Hz Block IV receiver and wide bandwidth Block III SDA. From these curves, one can determine the optimum modulation index for each P_T/N_0. To derive this value algebraically, one first expresses Eq. (2) as

$$BPS = \frac{\dfrac{P_T}{N_0}\,\eta_S}{\dfrac{ST_B}{N_0}}\sin^2\theta$$

The maximum data rate, BPS_{max}, can now be computed by setting the derivative of BPS with respect to θ equal to zero, yielding

$$\theta_{opt} = \tan^{-1}\left\{\frac{-2\,\eta_S}{\dfrac{d\eta_S}{d\theta}}\right\}_{\theta=\theta_{opt}}$$

This indicates that the optimum modulation index for a single-channel system is totally dependent on the proper characterization of the system losses.

B. Test Strategies and Preliminary Results

The end product of the project is to obtain DSN telemetry system performance using convolutionally coded data in terms of bit error probability *(BER)* vs ST_B/N_0 and the corresponding burst characteristics. Toward this end, we first proceed to determine the optimum modulation index. This is to be used to corroborate the theoretical value of the true optimum modulation index. Once this parameter is determined, the telemetry system performance for it is then obtained.

The results obtained so far have been for data rates 44.8, 67.2, 96.8, and 115.2 kbps. Figure 6 describes the telemetry system performance at data rate 67.2 kbps. The test conditions are given in Table 2. The true optimum modulation index for this rate appears in Fig. 6(a) to be about 80 deg, which is in agreement with the theoretical value. The curves *BER* vs ST_B/N_0 corresponding to modulation indices 79 and 80 deg are given in Fig. 6(b). The sample distribution plots of the burst lengths are given in Fig. 6(c)–(f). The average burst length vs modulation index and the average burst error vs modulation index are given in Fig. 6(g). The average burst length and average burst error vs ST_B/N_0 are given in Fig. 6(h). And finally, the MCD error rate calibration for this data is depicted in Fig. 4.

IV. Performance Tests at TDL

One purpose of the tests conducted at TDL is to measure system two-way radio losses using an operational MCD over various data rates for both S- and X-band receiver. Another purpose is to obtain telemetry system performance in terms of BER vs ST_B/N_0.

Equipment used for the tests includes the Block III exciter, Mariner Venus/Mercury transponder, X-band transmitter, Block III receiver (S-band), Block IV receiver (S- and X-band), Block III SDA, Block III SSA, and a production model MCD. Test data patterns include 31-bit, 127-bit, and 2047-bit PN codes. The detailed test equipment setup is shown in Fig. 7.

Figure 8 describes system two-way radio loss curves derived from measurements taken in TDL during January 1976, for code rate 7:½, 3 bit quantization. The figure provides BER vs ST_B/N_0 for various values of the uplink margin, $M_C = P_C/N_0\ 2B_{L0}$, where P_C is the carrier power and B_{L0} is the single-sided design point phase-lock-loop bandwidth. This parameter is selectable for each test from the dial at the receiver panel. Here the theoretically optimum downlink modulation indices, discussed in Section III, were used for all tests. This means that the ground receiver loop SNR was not held constant but was allowed to vary with signal level as it will be in an operational situation. These results are not exactly the same as will be obtained with the MJS'77 transponder, due to differences in receiver loop parameters, but are close enough to provide a basis for prediction of the MJS'77 losses.

The most obvious conclusion to be drawn from the data is that the X-band two-way radio losses are so great that they will impose operational limitations on the MJS'77 mission. In order to limit the loss to about 1 dB, the uplink carrier margin must be 35 dB or greater. This is equivalent to an uplink carrier power of −120 dBm, which is just about what can be achieved at Saturn, range = 10 AU, with a 100-kW, 64-m DSS. Operation at greater distances or with a 26-m DSS will require noncoherent operation of the X-band downlink.

The operational thresholds are also shown in Fig. 8. Further, the X-band telemetry threshold as a function of uplink margin is described in Fig. 9.

The difference between the X-band and S-band performance is believed due entirely to the greater turnaround phase jitter on the X-band signal due to the VCO phase noise being multiplied by a greater ratio (11/3 times). The magnitude of the problem can be reduced by increasing the frequency of the uplink signal (thus reducing the multiplication ratio) or by using a feed-forward technique for removing most of the phase jitter from the downlink. Using a feed-forward system has been demonstrated in the laboratory and resulted in almost no two-way degradation at uplink margins as low as 5 dB.

It is strongly recommended that both of the above solutions be investigated. It is probably too late to do anything about MJS, but the standard transponder should certainly include the feed-forward features.

The TDL MCD error rate calibration curve was previously given in Fig. 4. The telemetry performance curves in terms of BER vs ST_B/N_0 for rates 7.2 and 115.2 kbps are given in Fig. 10. The performance of code rates 1/2 and 1/3 at data rates 115.2 and 76.8 kbps, respectively, is given in Fig. 11. For BER's of 10^{-3} to 10^{-4}, the rate 1/3 code is 0.3 dB better. For a BER of 10^{-5}, the improvement is 0.25 dB.

V. Telemetry Performance for Radio Frequency Subsystem

Telemetry performance for the Radio Frequency Subsystem (RFS) using both the TDL telemetry simulator and the Mark III Data System (MDS) as sources is listed in Table 3 and plotted in Fig. 12. Telemetry performance is similar to that obtained previously during developmental tests and no anomalies were found.

The high rate (115.2 kbps) two-way telemetry loss at X-band was found to be slightly worse than that measured on the MVM'73 RFS. This was expected since the MJS'77 RFS has a wider bandwidth. The measured losses for both transponders are shown in Fig. 13. The effective telemetry loss at a threshold BER of (5.0×10^{-3}) as a function of uplink carrier margin is shown in Fig. 14. This shows that an uplink carrier margin must be at least 35 dB whenever high-rate X-band telemetry is being transmitted in the two-way coherent mode. With the present DSN capability, this characteristic precludes use of the two-way coherent mode with high-rate telemetry for ranges greater than 10.0 AU for a 100-kW, 64-m station or 2.0 AU for a 20-kW, 26-m station.

References

1. Benjauthrit, B., "Final Report on DSN Telemetry System Performance with Convolutionally Coded Data: Maximum Likelihood Decoding," in *The Deep Space Network Progress Report 42-33*, pp. 112–122, Jet Propulsion Laboratory, Pasadena, Calif., June 15, 1976.

2. Burow, N. A., "Acquisition of Node Synchronization by a Viterbi Decoder," Interoffice Memorandum 3397-76-15, September 8, 1976. Jet Propulsion Laboratory, Pasadena, Calif., Sept. 8, 1976 (an internal document).

Table 1. JPL MCD acceptance test data (averaged over 32 units)

Code rate		ST_B/N_o	No. bits	Bit error rate		Upper bound	Channel mean	Error rate std. dev.	Lower bound	Upper bound
				Mean	Std. dev.					
MCD-TPA	1/2	3.0	4.096×10^6	7.41×10^{-4}	1.82×10^{-6}	9.0×10^{-4}	11.5	0.51	10	13
		4.0	4.096×10^7	3.95×10^{-5}	6.24×10^{-8}	6.0×10^{-5}	7.9	0.62	7	9
		5.0	6.553×10^7	1.36×10^{-5}	7.95×10^{-9}	2.5×10^{-6}	5.0	0.33	4	6
	1/3	3.0	4.096×10^6	2.90×10^{-4}	2.47×10^{-6}	3.6×10^{-4}	11.1	0.45	10	12
		3.5	4.096×10^7	6.92×10^{-5}	2.77×10^{-8}	1.0×10^{-4}	9.7	0.44	9	11
		4.5	4.096×10^6	2.83×10^{-6}	5.11×10^{-7}	7.0×10^{-6}	7.1	0.24	6	8
MCD-DDA	1/3	3.0	4.096×10^6	2.88×10^{-4}	2.41×10^{-6}	3.6×10^{-4}	—	—	—	—

Table 2. Test conditions and results for 67.2-kbps, Block IV receiver, S-band

Test ID	Total bits ($\times 10^7$)	Mod index, deg	RVC IV BW, Hz	SDA III BW, Hz	AVE BER	AVE SER, %	MCD input ST_B/N_o, dB	AVE MCD NR
DA1	1.51	77	30	Medium	1.24×10^{-4}	5.97	3.85	7.75
2	1.42	78			1.48×10^{-4}	6.07	3.80	8.00
3	1.21	80			1.12×10^{-4}	5.60	4.03	7.75
4	1.38	79			1.25×10^{-4}	6.05	4.81	8.13
5	1.81	79			1.55×10^{-4}	5.96	3.85	7.88
6	1.41	79			8.00×10^{-5}	5.96	3.85	7.50
7	1.08	79			2.70×10^{-7}	3.02	5.48	3.13
8	1.10	79			0	1.46	6.77	1.13
DB1	1.35	77		Narrow	1.31×10^{-4}	5.99	3.84	7.50
2	1.30	78			1.10×10^{-4}	6.03	3.82	7.75
3	1.35	80			6.56×10^{-5}	5.46	4.09	7.25
4	1.33	79			1.39×10^{-4}	6.25	3.72	8.25
5	1.58	79			6.55×10^{-5}	5.76	3.95	7.38
6	1.06	79			1.00×10^{-4}	5.91	3.88	7.75
7	1.00	79			8.10×10^{-7}	2.97	5.51	3.13
8	1.57	79			0	1.44	6.80	1.00
DC1	1.24	77	10	Medium	1.35×10^{-4}	6.42	3.64	8.38
2	1.30	78			1.59×10^{-4}	6.41	3.65	8.38
3	1.37	79			1.53×10^{-4}	6.41	3.65	8.63
4	1.47	80			1.82×10^{-4}	6.42	3.64	9.00
5	1.58	80			4.98×10^{-5}	5.75	3.95	7.13
6	1.04	80			6.48×10^{-5}	5.84	3.91	8.00
7	1.05	80			2.70×10^{-7}	2.95	5.52	3.13
8	1.30	80			0	1.32	6.93	1.00
DD1	1.30	77		Narrow	7.57×10^{-5}	6.20	3.74	8.00
2	1.27	78			1.13×10^{-4}	5.89	3.89	7.00
3	1.33	79			8.72×10^{-5}	5.74	3.96	7.75
4	1.31	80			1.32×10^{-4}	6.03	3.82	8.25
5	1.54	80			6.44×10^{-5}	5.74	3.96	7.75
6	1.12	80			9.82×10^{-5}	5.92	3.87	7.88
7	1.15	80			0	2.97	5.51	3.13
8	1.10	80			0	1.35	6.90	1.00

Table 3. Measured telemetry performance

Band/test	M.I., deg	Bit rate, kbps	ST_n/N_o, dB	BER	Loop SNR, dB
X1	80.0	115.2	3.84	4.7×10^{-4}	15.4
X2	80.0	115.2	2.84	5.0×10^{-3}	14.4
X3	80.0	115.2	5.20	2.1×10^{-5}	15.2
X4	80.0	44.8	4.84	1.8×10^{-5}	13.1
X5[a]	79.5	115.2	3.08	2.0×10^{-3}	15.2
X6[a]	79.5	44.8	3.13	1.1×10^{-3}	12.1
X7[a]	79.5	29.9	3.09	1.5×10^{-3}	11.6
X8[a]	79.5	21.6	3.00	2.0×10^{-3}	10.6
X9[a]	72.0	7.2	3.06	1.4×10^{-3}	9.9
X10[a]	72.5	2.56	3.42	2.2×10^{-3}	8.5
X11[a]	65.0	1.20	2.78	3.5×10^{-3}	8.5
S1	45.8	2.56	3.07	1.1×10^{-3}	16.9

[a]These tests performed with MDS/RFS combined; others performed using TLM simulator for source.

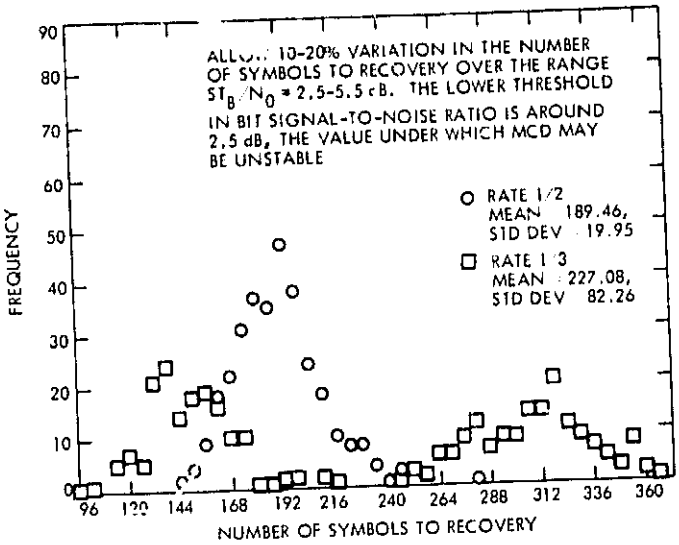

Fig. 1. Sample distribution plots of MCD symbol synchronization recovery for both code rates 1/2 and 1/3, ST_B/N_0 = 3 dB, 250 kbps

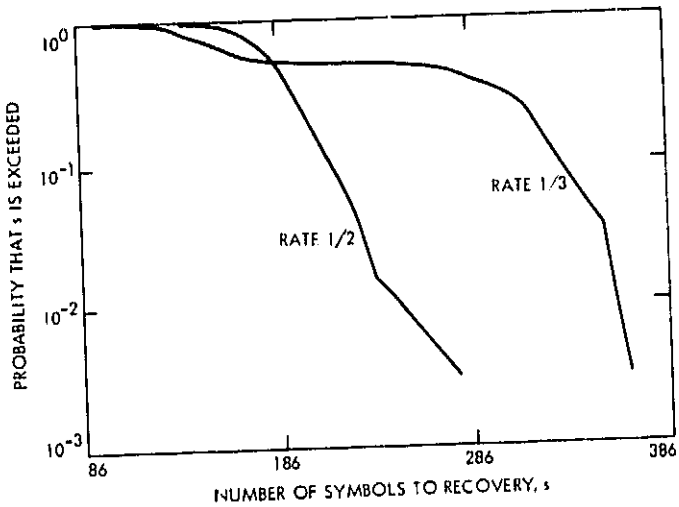

Fig. 2. Number of symbols to recovery S vs probability that S is exceeded for MCD symbol synchronization recovery of code rates 1/2 and 1/3

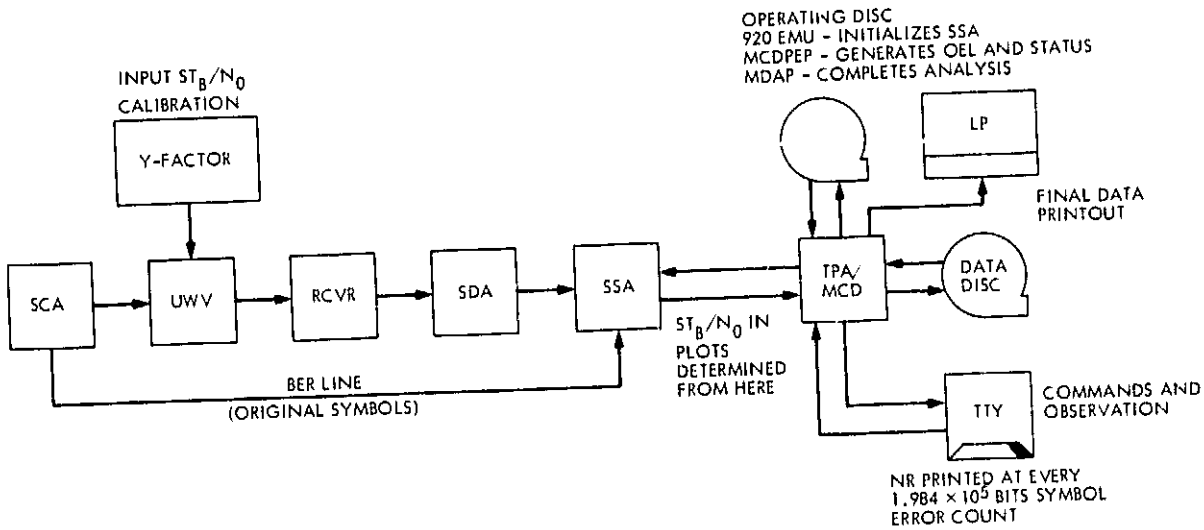

Fig. 3. MJS telemetry system test configuration at CTA 21

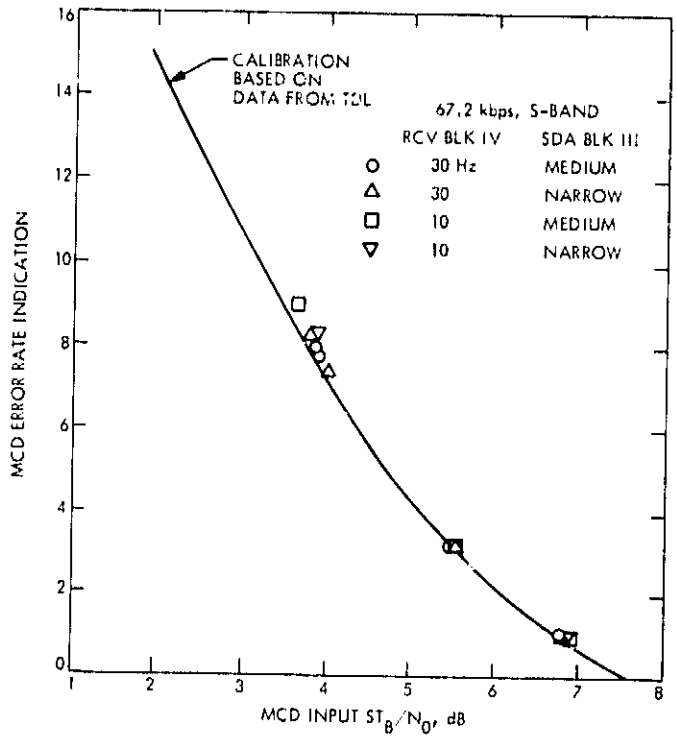

Fig. 4. MCD error rate calibration

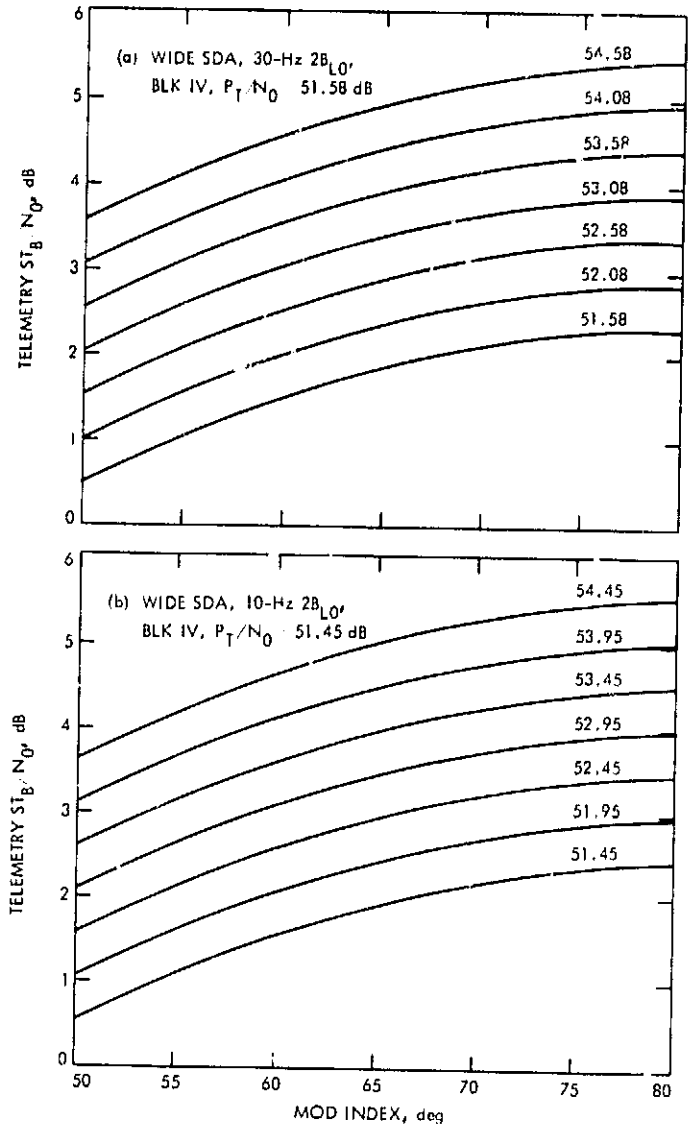

Fig. 5. ST_B/N_0 vs mod index at 67.2 kbps

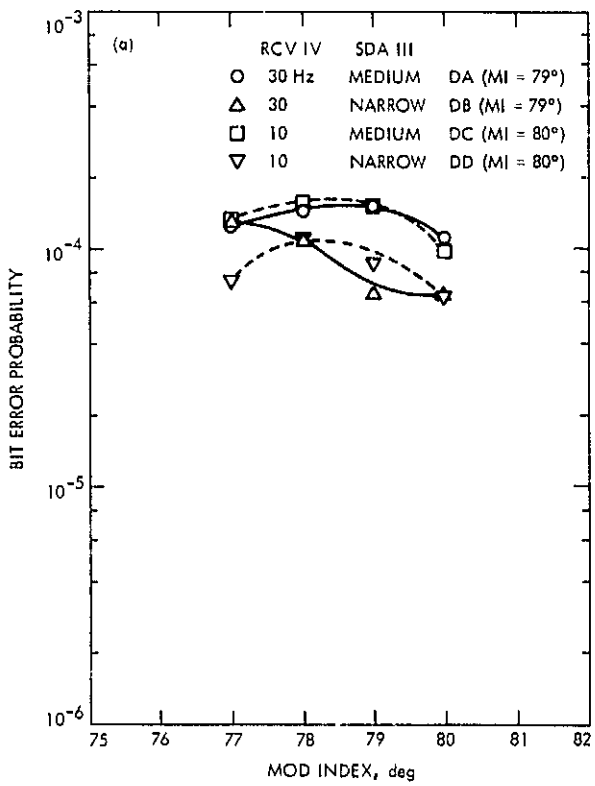

Fig. 6. Telemetry system performance at 67.2 kbps

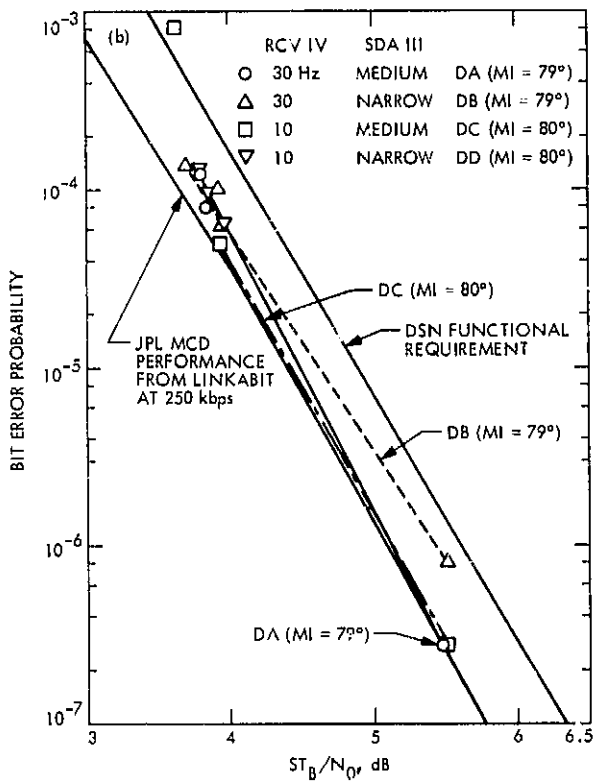

Fig. 6 (contd)

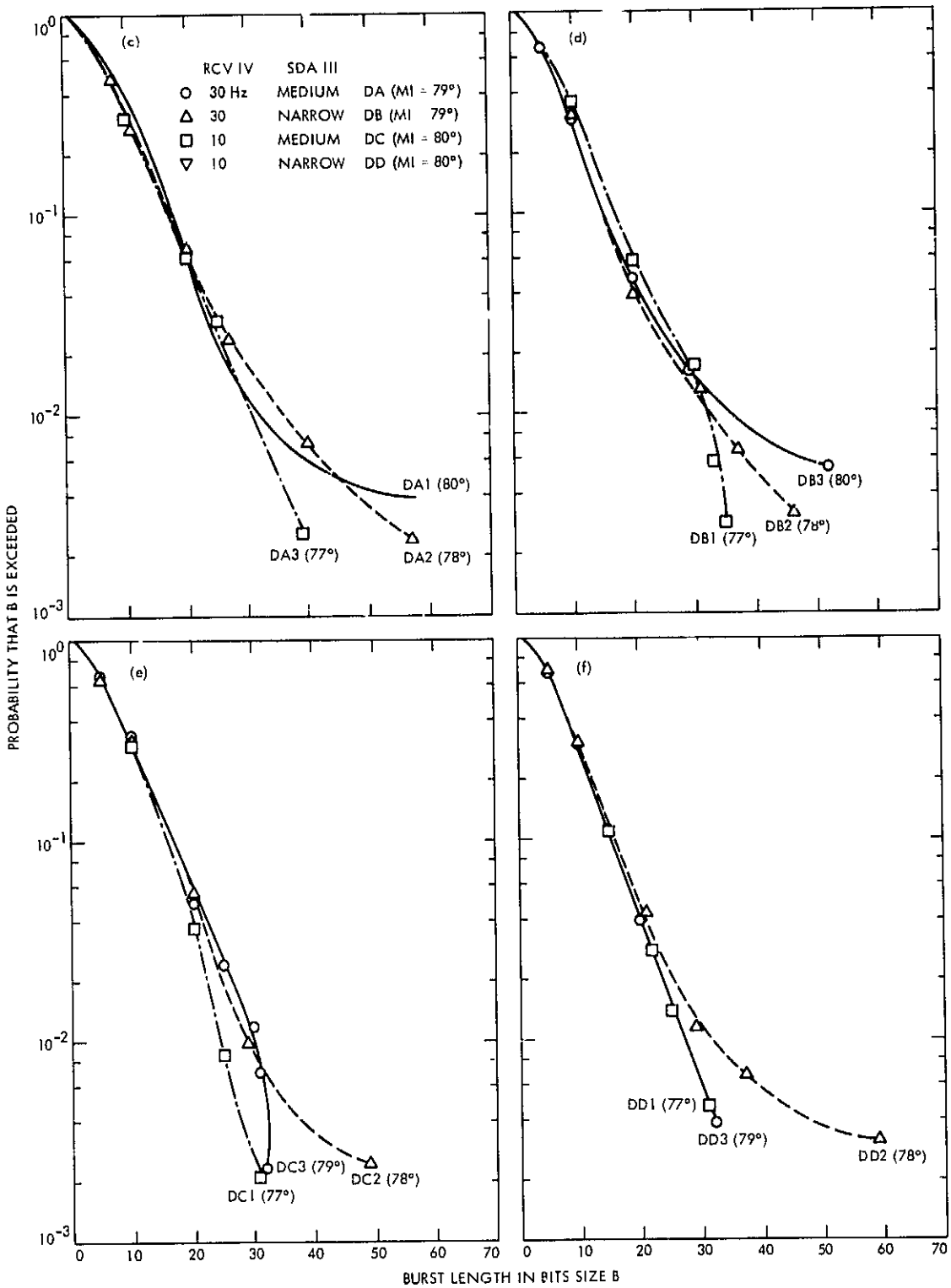
(c)
RCV IV SDA III
30 Hz MEDIUM DA (MI = 79°)
30 NARROW DB (MI 79°)
10 MEDIUM DC (MI = 80°)
10 NARROW DD (MI = 80°)
DA1 (80°)
DA3 (77°)
DA2 (78°)
(d)
DB3 (80°)
DB1 (77°)
DB2 (78°)
(e)
DC3 (79°)
DC2 (78°)
DC1 (77°)
(f)
DD1 (77°)
DD3 (79°)
DD2 (78°)
PROBABILITY THAT B IS EXCEEDED
BURST LENGTH IN BITS SIZE B

Fig. 6 (contd)

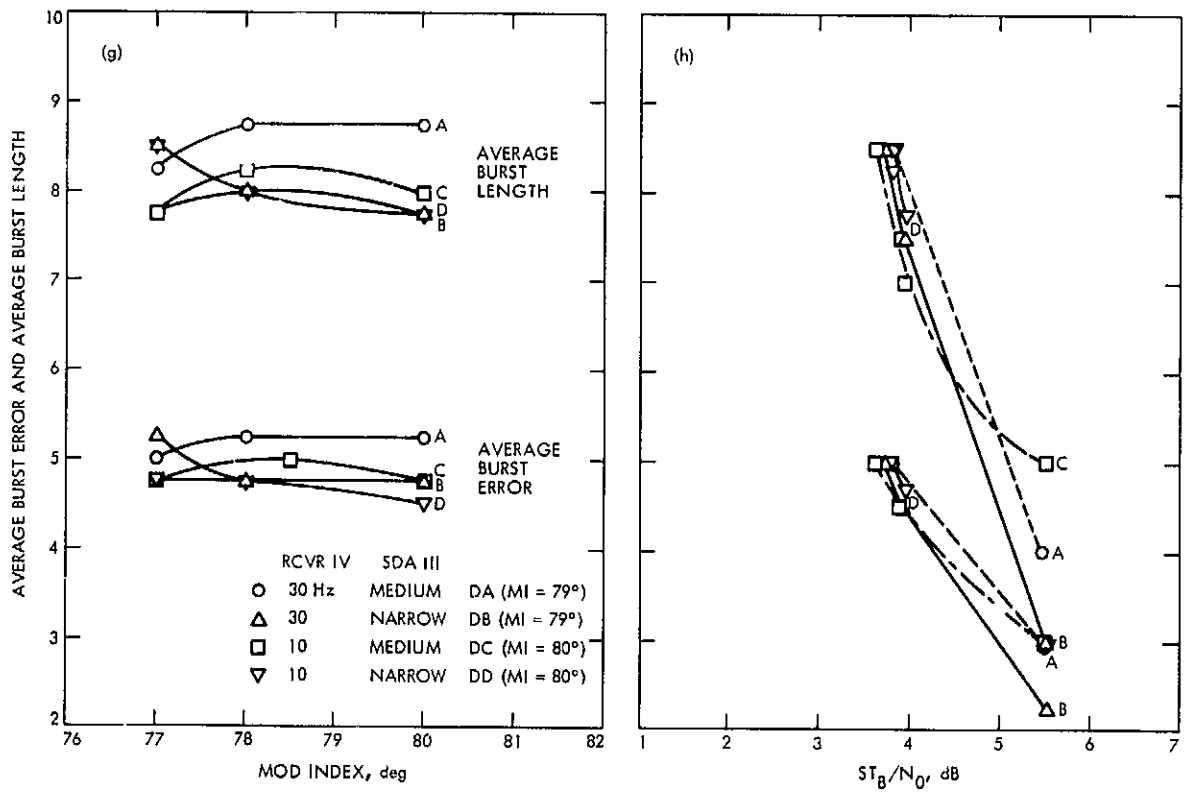
(g)
(h)
AVERAGE BURST ERROR AND AVERAGE BURST LENGTH
AVERAGE BURST LENGTH
AVERAGE BURST ERROR
RCVR IV SDA III
30 Hz MEDIUM DA (MI = 79°)
30 NARROW DB (MI = 79°)
10 MEDIUM DC (MI = 80°)
10 NARROW DD (MI = 80°)
MOD INDEX, deg
ST_B/N_0, dB

Fig. 6 (contd)

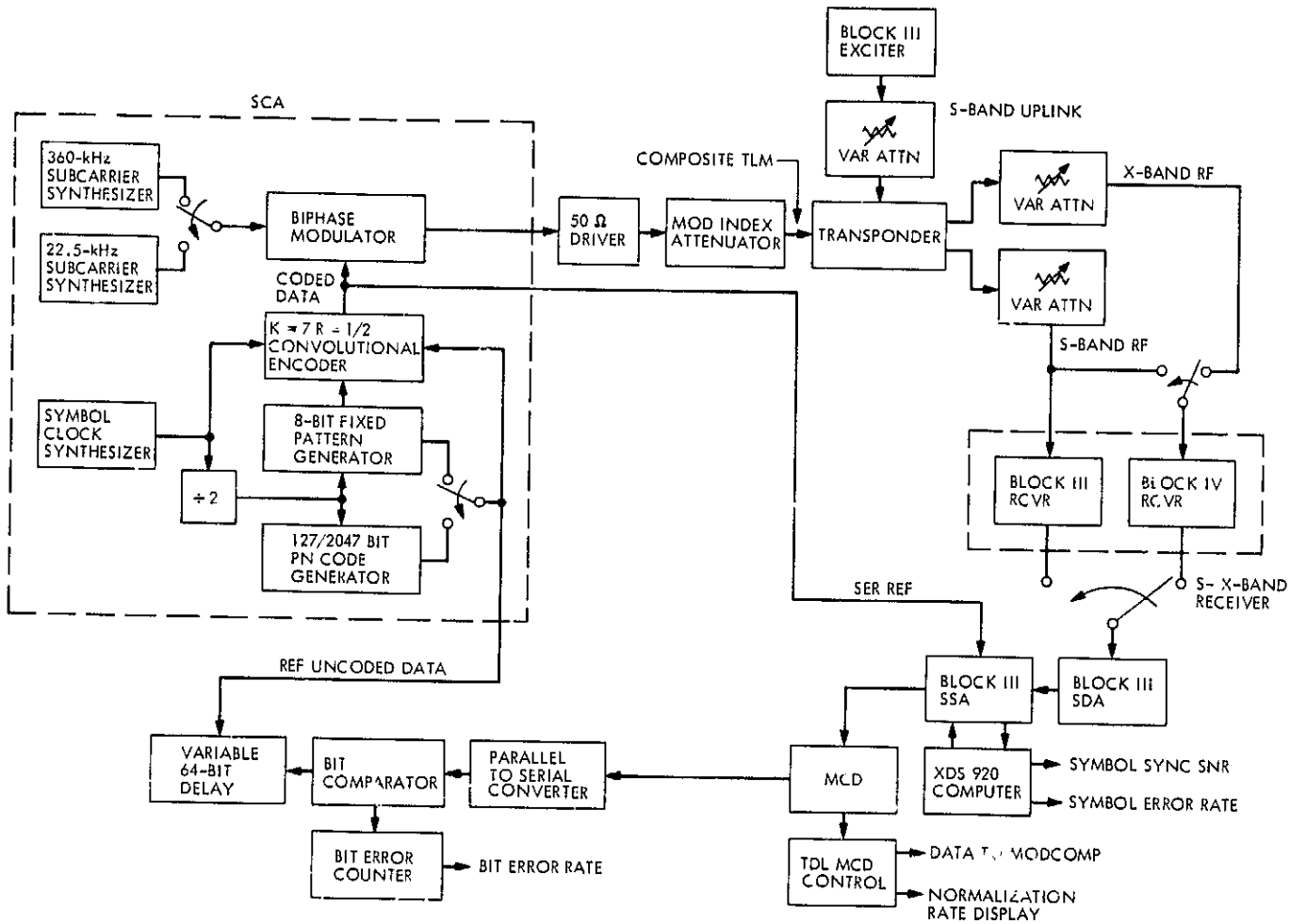

Fig. 7. MJS telemetry system configuration at TDL

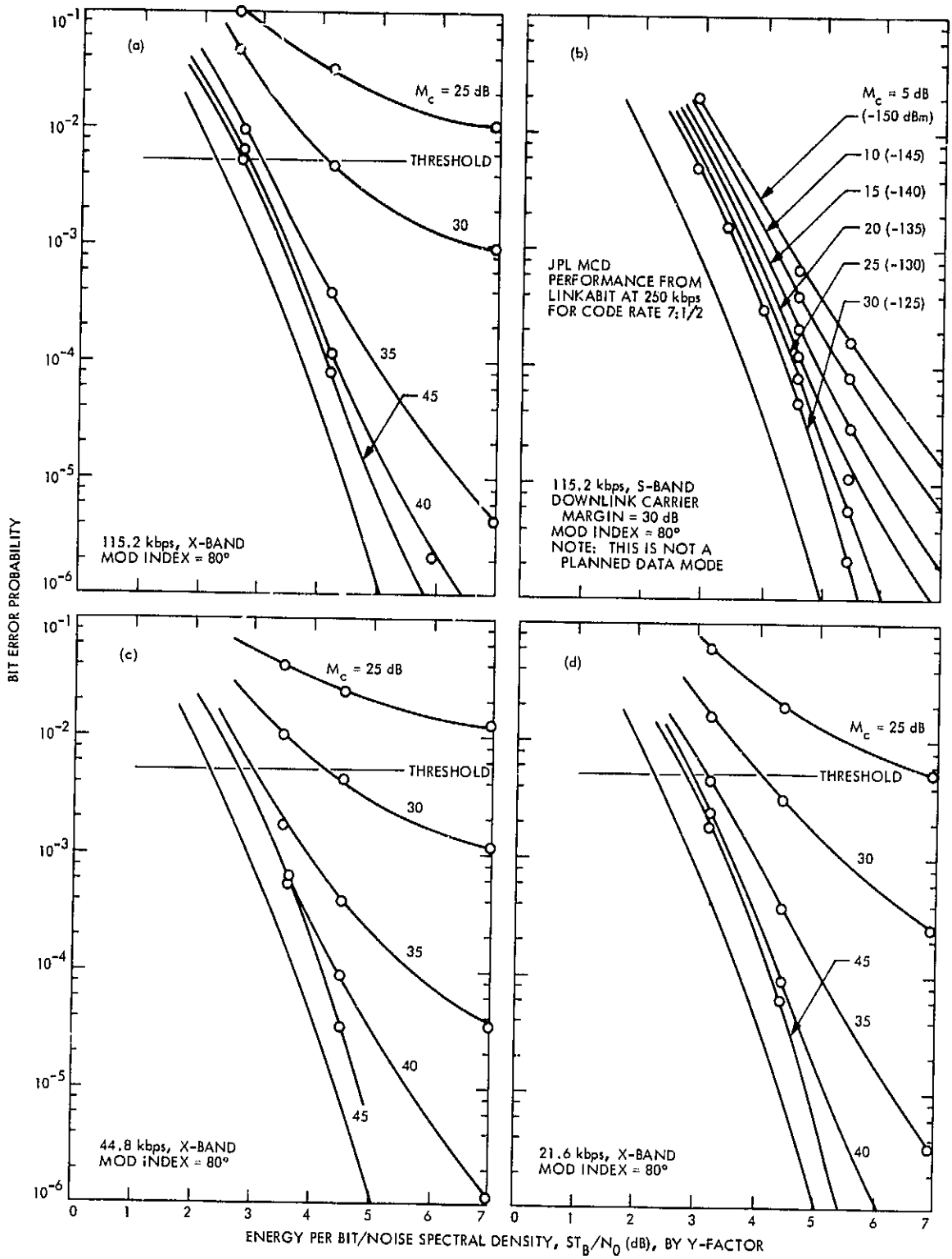

Fig. 8. X- and S-band two-way radio losses with various uplink carrier margins for data rates from 80 bps to 115.2 kbps, Block IV, 30 Hz

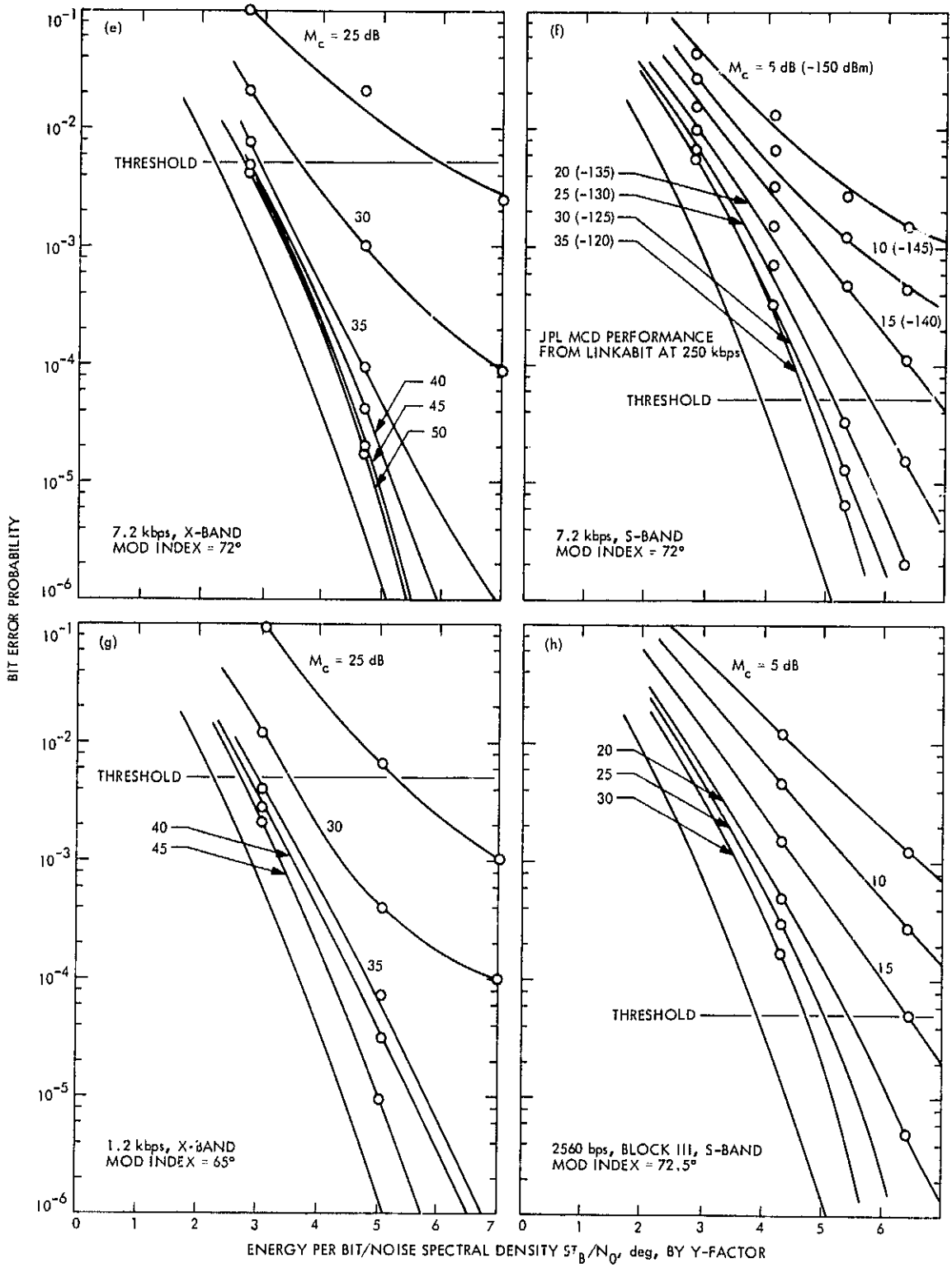
(e)
M_c = 25 dB
THRESHOLD
30
35
40
45
50
7.2 kbps, X-BAND
MOD INDEX = 72°
(f)
M_c = 5 dB (-150 dBm)
20 (-135)
25 (-130)
30 (-125)
35 (-120)
10 (-145)
15 (-140)
JPL MCD PERFORMANCE
FROM LINKABIT AT 250 kbps
THRESHOLD
7.2 kbps, S-BAND
MOD INDEX = 72°
(g)
M_c = 25 dB
THRESHOLD
40
45
30
35
1.2 kbps, X-BAND
MOD INDEX = 65°
(h)
M_c = 5 dB
20
25
30
10
15
THRESHOLD
2560 bps, BLOCK III, S-BAND
MOD INDEX = 72.5°
BIT ERROR PROBABILITY
10^{-1}
10^{-2}
10^{-3}
10^{-4}
10^{-5}
10^{-6}
0 1 2 3 4 5 6 7
ENERGY PER BIT/NOISE SPECTRAL DENSITY ST_B/N_0, deg, BY Y-FACTOR

Fig. 8 (contd)

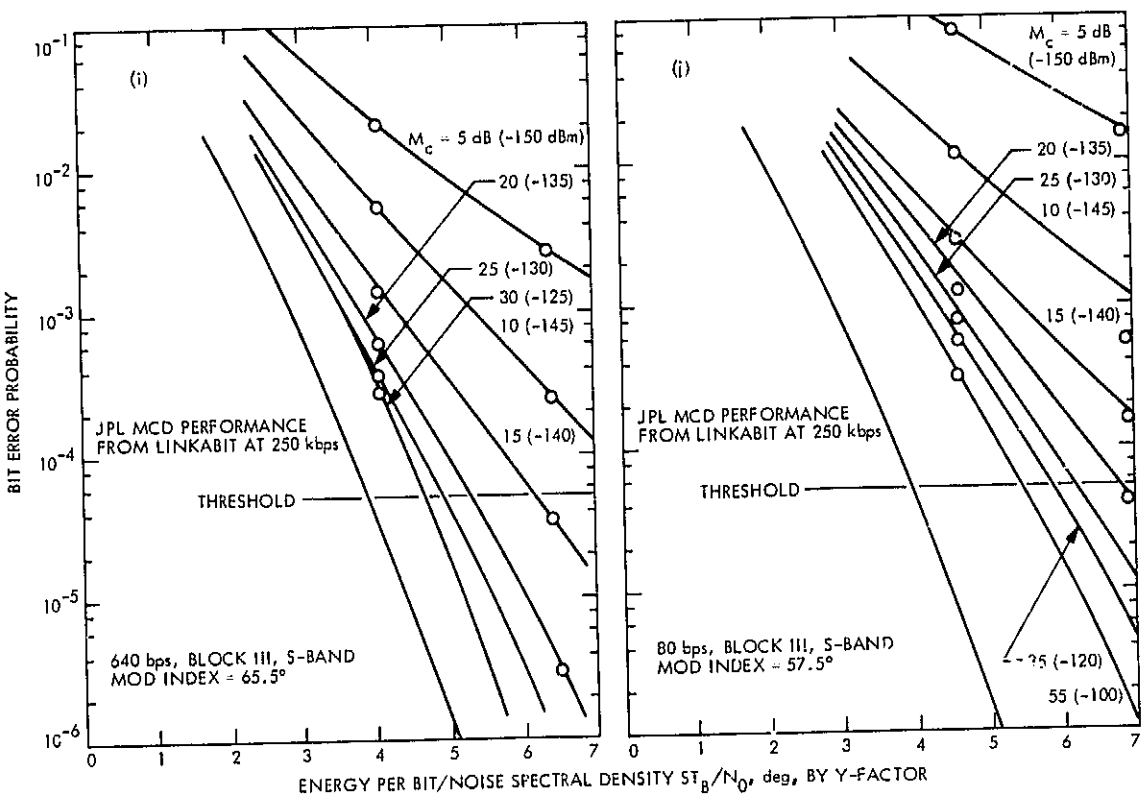
(i)
M_c = 5 dB (-150 dBm)
20 (-135)
25 (-130)
30 (-125)
10 (-145)
15 (-140)
THRESHOLD
JPL MCD PERFORMANCE
FROM LINKABIT AT 250 kbps
640 bps, BLOCK III, S-BAND
MOD INDEX = 65.5°
(i)
M_c = 5 dB
(-150 dBm)
20 (-135)
25 (-130)
10 (-145)
15 (-140)
THRESHOLD
JPL MCD PERFORMANCE
FROM LINKABIT AT 250 kbps
80 bps, BLOCK III, S-BAND
MOD INDEX = 57.5°
55 (-100)
BIT ERROR PROBABILITY
ENERGY PER BIT/NOISE SPECTRAL DENSITY ST_B/N_0, deg, BY Y-FACTOR

Fig. 8 (contd)

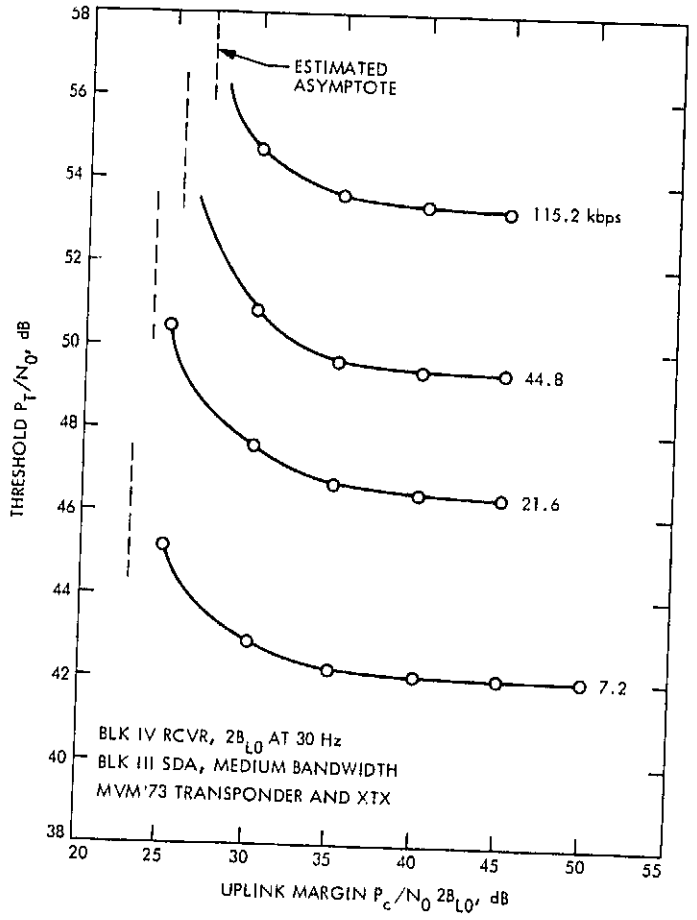

Fig. 9. X-band telemetry threshhold as a function of uplink margin

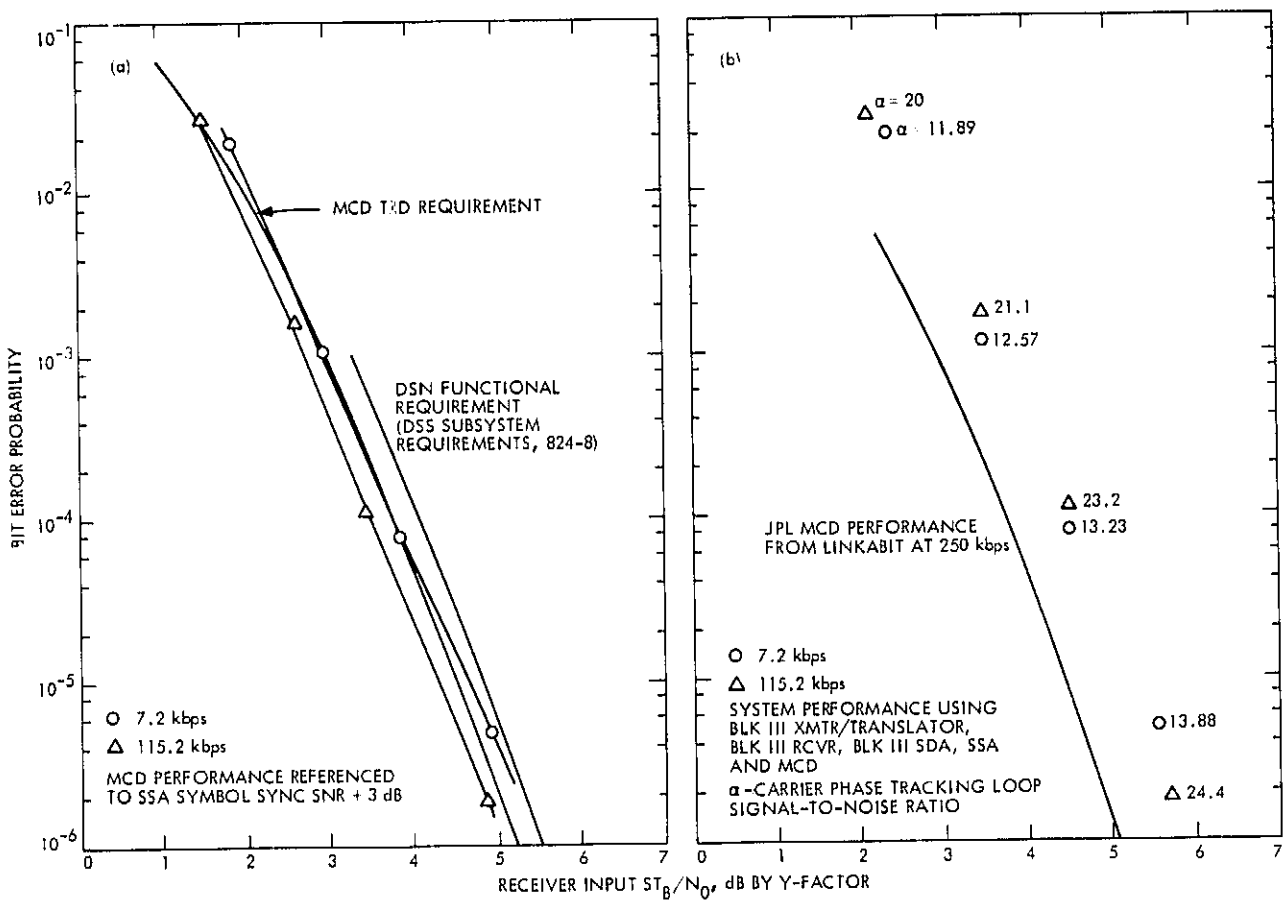

Fig. 10. Bit error probability vs ST_B/N_0 at 7.2 and 115.2 kbps

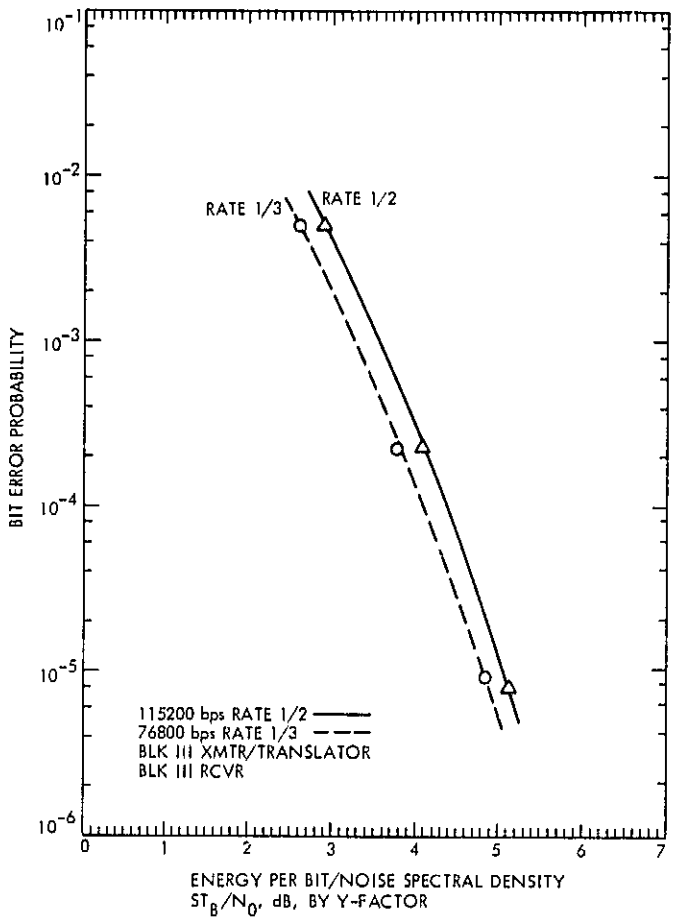

Fig. 11. Bit error probability vs ST_B/N_0 for code rate 1/2 and 1/3

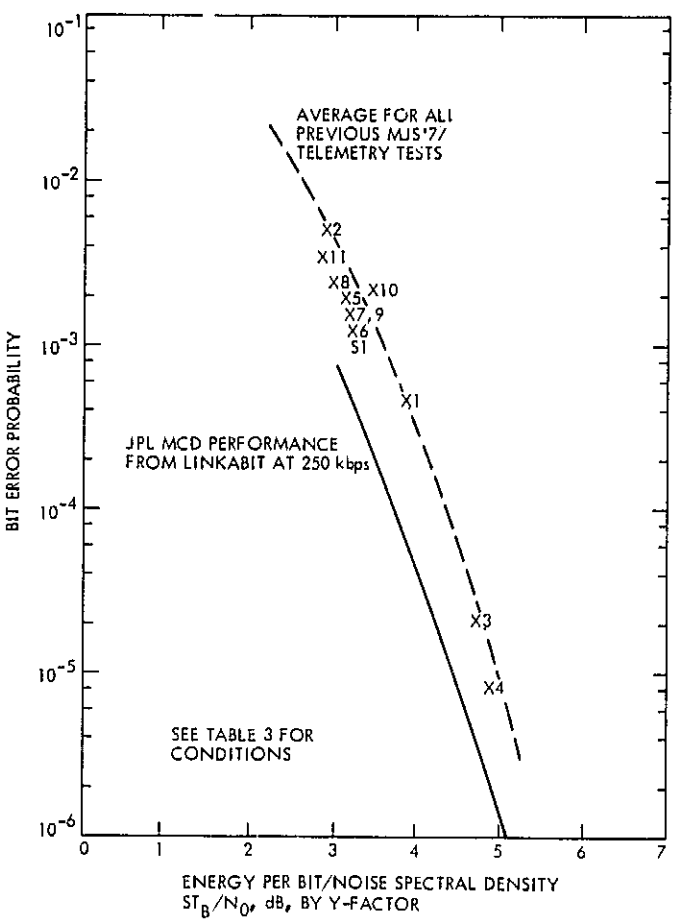

Fig. 12. Measured telemetry performance

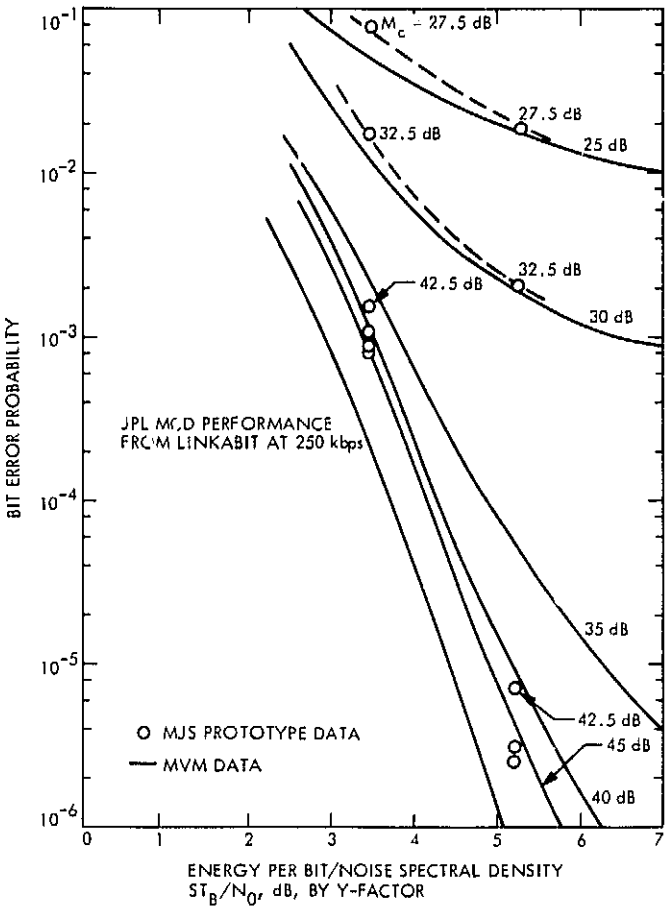

Fig. 13. Bit error probability vs ST_B/N_0 of two-way ratio loss, Block IV, X-band, 30 Hz at 115.2 kbps

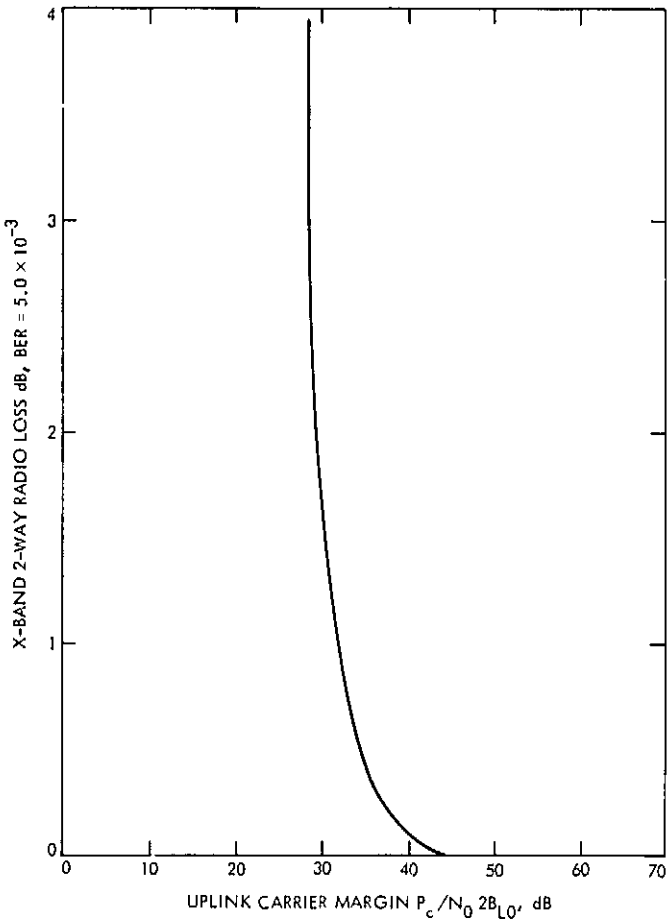

Fig. 14. X-band two-way radio loss vs uplink carrier margin

N77-14059

Modification of Hipotronics Discontinuity Enamel Wire Test for Wire Screening

W. D. Schreiner
Quality Assurance DSN and Mechanical Hardware Section

The Quality Assurance DSN and Mechanical Hardware Section and the Fabrication Section have redesigned the wire spindle section of the wire screening test equipment to prevent breakage of small gage magnet wire during testing operations.

I. Introduction

In the last year, use of magnet wire at JPL has increased dramatically. With emphasis being directed toward smaller and lighter packaging of electronics, the use of lighter gage wire has risen sharply.

Prior to its use, the wire is screened by Quality Assurance for defects. In attempting to perform screening tests with our existing test equipment on the smaller gage magnet wire, problems were encountered with repeated breakage of wire. After investigation and analysis, a deficiency was discovered in the design of the spindle that induced improper load and wire tension during testing operations.

II. Description of Equipment

The equipment used by Quality Assurance to perform the screening test is a Hipotronics Discontinuity Fnamel Wire Tester Model DT-1 (Fig. 1). This unit is designed to spark-test the insulation coating ot magnet wire and to record the number of defects.

The procedure is to set a spool of magnet wire on the left side spindle, remove a small amount of insulation from the end of the wire, feed the wire through the guide rollers and through the mercury bath, and then attach the end of the wire to the ground terminal of the takeup drum. The voltage range is selected and the machine is started, pulling the wire through the mercury bath. Any defect in the enamel coating completes the circuit through the mercury to ground and activates the defect counter. A footage counter is preset to run 30.5 meters for each test.

III. Problem

The problem experienced was frequent breakage of wire in the smaller gages (38 and under). This was caused by the manufacturer's design of the feed spindle (Fig. 2). The spindle was designed with radia, bearings only, with no means for supporting the weight of the spool. (A spool of wire weighs from 0.45 to 4.54 kg.) To adjust tension, a screw on the bottom required tightening or loosening.

This action exerted a compression load on bearings not designed for this purpose. Erratic operation was the result, causing constant breakage of wire.

IV. Solution

A redesign of the spindle was accomplished by the Quality Assurance DSN and Mechanical Hardware Section, and the Fabrication Section. The new design (Fig. 3) incorporates a compression bearing below the spindle to carry the load. In the main body there are two radial bearings. This combination provides smooth, free-running action regardless of weight. Tension is accomplished by use of a spring-loaded nylon button that presses against the main shaft; it is adjusted by a set screw. The result has been an extremely smooth operation with no breakage or loss of wire during test.

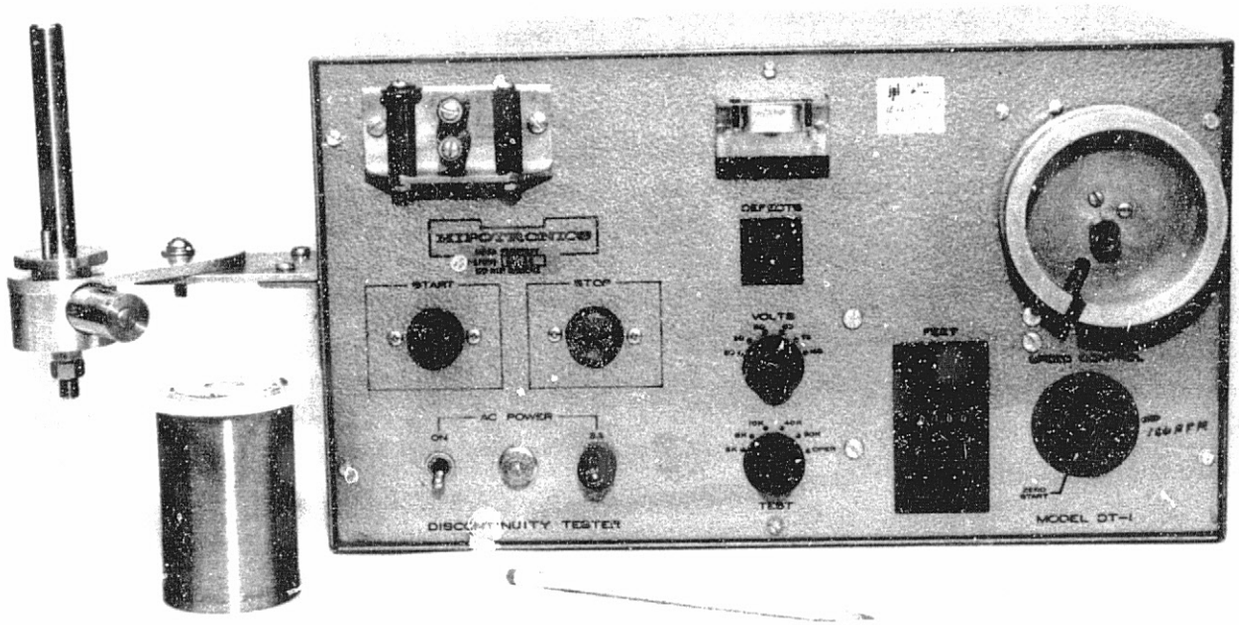

Fig. 1. Hipotronics Discontinuity Enamel Wire Tester Model DT-1

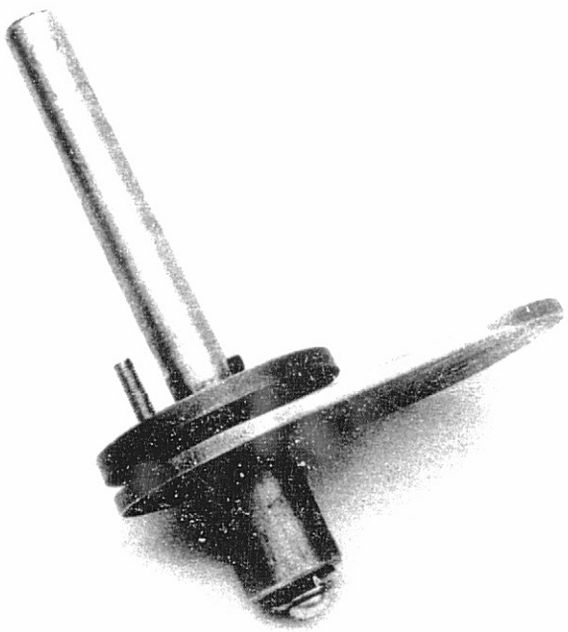

Fig. 2. Feed spindle, manufacturer's design

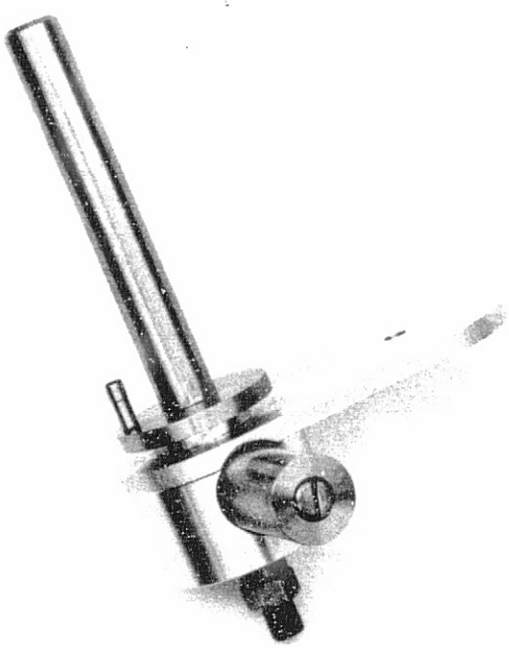

Fig. 3. Feed spindle, new design

REPRODUCIBILITY OF THE
ORIGINAL PAGE IS POOR

N77-14060

Two MBASIC Programs That Write Application Programs for Accessing a Database

R. M. Smith
DSN Facility Operations Section

A method was desired to relieve the tedium of writing and testing application programs. Two utility programs were developed to produce application programs that perform relational operations on data. No coding is performed by the user.

I. Introduction

The nature of the MBASIC Processor facilitates its use by people who are not primarily programmers and who may never have had any previous programming experience. Many managers, and other people needing to make use of management data, fall into this category of user. However, for many data users, programming is so much less important than data usage that it would be beneficial to reduce or eliminate programming in their data activities. One approach to minimizing programming time is to make use of a generalized application program similar to the one described in a previous article (Ref. 1). A generalized program, once written, allows the user to concentrate upon data usage rather than program writing. However, a generalized program requires that the user spell out an access strategy each time the program is used. If a specific application is required for repeated use, then a specialized application program is most desirable. Two different approaches to the use of specialized application programs were described in Refs. 2 and 3. This article describes the result of some preliminary efforts to design a simple method of producing an MBASIC application program while isolating the user from the task of writing code.

Application programs that extract data from a database may be data dependent (knowledge of data organization is built into the application program, making the program sensitive to changes in data organization) or may possess varying degrees of data independence (immunity of an application program to changes in data organization). The greater the degree of data independence, the less the effect of changes in the database. The programs described in this article are preprocessors that accept relational statements from a user, convert the statements to MBASIC code, and store the statements as an application program for later use.

II. Description of the Program 'WRITER'

'WRITER' produces specialized application programs with a moderate amount of data independence. User input to the program is fully prompted and makes use of relational operations (Refs. 4, 5) to specify database access. The relational operations may be invoked in any order repeatedly or used singly. Figure 1 illustrates a session invoking a restriction and a projection in sequence. Figure 2 illustrates the same process in relational notation. Figure 3 is a simplified flow diagram of the program showing the iterative nature of the main program in accepting user input and choosing a specified subprogram to assemble program statements.

In a typical sequence of events, the user

1. Enters the name of the new program to be written.
2. Enters the type of relational operation.
3. Enters the parameters that describe the selected relational operation.

'WRITER' then assembles a program by the following process:

1. Copies a set of generalized code lines to a temporary program file.
2. Appends code lines (to the temporary program file) that are created by 'WRITER' and are specific to the user's application.
3. Appends standardized subroutines (stored for this purpose) for each relational operation involved.
4. Copies the temporary program to a file named by the user.

Figure 4 is a copy of the program produced by 'WRITER' using the process depicted in Fig. 1. Line 100 and lines 902 through 918 are the generalized code lines mentioned previously. Lines 2000 through 2320 and 3000 through 3310 are standardized subroutines for a projection and restriction, respectively. (Lines 5000 through 5090 update a temporary directory relation that describes data files accessed by the application program.)

III. Description of the Program 'WRITPR'

'WRITPR' produces specialized application programs with no data independence. User input is fully prompted and makes use of relational operations (Refs. 4, 5) to specify database access. Figure 5 illustrates a session invoking a restriction and projection (see relational notation in Fig. 2). Figure 6 is a simplified flow diagram of the program. The user prompting sequence for 'WRITPR' is similar to that of 'WRITER' but 'WRITPR' differs in its approach to writing the application program (compare Figs. 3 and 6). 'WRITPR' assembles a program by writing code lines (on the program named by the user) that are specific to the user's application. Figure 7 is a copy of the program produced by 'WRITPR' using the process depicted in Fig. 5.

IV. Miscellaneous Information

To produce code that is specific to the user's application, both programs use "WRITE ON" statements that incorporate variables and "counters" into a completed statement for the application program. Examples of this process are shown in Figs. 8, 9, and 10 and are taken from the program 'WRITPR'. Figure 8 shows the lines of code that produce lines 110 and 120 of the program presented in Fig. 7. The code lines in Fig. 9 produce line 130 of Fig 7, and the code lines in Fig. 10 produce line 150 of Fig. 7.

Each of the sessions (illustrated in Figs. 1 and 5) requires approximately 3 to 4 min of terminal time and produces programs that are fully functional, requiring no testing of the MBASIC code. Both provide the user with a uniform, extremely simple process for data access. Figure 11 illustrates the data output produced by the application programs written by 'WRITER' and 'WRITPR'.

Data files accessed by these programs must be in, at least, first normal form. The file used in this article (Fig. 12) is in third normal form (Ref. 4).

References

1. Smith, R. M., "An MBASIC Application Program for Relational Inquiries on a Database," in *The Deep Space Network Progress Report 42-34,* Jet Propulsion Laboratory, Pasadena, Calif., August 15, 1976.

2. Smith, R. M., "A Relational Database Implemented Using MBASIC," in *The Deep Space Network Progress Report 42-30,* Jet Propulsion Laboratory, Pasadena, Calif., December 15, 1975.

3. Maiocco, F. R., and Hume, J. P., "Computerizing Goldstone Facility Maintenance Data for Management Decisions," in *The Deep Space Network Progress Report 42-32,* Jet Propulsion Laboratory, Pasadena, Calif., April 15, 1976.

4. Date, C. J., *An Introduction to Database Systems,* Addison-Wesley, 1975.

5. Codd, E. F., "A Relational Model of Data for Large Shared Data Banks," *Communications of ACM,* Vol. 13, No. 6, June 1970.

```
RUN
ENTER NAME OF NEW PROGRAM: INEW

ENTER RELATIONAL OPERATION (R,P,J) OR "STOP": R
 SOURCE RELATION: RMS*EQPT.ASSIGNMENT
     DOMAIN NAME: OWNER
LOGICAL OPERATOR: =
    DOMAIN VALUE: 12
      PROJECT TO: *FILE

ENTER RELATIONAL OPERATION (R,P,J) OR "STOP": P
     SOURCE RELATION: *FILE
 QUANTITY OF DOMAINS: 3
     TARGET RELATION: TERMINAL
        DOMAIN NAMES: CON,OPSTAT,LOCATION

ENTER RELATIONAL OPERATION (R,P,J) OR "STOP": STOP
TEST INEW
```

Fig. 1. Illustration of a session at a terminal using WRITER' to create an application program (User responses are to the right of each colon.)

'RMS*EQPT.ASSIGNMENT' | OWNER = 12

π TERMINAL (CON, OPSTAT, LOCATION)

Fig. 2. Relational notation describing the process illustrated in Figs. 1 and 5

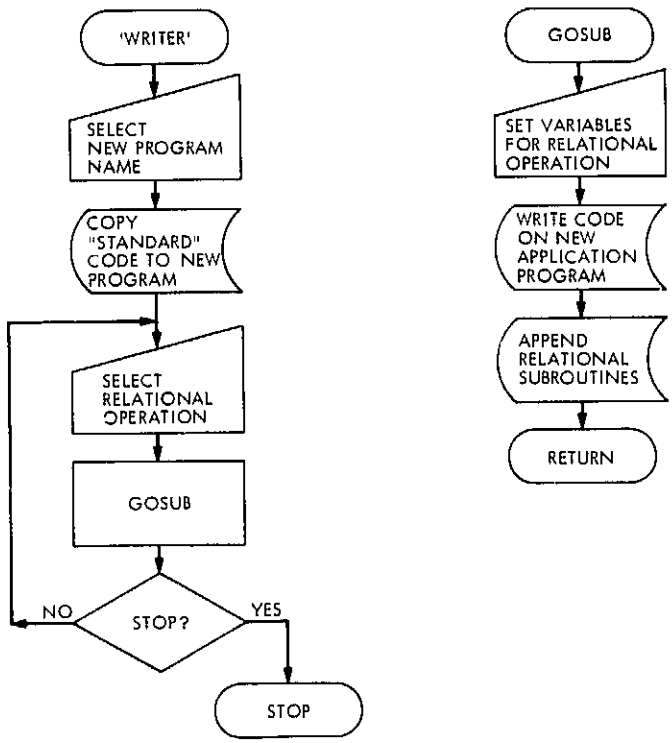

Fig. 3. Simplified flow diagram of 'WRITER'

```
COPY 'INEW' TO TERMINAL
100 JOIN=1000,PROJ=2000,REST=3000,NN=44,TARG=5000
110 COPY 'RMS◆EQPT.RREL' TO '◆INEW'
120 DIR$='◆INEW'
130 FL1$='RMS◆EQPT.ASSIGNMENT',DX$='OWNER',LO$='=',DV$='12'
140 PE$='◆FILE'
150 GOSUB REST
160 GOSUB TARG
170 RENAME '◆HOLD1  AS'◆FILE
180 FL1$='◆FILE',QD= 3
190 STRING DP$(QD)/'CON','OPSTAT','LOCATION'/
210 NN=32
220 GOSUB PROJ
902 STRING RCD(1)
904 OPEN '◆HOLD1',INPUT,1
906 AT ENDFILE(1) GO TO 914
908 INPUT FROM 1 USING '(#)':RCD(1)
910 PRINT RCD(1)
912 GO TO 908
914 CLOSE 1
916 REMOVE DIR$
918 STOP CHAR(13)◆'END OF RUN'&

2000 OPEN '◆STO1',OUTPUT,3
2010 FLGQ=0
2020 DIM F$(1),D(1),T(1),D$(1)
2030 OPEN DIR$,INPUT,4
2040 AT ENDFILE(4) GO TO 2140
2050 INPUT FROM 4:F$(1),D(1),T(1),D$(1)
2060 STRING DOM(T(1))
2070 IF F$(1)=FL1$ THEN WRITE ON 3:D(1):',':D$(1) ELSE GO TO 2100
2080 FLGQ=FLGQ+1
2090 DOM(FLGQ)=D$(1)
2100 IF F$(1)=FL1$ THEN GO TO 2050
2110 N=D(1)
2120 IF T(1)=D(1) THEN GO TO 2140
2130 GO TO 2050
2140 CLOSE 3,4
2150 Z=T(1)
2160 DIM DN(QD),D(1),D$(1),K$(Z)
2170 OPEN '◆STO1',INPUT,3
2180 AT ENDFILE(3) GO TO 2240
2190 INPUT FROM 3:D(1),D$(1)
2200 FOR I=1 UNTIL I=QD+1
2210 IF D$(1)=DP$(I) THEN DN(I)=D(1)
2220 NEXT I
2230 GO TO 2190
2240 CLOSE 3
2250 OPEN FL1$,INPUT,3
2260 OPEN '◆HOLD1',OUTPUT,4
2270 AT ENDFILE(3) GO TO 2310
2280 INPUT FROM 3:K$(J) FOR J=1 TO Z
2282 FOR I=1 UNTIL I=QD+1
2284 FOR J=1 UNTIL J=Z+1
2285 IF I<QD THEN CH=NN ELSE CH=13
2286 IF J=DN(I) THEN WRITE ON 4 USING '(#)':K$(J):CHAR(CH)
2288 NEXT J
2290 NEXT I
2300 GO TO 2280
2310 CLOSE 3,4
2320 RETURN&
```

Fig. 4. Data independent application program produced by using 'WRITER'

```
3000 OPEN '◆STO1',OUTPUT,3
3002 FLGQ=0
3005 DIM F$(1),D(1),T(1),D$(1)
3010 OPEN DIR$,INPUT,4
3020 AT ENDFILE(4) GO TO 3090
3030 INPUT FROM 4:F$(1),D(1),T(1),D$(1)
3035 STRING DOM(T(1))
3040 IF F$(1)=FL1$ THEN WRITE ON 3:D(1):',':D$(1) ELSE GO TO 3050
3045 FLGQ=FLGQ+1
3046 DOM(FLGQ)=D$(1)
3050 IF F$(1)=FL1$ THEN GO TO 3030
3060 N=D(1)
3070 IF T(1)=D(1) THEN GO TO 3090
3080 GO TO 3030
3090 CLOSE 3,4
3100 DIM D1(1),D2$(1)
3110 STRING A$(N)
3120 OPEN '◆STO1',INPUT,3
3130 AT ENDFILE(3) GO TO 3170
3140 INPUT FROM 3:D1(1),D2$(1)
3150 IF D2$(1)=DX$ THEN GO TO 3170
3160 GO TO 3140
3170 CLOSE 3
3180 Q=D1(1)
3190 IF LO$='=' THEN R=0 ELSE GO TO 3210
3200 GO TO 3240
3210 IF LO$='>' THEN R=1 ELSE GO TO 3230
3220 GO TO 3240
3230 IF LO$=CHAR(60) THEN R=-1
3240 OPEN '◆HOLD1',OUTPUT,5
3250 OPEN FL1$,INPUT,4
3260 AT ENDFILE(4) GO TO 3300
3270 INPUT FROM 4:A$(I) FOR I=1 TO N
3280 IF COMP(A$(Q),DV$)=R THEN WRITE ON 5 USING '(#)':&
    A$(I):CHAR(NN) FOR I=1 TO N-1\A$(N):CHAR(13)
3290 GO TO 3270
3300 CLOSE 4,5
3310 RETURN&

5000 OPEN '◆TRANSF',OUTPUT,1
5010 WRITE ON 1:RE$:',':I:',':FLGQ:',':DOM(I) FOR I=1 TO FLGQ
5020 CLOSE 1
5030 APPEND '◆TRANSF' TO DIR$
5040 RETURN&
```

Fig. 4 (contd)

```
LOAD 'WRITPR'
>RUN
ENTER NAME OF NEW PROGRAM: DNEW
SELECT A RELATIONAL OPERATION (REST,PROJ,JOIN) OR ENTER "STOP": REST
     SOURCE RELATION: RMS•EQPT.ASSIGNMENT
          DOMAIN NAME: OWNER
     LOGICAL OPERATOR: =
          DOMAIN VALUE: 12
            PROJECT TO: TERM
PROJECT ALL DOMAINS? N
ENTER QUANTITY OF DOMAINS: 3
ENTER NAMES OF DOMAINS: CON,OPSTA,LOCAT
SELECT A RELATIONAL OPERATION (REST,PROJ,JOIN) OR ENTER "STOP": STOP
TEST 'DNEW'

END OF RUN
>
```

Fig. 5. Illustration of a session at a terminal using 'WRITPR' to create an application program (User responses are to the right of each colon.)

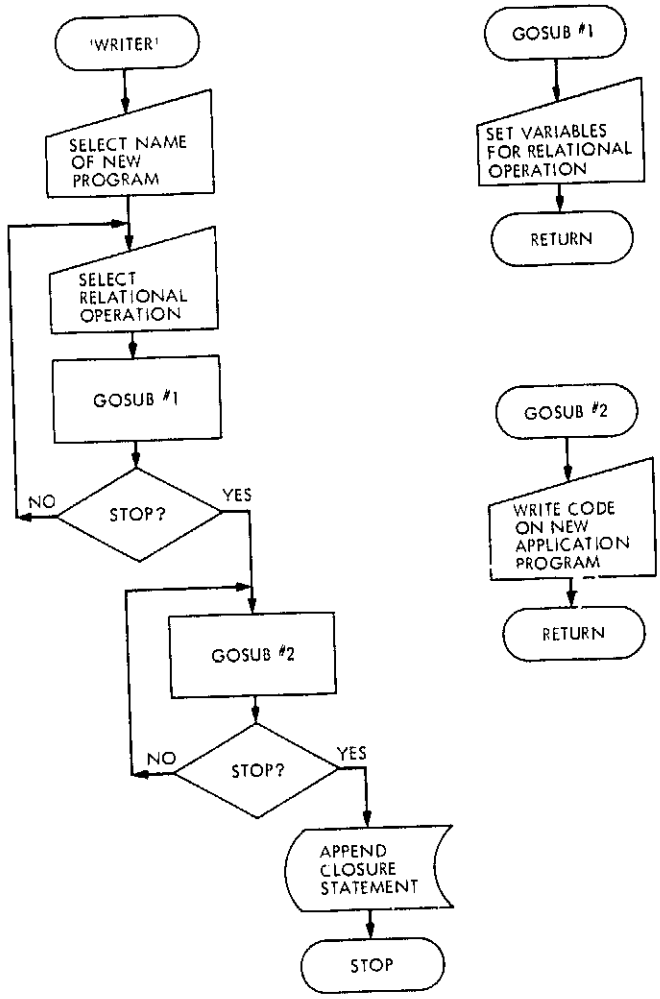

Fig. 6. Simplified flow diagram of 'WRITPR'

```
COPY 'DNEW' TO TERMINAL
100 STRING CON1,OWNER1,LOCAT1,OPSTA1,RECDT1
110 OPEN 'RMS$EQPT.ASSIGNMENT',INPUT, 1
120 AT ENDFILE( 1) GO TO  160
130 INPUT FROM  1:CON1,OWNER1,LOCAT1,OPSTA1,RECDT1
140 IF OWNER1='12' THEN PRINT CON1;OPSTA1;LOCAT1
150 GO TO  130
160 CLOSE I FOR I=1 TO  1
170 STOP CHAR(13)+'END OF RUN'
```

Fig. 7. Data dependent application program produced by using 'WRITPR'

```
3170 LINE=LINE+10
3180 WRITE ON 1:STR(LINE):' OPEN ':'<'>':SR1$(JJ):'<'>':',INPUT,':JJ
3190 LINE=LINE+10
3200 WRITE ON 1:STR(LINE):' AT ENDFILE(':JJ:') GO TO ':
     LINE+30+10*R
>
```

Fig. 8. Sample code lines from 'WRITPR' (lines 110 and 120 of Fig. 7)

```
3210 LINE=LINE+10
3220 WRITE ON 1 USING '(#)':STR(LINE):' INPUT FROM ':JJ:':'
     \DOM(I):STR(JJ):CHAR(44) FOR I=1 TO N-1\DOM(N):
     STR(JJ):CHAR(13)
```

Fig. 9. Sample code lines from 'WRITPR' (line 130 of Fig. 7)

```
3250 LINE=LINE+10
3260 WRITE ON 1:STR(LINE):' GO TO ':LINE-(10+10*R)
```

Fig. 10. Sample code lines from 'WRITPR' (line 150 of Fig. 7)

REPRODUCIBILITY OF THE
ORIGINAL PAGE IS POOR

```
LOAD 'DNEW'
>RUN
BB5C11    DL     12
CR6B12    US     1Y

END OF RUN
>


LOAD 'INEW'
>RUN
BB5C11 DL 12
CR6B12 US 1Y

END OF RUN
>
```

Fig. 11. Data printout resulting from running 'WRITPR' and 'WRITER'

```
>COPY 'RMS◆EQPT.ASSIGNMENT' TO TERMINAL
AA3A12,1Y,1Y,DL,010675
AB6C21,1X,1X,DL,170273
CD3B15,1X,1X,SP,121072
BB5C12,14,14,DL,091274
AX3B09,11,1Y,ER,190176
DA4C12,1X,1X,DL,071071
BB5C11,12,12,DL,091274
AR7D15,1Y,1X,US,250276
BB5C13,11,11,SP,091274
CC7C02,1X,1X,US,151172
CX5B13,1Y,1Y,DL,151071
CR6B12,12,1Y,US,110376
>
```

Fig. 12. Structure and content of the relation (data file) used in this article

N77-14061

Differential Range Validation: A New Technique for Near-Real-Time Validation of Multistation Ranging System Data

A. L. Berman
DSN Network Operations Section

Near-real-time validation of ranging system data is currently restricted to multiple range acquisitions during single passes (Pseudo-DRVID). This article describes a new technique ("Differential Range Validation") which utilizes predicted range and doppler pseudo-residuals to validate two-station, contiguous-pass range acquisitions down to the 10-meter level.

I. Introduction

During the first part of this decade, near-real-time validation of ranging data was only sporadically attempted and far less often successful. In March of 1975, this author introduced the "Pseudo-DRVID" Technique (see Ref. 1), which gave the Deep Space Network (DSN) the first viable near-real-time ranging validation capability. Since then, "Pseudo-DRVID" has enjoyed considerable success in validating multiple range acquisitions during single passes. However, there still remained a persistent and unfulfilled desire to be able to validate range acquisitions between two or more Deep Space Stations (DSSs). Responding to this need, this report presents a technique to validate two-station, contiguous-pass range acquisitions—hereafter to be referred to as "Differential Range Validation."

II. The Differential Concept

The reasons why Planetary Ranging Assembly (PRA) range acquisitions cannot be simply compared to predictions[1] are thoroughly explored in Ref. 1. Suffice it to say here that the range ambiguity values are (or should be!) frugally chosen to be only slightly larger than prediction (or orbit determination) errors, and this straightforwardly causes a direct comparison of PRA measurements to predictions to be without meaning in the conventional sense of a "residual." No matter that the *absolute* range error in predictions may be kilometers or tens of kilometers—it

[1]Here considered to be output from the PREDIK program. PREDIK is the Network Operations Control Center (NOCC) Sigma 5 tracking prediction program. Inputs to PREDIK are the Simulation Output Program (SOP) and Fast Phi-Factor Generation Program (FPGP).

is, in general, true that the *growth* of predicted-range error (excepting orbital and encounter phases!) is frequently of the magnitude:

$$-0.1\ \text{Hz}$$

This would map into an increase in predicted-range error over (say) five hours of:

$$\frac{0.1\ \text{cycle}}{\text{second}}\left[\frac{1\ \text{meter}}{15.3\ \text{cycles}}\right][18{,}000\ \text{seconds}] = 118\ \text{meters}$$

At the same time, the *absolute* range change over the same 5-hour period may easily be 100,000 km or more. This then motivates the central concept of the Differential Range Validation Technique:

> PRA (or Mu II for that matter) range measurements between two different DSSs can be validated with a high degree of confidence by comparing the *differenced* range acquisitions to the *differenced* predicted range.

Even better, one is not constrained by the accuracy in predicted-range error change over several hours. In near-real-time, one is automatically given via the Network Operations Control Center (NOCC) Pseudo Residual Program a frequent measurement of the *rate of growth* of the predicted-range error—the *doppler pseudo-residual*. Obviously, one can easily and substantially correct differenced predicted range by simply adding a term computed directly from the observed doppler pseudo-residual. The specifics of the Differential Range Validation technique are presented in the following section.

III. The Differential Range Validation Algorithm

One starts by noting the relationship between range and the output of the PRA:

$$R(t) = K[M(t)] + RPRA(t)$$
$$0 \le RPRA(t) < K$$

where

$R(t)$ = round trip range at time t

K = ambiguity resolution factor: a quantized input, in units of $R(t)$

$M(t)$ = integer, determined from independent orbital knowledge

$RPRA(t)$ = "scaled" output of the PRA, i.e., in the same units as $R(t)$

Additionally, the following parameters are required for a complete description of the algorithm:

X_i = parameter X applicable to DSS_i

TSF_i = track synthesizer frequency, Hz

N_i = number of components

$$K_i = K_i(TSF_i, N_i) = \frac{c}{48(TSF_i)}\left[2^{(N_i+10)}\right]$$

= ambiguity

c = speed of light, m/s

$R_{ai}(t)$ = actual round trip range, m

$R_{pi}(t)$ = predicted round trip range, m

$$M_{ai}(t) = [R_{ai}(t) - R_{ai}(t) \text{ modulo } K_i]/K_i$$

$$M_{pi}(t) = [R_{pi}(t) - R_{pi}(t) \text{ modulo } K_i]/K_i$$

$PRTR_i$ = PRA range measurement, range units (RU)

$$RPRA_i(t) = \frac{c}{48(TSF_i)}[PRTR_i], \text{m}$$

$T0$ = PRA acquisition time

$Bias_i$ = station range bias RU

Now consider a PRA acquisition at DSS 1 with a $T0 = t_1$ and a subsequent PRA acquisition at DSS 2 with a $T0 = t_2$:

$$R_{a1}(t_1) \cong K_1[M_{a1}(t_1)] + RPRA_1(t_1)$$
$$R_{a2}(t_2) \cong K_2[M_{a2}(t_2)] + RPRA_2(t_2)$$

and

$$\Delta R_a \equiv R_{a2}(t_2) - R_{a1}(t_1)$$
$$\cong RPRA_2(t_2) - RPRA_1(t_1) + \{K_2[M_{a2}(t_2)] - K_1[M_{a1}(t_1)]\}$$

Now in Pseudo-DRVID, one could reasonably assume the same number of components and the same track synthesizer frequency for each range acquisition during the same pass, and hence all relevant quantities would

have the same ambiguity as a modulus. For range acquisitions at different DSSs, however, one might find different numbers of components:

$$N_2 \neq N_1$$

and one can certainly expect the track synthesizer frequencies to be different:

$$TSF_2 \neq TSF_1$$

If the number of components only were different, all quantities could easily be operated on by the smaller modulus (ambiguity), since

$$\frac{K_j}{K_i} = 2^{(N_j - N_i)} = \text{integer}, \qquad N_j > N_i$$

However, even minor changes in TSF have a dramatic effect on the actual PRA measurement. Consider the following example:

$$N_1 = N_2 = 10 \text{ components}$$

$$R_{a1} = R_{a2} = 3 \times 10^{11} \text{ m}$$

Now let

$$TSF_1 = 22000000 \text{ Hz}$$

so that

$$K_1 = 297684.8679 \text{ m}$$

and

$$RPRA_1 = R_{a1} \text{ modulo } K_1 = 36905 \text{ m}$$

Similarly,

$$TSF_2 = 22000010 \text{ Hz}$$

$$K_2 = 297684.7325 \text{ m}$$

$$RPRA_2 = R_{a2} \text{ modulo } K_2 = 173289 \text{ m}$$

with a difference in PRA measurements of:

$$\Delta RPRA = RPRA_2 - RPRA_1 = 136384 \text{ m}$$

To compensate for the different ambiguities, the range acquisition performed with the larger ambiguity (say K_2) is "transformed" to an "equivalent" range acquisition at the smaller ambiguity (K_1). This is accomplished by writing:

$$K_2[M_{a2}(t_2)] = K_1 L + \epsilon; \qquad L = \text{integer}$$

or

$$\epsilon = (K_2[M_{a2}(t_2)]) \text{ modulo } K_1$$

One can now operate on ΔR_a with the ambiguity K_1 as follows:

$$\Delta R_a \cong RPRA_2(t_2) - RPRA_1(t_1) + \epsilon + \{K_1 L - K_1[M_{a1}(t_1)]\}$$

and

$$\Delta RPRA \cong (\Delta R_a) \text{ modulo } K_1 \cong RPRA_2(t_2) - RPRA_1(t_1) + \epsilon$$

with

$$\epsilon = (K_2[M_{a2}(t_2)]) \text{ modulo } K_1$$

Unfortunately, one does not have $M_{a2}(t_2)$; however if one assumes

$$M_{p2}(t_2) \approx M_{a2}(t_2)$$

then

$$\epsilon \approx (K_2[M_{p2}(t_2)]) \text{ modulo } K_1$$

One can easily see that even if predictions were in error by several times the ambiguity

$$M_{a2}(t_2) - M_{p2}(t_2) = J; \qquad J = \text{small integer}$$

the error in ϵ would still be extremely small:

assume $\Delta TSF = TSF_2 - TSF_1$

$$I = \text{arbitrary integer}$$

$$\epsilon + \Delta\epsilon = (K_2[M_{a2}(t_2) - J]) \text{ modulo } K_1$$

$$\Delta\epsilon = (K_2 M_{a2}(t_2) - JK_2) \text{ modulo } K_1 - \epsilon$$

$$= \{[K_2 M_{a2}(t_2)] \text{ modulo } K_1 - \epsilon\} + (-JK_2) \text{ modulo } K_1 + IK_1$$

$$= (-JK_2) \text{ modulo } K_1 + IK_1$$

Now

$$K_2 = K_1 2^{(N_2-N_1)}\left(1 - \frac{\Delta TSF}{TSF_2}\right)$$

so that

$$\Delta\epsilon = \left(-JK_1 2^{(N_2-N_1)}\left[1 \quad \frac{\Delta TSF}{TSF_2}\right]\right)\text{modulo } K_1 + IK_1$$

$$= (-JK_1 2^{(N_2-N_1)})\text{ modulo } K_1$$

$$+ \left(JK_1 2^{(N_2-N_1)}\left[\frac{\Delta TSF}{TSF_2}\right]\right)\text{modulo } K_1 + IK_1$$

$$= \left(JK_1 2^{(N_2-N_1)}\left[\frac{\Delta TSF}{TSF_2}\right]\right)\text{modulo } K_1 + IK_1$$

but since

$$\left|JK_1 2^{(N_2-N_1)}\frac{\Delta TSF}{TSF_2}\right| << K_1$$

then

$$\Delta\epsilon = JK_1 2^{(N_2-N_1)}\frac{\Delta TSF}{TSF_2} + IK_1$$

and

$$(\Delta\epsilon)\text{ modulo } K_1 = JK_1 2^{(N_2-N_1)}\frac{\Delta TSF}{TSF_2}$$

Finally, one obtains the difference in predicted range:

$$\Delta R_p = R_{p2}(t_2) - R_{p1}(t_1)$$

and

$$\Delta RPRA_p = (\Delta R_p)\text{ modulo } K_1$$

$$= (R_{p2}(t_2) - R_{p1}(t_1))\text{ modulo } K_1$$

One now has the differential quantity of interest:

$$\Delta RPRA - \Delta RPRA_p = RPRA_2(t_2) - RPRA_1(t_1) + \epsilon - (R_{p2}(t_2) - R_{p1}(t_1))\text{ modulo } K_1$$

with

$$\epsilon \equiv (K_2[M_{p2}(t_2)])\text{ modulo } K_1$$

or

$$\Delta RPRA - \Delta RPRA_p = \{RPRA_2(t_2) - RPRA_1(t_1) + K_2[M_{p2}(t_2)] + R_{p1}(t_1) - R_{p2}(t_2)\}\text{ modulo } K_1$$

IV. Correction of Predicted Range via Use of the Doppler Pseudo-Residual

As mentioned in Section II, the accuracy of the range prediction used in differential range validation can be substantially improved by merely utilizing the already automatically provided doppler pseudo-residual. To facilitate the discussion, define the notation

$$\Delta X(t) \equiv X(t_2) - X(t_1)$$

$$\delta X(t) \equiv X_a(t) - X_p(t)$$

where

$X_a(t)$ = "actual" quantity at time t

$X_p(t)$ = "predicted" quantity at time t

Thus,

$$\delta R(t) \equiv R_a(t) - R_p(t)$$

= predicted-range error at time t

Let one now assume a prediction error over a short time period (several hours) of the form:

$$\delta R(t) \approx A + Bt + Ct^2$$

and hence:

$$\frac{d}{dt}[\delta R(t)] \approx B + 2Ct$$

Now

$$D2(t) = 96\frac{240}{221}TSF_R - 96\frac{240}{221}TSF_T\left(1 - \frac{1}{c}\frac{dR}{dt}\right) + Bias_d$$

where

$D2(t)$ = two-way doppler

TSF_R = received track synthesizer frequency

TSF_T = transmitted track synthesizer frequency

$Bias_d$ = doppler bias

so that (with $TSF_T \equiv TSF$)

$$\delta D2(t) = \left(\frac{96}{c}\right)\frac{240}{221}TSF\left\{\frac{dR_a}{dt} - \frac{dR_p}{dt}\right\}$$

$$= \left(\frac{96}{c}\right)\frac{240}{221}TSF\left\{\frac{d}{dt}[\delta R]\right\}$$

$$=$$ value of doppler pseudo-residual

Thus one has

$$\delta D2(t_2) = \left(\frac{96}{c}\right)\frac{240}{221}TSF\{B + 2Ct_2\}$$

$$\delta D2(t_1) = \left(\frac{96}{c}\right)\frac{240}{221}TSF\{B + 2Ct_1\}$$

and

$$\{\delta D2(t_1) + \delta D2(t_2)\}$$

$$= \left(\frac{96}{c}\right)\frac{240}{221}TSF\{B + 2Ct_1 + B + 2Ct_2\}$$

$$= \left(\frac{96}{c}\right)\frac{240}{221}TSF\{2(B + C[t_1 + t_2])\}$$

Now the quantity one is interested in is the range error *change*, $\Delta\delta R$, from t_1 to t_2:

$$\Delta\delta R = \delta R(t_2) - \delta R(t_1)$$

$$= A + Bt_2 + Ct_2^2 - (A + Bt_1 + Ct_1^2)$$

$$= B(t_2 - t_1) + C(t_2^2 - t_1^2)$$

$$= (t_2 - t_1)[B + C(t_2 + t_1)]$$

$$= (t_2 - t_1)\left[\frac{c}{96}\left(\frac{221}{240}\right)\frac{1}{TSF}\left\{\frac{\delta D2(t_1) + \delta D2(t_2)}{2}\right\}\right]$$

which is to say that one can incorporate almost exactly predicted-range error growth up to second order:

$$\delta R(t) = R_a(t) - R_p(t)$$

$$\approx A + Bt + Ct^2$$

by simply using the observed doppler pseudo residuals at t_1 and t_2:

$$\delta D2(t_1), \delta D2(t_2)$$

in a form as follows:

$$\Delta R_p' = \Delta R_p + \Delta\delta R$$

$$= R_{p2}(t_2) - R_{p1}(t_1)$$

$$+ (t_2 - t_1)\left[\frac{c}{96}\frac{221}{240}\frac{1}{TSF}\left\{\frac{\delta D2(t_1) + \delta D2(t_2)}{2}\right\}\right]$$

V. Final Expression for Differential Range Validation

Incorporating the station range delays and the doppler pseudo-residual correction, one arrives at the final expression:

$$\Delta RPRA - \Delta RPRA_p =$$

$$\Big\{RPRA_2(t_2) - RPRA_1(t_1) + K_2[M_{p2}(t_2)]$$

$$- \frac{c}{48}\left[\frac{Bias_2}{TSF_2} - \frac{Bias_1}{TSF_1}\right] + R_{p1}(t_1) - R_{p2}(t_2)$$

$$- (t_2 - t_1)\left[\frac{c}{96}\frac{221}{240}\left(\frac{1}{2}\right)\left\{\frac{\delta D2(t_1)}{TSF_1} + \frac{\delta D2(t_2)}{TSF_2}\right\}\right]\Big\} \text{ modulo } K_1$$

VI. Preliminary Results of Differential Range Validation

Twelve cases of Viking two-station, contiguous-pass range acquisitions were compared with the differential range validation technique; the results are presented in Table I. The twelve cases presented in Table 1 produced the following composite result:

$$|\Delta RPRA - \Delta RPRA_p|_{avg} = 9.5\,\text{m}$$

It is noteworthy that these results were obtained via the exclusive use of routine tracking predictions.

An HP9810 program containing the differential range validation algorithm (see Ref. 2) has been delivered to the Network Analysis Team, Tracking (NAT Track), and the technique is considered operational.

VII. Summary

Attempts to validate ranging system data in near-real-time prior to 1975 were generally unsuccessful. In 1975, the Pseudo-DRVID technique was introduced, and it

proved quite successful in the near-real-time validation of multiple range acquisitions during single passes. However, there still existed a need to be able to validate ranging data between separate DSSs. The differential range validation technique presented in this report answers this need by providing a practical method of validating two-station, contiguous-pass range acquisitions down to the 10-meter level during cruise phases.

Acknowledgments

I would like to thank G. L. Spradlin, who encouraged me in undertaking this effort, L. E. Bright, who managed to shoehorn the algorithm into an H.P. calculator and additionally supplied the test case results presented here, and S. T. Rockwell, who aided in the initial investigation of the technique.

References

1. Berman, A. L., "Pseudo-DRVID: A New Technique For Near-Real-Time Validation of Ranging System Data," The Deep Space Network Progress Report 42-29, Jet Propulsion Laboratory, Pasadena, Calif., Oct. 15, 1975.

2. Bright, L. E., "Release of HP 9810 Calculator Program for Differential Range Validation" (to be published as a JPL internal document).

Table 1. Differential range validation results

Case	DOY, 1976	S/C	DSSs	$\Delta t = t_2 - t_1$, hr:min	$\Delta RPRA - \Delta RPRA_p$, m
1	152	27	61-11	17:45	13.1
2	153	27	61-11	1:40	5.8
3	156	27	63-11	12:08	−15.0
4	157	27	43-63	55	9.3
5	210	30	11-42	4:45	5.3
6	210	30	11-42	1:10	11.1
7	211	30	42-61	1:17	9.4
8	211	30	61-11	1:14	−5.2
9	213	30	61-11	4:21	−6.1
10	216	30	42-61	1:20	17.5
11	217	30	61-11	10:21	13.0
12	217	30	42-61	1:17	3.0

N77-14062

The 1976 Helios and Pioneer Solar Conjunctions—Continuing Corroboration of the Link Between Doppler Noise and Integrated Signal Path Electron Density

A. L. Berman, J. A. Wackley, and S.T. Rockwell
DSN Network Operations Section

Observed doppler noise (rms phase jitter) from the 1976 solar conjunctions of the Helios 1 and 2 and the Pioneer 10 and 11 spacecraft was processed with a recently developed doppler noise model "ISEDB." Good agreement is obtained between the observed data and the model. Correlation is shown between deviations from the ISEDB model and sunspot activity, but it is insufficient to be modeled. Correlation is also shown between ISEDB model deviations for (spacecraft) signal paths on the same side of the sun.

I. Introduction

Utilizing observed doppler noise data from the 1975 Helios 1, Pioneer 10 and Pioneer 11 Solar Conjunctions, the authors have constructed a geometric model (the "ISED" series) for plasma-induced doppler noise (rms phase jitter). The functional form of the model was developed by assuming that doppler noise was proportional to the integrated signal path electron density, with the electron density assumed to be:

$$N_e(r) = \frac{A}{r^6} + \frac{B}{r^{2.3}}$$

r = heliocentric distance

Reference 1 describes a modification to the model ("ISEDB") which accounts for heliocentric latitude; Refs. 2 through 5 document the development of the basic model. The most recent model—ISEDB—is defined as follows:

$$ISEDB = \left[\left(\left\{A_0\left[\frac{\beta}{(\sin\alpha)^{1.3}}\right]F(\alpha,\beta) + A_1\left[\frac{1}{(\sin\alpha)^5}\right]\right\}10^{-A_2(\phi_e - 90)}\right)^2 + (0.0015)^2\right]^{1/2}$$

where

$$F(\alpha,\beta) = 1 - 0.05\left\{\frac{(\beta - \pi/2 + \alpha)^3 - (\alpha - \pi/2)^3}{\beta}\right\}$$

$$- 0.00275\left\{\frac{(\beta - \pi/2 + \alpha)^5 - (\alpha - \pi/2)^5}{\beta}\right\}$$

α = Sun-Earth-Probe angle (SEP), rad

β = Earth-Sun-Probe angle (ESP), rad

and

ϕ_s = heliographic latitude, deg

$= \sin^{-1}[\cot\alpha(-\cos\delta_d \sin\alpha_{ra} \sin\epsilon + \sin\delta_d \cos\epsilon)]$

α_{ra} = right ascension

δ_d = declination

ϵ = the obliquity of the ecliptic (23.445 deg)

with

$A_0 = 9.65 \times 10^{-4}$

$A_1 = 5 \times 10^{-10}$

$A_8 = 9 \times 10^{-1}$

It will be the intent of this article to ascertain if the Helios 1 and 2 and the Pioneer 10 and 11 observed doppler noise continues to be well represented by the ISEDB model.

II. Data Description

The data consists of pass average, good, two-way doppler noise collected during the following time intervals (DOY = Day of Year, 1976):

Spacecraft	Begin (DOY)	End (DOY)
Pioneer 10	51	175
Pioneer 11	79	215
Helios 1	75	293
Helios 2	90	293

All doppler data was taken at a 60-sec sample rate with the exception of some Helios 2 passes, which utilized doppler sample rates of either 10 or 1 second. In these cases, the following relationship was used to transform the doppler noise from the actual sample rate to an "equivalent" 60-s sample rate:

$$noise_{SR1} = noise_{SR2}\left(\frac{SR2}{SR1}\right)^{0.285}$$

where

$SR1,2$ = *sample rate* 1, 2

The collected noise data was fit with the ISEDB model and a new A_0 was selected to minimize the standard deviation of the residuals:

$$A_0 = 11.21 \times 10^{-4}$$

Scatter diagrams for the data (observed doppler noise vs the ISEDB model) are seen as follows:

Fig. 1—Pioneer 10

Fig. 2—Helios 1

Fig. 3—Helios 2

Fig. 4—Combined

while the following figures present observed doppler noise and the ISEDB model as a function of DOY:

Fig. 5—Pioneer 10

Fig. 6—Pioneer 11

Fig. 7—Helios 1

Fig. 8—Helios 2

Examination of these figures leads one to conclude in a qualitative sense that the (ISEDB) model continues to be in good agreement with the doppler noise observations during the 1976 Pioneer 10 and 11 and Helios 1 and 2 solar conjunctions. The statistics of the observed doppler noise as fit to the ISEDB model were as follows, with "dB" = $10\log_{10}$ (observed noise/ISEDB):

	Pioneer 10	Pioneer 11	Helios 1	Helios 2	All
σ, dB	2.04	1.77	2.47	2.65	2.28
Bias, dB	−0.37	−0.01	−0.63	+1.36	+0.02

III. Correlation of Observed Doppler Noise With Sunspot Activity

In Ref. 2, the authors attempted to correlate observed doppler noise with sunspot activity (the "RISED" model). Although a quantitative correlation with sunspot activity (as measured by R_Z = Zurich (daily) sunspot index) was demonstrated, it was not (at that time) considered optimistically. The data presented in this report was processed with the RISED model (now "RISEDB"), and a new A_0 to minimize the standard deviation was computed to be

$$A_0 = 10.16 \times 10^{-4}$$

Basically, the RISEDB performance (as compared to the ISEDB modeling) can be summarized by spacecraft as follows:

Pioneer 10—significant degradation

Pioneer 11—minor improvement

Helios 1 —significant improvement

Helios 2 —unchanged

All —minor improvement

The statistics are as follows:

	Pioneer 10	Pioneer 11	Helios 1	Helios 2	All
σ, dB	2.25	1.72	2.20	2.65	2.22
Bias, dB	−0.43	+0.30	−0.53	+1.06	+0.05

ISEDB residuals, "smoothed/phased" sunspots ($\equiv XR_2$; see Ref. 2), and RISEDB residuals are seen in the following figures:

Fig. 9 —Pioneer 11

Fig. 10—Helios 1

Fig. 11—Helios 2

Regions which appear to show evidence of correlation between observed doppler noise and sunspot activity are as follows:

Pioneer 11, DOY 80–145 (Fig. 9)

Helios 1, DOY 75–175 (Fig. 10)

Helios 2, DOY 90–135 (Fig. 11)

However, these regions must be balanced against regions of little or even negative correlation, as follows:

Pioneer 11, DOY 175–195 (Fig. 9)

Helios 1, DOY 185–255 (Fig. 10)

Helios 2, DOY 140–170 (Fig. 11)

IV. Multispacecraft Correlation

One would expect to see good correlation between ISEDB residuals from different spacecraft, as long as the signal paths are on the same side of the sun. Figure 12 shows ISEDB residuals for Pioneer 10, Pioneer 11, and Helios 2 when these signal paths were east (left) of the sun, while Fig. 13 shows ISEDB residuals for Pioneer 10, Pioneer 11, Helios 1, and Helios 2 when these signal paths were west (right) of the sun. Regions of correlation between various spacecraft are as follows:

HE 1/HE 2, DOY 90–134 (Fig.13)

PN 11/HE 1, DOY 180–215 (Fig. 13)

PN 10/PN 11, DOY 80–105 (Fig. 12)

V. Summary

Observed doppler noise data from the 1976 solar conjunction phases of the Pioneer 10 and 11 and the Helios 1 and 2 spacecraft was fit to the ISED model ("ISEDB") and subsequently shown to be in good agreement with the model—thus continuing to corroborate the direct link between observed doppler noise and integrated signal path electron density. Some evidence of correlation between sunspot activity and doppler noise is seen (the RISED model), but the relationship is insufficient to model in a quantitative fashion. Finally, correlation between doppler noise deviations from the ISEDB model continue to be seen for (spacecraft) signal paths on the same side of the sun.

Acknowledgments

The authors would like to thank C. Darling and M. F. Cates, who rendered the illustrations, and J. DeNino, who typed this article.

References

1. Berman, A. L., Wackley, J. A., Rockwell, S. T., and Yee, J. G., "The Pioneer 11 1976 Solar Conjunction: A Unique Opportunity to Explore the Heliographic Latitudinal Variations of the Solar Corona," in *The Deep Space Network Progress Report 42-35*, Jet Propulsion Laboratory, Pasadena, Calif., Oct. 15, 1976.

2. Berman, A. L., and Wackley, J. A., "Doppler Noise Considered as a Function of the Signal Path Integration of Electron Density," in *The Deep Space Network Progress Report 42-33*, Jet Propulsion Laboratory, Pasadena, Calif., June 15, 1976.

3. Berman, A. L., "Analysis of Solar Effects Upon Observed Doppler Data Noise During the Helios 1 Second Solar Conjunction," in *The Deep Space Network Progress Report 42-32*, Jet Propulsion Laboratory, Pasadena, Calif., April 15, 1976.

4. Berman, A. L., and Rockwell, S. T., "Correlation of Doppler Noise During Solar Conjunctions with Fluctuations in Solar Activity," in *The Deep Space Network Progress Report 42-30*, Jet Propulsion Laboratory, Pasadena, Calif., Dec. 15, 1975.

5. Berman, A. L., and Rockwell, S. T., "Analysis and Prediction of Doppler Noise During Solar Conjunctions," in *The Deep Space Network Progress Report 42-30*, Jet Propulsion Laboratory, Pasadena, Calif., Dec. 15, 1975.

6. Berman, A. L., "Solar Plasma Induced Doppler Noise Dependence Upon Sample Rate," IOM 421G-76-155, July 13, 1976 (a JPL internal document).

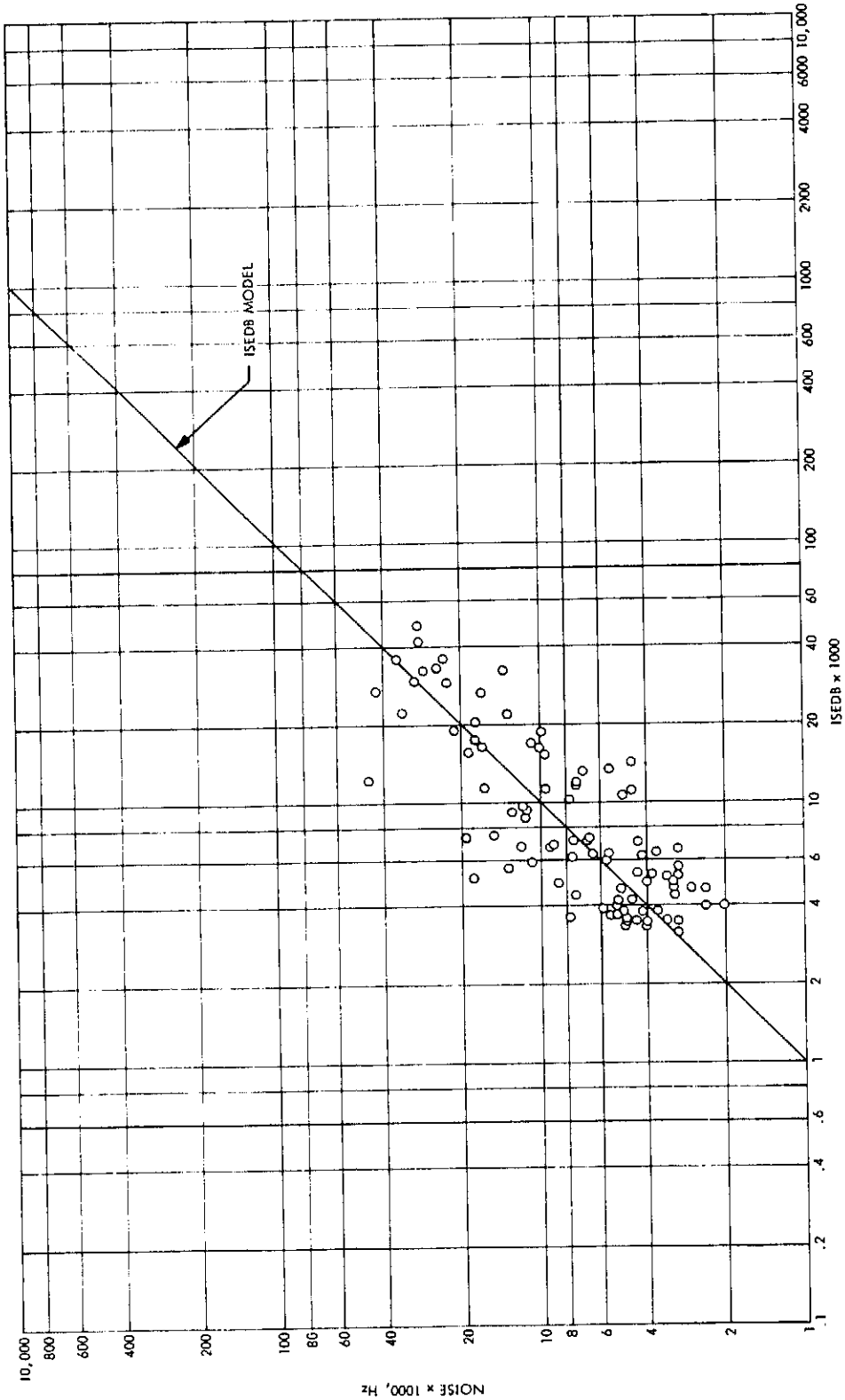

Fig. 1. Pioneer 10 (S/C 23) 1976 solar conjunction, observed doppler noise vs the ISEDB model

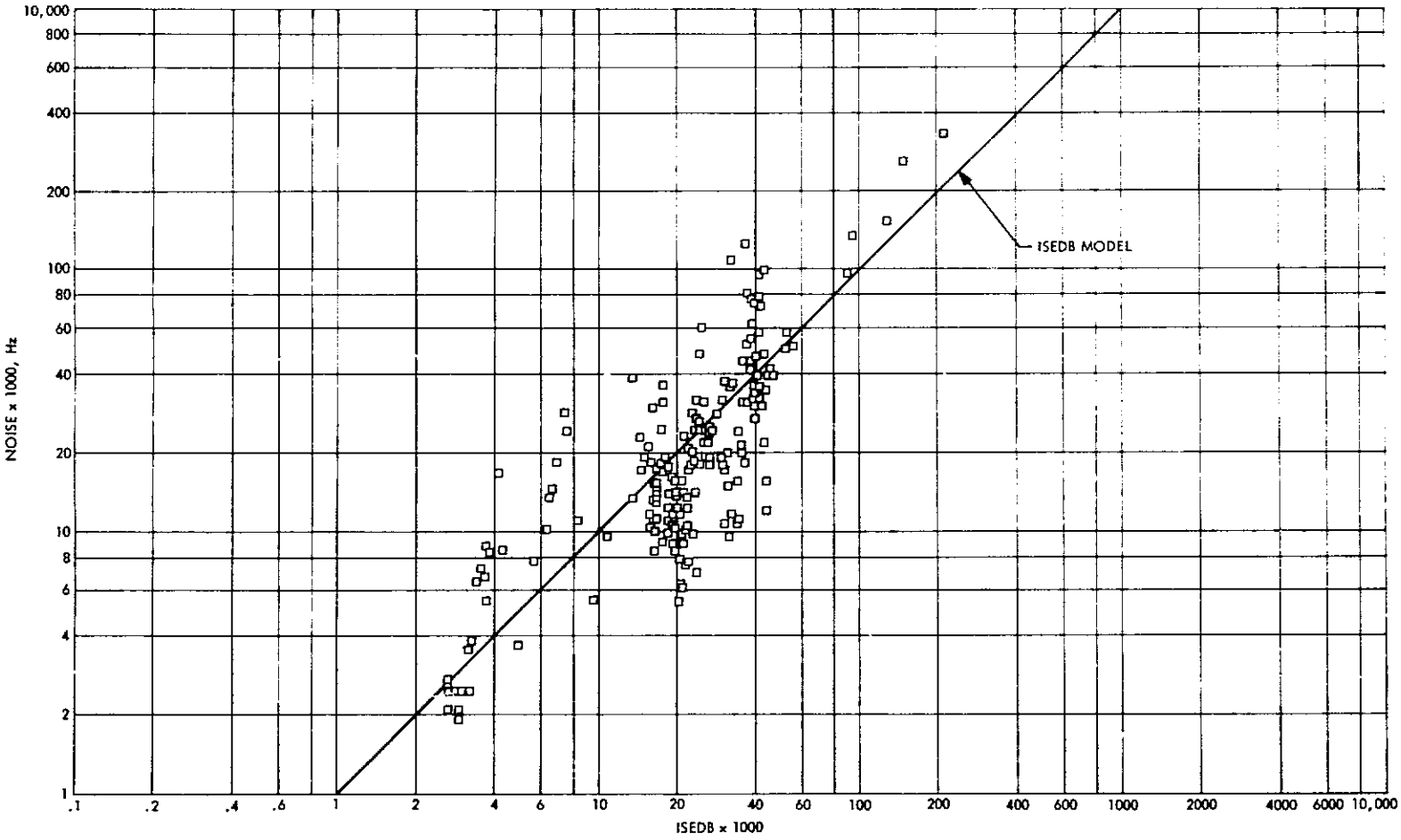

Fig. 2. Helios 1 (S/C 90) 1976 solar conjunction, observed doppler noise vs the ISEDB model

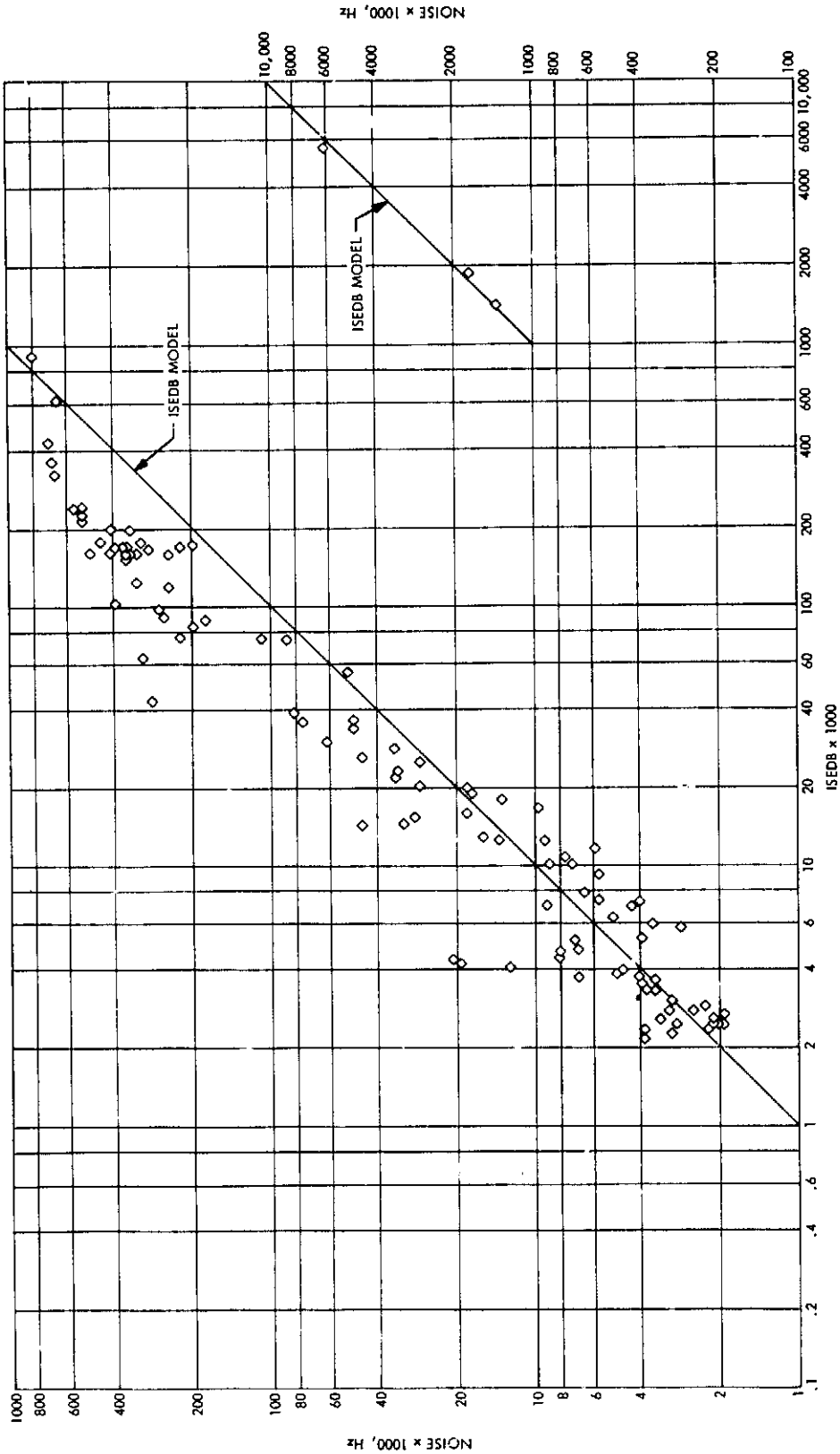

Fig. 3. Helios 2 (S/C 91) 1976 solar conjunction, observed doppler noise vs the ISEDB model

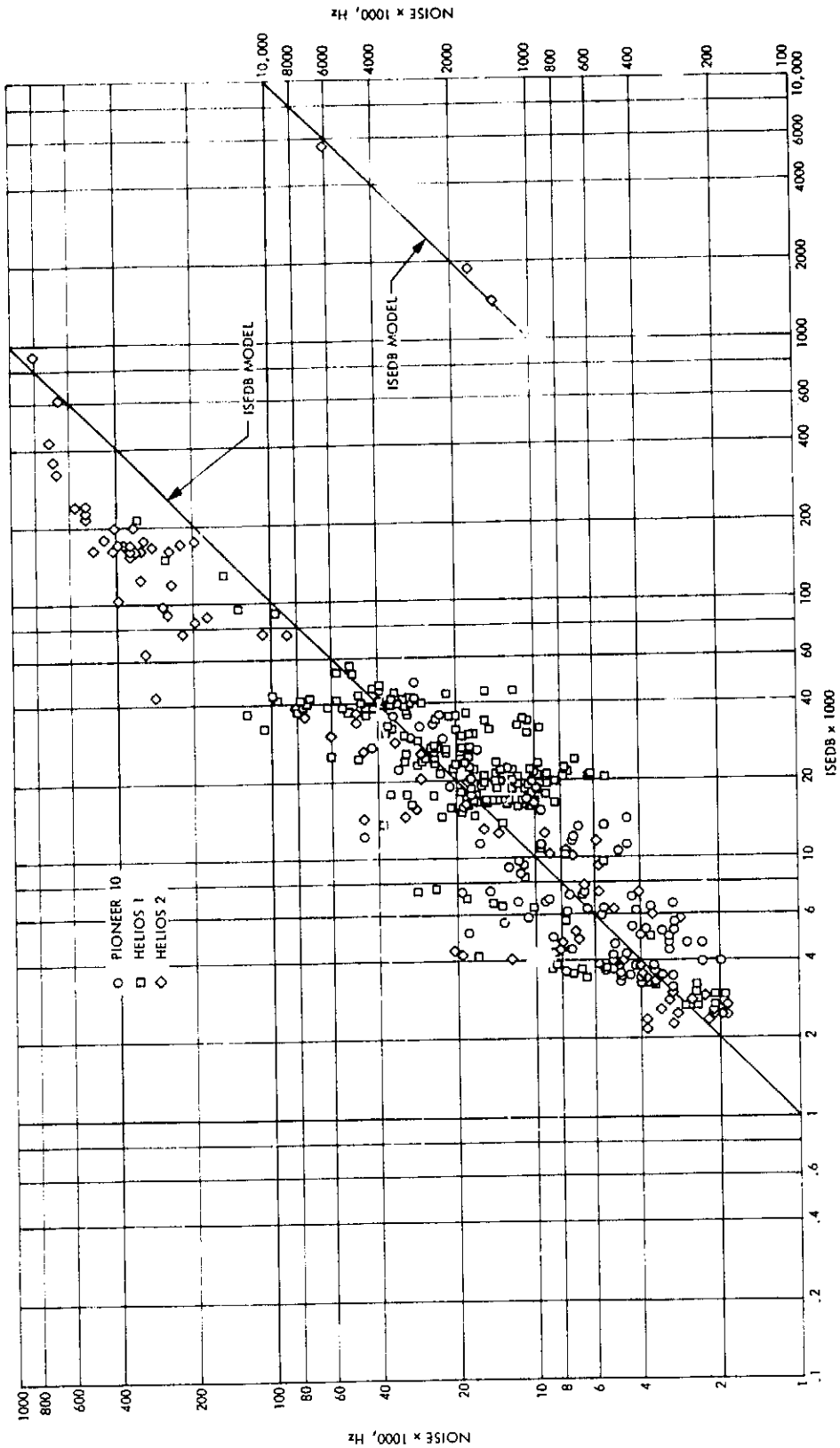

Fig. 4. Early 1976 solar conjunction mission composite, observed doppler noise vs the ISEDB model

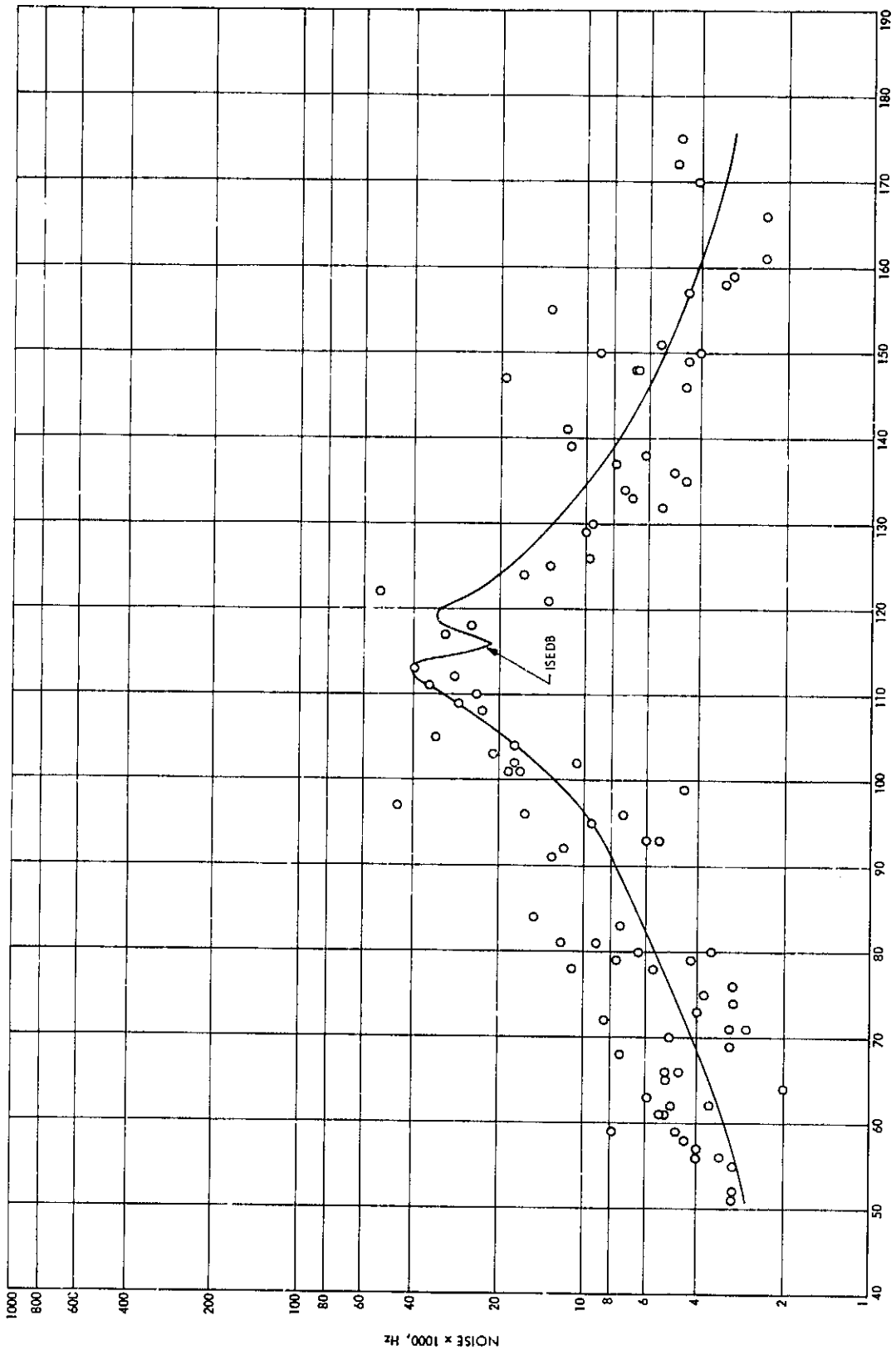

Fig. 5. Pioneer 10 1976 solar conjunction, observed doppler noise and the ISEDB model vs day of year

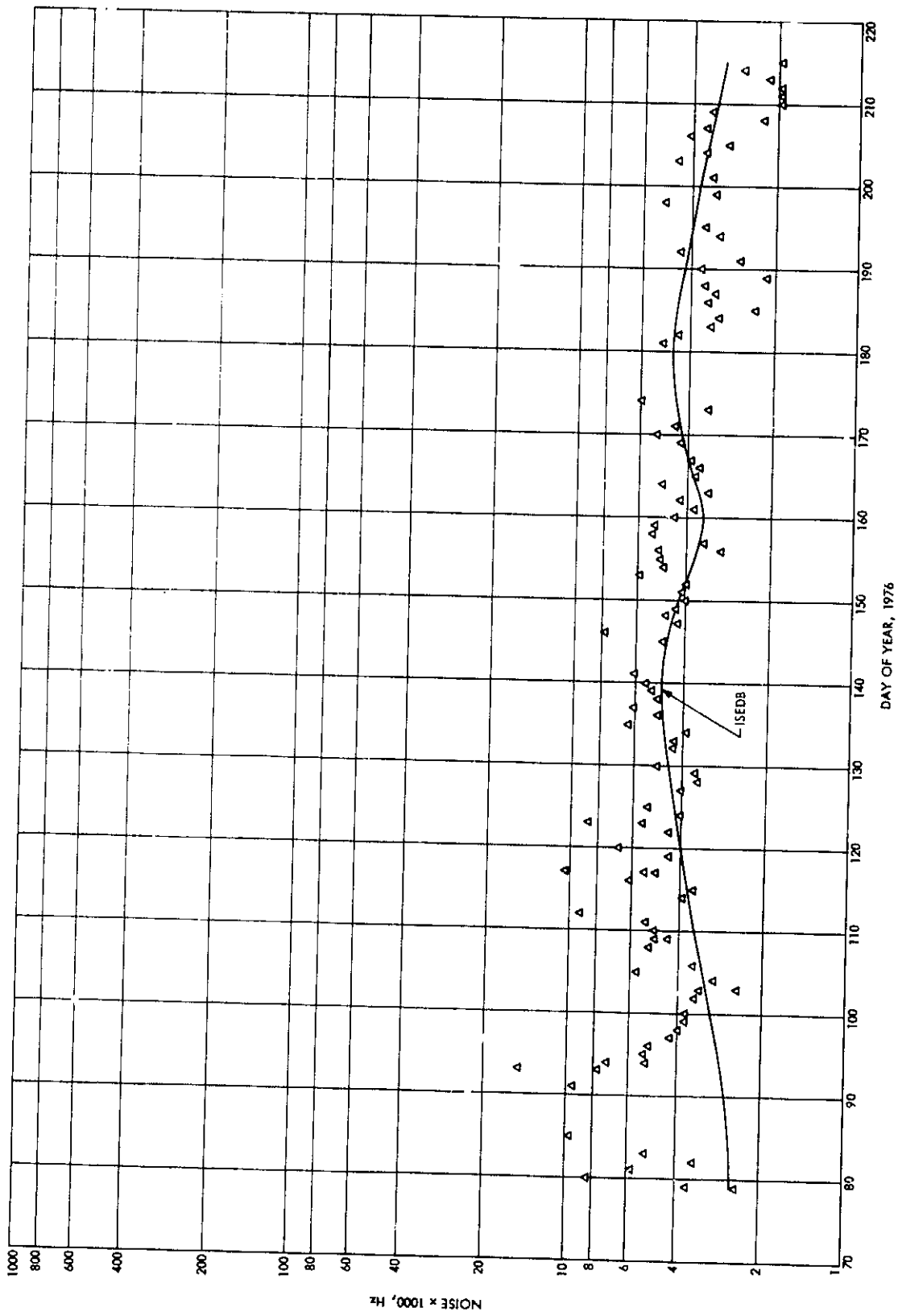

Fig. 6. Pioneer 11 1976 solar conjunction, observed doppler noise and the ISEDB model vs day of year

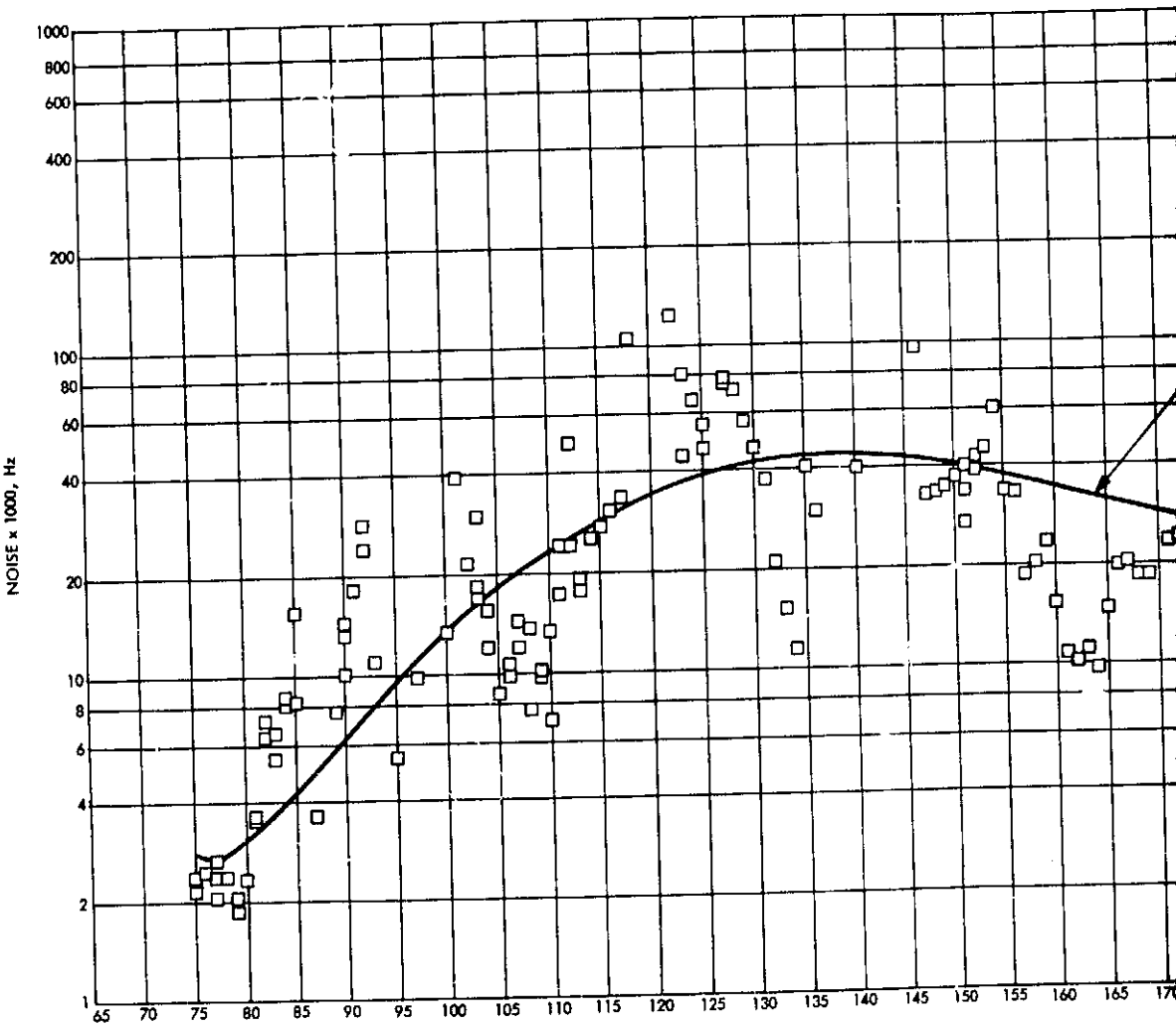

FOLDOUT FRAME 1

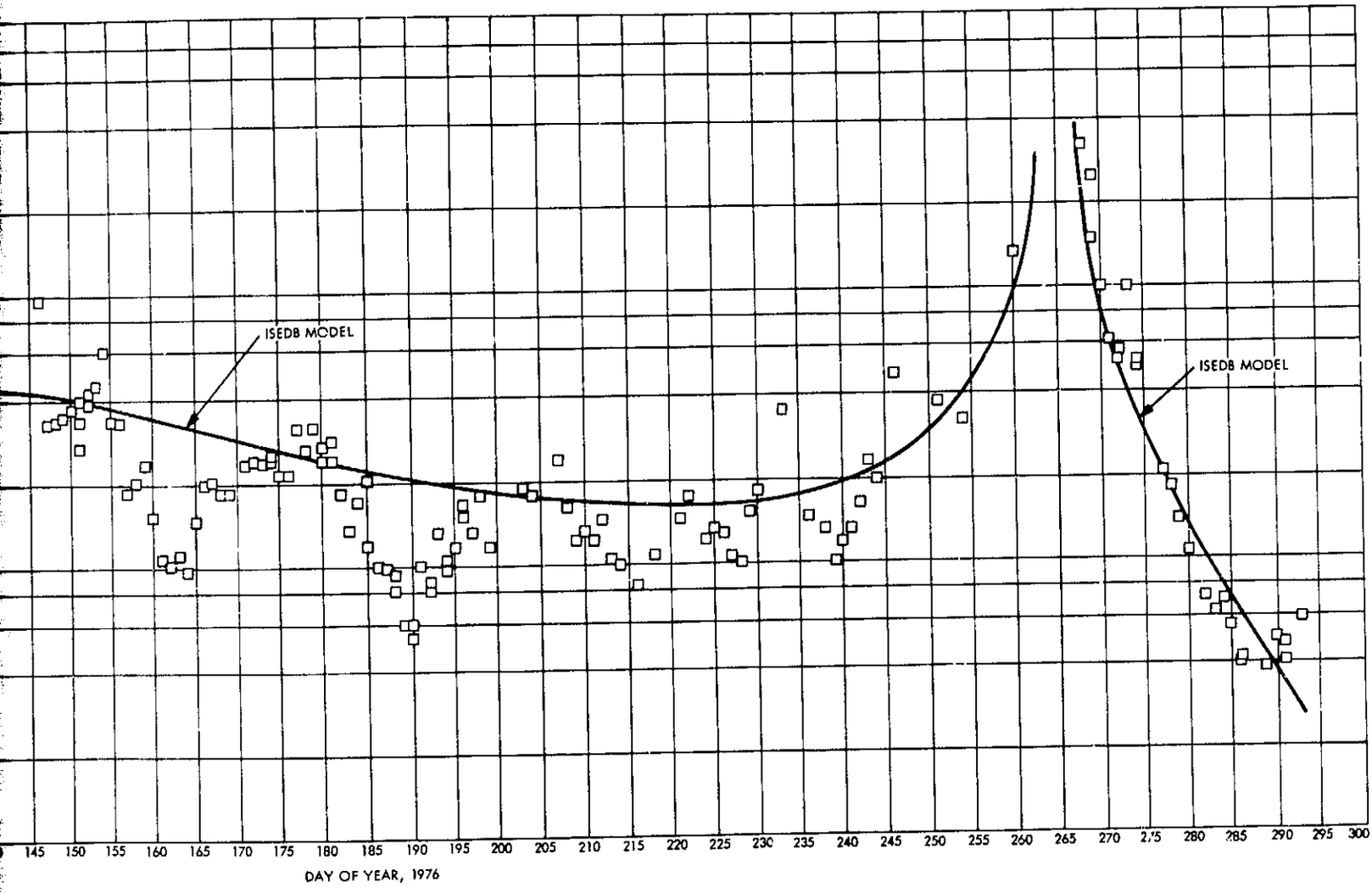

Fig. 7. Helios 1 1976 solar conjunction, observed doppler noise and the ISEDB model vs day of year

REPRODUCIBILITY OF THE
ORIGINAL PAGE IS POOR

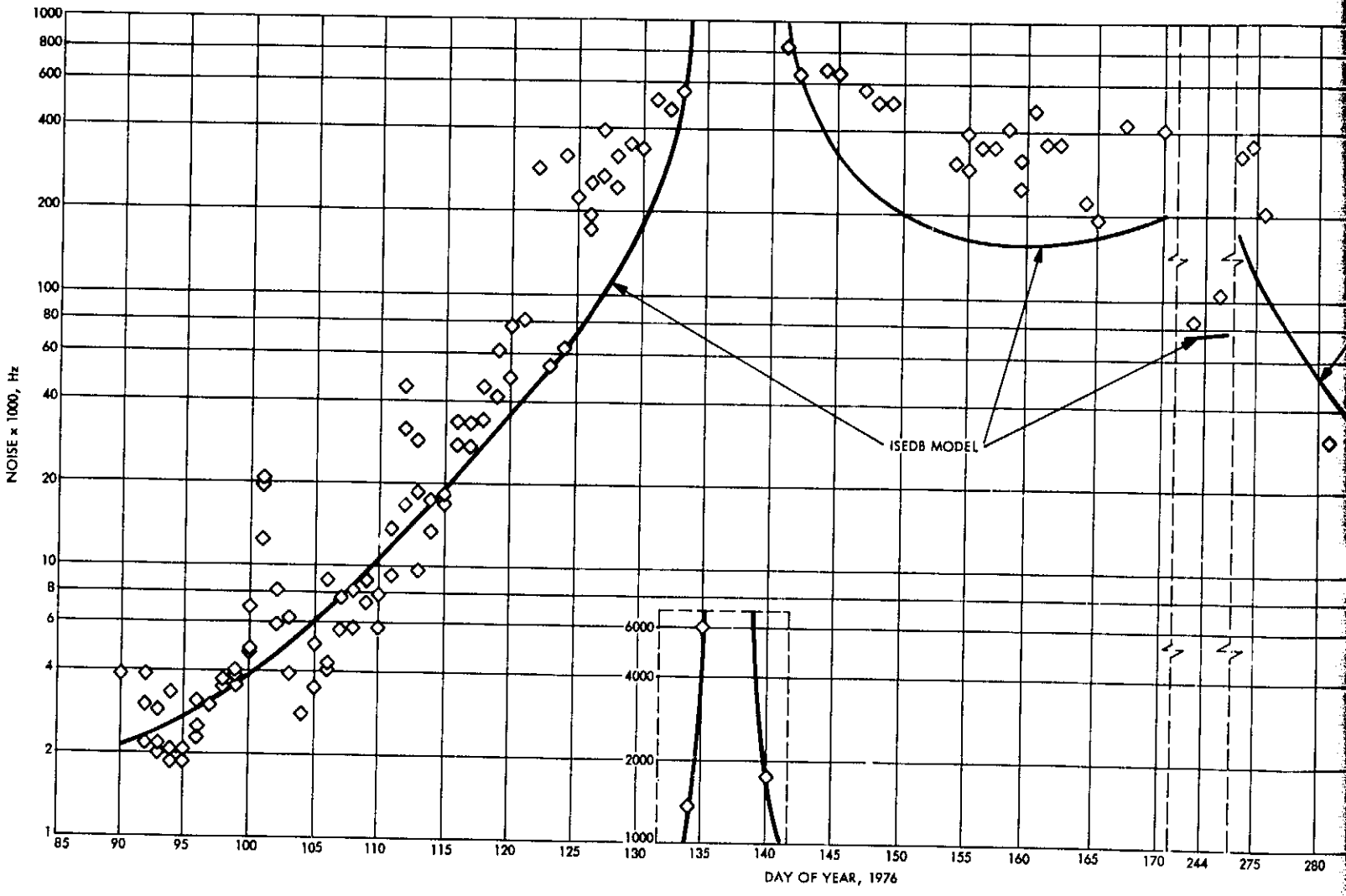

Fig. 8. Helios 2 1976 solar conjunction, observed doppler noise and the ISEDB model vs day of year

FOLDOUT FRA

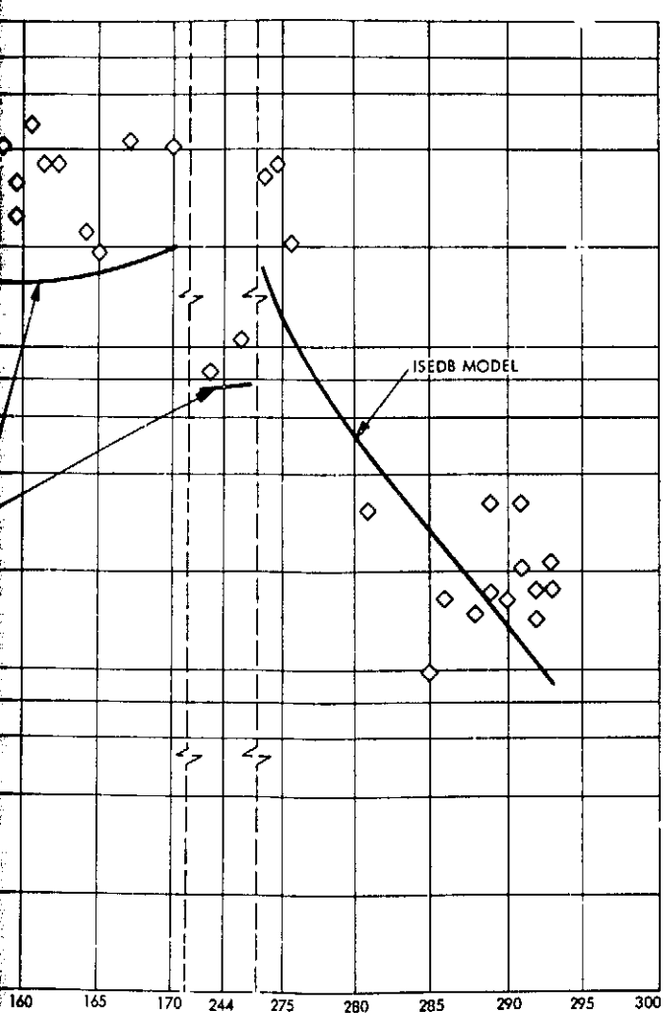
ISEDB MODEL
160
165
170
244
275
280
285
290
295
300

REPRODUCIBILITY OF THE
ORIGINAL PAGE IS POOR

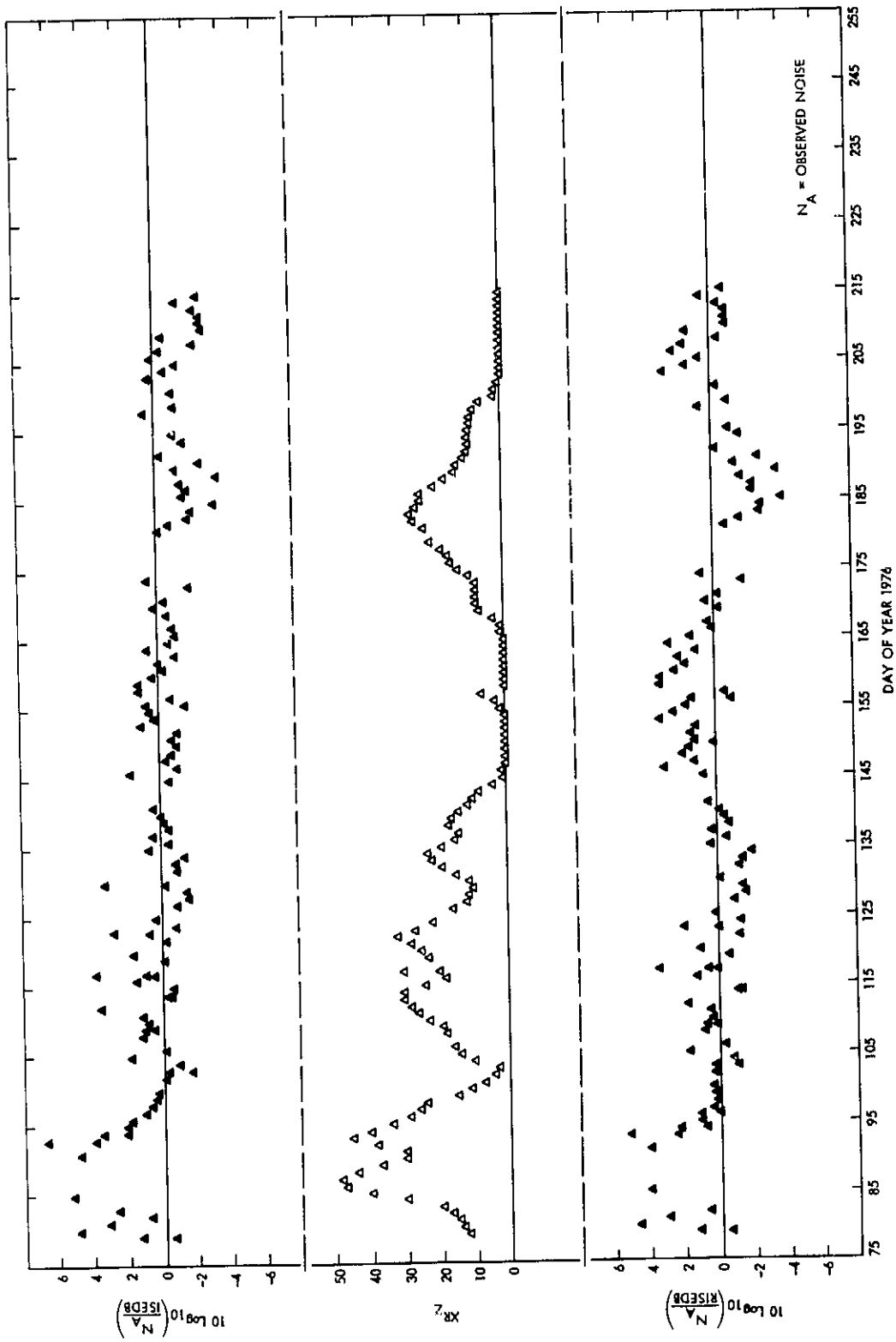

Fig. 9. Pioneer 11 1976 solar conjunction, ISEDB residuals, RISEDB residuals and (smoothed/phased) sunspots vs day of year

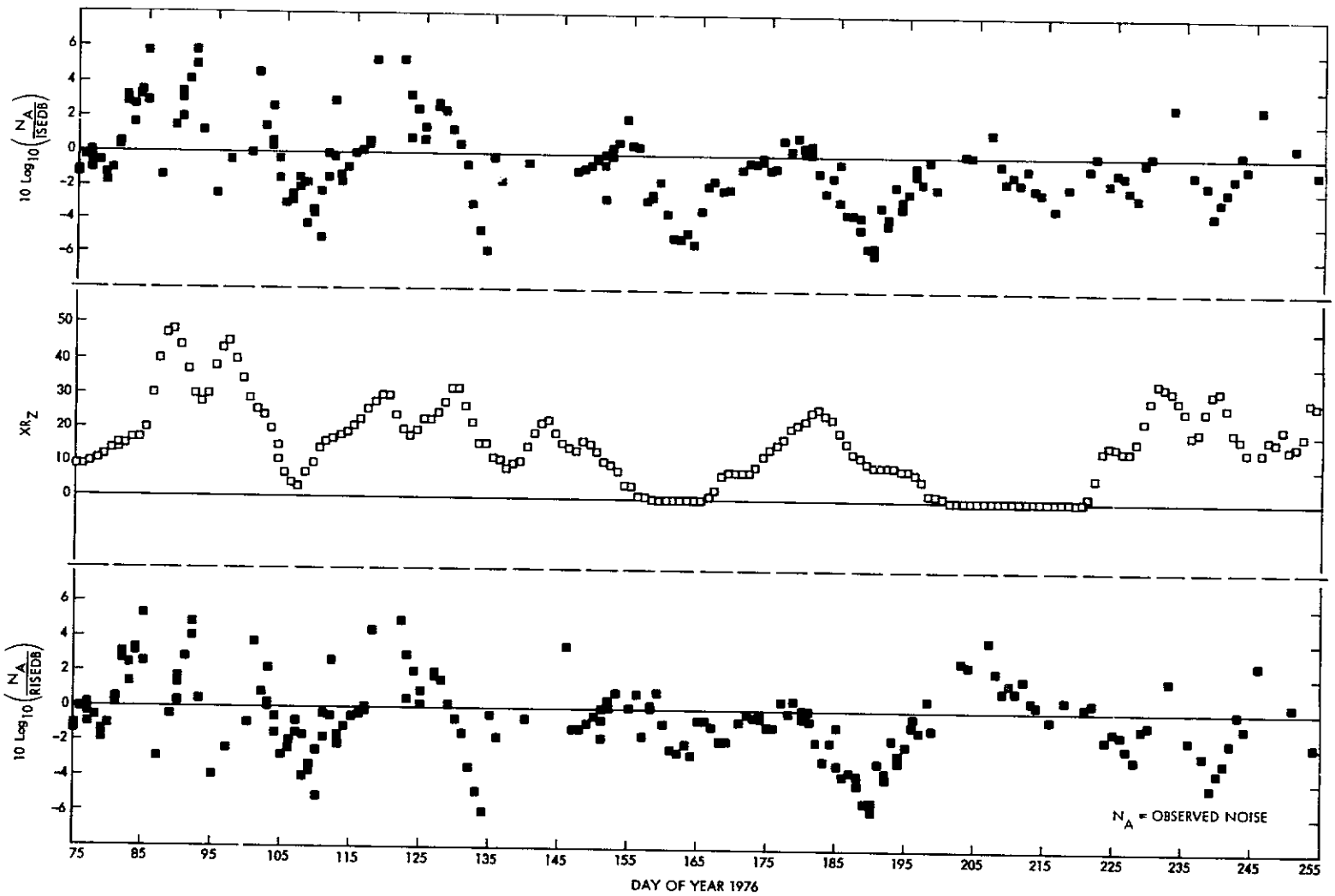

Fig. 10. Helios 1 1976 solar conjunction, ISEDB residuals, RISEDB residuals and (smoothed/phased) sunspots vs day of year

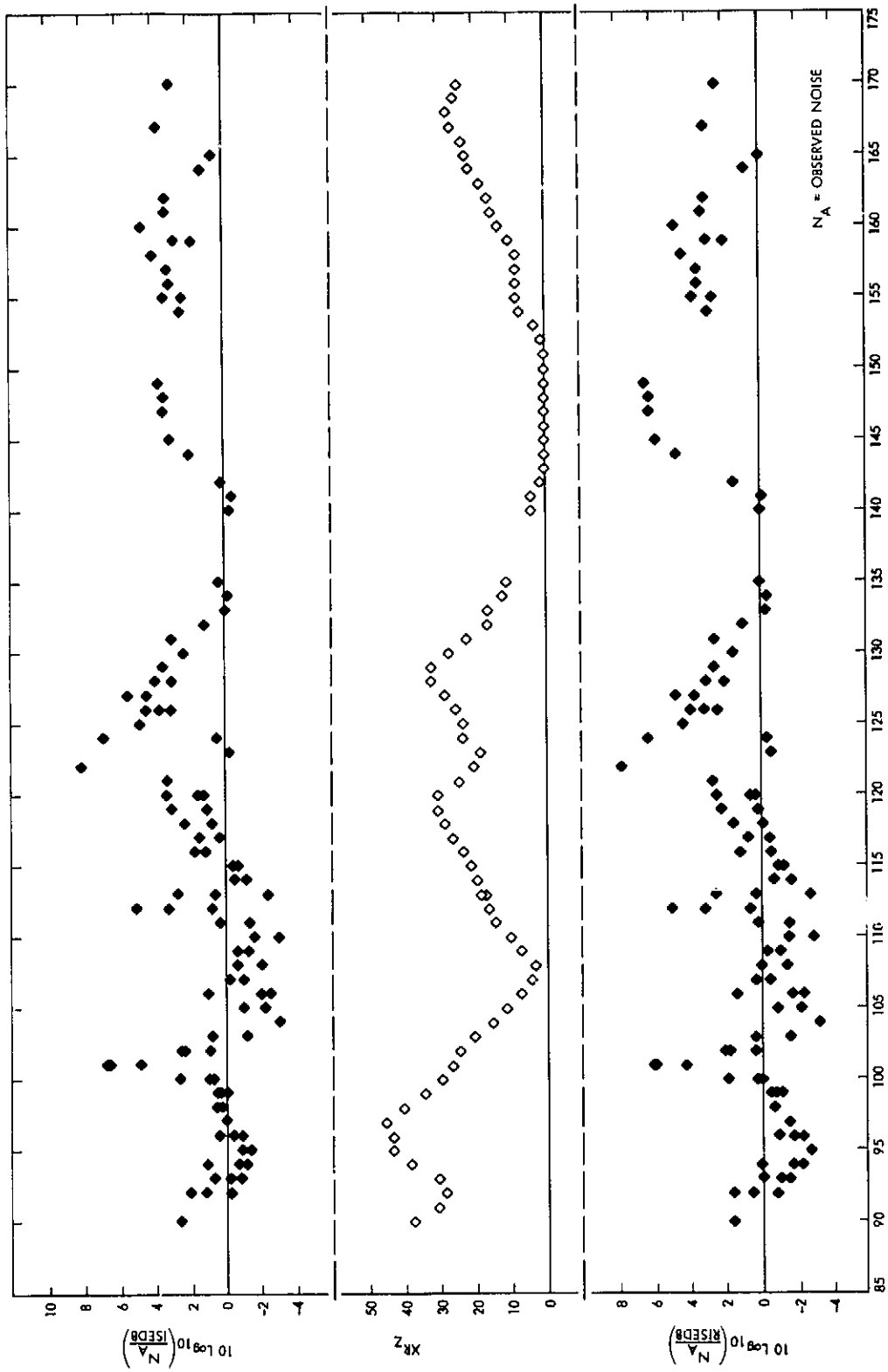

Fig. 11. Helios 2 1976 solar conjunction, ISEDB residuals, RISEDB residuals and (smoothed/phased) sunspots vs day of year

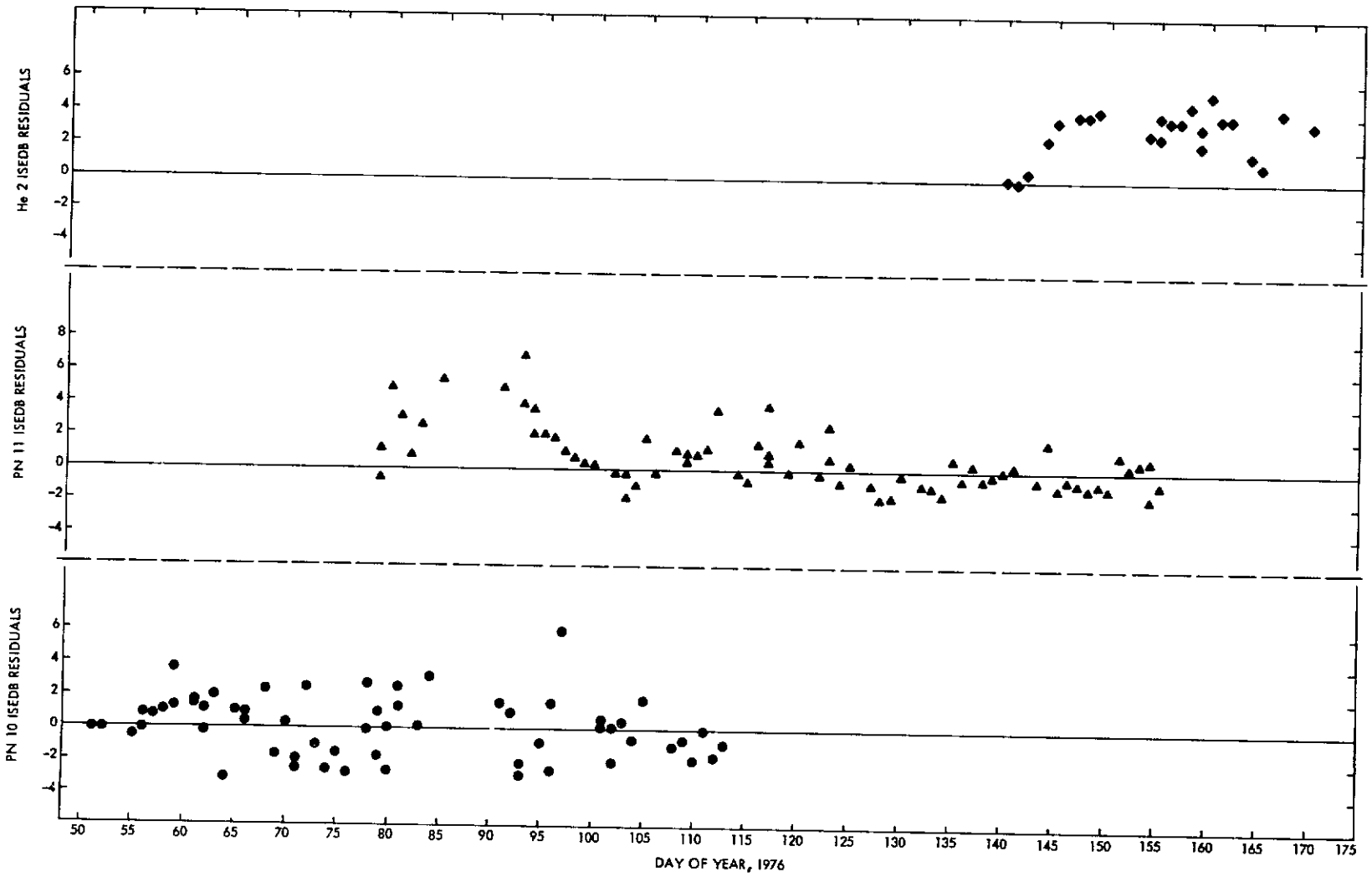

Fig. 12. Multispacecraft ISEDB residual comparisons for signal paths east of the sun

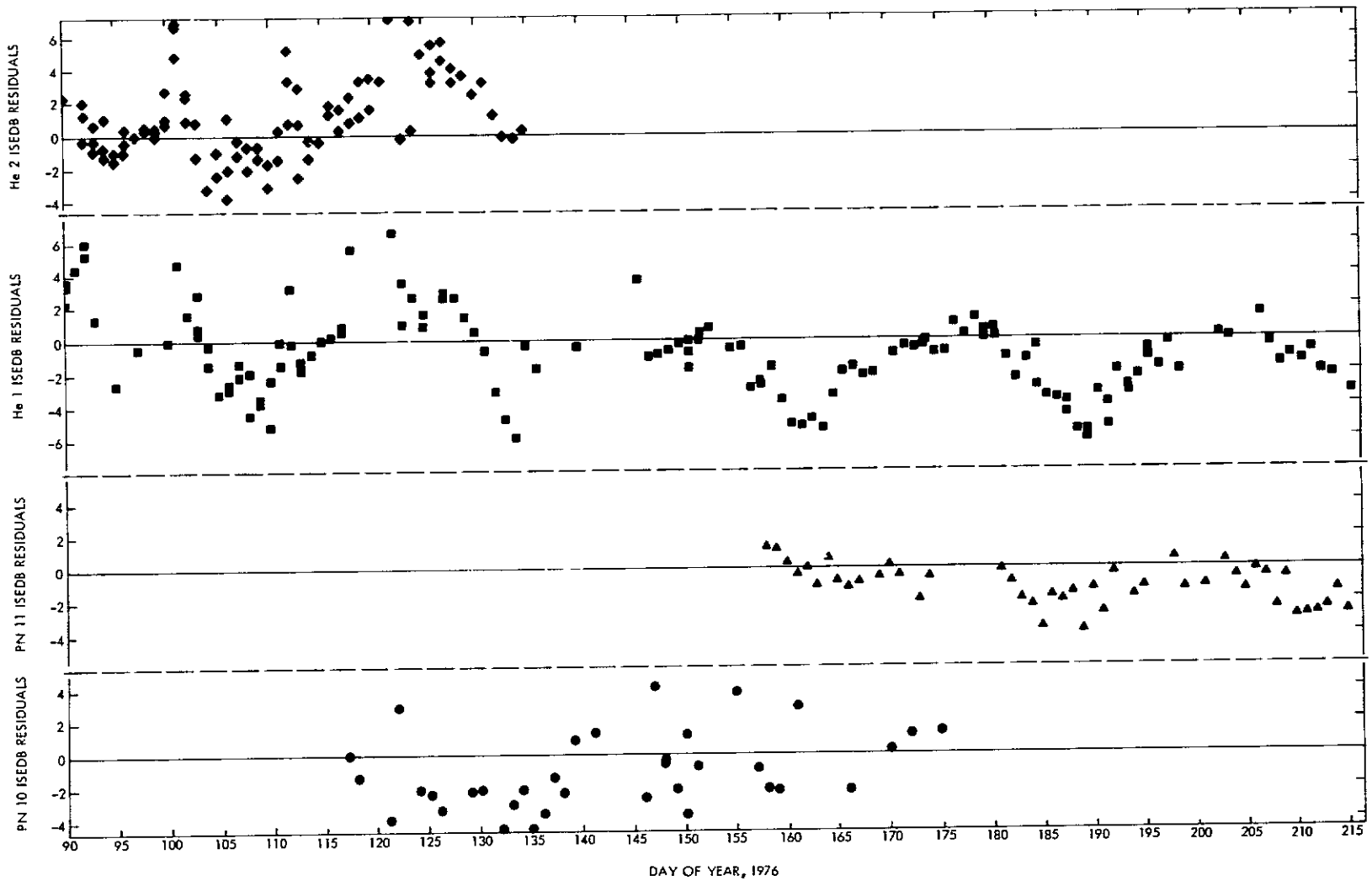

Fig. 13. Multispacecraft ISEDB residual comparisons for signal paths west of the sun

N77-14063

DSS Range Delay Calibrations: Current Performance Level

G. L. Spradlin
DSN Network Operations Section

It is the intent of this report to describe a task undertaken approximately 18 months ago, under the auspices of the Ranging Accuracy Team, to develop a means for evaluating Deep Space Station (DSS) range delay calibration performance, and through which inconsistencies frequently noted in these data could be resolved. Development of the DSS range delay data base is described. The data base is presented with comments regarding apparent discontinuities. Data regarding the exciter frequency dependence of the delay values are presented, and the report concludes by noting the improvement observed in the consistency of current DSS range delay calibration data over the performance previously observed.

I. Introduction

The measurement of the distance, or range, to a spacecraft, as accomplished by the DSN Ranging Subsystem, is essentially a precision measurement of the time interval between transmission and receipt of a binary-coded signal called the range code. Unfortunately, the time interval (from transmission to receipt of the range code) measured by the Ranging Subsystem is not the desired measurement. For the purposes of orbit determination, the measurement needed must be from the defined station location to a reference point on the spacecraft and back, and therefore, the delay actually measured by the Ranging Subsystem must be modified (corrected) to account for delays of the range code that are not part of this reference-point-to-reference-point measurement. Among other correction factors that must be applied to the measured value to obtain the desired value is the delay experienced by the range code as it passes through the station equipment, or the station range delay.

Historically, the station range delay has been considered one of the largest contributors to inaccuracies in spacecraft range measurements despite the measurement (calibration) of the station's range delay prior to and immediately after each spacecraft track during which range data were taken. Inconsistencies and apparent errors in the station range delay calibration could be expected to contribute at least several meters of uncertainty to the spacecraft range measurement. The inconsistencies of

station range delay calibrations were recognized by the Ranging Accuracy Team as being incompatible with the stringent range accuracy requirements of future missions, and hence, one of the initial tasks undertaken by the team was to develop a data base from which current performance could be ascertained, and improvement monitored. This report describes this effort, and delineates the current station range delay calibration performance.

II. Establishing The Data Base

It was decided in early June 1975 that the data base would not include any currently available data, nor would it include station range delay calibrations as reported via the station posttrack reports. Instead, each station capable of ranging was requested to perform special range delay calibration measurements.

To provide control over the conditions under which the measurements were to be made, each station was requested to use a specific set of parameters including specifications of range code component integration times, level of carrier suppression, downlink signal level, antenna pointing angles, and uplink power level. The report from the station was to include, in addition to the range delay calibration, five postrange acquisition Differenced Range Versus Integrated Doppler (DRVID) values so that the range delay calibration could be corrected for waveform distortion, exciter frequency, the number of the receiver used, and which maser was used.

It was originally thought that a one-month period of data collection would provide a sufficient data base; however, due to a lack of available time at the stations to perform unscheduled activities, far too few measurements were made available to constitute a data base. Time for the stations to take the needed measurements was then made available through the Deep Space Network (DSN) Scheduling Office. The measurements were to be made on a noninterference basis during or immediately after normal station posttrack countdown procedures. One-half hour was added to the allotted time for the normal posttrack procedures to help alleviate any time bind that might be caused by making the additional measurements. Measurements were scheduled to be made at each station as frequently as once per day with no more than seven days between measurements, depending upon station time availability. Also, the time span over which data would be collected was extended from the original one month period to a six-month period.

Coincident with the effort to establish a data base, a task was undertaken to reevaluate and update the standard pre- and posttrack range delay calibration procedures, including the reporting format (Post Track Report). Provisions were made in the new procedures to incorporate the controlled range delay calibration into the standard station procedures. The Post Track Report format was redesigned to provide detailed information regarding configuration, and to provide the needed data to ascertain the health of the ranging subsystem. The obvious advantage of the aforementioned incorporation is that the data base would now receive almost continuous inputs as a product of normal station operations, and station range delay calibration performance could be more closely monitored.

After a confidence-building period of approximately one month, the specially scheduled calibrations were discontinued, and the new Post Track Report was adopted as the data source for the data base. A copy of the portion of the new Post Track Report format containing range calibration information is shown as Fig. 1. Item A.3 contains the station range delay calibration data, and the necessary configuration information. The information used as input to the data base is found in items 3.(a).1 and .2, and 3.(b).1 and .2. The numbers reported here by the stations are converted from the frequency dependent unit of measurement (Range Unit, RU) output by the ranging subsystem, after adjustment by the DRVID correction, to meters (one-way) for ease of comparison with flight project navigation and radio science requirements, and for entry into the data base.

III. The Data Base

Station range delay calibration data extracted from the data base and plotted in meters (one-way) versus day of year are presented in Figs. 2 through 10. Specific station performance will not be detailed at this point. Instead, it is intended simply to present the data base, and to explain peculiarities, events, and characteristics that can be seen in the plotted data. A more detailed analysis of the data will be presented in a subsequent section of this report.

A. Goldstone, Pioneer, DSS 11

DSS 11 is the station to have most recently acquired a ranging capability, this event occurring approximately sixty days after data collection began from other stations. Early data from DSS 11 indicated that, for whatever reason, this station did not reflect the inconsistency of range calibrations noted in the early data from other stations. In fact, it became an interim goal to try to improve the performance of other stations to that level already being achieved at DSS 11. As indicated on this station's plot, an Engineering Change Order (ECO) that

altered the station range delay calibration path was installed temporarily, day 63 through day 70, and permanently on day 158. All calibrations indicated on this plot were made using Maser 1 and Receiver 1.

B. Goldstone, Mars, DSS 14

Figure 3 is a plot of DSS 14 S-band calibrations. All data were taken using the S-Band Polarization Diversity (SPD) maser and primarily Receiver 3 of the Block IV Receiver-Exciter Subsystem, although there is a scattering of points taken using Receiver 4. Also, all calibrations were made using the Block IV doppler translator instead of a dish mounted Zero Delay Device (ZDD); both devices perform the function of simulating a spacecraft by converting a transmit-level frequency to a receive-level frequency.

Prior to day 90, DSS 14, like other stations in the Network, utilized the Planetary Ranging Assembly (PRA) to conduct spacecraft ranging. On day 90 an R&D ranging machine, the MU II, was installed to provide range data enhancement for the Helios project at superior conjunction. The MU II has been retained at DSS 14, and is currently used for both Viking and Helios ranging operations.

Figure 4 presents DSS 14 X-band range calibrations. The family of points seven to eight meters below the major point grouping represents a periodically occurring anomaly that recently has been determined to be the result of a procedural error (incorrect switch position) during the range delay measurement.

C. Australia, Weemala, DSS 42

DSS 42 range calibrations presented in Fig. 5 were taken using Receiver 5, Maser 1, and a dish-mounted ZDD.

As mentioned earlier, DSS 11 did not indicate the inconsistency in range calibrations noted elsewhere in the Network. As data collection progressed, it became quite clear that DSS 42 was unable to provide consistent calibrations, and that the problem was not due to an equipment failure, nor was it procedural in nature. It also became clear that DSS 42 range calibrations were highly exciter reference frequency dependent, and that the calibrations at DSS 11 were not. Further, it was found that the locations of the dish-mounted ZDDs at these two stations were radically different, and that a poor location of the ZDD could result in the calibration inconsistency being observed, the apparent result of signal multipath effects. A pragmatic decision was made to relocate the DSS 42 ZDD to a position on the antenna identical to that where the ZDD was located on the DSS 11 antenna. This was done on day 114 with an obvious and dramatic reduction in range calibration inconsistency. An additional small step in the plotted calibrations can be seen to occur on day 140 coincident with a klystron change.

D. Australia, Ballima, DSS 43

DSS 43 calibrations presented in Fig. 6 reflect a multiplicity of configurations. The majority of data collected prior to day 30 of 1976 were taken using the Block III Receiver-Exciter Subsystem, Receiver 1, the SPD Maser, and a dish-mounted ZDD. After day 30, the Block IV Receiver-Exciter Subsystem became the prime data source, and data from Receivers 3 and 4 in conjunction with the SPD maser are represented. As with DSS 14, all Block IV measurements utilized the Block IV doppler translator.

Calibrations made at DSS 43, while using the dish-mounted ZDD, again indicate a strong exciter-frequency dependence. The apparent increase in the calibration measurement after day 260 of 1975 resulted from work done in the tricone area of the antenna, but did not appear to significantly alter the apparent frequency dependence of the dish-mounted ZDD calibrations.

The cause of the dramatic improvement indicated after day 140 is not clearly understood, but it is felt to be the result of possibly two things: (1) stringent configuration control exercised per Viking project requirements, and (2) a significant decrease in the frequency dependence of range calibrations made using the doppler translator (possibly due to an inadvertent but fortunate elimination of a multipath or leakage problem).

Figure 7 presents DSS 43 X-band range calibration data. Again a distinct change in the plot occurs at day 140. With the exception of the anomalous calibrations reported on day 142 and day 162, all calibrations after day 140 fall into one of two distinct families of points. Tests conducted at DSS 43 indicate that while there is only a minor change in the S-band range calibration value as exciter frequency is changed, the change in the X-band calibration value is quite significant. This the two families are not unexpected, as the upper grouping of points represents calibrations extracted from Viking Orbiter 1 Post Track Reports (i.e., the calibrations were made in the region of frequency channel nine), and the lower point grouping from Viking Orbiter 2 Post Track Reports (calibrations made in the region of frequency channel 20).

E. Spain, Robledo, DSS 61

DSS 61 range delay calibrations shown in Fig. 8 were made using Receiver 5, Maser 1, and a dish-mounted ZDD.

The small grouping of points between days 261 and 282 of 1975 at approximately the 360-meter level reflects the temporary insertion of an additional cable in the range delay calibration path during station troubleshooting of a ranging subsystem problem. There is no available explanation for a similar family of points between days 43 and 76 of 1976.

Although it is not obvious by inspection of DSS 61 range delay calibrations presented on Fig. 8, tests conducted at DSS 61 indicated that this station's range calibration value was also exciter-frequency dependent and, like DSS 42, the DSS 61 ZDD was relocated to a position similar to the DSS 11 ZDD location on that antenna. The ZDD relocation occurred on day 77 of 1976, after which a clear improvement was observed in the range calibration consistency. An additional discontinuity and noted increase in frequency dependence is observed on day 139, coincident with an S-band mixer change.

F. Spain, Robledo, DSS 63

Like DSS 43, DSS 63 range calibrations presented in Fig. 9 indicate that a number of configurations were used for calibrations at this station through day 125 of 1976. Data prior to day 300 of 1975 reflect use of the Block III Receiver 1, the SPD maser, and a dish-mounted ZDD. Measurements after day 4 and before day 112 reflect mixed use of Block IV Receivers 3 and 4, the SPD maser, and the Block IV doppler translator. With the exception of four points, all measurements after day 112 were made using Receiver 3, the SPD maser, and the Block IV doppler translator.

Use of the high-power klystron at DSS 14 and DSS 43 has not been mentioned, as use of this device has not had a significant impact on the reported range delay calibration. This statement cannot be made of calibrations reported at DSS 63. For an unknown reason the use of the high-power klystron at DSS 63 does result in a significantly different range delay. The family of points between 648 and 651 meters reflects its use.

The increased point-to-point consistency of calibrations after day 135 is again attributed to tight station configuration control, a result of Viking Project support.

Figure 10 presents DSS 63 X-band range calibration data. The data were taken using primarily Receiver 4; however, a scattering of points representing Receiver 3 is also present.

The family of points between roughly 624 meters and 628 meters is representative of use of the high-power klystron (denoted by the "H," above the plotted point), and an anomaly recently traced to a faulty relay in the Block IV X-band doppler translator.

Again there is a general reduction in the scatter of the calibrations after day 130, and as with the S-band calibrations, it is felt this phenomenon is attributable to configuration control.

IV. Calibration Performance Analysis

The frequency dependence of the station range delay calibrations has been mentioned numerous times in the preceding section of this report. The cause of the frequency dependence of the range delay is not clearly understood as of this writing. In fact, the extent to which it is a problem is also not clear. In an effort to understand how the range delay varies as a function of frequency, each station capable of ranging has been requested to conduct a "Range Delay Versus Frequency Test." Essentially, the test simply provides calibration data at channel center frequencies, channels 5 through 26.

It was previously mentioned that DSS 11 did not reflect the frequency dependence noted in data from DSS 42 and DSS 61, and that the ZDDs at DSS 42 and DSS 61 were relocated to agree positionally with the DSS 11 ZDD location, in an apparently successful attempt to reduce the DSS 42 and 61 frequency dependencies. Figure 11 presents the results of a range delay versus frequency test conducted at DSS 11 on day 252 of 1975. Clearly, there is a variation of the range delay with change in frequency; however, the peak-to-peak change is only about 1.5 meters. Compared to the approximate 8-meter and 7-meter changes seen on Figs. 12 and 13 (DSS 42 and DSS 61, respectively) DSS 11 appears relatively insensitive to changes of frequency.

Figures 14 and 15 present DSS 42 and DSS 61 range delay versus frequency data after relocation of their ZDDs. The reduction in frequency dependence is noticeably significant with both stations showing a range delay variation with frequency change of roughly 2 to 3 meters peak-to-peak.

Tests run at DSS 14 and DSS 43 also indicate a range delay variation with frequency change. The results of the DSS 14 test are shown in Fig. 16 (S-band) and Fig. 17 (X-band) with indicated peak-to-peak changes of approximately 6 meters and 3 meters respectively. The DSS 43 results shown in Fig. 18 (S-band) and Fig. 19 (X-band) indicate an S-band peak-to-peak change of about 3 meters, and an X-band peak-to-peak change of roughly 6 meters, and for an unknown reason, a significantly different profile.

Test data from DSS 63 are not yet available; however, inspection of range delay information in the data base indicates that neither the S-band nor X-band range delay calibrations vary significantly as a function of frequency.

Each spacecraft tracked by the DSN is assigned and communicates within a particular frequency channel. All station range delay calibrations made and reported via the Post Track Report are measured at a frequency within the frequency channel assignment of the spacecraft whose track is being reported upon. With the information presented above (a station's range delay calibration is frequency dependent), the consistency or repeatability of a station's range delay calibration cannot clearly be ascertained without consideration of the spacecraft (or spacecraft frequency channel assignment) as an independent variable. That is, the determination of the consistency of a station's range delay calibration should be based upon a consistent spacecraft (i.e., consistent frequency), as much as it would upon use of a consistent station hardware configuration (same receiver, same maser, etc.).

The data presented in the data base consist primarily of range delay calibrations extracted from Post Track Reports for Viking Orbiter 1 (VO-1) and Viking Orbiter 2 (VO-2). The information presented in Table 1 describing station range delay calibration performance was constructed considering the spacecraft as an independent variable. The mean and standard deviation (1 σ) were computed using the last N range delay calibrations (excluding known anomalous points mentioned earlier) reported from each station. The mean for each configuration has been indicated on the data base plots (Figs. 2 through 10). Only those station hardware configurations recently and frequently used have been considered.

It was mentioned at the beginning of this report that station range delay calibrations have historically been considered a major source of inaccuracies in the measurement of spacecraft range, and that the inconsistencies in the station calibrations were suspected to have contributed up to several meters of uncertainty to the range measurement.

Data presented in Figs. 2 through 10 clearly indicate that unexplained point-to-point inconsistencies of from 5 to 10 meters were commonplace in the calibrations recorded during the first several months of data collection. The data base also delineates that by relocation of the ZDDs at DSS 42 and DSS 61, stringent configuration control at all stations, an increasing knowledge of the sensitivity of the range delay to many variables, and continuous monitoring and feedback regarding calibration performance to the stations, the consistency of the calibrations has been greatly increased, and point-to-point consistency of less than one meter (1 σ) is the current level of performance.

V. Summary

Station range delay calibrations have long been considered one of the major contributors to inconsistencies observed in spacecraft range measurements. Recognition of this plus knowledge of future mission needs for highly accurate range data led to an effort undertaken by the Ranging Accuracy Team, to acquire knowledge regarding the current ability of the Network to provide consistent range delay calibrations, and to develop a data base through which improvements in calibration performance could be monitored.

It has been the intent of this report to describe the data base development, graphically present the data base, and to provide some explanation of trends or characteristics that are observed in the graphical presentation. A substantial amount of data is presented regarding one easily discernible characteristic—the frequency dependence of the range delay.

Table 1 is presented at the conclusion of the analysis section, and provides a summary of station range delay calibration performance. The mean and standard deviations for each frequently used station configuration (receiver, maser, and spacecraft) are presented. It can be seen that station calibrations are now quite consistent, with the standard deviations being generally less than one meter. This represents a significant improvement over the 5- to 10-meter variations observed early during the data base development.

Table 1. Station range delay calibration performance

DSS	Configuration	N	MEAN, m	σ, m
11	RCVR1/TWM1/VO-1	33	307.0	0.4
	RCVR1/TWM1/VO-2	62	306.2	0.4
14	RCVR3/SPD/VO-1	57	493.5	0.5
	RCVR3/SPD/VO-2	30	495.6	0.4
	RCVR4/XRO/VO-1	53	481.7	0.6
	RCVR4/XRO/VO-2	23	482.5	0.3
42	RCVR5/TWM1/VO-1	8	381.7	0.6
	RCVR5/TWM1/VO-2	33	382.1	0.5
43	RCVR3/SPD/VO-1	43	509.1	0.3
	RCVR3/SPD/VO-2	22	508.7	0.3
	RCVR4/XRO/VO-1	41	498.0	0.7
	RCVR4/XRO/VO-2	20	494.7	0.6
61	RCVR5/TWM1/VO-1	12	353.5	0.9
	RCVR5/TWM1/VO-2	35	350.9	0.7
63	RCVR3/SPD/VO-1	36	656.7	0.5
	RCVR3/SPD/VO-2	29	657.3	0.5
	RCVR4/XRO/VO-1	31	634.1	0.5
	RCVR4/XRO/VO-2	29	635.0	0.5

A. MISSION INDEPENDENT.

1. DSS_____; DAY_____; PASS_____: MISSION_____; S/C ID_____.

2. ACQUISITION_____Z; END OF TRACK_____Z.

3. RANGE DELAY:

(a) S-BAND PRETRACK MEASUREMENTS AT -150 DBM (1, 2) AND AT EXPECTED SIGNAL LEVEL (3, 4):

1. RANGE _____ RU; DRVID ____ RU; S/L -150 DBM; RDA ATTR_____ DB
2. RANGE _____ RU; DRVID ____ RU
3. RANGE _____ RU; DRVID ____ RU; S/L _____DBM; RDA ATTR_____ DB
4. RANGE _____ RU; DRVID ____ RU

XMTR PWR___KW; EXC NO. _____; TWM _____ ; RCVR NO. _____
EXC FREQ _____ HZ; CARRIER SUPPRESSION (3 and 4) _____ DB

(b) X-BAND PRETRACK MEASUREMENTS AT -150 DBM (1, 2) AND AT EXPECTED SIGNAL LEVEL (3, 4):

1. RANGE _____ RU; DRVID ____ RU; S/L -150 DBM; RDA ATTR_____ DB
2. RANGE _____ RU; DRVID ____ RU
3. RANGE _____ RU; DRVID ____ RU; S/L _____DBM; RDA ATTR_____ DB
4. RANGE _____ RU; DRVID ____ RU

TWM_____ ; RCVR NO. _____

(c) S-BAND POST TRACK MEASUREMENTS AT ACTUAL SIGNAL LEVEL OF THE PASS:

RANGE _____ RU; DRVID ____ RU; S/L_____DBM; RDA ATTR_____
RANGE _____ RU; DRVID ____ RU
XMTR PWR___KW; EXC NO. _____; TWM _____ ; RCVR NO. _____
EXC FREQ_____HZ; CARRIER SUPPRESSION_____ DB
XMTR PWR DURING PASS_____ KW; KLYS NO. _____

(d) X-BAND POST TRACK MEASUREMENTS AT ACTUAL SIGNAL LEVEL OF THE PASS:

RANGE _____ RU; DRVID ____ RU; S/L_____ DBM; RDA ATTR_____
RANGE _____ RU; DRVID ____ RU

TWM_____ ; RCVR NO. _____

(e) REMARKS: *

4. STATION TIME OFFSET WITH RESPECT TO DSN MASTER:

(a) OFFSET_____, UNCERTAINTY _____REFERENCED TO___**_____.

(b) TIMING SYSTEM RESET SINCE LAST POST TRACK REPORT:
MAGNITUDE _____, DIRECTION _____.

5. SYSTEM NOISE TEMPERATURE _____ DEG. K

6. EQUIPMENT FAILURES OR ANOMALIES (indicate start and end times or start and estimated time for return to operation. Reference TFR(s) and DR(s).)

Fig. 1. Post Track Report format

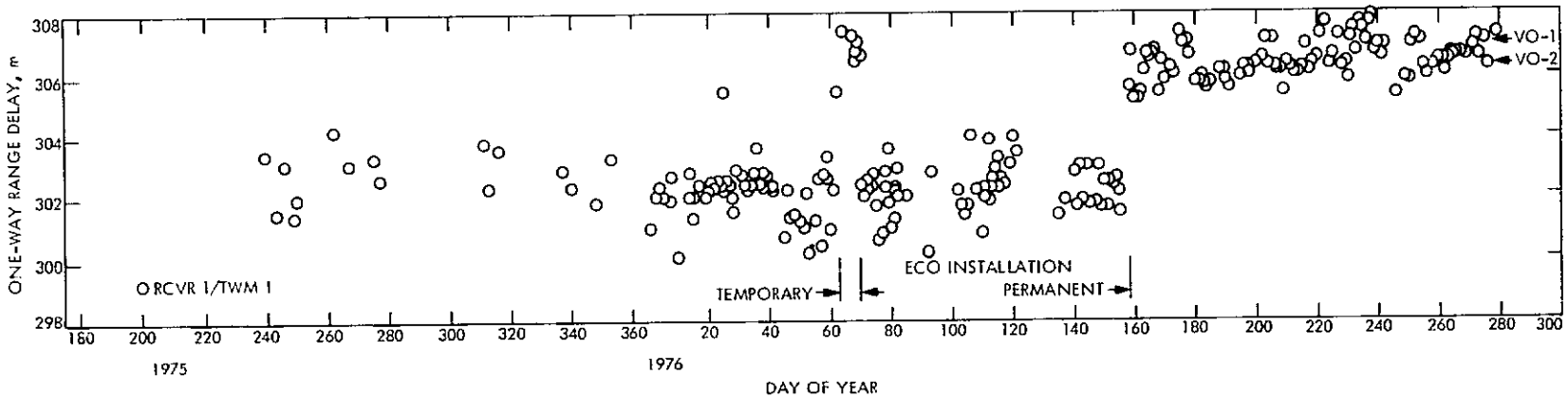

Fig. 2. Station range delay calibration data, DSS 11

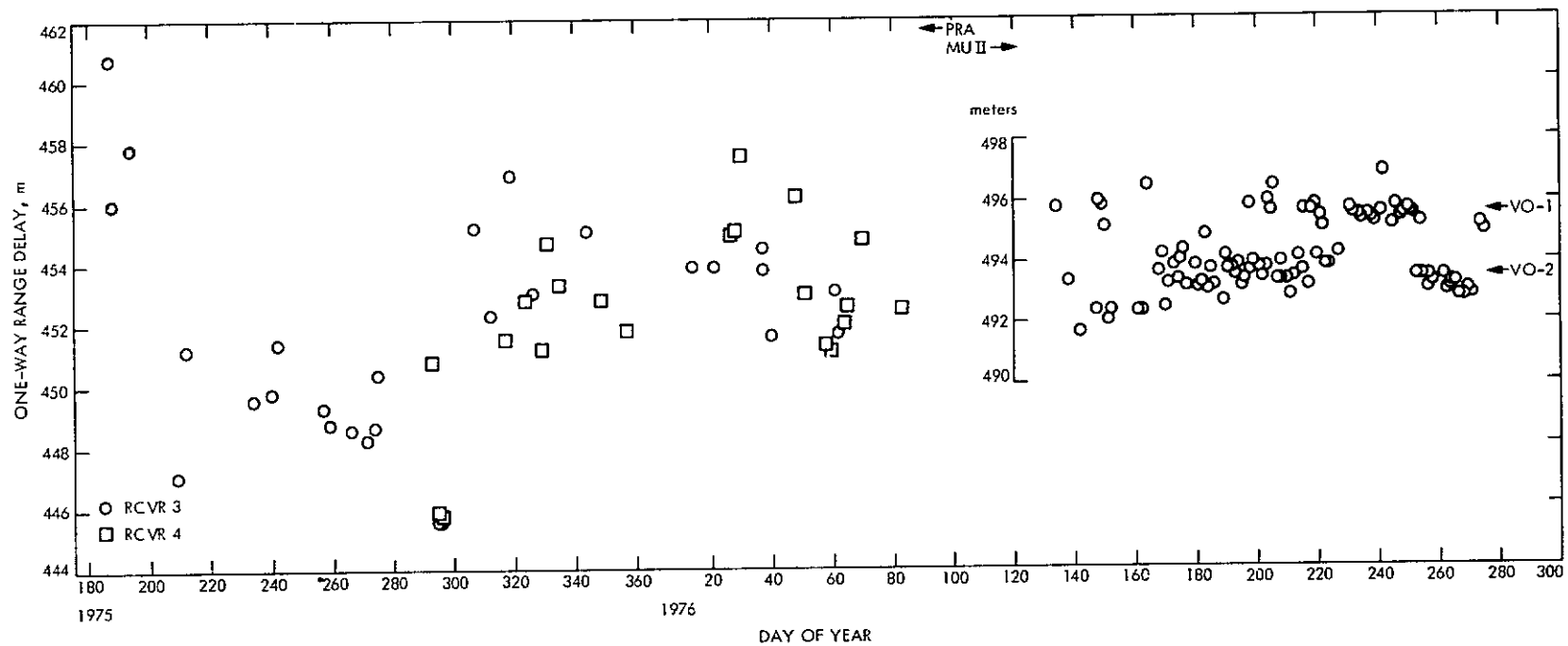

Fig. 3. Station range delay calibration data, DSS 14 S-band

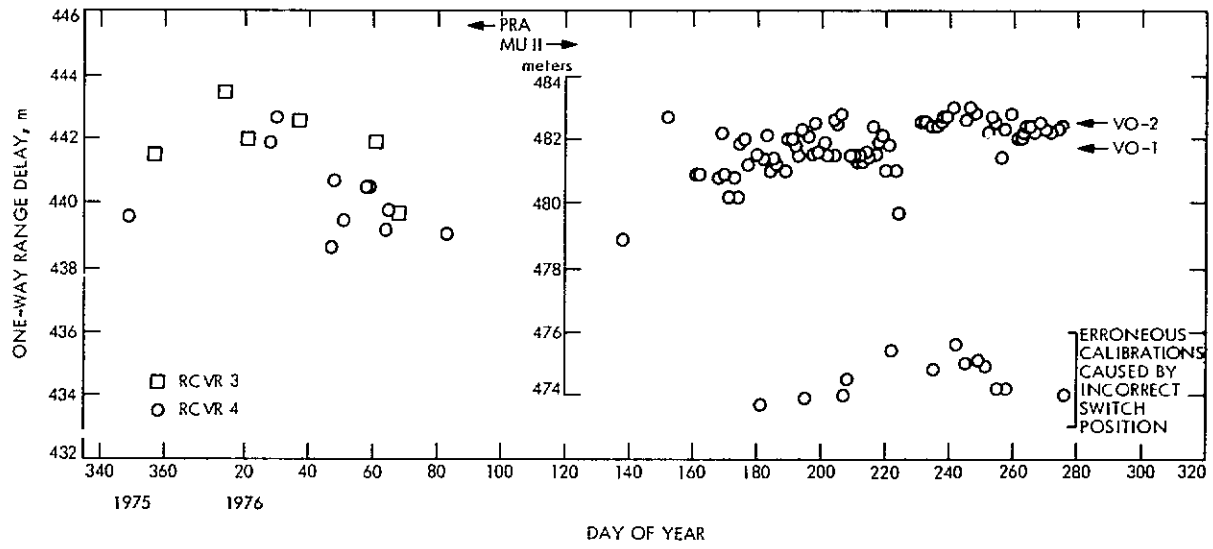

Fig. 4. Station range delay calibration data, DSS 14 X-band

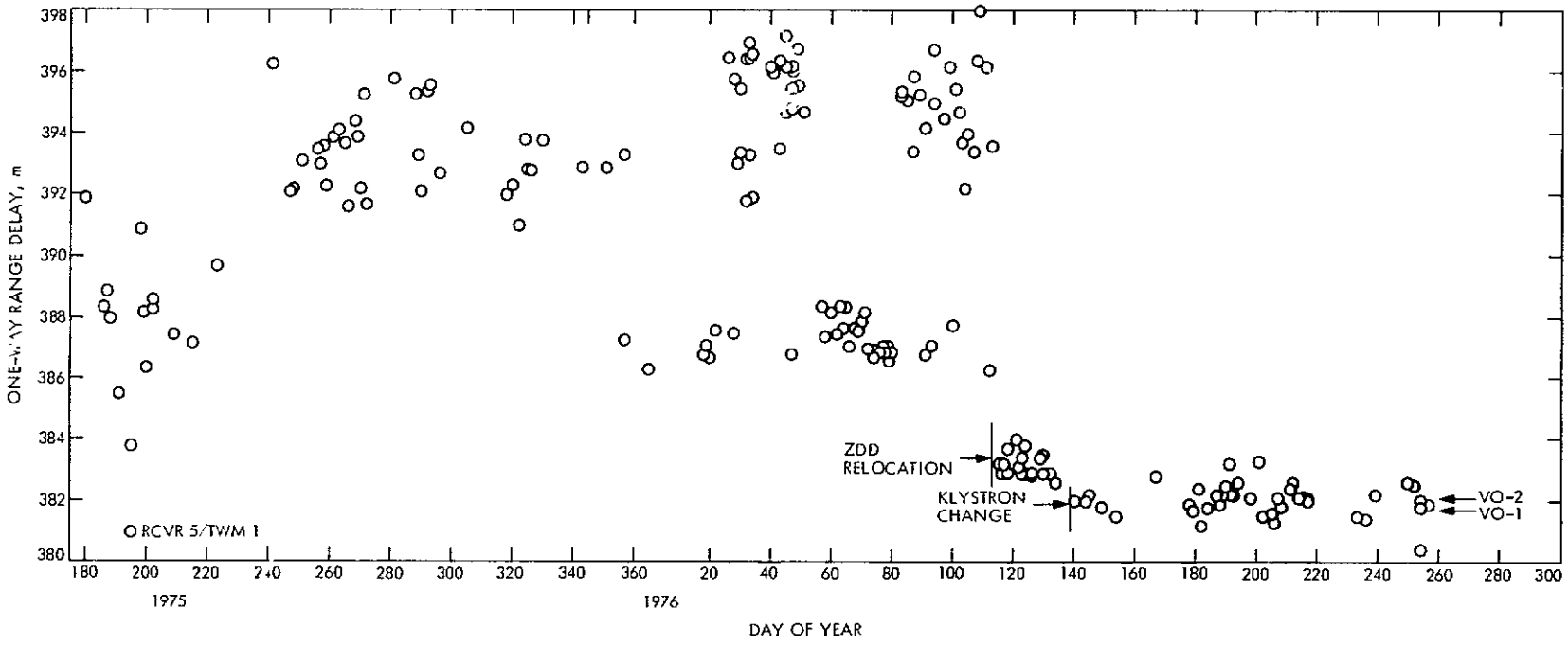

Fig. 5. Station range delay calibration data, DSS 42

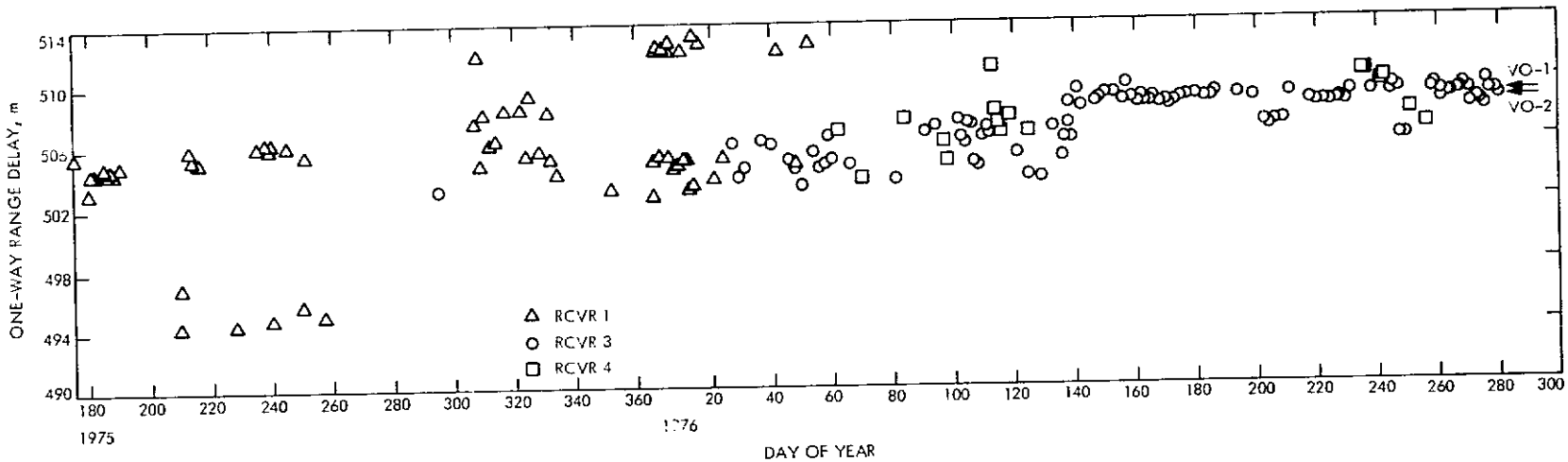

Fig. 6. Station range delay calibration data, DSS 43 S-band

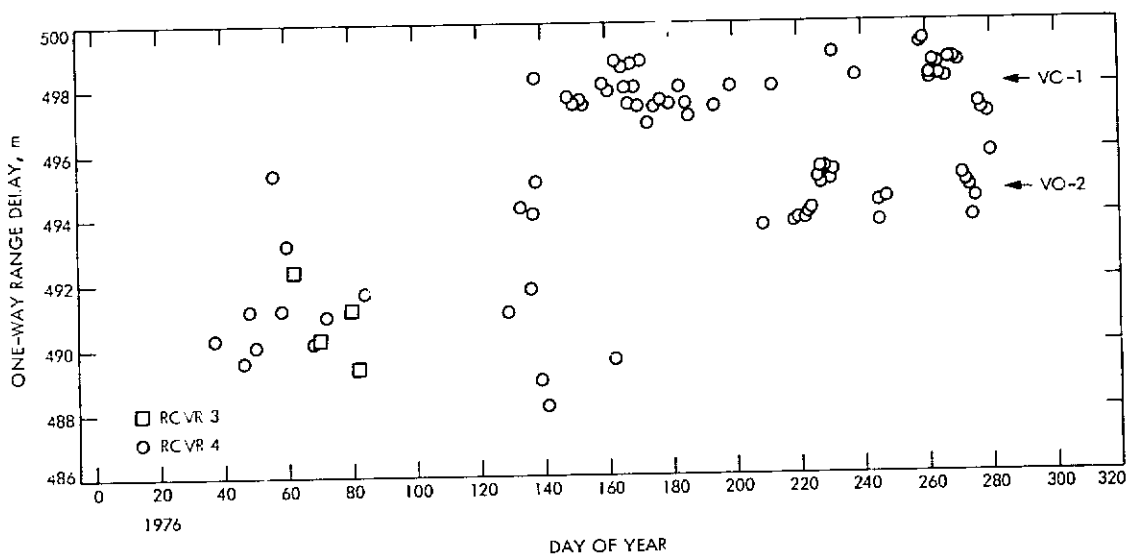

Fig. 7. Station range delay calibration data, DSS 43, X-band

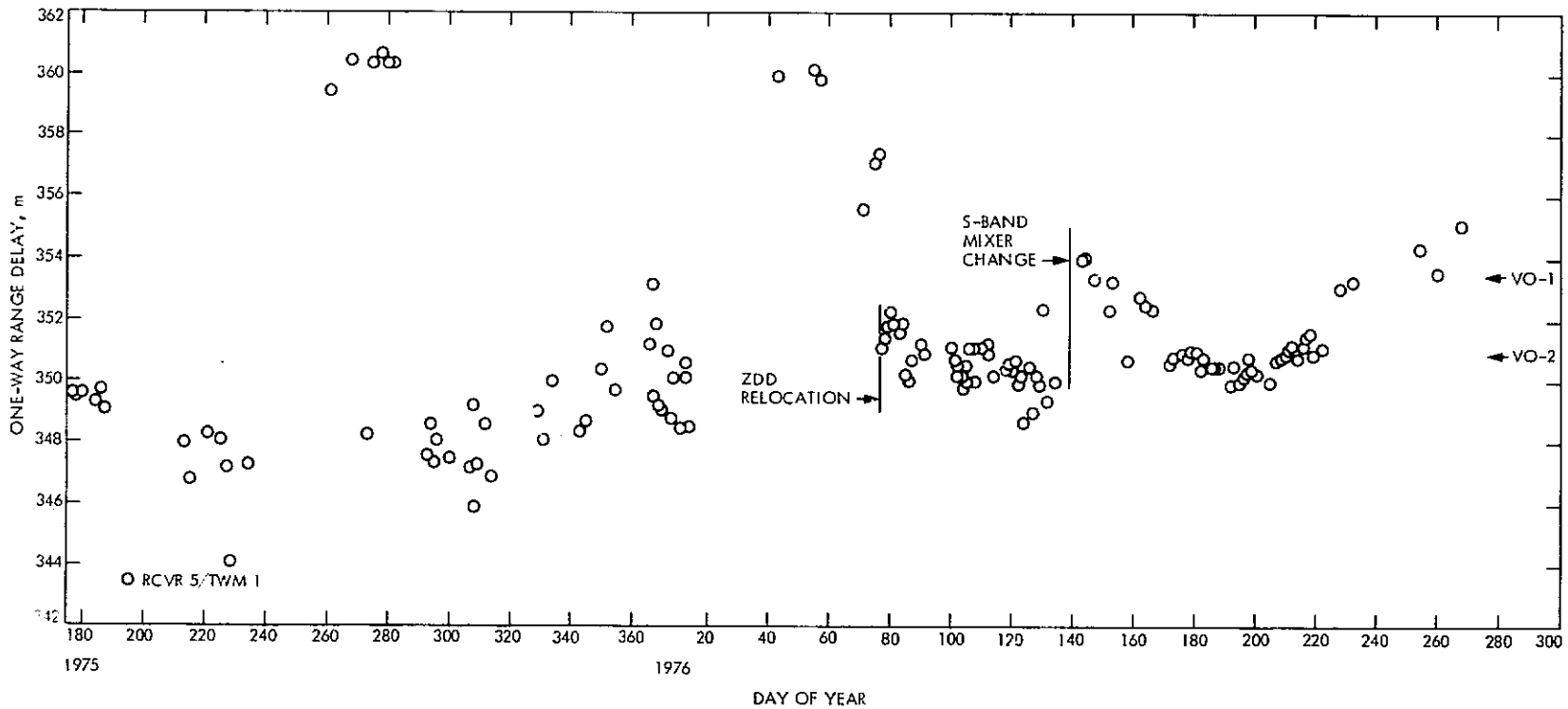

Fig. 8. Station range delay calibration data, DSS 61

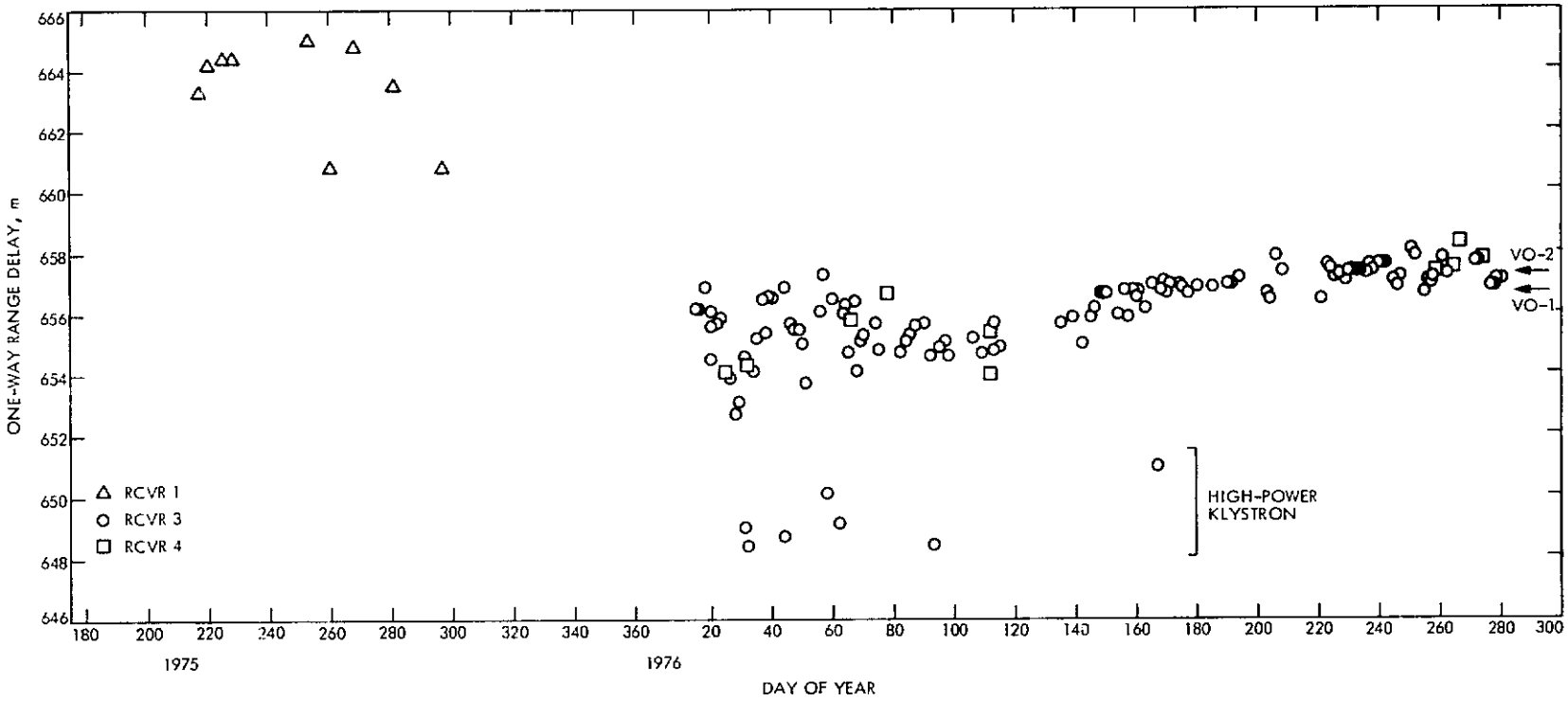

Fig. 9. Station range delay calibration data, DSS 63 S-band

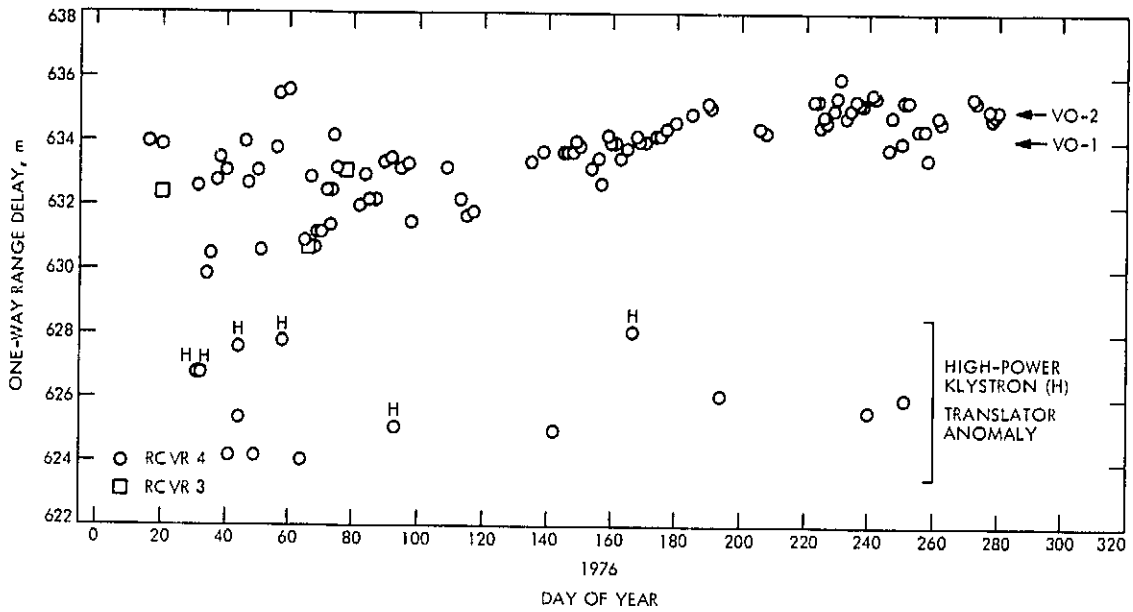

Fig. 10. Station range delay calibration data, DSS 63 X-band

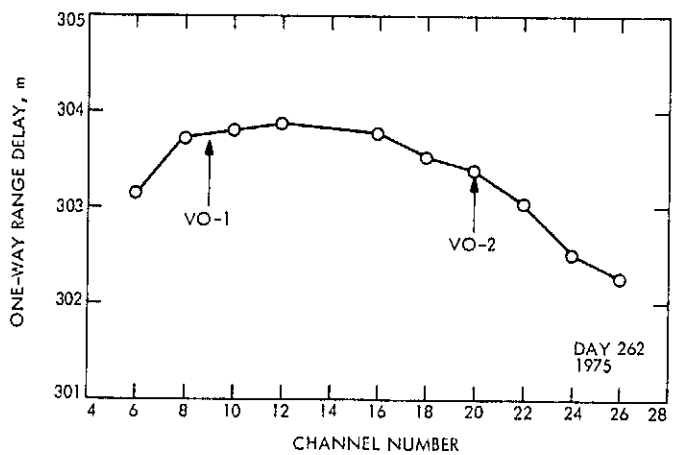

Fig. 11. DSS 11 station range delay versus frequency

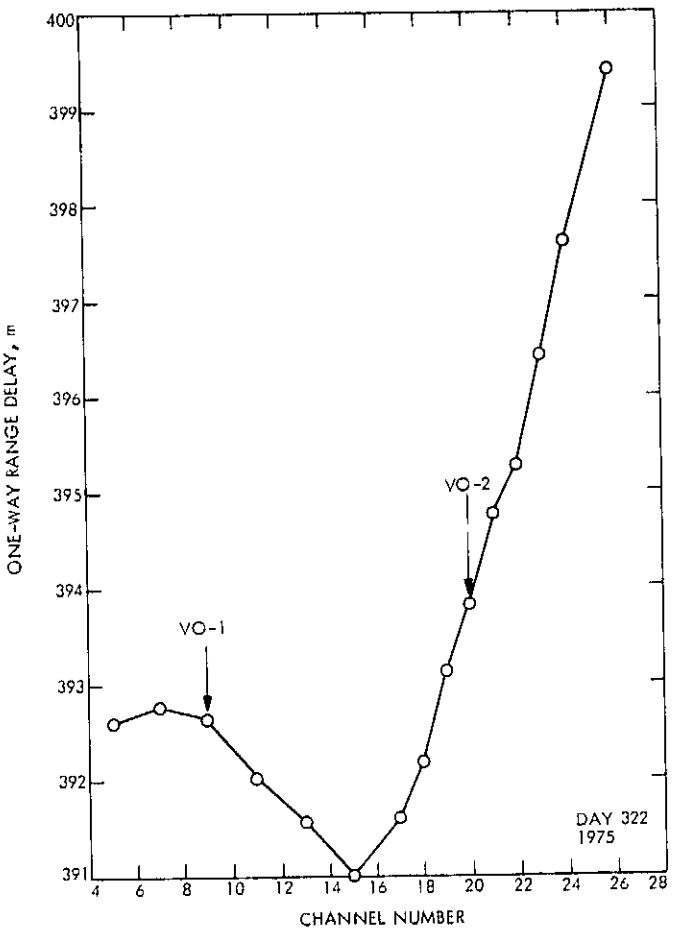

Fig. 12. DSS 42 station range delay versus frequency prior to ZDD relocation

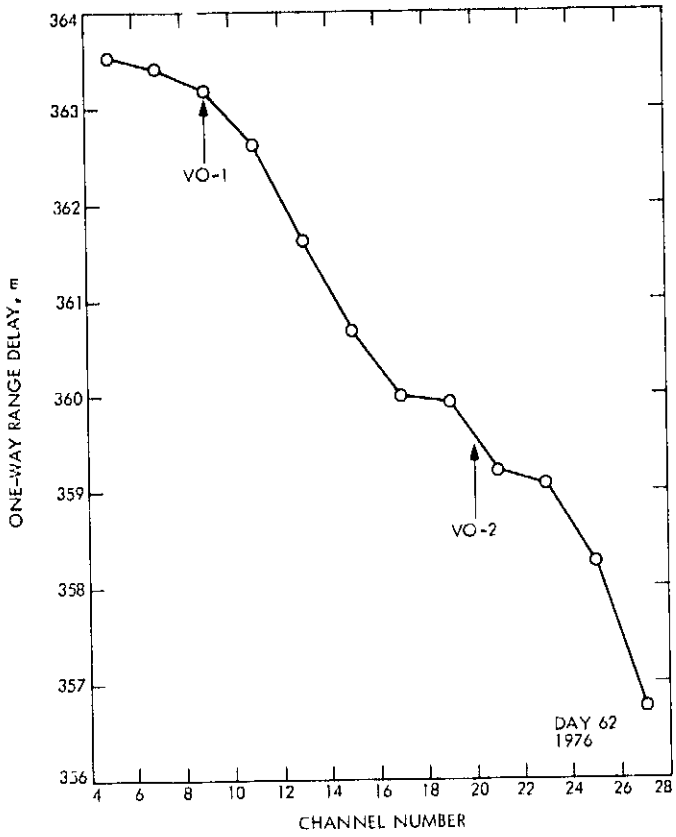

Fig. 13. DSS 61 station range delay versus frequency prior to ZDD relocation

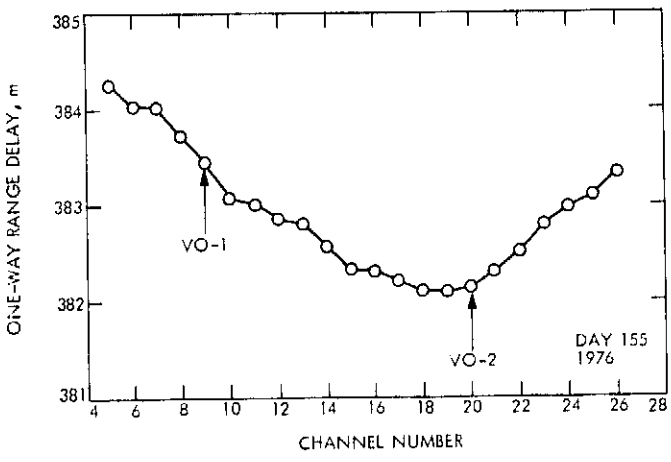

Fig. 14. DSS 42 station range delay versus frequency after ZDD relocation

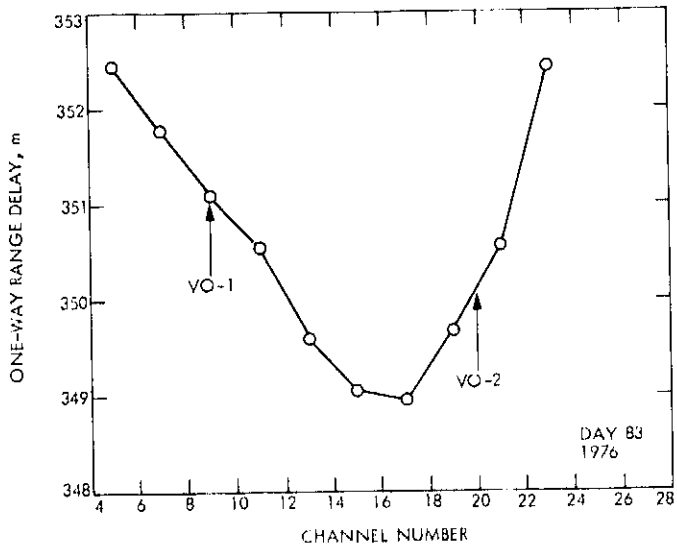

Fig. 15. DSS 61 station range delay versus frequency after ZDD relocation

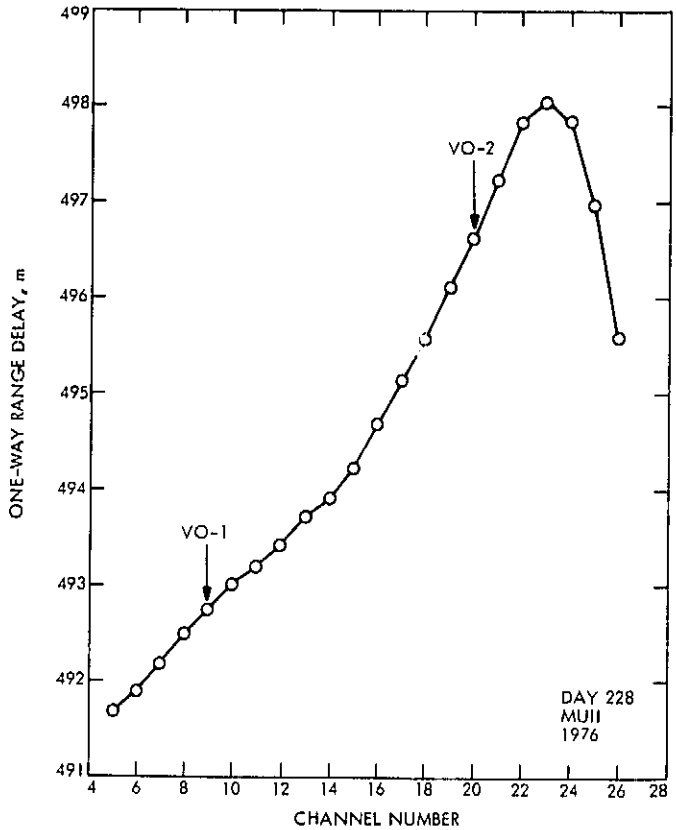

Fig. 16. S-band range delay versus frequency

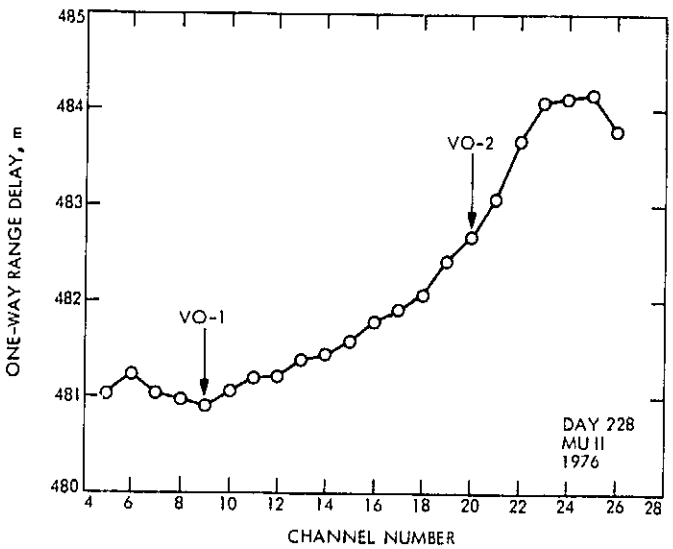

Fig. 17. DSS 14 X-band range delay versus frequency

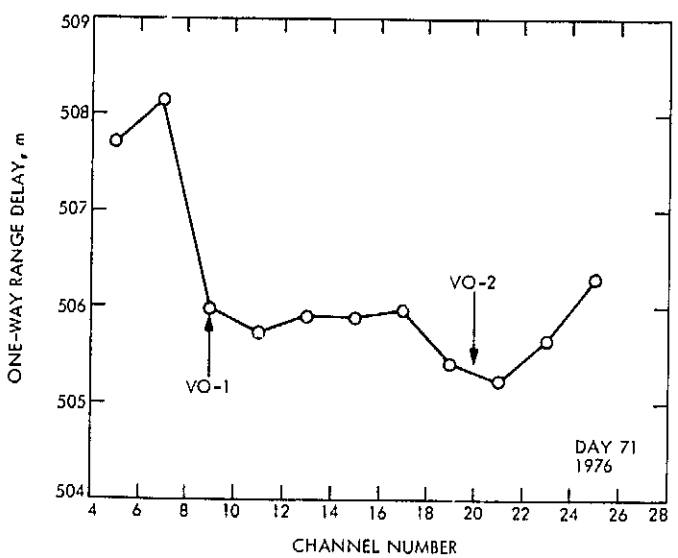

Fig. 18. DSS 43 S-band range delay versus frequency

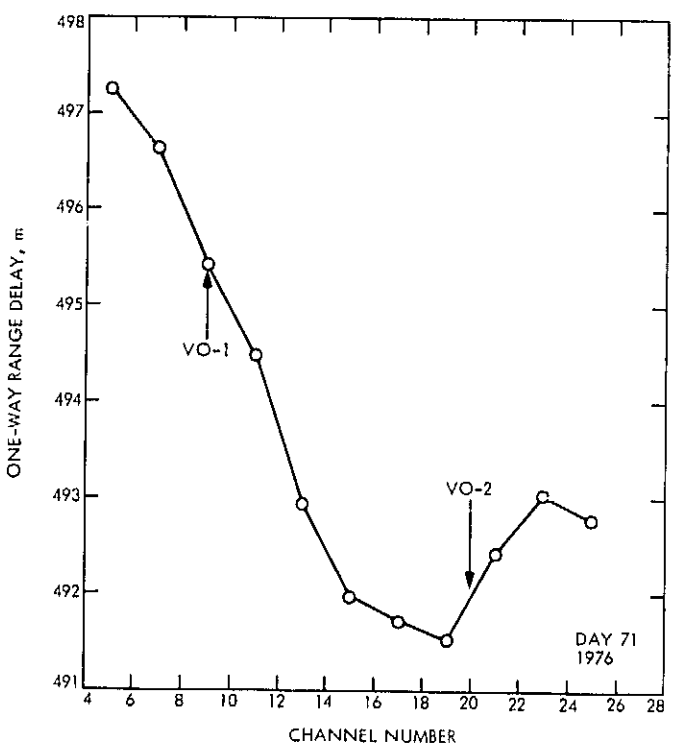

Fig. 19. DSS 43 X-band range delay versus frequency

N77-14064

DSN Research and Technology Support

E. B. Jackson
Radio Frequency and Microwave Subsystems Section

The activities of the Venus Station (DSS 13) and the Microwave Test Facility (MTF) during the period June 14 through October 10, 1976, are discussed and progress noted.

Continuing remote controlled pulsar observations are noted, along with routine observations of 22 pulsars. Preliminary installation of equipment for planned unattended operation of the Venus Station is reported, along with extensive measurements and performance evaluation of the 26-m antenna. Support of the X-band radar at the Mars Station (DSS 14), and stability and reliability testing of the DSS 13 receiving system is reported. Klystron testing and other DSN support activities of the DSN High-Power Transmitter Maintenance Facility are noted, along with energy conservation modifications to two buildings at DSS 13. Radio Science experiment support included Planetary Radio Astronomy, Pulsar Rotation Constancy, Interstellar Microwave Spectroscopy and Very Long Baseline Interferometry observations. An increased schedule of clock synchronization transmissions, planned on five-day centers, is noted, as 39 transmissions were made to Australia, DSS 43, and Spain, DSS 63.

I. Development Support Group

The activities of the Development Support Group, in operating the Venus Station (DSS 13) and the Microwave Test Facility (MTF) during the period June 14 through October 10, 1976, are discussed.

II. Station Automation

In support of RTOP 68 (Station and Network Monitor and Control Technology Development) and RTOP 69 (Tracking Station Systems Technology), DSS 13 will be the demonstration station with which remotely operated, unattended tracking operation is demonstrated.

The first phase, remote controlled observation of pulsars has been demonstrated on several occasions. During this period, 35 station support hours, of which 6 hours were remote controlled tracking, were utilized in support of this project. During the remote controlled pulsar observations, pulsars 0031–07, 0329+54, 0355+54, 0628–28, 0736–40, and 0833–45 were successfully observed without intervention by on-station personnel. The rest of the

support time was devoted to troubleshooting and performance measurement.

III. Pulsar Observations

In support of the Radio Science Experiment "Pulsar Rotation Constancy" (OSS 188-41-51-09), DSS 13 provided 130-3/4 hours of observations, during which the emissions from the pulsars tabulated in Table 1 were recorded. These data, recorded at 2388 MHz, left circular polarization (LCP), are used to determine precise pulse-to-pulse spacing, changes in this spacing, pulse shape, and pulse power content of the signals received from these pulsars.

IV. Maser-Receiver-NAR Reliability-Stability Testing

Reliability and stability testing of the DSS 13 total receiving system is conducted during nonmanned station periods. The 26-m antenna is prepositioned to a fixed azimuth and elevation and the Noise Adding Radiometer (NAR) data collection system automatically records total receiving system temperature as the 26-m antenna beam is swept across the sky by the rotation of Earth. During this period, the antenna was fixed in azimuth at 360 degrees and progressively positioned from 49.9 to 49.1 degrees elevation, and 496-/2 hours of testing were automatically performed. This testing is performed at 2295 MHz, using right circular polarization (RCP) on the 26-m antenna.

V. Unattended Operation, DSS 13

In preparation for the planned unattended operation of DSS 13, the Polarization Diversity S-Band (PDS) feedcone removed from DSS 14 has been modified into a feedcone having all the capabilities of an S-Band Polarization Diversity (SPD) feedcone, except simultaneous reception of two polarizations, but using only two waveguide switches instead of three. Two Block III Receiver-Exciters, obtained surplus from the Spaceflight Tracking and Data Network (STDN), have been installed in the Operations and Data Processing building at DSS 13 and completely checked out with the STDN and DSN frequency converters. The first "milestone" demonstration is planned to be an automated telemetry reception track from a spacecraft in March, 1977.

VI. 26-m Antenna Measurements and Evaluation

In order to evaluate the effects of several years of experimental operation on the stability of the surface panel adjustments, careful measurements of the surface deviation from the desired parabola were made on the 26-m antenna. Measurements were made at three different elevation angles: near zenith, near horizon, and at 33 degrees. The subreflector was removed and returned to JPL for precision measurements, and installation of a removable vertex plate. While the feedcone was off the antenna, antenna waveguide run measurements were made in preparation for installation of the modified feedcone described above, designated SVU (*S*-band, *V*enus, *U*nattended).

Replacement of the oil seal on one elevation ball screw was performed, and an examination of the gearbox was made to ensure that no hidden damage existed. The oil seal replacement solved the oil leakage problem, and, although brass shavings and a piece of broken gear were found in the gearcase, no immediate problem is foreseen.

After reinstallation of the subreflector, new vertex plate, and feedcone, pointing evaluation tracks were performed, using an automated program called SCOUR (*SCan* and *COrrect Using Receiver*), which utilizes the SDS-930 to provide antenna control. Using Virgo A, 3C144, and 3C273 as sources, 21-1/2 hours of pointing error evaluation were performed.

Several problems were experienced with the S-band maser refrigerator with which the 26-m antenna is equipped. During this period, the displacer crosshead drive has been overhauled and replaced twice. The system is working correctly at this time, although some audible roughness exists in the drive mechanism.

VII. X-Band Radar, 8495 MHz, 400 W

During a series of radar observations of the comet D'Arrest, the VA949J klystrons used as final amplifiers failed and were removed. In preparation for restoring the system to service, the traveling-wave tube amplifiers (TWTA) used as klystron drivers were tested, and the TWT power supplies (Logimetrics Corp. Model A300) were modified, with a new HV cable connector for improved reliability. This modification required fabrication of a complete new back panel assembly and rearrangement of connectors. After modification, one of the three power supplies developed an intermittent fault and was repaired. At this time, the TWTAs are operational.

VIII. Energy Conservation

The Operations and Data Processing (G-51) and Laboratory and Office (G-60) buildings at the Venus

Station have each been equipped with a time clock with which the lighting (interior and exterior) and air conditioning are operated. The air conditioning is on a multiday time clock, while the office and laboratory lighting is controlled by personnel-set timers, with a total time of 10 hours available. Excluding the transmitting systems, the air conditioning systems at Venus are the largest users of electricity, and automatic turnoff of this usage when the station is not manned will reduce consumption.

IX. Deep Space Network High-Power Transmitter Maintenance Facility (DSN HPTMF)

The X-3070 klystron loaned to Arecibo Radio Observatory has been returned in apparent good condition as evidenced by a vacuum check. Arecibo did not find it necessary to use this klystron.

At the request of the Transmitter Cognizant Operating Engineer (COE), a klystron socket tank, klystron focusing magnet, magnet adapter and 500-kW RF water load were loaned to Varian Corporation to be used in testing a repaired DSN 100-kW klystron. These items were returned after testing was completed.

In continuing support of the DSN mission, four each, 20-kW klystrons, Varian Model 5K70SG, were tested to assure usability in case of need. (These klystrons had been obtained from the STDN.) Two of the four klystrons meet all applicable specifications. Three arc detectors, fabricated by a vendor, were checked, wiring errors corrected, repairs made where necessary, and operation and response time verified. Additionally, a light source and power supply for the crowbar on the HV power supply at DSS 14 were repaired.

Routine scheduled maintenance was performed on the 20-kW test transmitters, and the DSS 13 transmitter control system was converted to the same solid state configuration used in the DSN. During this maintenance period, a documentation update program was started to ease the planned configuration of the system for unattended operation for uplink transmissions to spacecraft. During this maintenance period, the X-3070 magnet used in the Advanced Systems Demonstration transmitter failed due to inadequate coolant flow, and the system is currently inoperative.

As part of a program to improve the spectral purity of the uplink transmissions, a high-resolution spectrum analysis was made of the carrier emitted by the 20-kW test transmitters and also of the HV power supply used with these transmitters. The same spectral components, at similar relative amplitudes, were found in both the RF and HV dc spectra. Detailed analysis is being performed.

X. Planetary Radio Astronomy

In support of the Radio Science experiment "Planetary Radio Astronomy" (OSS 196-41-73-01), DSS 13 measures and records the radiation received at 2295 MHz from the planet Jupiter and various radio calibration sources. These measurements use the 26-m antenna, the S-band station receiving system, and the NAR. During this period, 109-3/4 hours of observations were made, during which the radiation received from Jupiter and the calibration sources tabulated in Table 2 were measured and recorded.

XI. Interstellar Microwave Spectroscopy

In support of the Radio Science Experiment "Interstellar Microwave Spectroscopy" (OSS 188-41-52-12) DSS 13 provided 23 hours of station support, including 17-3/4 hours of tracking reception at 2273.5 and 2321.729 MHz. Sources used for this experiment included 3C58, NGC 7822, and 118 + 48.

XII. VLBI Support

In support of the several programs that utilize Very Long Baseline Interferometry (VLBI) techniques, DSS 13 devoted 6-3/4 hours of tracking to check out new equipment utilized for this purpose. Sources observed were 3C84 and 3C273.

XIII. Clock Synchronization System

The interval between transmission of clock synchronization signals was shortened at the request of the Viking Project. This increased transmission schedule, programmed on five-day centers, was instituted in support of the encounter, orbit, and landing phases of Vikings I and II spacecraft with Mars.

Although Spain, DSS 63, had some difficulty with their receiving system, 18 transmissions were made to them as scheduled by DSN Scheduling. Another 21 transmissions were made to Australia DSS 43, for a total transmission time of 40-3/4 hours. Both stations are now reporting good reception and correlation with their local station clocks.

Table 1. Pulsars observed at DSS 13, June 14 through October 10, 1976

0031−07	0833−45	1818−04
0329+54	1133+16	1911−04
0355+54	1237+25	1929+10
0525+21	1604−00	1933+16
0628−28	1642−03	2021+51
0736−40	1706−16	2045−16
0823+26	1749−28	2111+46
		2218+47

Table 2. Radio calibration sources observed at DSS 13, June 14 through October 10, 1976

3C17	3C273	3C418
3C48	3C274	NRAO530
3C84	3C279	OJ287
3C123	3C286	PKS0237-23
3C138	3C309.1	PKS2134-00
3C145	3C345	Virgo A
3C147	3C348	
3C218	3C353	

NASA−JPL−Coml., L A., Calif